12-2014

Thermodynamic Modeling of Uranium and Oxygen Containing Ternary Systems with Gadolinium, Lanthanum, and Thorium

Jacob Wesley McMurray
University of Tennessee - Knoxville, jmcmurr6@vols.utk.edu

To the Graduate Council:

I am submitting herewith a dissertation written by Jacob Wesley McMurray entitled "Thermodynamic Modeling of Uranium and Oxygen Containing Ternary Systems with Gadolinium, Lanthanum, and Thorium." I have examined the final electronic copy of this dissertation for form and content and recommend that it be accepted in partial fulfillment of the requirements for the degree of Doctor of Philosophy, with a major in Energy Science and Engineering.

Theodore M. Besmann, Major Professor

We have read this dissertation and recommend its acceptance:

Claudia J. Rawn, Brian D. Wirth, James R. Morris

Accepted for the Council:

Carolyn R. Hodges

Vice Provost and Dean of the Graduate School

(Original signatures are on file with official student records.)

Thermodynamic Modeling of Uranium and Oxygen Containing Ternary Systems with Gadolinium, Lanthanum, and Thorium

A Dissertation Presented for the
Doctor of Philosophy
Degree
The University of Tennessee, Knoxville

Jacob Wesley McMurray
December 2014

Dedicated to my wife

Perla McMurray

my children

Audrey and Samuel McMurray

and my parents.

Ron and Teddi McMurray

ACKNOWLEDGEMENTS

"No man is an island entire of itself; every man is a piece of the continent, a part of the main; if a clod be washed away by the sea, Europe is the less, as well as if a promontory were, as well as any manner of thy friends or of thine own were; any man's death diminishes me, because I am involved in mankind. And therefore never send to know for whom the bell tolls; it tolls for thee." – John Donne

The words of John Donne, the epigraph for Ernest Hemingway's 1940 novel *For Whom the Bell Tolls* and likely the inspiration for the title, still stirs my spirit and embodies my philosophy on life; we all need one another, we are all in this thing together. To believe that any one person can create anything of value in a vacuum is *hubris of the gods*. I am therefore, profoundly grateful to Dr. Lee Riedinger, Dr. Mike Simpson, Dr. Jim Roberto, and the Bredesen Center for Interdisciplinary Research and Graduate Education for this remarkable opportunity to contribute to science and potentially impact energy issues. I am eternally grateful to Dr. Theodore M. Besmann, my mentor, for his instruction, patience and confidence in the skills I developed under his tutelage.

A special thanks to Stewart Voit for fabricating samples, sharing laboratory expertise, and at – length discussions on the science behind our experimental measurements and Dr. Dongwon Shin for impromptu thermodynamic modeling lectures. I am grateful to Dr. Jaime Morris, Dr. George Pharr, Dr. Brian Wirth, and Dr. Claudia Rawn for their contribution to my education and agreeing to take part as members of my dissertation committee. The cooperation of my classmates, to whom I owe much gratitude for many hours of study, was instrumental in my success as a student. Finally, I must acknowledge my family for their advice, moral, emotional, and financial support.

Research supported by the US Department of Energy, Office of Nuclear Energy, Fuel Cycle Technology Program.

ABSTRACT

The CALPHAD method is used to assess the thermodynamic properties and phase relations in the U-M-O system where M = Gd, La, and Th. A compound energy formalism (CEF) model for fluorite $UO_{2\pm x}$ [urania] is extended to represent the complex $U_{1-y}M_yO_{2\pm x}$ [urania solid solution] phases. The lattice stabilities for fictive GdO_2 [gadolinia] and LaO_2 [lanthana] fluorite structure compounds are calculated from density functional theory (DFT) for use in the CEF for $U_{1-y}M_yO_{2\pm x}$ [urania solid solution phase] while U^{6+} [uranium 6 plus cation] is introduced into the cation sublattice of the CEF for $U_{1-y}M_yO_{2\pm x}$ [urania solid solution phase] to better reproduce phase relations in U-Ln-O systems at high fixed trivalent Ln [lanthanide] compositions. Tentative Gibbs functions and CEF representations for the fluorite derivative rhombohedral phases were developed and the two-sublattice liquid model (TSLM) was used to describe the melt.

Equilibrium oxygen pressures over $U_{1-y}Th_yO_{2\pm x}$ [urania thoria solid solution] were obtained from thermogravimetric measurements and used together with those reported in the literature, phase relations, and other experimentally determined thermodynamic values to fit adjustable parameters of the CEF and TSLM along with the standard state enthalpy and entropy of the Gibbs functions representing the stoichiometric compounds. The models can be extended to include other actinides and fission products to develop higher order multi-component system assessments to support further experimental efforts and the development of multi-physics fuel performance simulation codes.

TABLE OF CONTENTS

LIST OF TABLES

LIST OF FIGURES

CHAPTER 1

INTRODUCTION

"The ultimate purpose of the fuel-pin analysis may be simply stated: given the geometry of the fuel element (i.e., the fuel radius, the cladding thickness, and the size of the fuel-cladding gap), the initial composition and porosity of the fuel, and the power history at which the pin is to operate, to calculate the length of time that the cladding performs its primary function of separating the coolant from the fuel."—D.R. Olander

Reliable and sustainable energy is the cornerstone of a robust economy on which any healthy and thriving society is based. The industrial age owes its existence, in large part, to the availability of inexpensive and vast quantities of fossil fuels, particularly coal and crude oil. There is no doubt technology would not have progressed to today's level if it weren't for these natural resources to power scientific study and discovery. In industrialized nations, the ordinary citizen has historically had access to affordable energy from abundant fossil fuel sources like coal, oil, and natural gas enabling use of state of the art technological implements that facilitate entrepreneurship, industry, economic growth and a higher quality of life. Unfortunately, since the dawn of the Industrial Revolution, the world's deposits of fossil fuels have been significantly depleted to the point that the most easily accessible reserves have been harvested. Those that remain are increasingly more expensive to extract and yield lower energy return on energy invested (EROEI).

The world has consumed over 1.2 trillion barrels of oil since the beginning of the petroleum age in 1859 [1] and peak oil production is estimated to occur sometime in the

2030s [2]. While remaining crude oil reserves are estimated to be around 9 trillion barrels, only about 1 trillion are in proven economically profitable locations [1] meaning the rest will require more capital investment and yield lower EROEI. While the outlook for other fossil fuels, like coal and natural gas, is not so bleak, it is becoming more difficult to recover these resources. Furthermore, the scientific community has come to the consensus that carbon emissions, the result of fossil fuel energy production, are altering the climate of our planet. The situation is only exacerbated by population growth and greater wealth of developing nations while the depletion rate of existing reserves is compounded by lower EROEI.

It is clear from Fig. 1.1 that the trend is towards a more crowded and energy demanding planet. Consumption of all forms of energy is expected to double by 2050 [3] and the world's fossil fuel reserves will steadily deplete, energy will become more expensive, and the dream of perpetual human progress will ineluctably vanish without a sustainable substitute. There is a need to supplant carbon based energy sources with feasible and sustainable alternatives due to the finite supply of traditional these fossil fuels and the deleterious effects of their emissions on the environment.

For this reason, nuclear energy must play an important role in powering the world's future. In the short term, its use must increase to keep up with demand and avoid undesirable carbon emissions. This can be achieved by building new nuclear power plants and through better more efficient use of existing ones. Furthermore, nuclear energy constitutes a significant portion of the world's energy portfolio that cannot be quickly and easily replaced. This work aims to address one small but significant part of larger efforts to develop physics based fuel performance simulation programs that could potentially extend the life of existing reactor materials and/or aid in the qualification process of new ones to ultimately increase the economic viability of nuclear power for electricity generation.

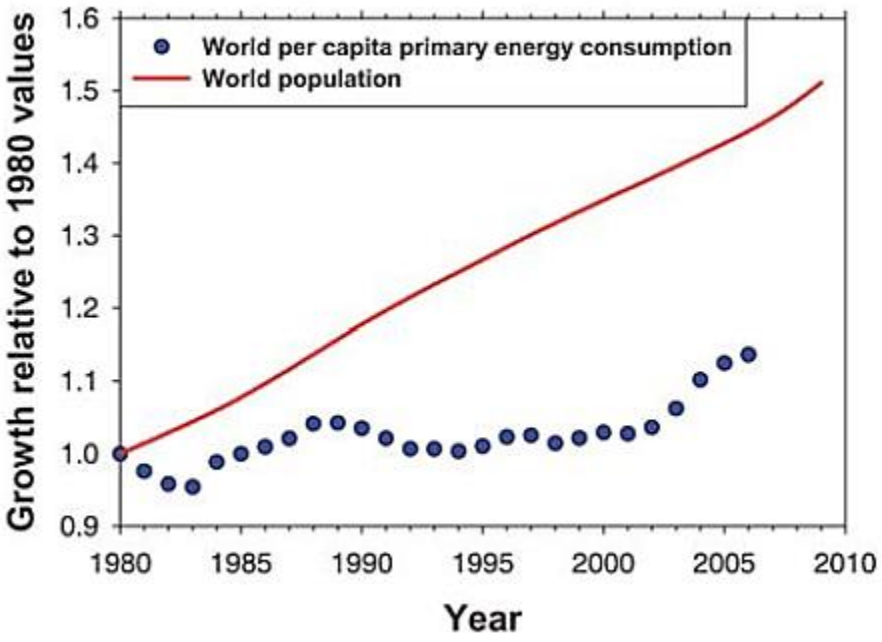

Fig. 1.1. Energy consumption and population growth versus time from www.census.gov and www.eaia.gov.

1.1 Nuclear power

Electricity from a nuclear power plant is produced by converting liquid water into steam using the heat generated from a nuclear reaction. The steam then turns a turbine that coverts this work energy into electricity. In a light water reactor (LWR), the principle reaction is a fissioning of the uranium isotope ^{235}U and that of bred ^{239}Pu that produces two atoms whose mass sum to less than that of the uranium or plutonium; thus, the loss of mass is manifested as heat energy and quantified by the famous Einstein equation $E=mc^2$. For perspective, a single fuel pellet typical for an LWR weighs about 4 grams and can generate about as much energy as 800 kg of coal [4].

There is no CO_2 or other air pollutants emitted during the fuel consumption stage and, relative to the amount of energy they produce, nuclear power plants have a small carbon footprint even when considering the construction stage of their implementation. Therefore, this means of energy production has a significant impact on reducing carbon emissions believed to be the major cause of global climate change. There are drawbacks, however; a major issue is radioactive by-products from the extraction, fabrication, and consumption stages of the process [5]. The industry is heavily regulated and this combined with the managing of high level radioactive waste adds significant costs to this form of power generation.

In the United States there are about 100 operating commercial reactors and all of them are LWRs that use urania, or UO_2, as a fuel source in the form of a cylindrical pellet with a diameter around 6.3 mm and a height of about 12 mm; the geometry is illustrated in Fig. 1.2,. In the Westinghouse NSSS Model 412 commercial PWR, the pellets are stacked in a fuel pin, or rod, about 186 deep [6]. Two hundred and sixty four pins are bundled together to form the fuel assembly shown in Fig. 1.3; there can be 193 fuel assemblies in a reactor core. In general the fuel stack, pins per assembly, and assemblies per core vary depending on type of reactor (PWR or BWR) and core design (Westinghouse, Hitachi, B&W, etc.).

An important component of LWR fuel rod design is the zirconium alloy cladding material that separates the ceramic pellet from a coolant loop and serves two general purposes. First, it is a containment vessel for the radioactive fission and activation products that are generated within the fuel pin during operation. Second, it protects the ceramic urania fuel pellet from the water used in the coolant loop which would otherwise chemically react by oxidizing UO_2, potentially producing dangerous quantities of hydrogen gas and releasing radionuclides. The reaction is given by Eq. 1. 1.

$$UO_2 + xH_2O \leftrightarrow UO_{2+x} + xH_2 \qquad \textbf{1. 1}$$

1.2 Fuel and fission product chemistry

The oxygen potential, given by Eqn. 1. 2, is the partial molar Gibbs free energy for O_2 and is the most significant chemical property in a nuclear fuel element [7].

$$\mu_{O_2} = {}^{\circ}G_{O_2} + RT \ln p_{O_2} \qquad \textbf{1. 2}$$

Here, p_{O_2} is a dimensionless quantity defined by the oxygen pressure divided by the standard state pressure of 1 bar, R is the ideal gas constant, T is the absolute temperature, and ${}^{\circ}G_{O_2}$ is the standard state Gibbs energy.

Pure urania is often represented with the formula $UO_{2\pm x}$ since it can be a non-stoichiometric oxide at elevated temperatures and exhibits a wide homogeneity range as can be seen from the phase diagram presented in Fig. 1.4. The composition of $UO_{2\pm x}$ is often expressed as an oxygen-to-metal ratio or O/M. The μ_{O_2} determines whether or not

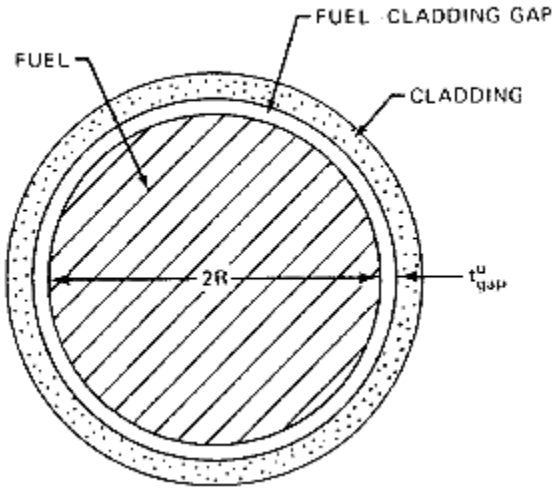

Fig. 1.2. Cross section of a nuclear fuel rod from Olander [7].

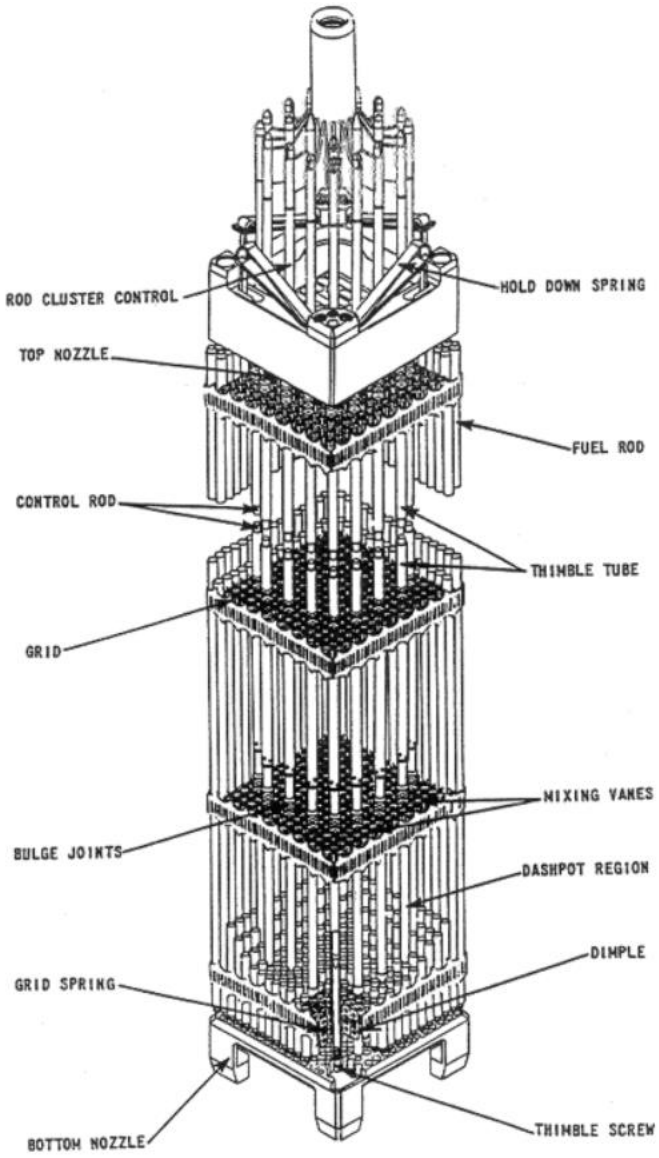

Fig. 1.3. Diagram illustrating the major components of the fuel assemblage taken from [8].

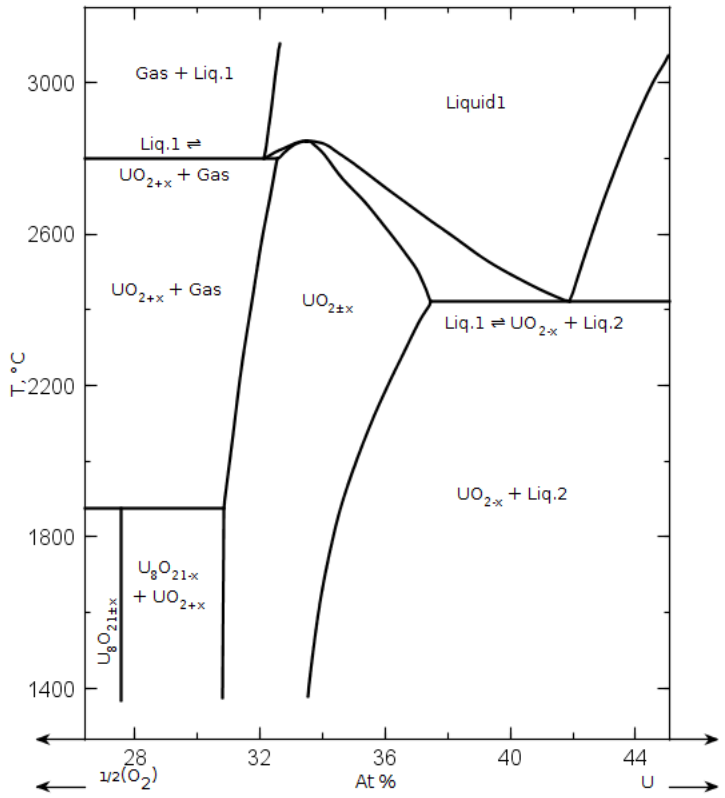

Fig. 1.4. Section of the phase relations in the U – O system in the vicinity of the fluorite solid solution from [9].

the cladding undergoes some oxidation, the phases present, and the O/M of $UO_{2\pm x}$ which in turn affects many properties of the fuel.

Stated another way, μ_{O_2} is determined by the composition and temperature of the urania phase. In a fuel element, this relationship is complicated by a steep temperature gradient and the generation of fission products. The temperature profile creates chemical potential imbalances that drive species (O, FP's) transport and redistribution in the fuel element. Furthermore, when a uranium atom absorbs a thermal neutron and fissions, the result is one atom around 1/3 and the other about 2/3 the mass of U^{235}. This gives a bimodal distribution as can be seen in Fig. 1.5. Many high yield FP's are soluble in the fluorite matrix and therefore significantly affect the oxygen potential of the phase. Among these are Y, La, Ce, Pr, and Nd.

Apart from the rare-earths, Y, and Pu that dissolve in the fluorite matrix, fissioning of a uranium atom results in elements that form separate oxides, metallic inclusions, and gasses. A graphic of this complex behavior resulting from irradiation is given in Fig. 1.6 after Olander [7]. The noble gasses Xe and Kr constitute the majority of the vapor phase fission products. These elements are largely insoluble in the fluorite phase, coalesce to form bubbles that cause the fuel to swell, or migrate to grain boundaries and cracks where they can escape into the plenum and gap region increasing the fuel pin pressure and decreasing the thermal conductivity of the fuel-clad gap. The elements present from fission and activation, both solid and gaseous, determine thermal properties as well as influence the degree of swelling that a fuel pellet experiences.

1.3 Computational thermodynamics coupled fuel performance simulations

It is important that commercial nuclear reactors operate within the limits of design to ensure safe and effective delivery of electrical power. The fundamental physics of many of the phenomena that occur in a fuel element during normal operation are still

poorly understood [10], thus many performance simulators rely heavily on empirical relations [11] that suffer from two major problems. First, they cannot be extrapolated outside of the range of validation; second, they require a vast amount of resources to acquire the necessary knowledge for successful implementation. As a result, an effort to model behavior of an operating fuel element using a multi-physics approach is the subject of intense interest spanning multiple disciplines. The first step is to benchmark the simulation codes to conventional oxide fuel systems since a tremendous amount of experimental data already exists for them. From this, the development of next generation advanced reactor materials can be designed and qualified with the aid of these powerful computational predictive aids; the simulation results can be subsequently validated by experiments translating into huge savings in time and treasure.

Application of thermodynamics is an important component of many continuum scale simulations. The high operating temperatures of a reactor result in a rapid approach to equilibrium; however, many phenomena are dominated by transport processes. Here, thermodynamic arguments are necessary but not sufficient for understanding thermal and atomic diffusion in fuel [7]. Figure 1.7 captures the essence of the engineering approach, that is to discretize the system to simulate the fuel behavior on a continuum scale using a finite difference, finite volume, or finite element method [12]. Each finite unit is considered to be an isolated isothermal-isobaric system in *local thermodynamic equilibrium* (LTE). Since reactors operate in a temperature regime that result in comparatively short reaction times, even in the solid state, and since the time increment in nuclear performance simulations are typically very long [13], chemical kinetics are rendered practically insignificant and the LTE assumption is a reasonable one. Therefore, thermodynamic models are useful for determining the chemical state and the material properties of the fuel; these are important inputs for representing many kinetically driven processes like phase transformations, microstructural evolution and transport phenomenon. For example, the O/M, and therefore the equilibrium oxygen interstitial and vacancy concentrations, affects many of the properties of UO_2; there is already an

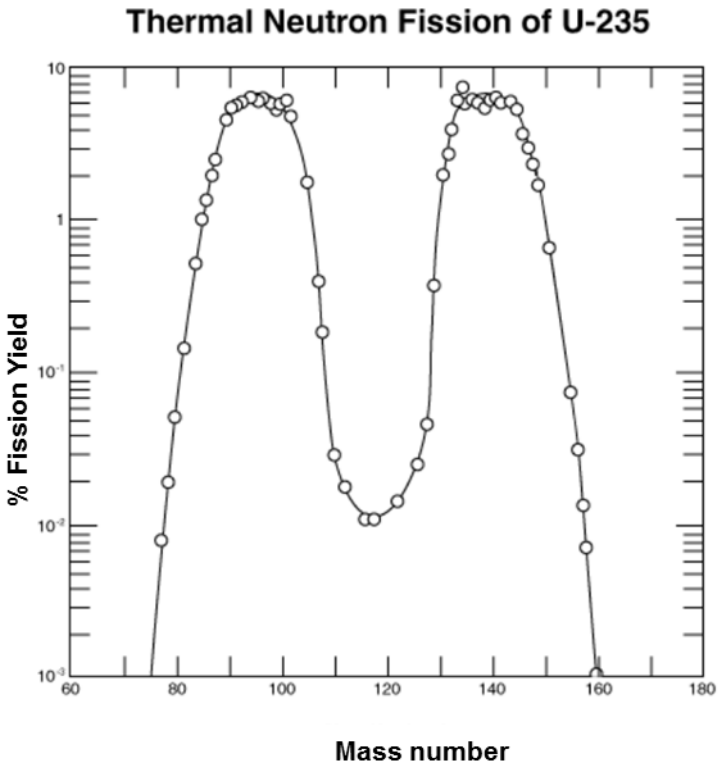

Fig. 1.5. Percent yield by mass number from fissioning of uranium after absorption of a thermal neutron modified after Olander [7].

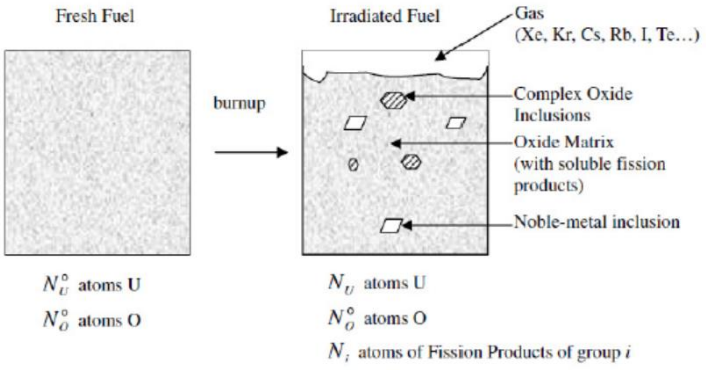

Fig. 1.6. Graphic of the microstructural evolution that occurs in fuel with irradiation modified after Olander [7].

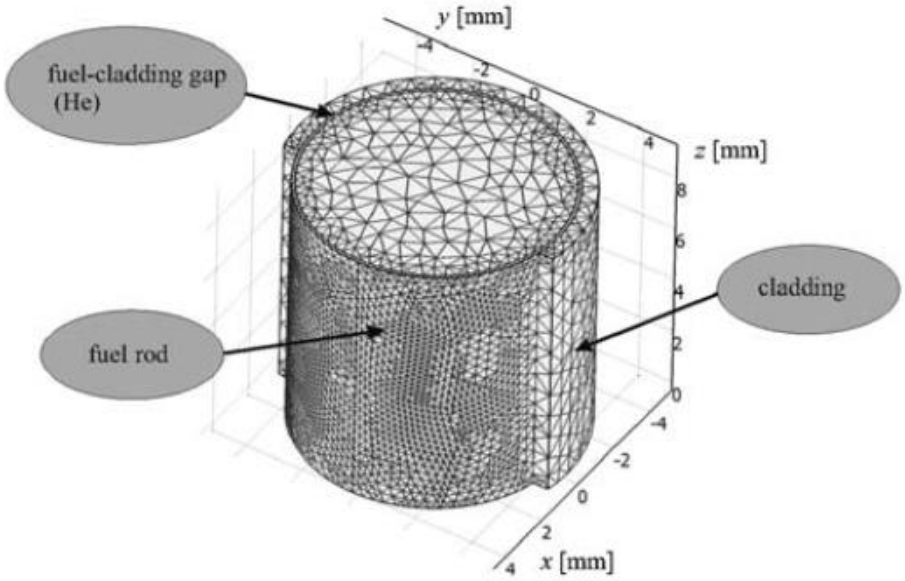

Fig. 1.7: Discretized section of a fuel element for continuum simulation from [10].

effort within the CALPHAD (**CAL**culation of **PHA**se **D**iagrams) community to couple the CEF representation for $UO_{2\pm x}$ to diffusivity relations [14].

1.4 Goals of research

An aim of this effort is a more robust description of the thermodynamics of the U-Gd-O, U-La-O, and U-Th-O ternaries in order to better understand the chemical behavior at equilibrium and the non-equilibrium driving forces of high burnup nuclear fuel. This is accomplished by developing Gibbs energy models of the phases that constitute each system within a framework that allows for their extension and/or integration into higher ordered multicomponent thermodynamic assessments as part of larger nuclear fuel database development efforts. The CALPHAD methodology is used, therefore the models are selected to represent the physical and chemical properties of each phase as best as possible; for example the structure and ordering of the crystalline phases are considered when constructing a sublattice model. Further, reproducing the behavior associated with oxygen non-stoichiometry of many of the phases is facilitated by the use of multiple cation oxidation states to maintain charge neutrality. These types of considerations permit extrapolations with a higher degree of confidence and model development based on representations of analogous structures in similar systems.

CHAPTER 2

THERMODYNAMIC MODELING OF COMPLEX CRYSTALLINE PHASES AND IONIC LIQUIDS

"Computational thermodynamics is a phenomenological scientific discipline that enables metallurgical engineers and materials scientists to calculate phase diagrams and to numerically simulate and study phase equilibria and phase transformations. The thermodynamic properties as a function of composition and temperature can also be calculated." – CALPHAD website

Over 40 years ago, Larry Kaufman and Himo Ansara organized the first CALPHAD meeting with the aim of developing a framework for self-consistent modeling of combined thermodynamic properties and phase equilibria—this became known as the CALPHAD method. Since then, CALPHAD has become more of a movement than a method with a membership organization growing in both the number of scientists employing the approach and the scope of materials to which the methodology is applied as well as a flagship journal *CALPHAD – Computer coupling of phase diagrams and thermochemistry*. Advances in science and computing performance have facilitated the implementation of theoretical first principles calculations into thermodynamic assessments and the development of sophisticated commercial computational thermodynamic software packages like Factsage® and Thermocalc®, to be discussed in

more detail in Section 2.2; these achievements have grown from and form a fundamental part of present day CALPHAD [15].

2.1 CALPHAD methodology

In the CALPHAD approach, all available data are critically assessed and utilized to build the most accurate and comprehensive representation of the phases in a system. The aim is self-consistent models that predict thermodynamic properties and equilibria to be used for phase diagram construction that can be confidently extrapolated beyond the range of validation. The ultimate goal is the development of databases for systems of technological importance that can be extended to represent higher ordered multicomponent systems *ad hoc*; this is facilitated by models based on the physical and chemical properties of the phases, for example the crystallography, bonding, order-disorder transitions, and magnetism [16]. Databases and models should be constantly updated and improved. A core tenet of the CALPHAD methodology is the periodic re-assessment of systems, a re-examination of the existing data from which they are determined, and new experiments for validation of the models in extrapolated regions.

A graphic of the CALPHAD approach relating the associated individual components to the methodology is given in Fig. 2.1. The use of first principles methods, particularly density functional theory (DFT), has come to play an increasingly important role in CALPHAD modeling to determine thermodynamic values that are difficult or otherwise impossible to obtain experimentally, such as properties of meta-stable or unstable phases. The structure of crystalline materials should inform the selection or development of models that can represent the defects and site occupancy of the species comprising the solid; this information can generally be determined from X-ray diffraction (XRD) analyses. Once a model is chosen to represent the phase, thermodynamic data determined from experimental or *ab initio* techniques are used to optimize the adjustable parameters of the model using a computational software package.

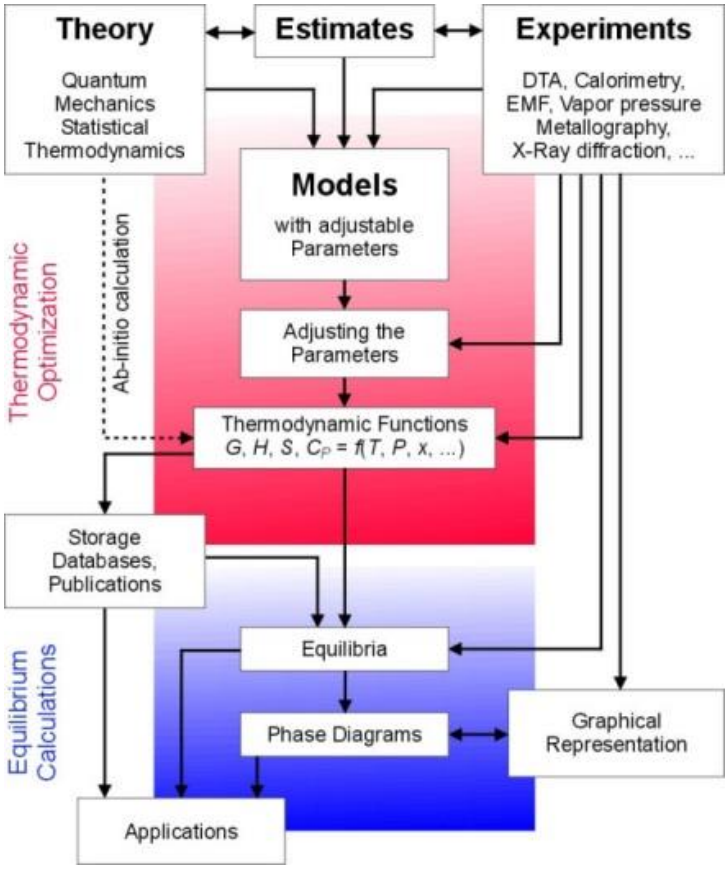

Fig. 2.1 Flow chart for CALPHAD computer coupling of phase diagram construction and thermochemistry after Zinkevich [17].

.

2.2 Computational thermodynamic codes

In the 1950s, White et al. [18] developed an algorithm for minimization of the Gibbs energy of multicomponent gas mixture for computer implementation using the method of steepest descent. While techniques have evolved over the years for thermodynamic equilibrium calculations for ever more complex solution phases and multi-component systems, most are variations of the method of White et al. and all are based on one fundamental concept, that is attaining the global minimum of the total Gibbs energy satisfying the condition of conservation of mass [12].

The two most robust and widely cited CT software packages in the open literature are Factsage® and Thermocalc®. Factsage uses an equilibrium solver developed for the SOLGASMIX code by Eriksson [12, 19-21] while Thermocalc is based on an algorithm after Hillert and Jansson [22]. The fundamental operation of both programs is essentially the same allowing for versatile thermodynamic properties output and phase diagram construction. They also include an optimization module for fitting adjustable parameters of Gibbs functions and solution models using thermodynamic values and phase equilibria data. Both Factsage and Thermocalc have an established record of use for modeling of nuclear materials systems and are capable of handling 48 and 20 components respectively [12]. Other commercial thermodynamic packages include Thermosuite, MTDATA, PANDAT, HSC, and MALT to name a few [23]. These software facilitate the use of sophisticated models needed to describe many of the complex crystalline and liquid solution phases to be discussed in the next section

2.3 Sublattice models

The modeling of complex interstitial and substitutional solutions of crystalline phase can best be accomplished with a sublattice approach using either a reciprocal solid solution (RSS) or compound energy formalism (CEF) model. The two are not easily distinguishable as the RSS is a special case of the CEF. Another difference lies in the

fact that the CEF is a broadly applied formalism approach for which the RSS, depending on the chemical formula of the crystal, could be a model used within the CEF framework.

Since the CEF assumes the general form of the sublattice model it will be used here to generate a description. The long range ordering (LRO) of a crystal with multiple sites, or sublattices, on which mixing takes place gives rise to an entropy of mixing term expressed as:

$$S^{CEF} = -R\left(\sum_s \sum_J n^s y_J^s \ln y_J^s\right) \qquad \textbf{2. 1}$$

where y_J^s is the site fraction for end-member J of the constituent on sublattice *s* and n^s is the stoichiometric coefficient of sublattice *s*. There is a mechanical mixture of all the end-member *compounds*, called a surface of reference ($G^{s.r}$); that is, all possible combinations of the members from different sublattices. Here, the term *compound* is italicized and loosely applied since some combinations may be unphysical or fictive, meaning that they only exist in solution and not as a pure substance. The surface of reference is described in general mathematical terms as:

$$G^{s.r.} = \sum_J {}^oG_J \prod_s y_J^s \qquad \textbf{2. 2}$$

where ${}^oG_J$ is the Gibbs energy for end-member *J* and the $\prod_s y_J^s$ term accounts for all the sublattices that contain components of end-member *J*. Combining Eqns. 2. 2 and 2. 3 and adding ${}^{xs}G$ gives the common form of the molar Gibbs energy CEF expression:

$$G^{CEF} = \sum_J {}^oG_J \prod_s y_J^s + RT\left(\sum_s \sum_J n^s y_J^s \ln y_J^s\right) + {}^{xs}G \qquad \textbf{2. 3}$$

where ${}^{xs}G$, the excess Gibbs energy, represents interactions between constituent members of the same sublattice. It is expressed as a Redlich-Kister [24] polynomial in terms of site fractions as:

$${}^{xs}G = \prod_s y_J^s \left[y_K^i \sum_{n=0}^{N} \left(y_J^i - y_K^i\right)^n \times {}^nL_{J\cdot K} \right] \qquad \textbf{2. 4}$$

where y_K^i and y_J^i are the interacting constituents of sublattice *i*.

The interaction parameters, ${}^nL_{J\cdot K}$, are represented as a function of temperature following the form:

$${}^nL_{J\cdot K} = a + bT + cT\ln T + dT^2 + eT^3 \ldots \qquad \textbf{2. 5}$$

Liquid mixtures can be represented with a regular solution model but a tendency for ordering necessitates a more sophisticated approach that directly treats interactions among constituents. While the technique of including associates can achieve this purpose, an alternative is the two-sublattice liquid model (TSLM) that can be used to describe the ordering in ionic melts [25]. The TSLM is based on the concept first proposed by Temkin [26] for salt melts where each atom is practically surrounded by unlike atoms and cations mix at random only with each other while anions randomly mix exclusively with other anions. The situation is conveniently represented with two

sublattices, one for the cations and one for anions, and the melt is described with the same approach used for crystalline phases with LRO [25].

Hillert et al. [25] made modifications to extend the application of the TSLM to include components with multiple valences and by allowing the stoichiometry to vary to represent the liquid over the entire compositional domain. Vacancies and associates, both neutral and charged were also introduced to better describe the tendency to order in ionic melts. Within the TSLM framework, electroneutrality is defined as:

$$P = \sum_j \nu_j y_{A_j} + Q y_{Va} \qquad \textbf{2. 6}$$

$$Q = \sum_i \nu_i y_{C_i} \qquad \textbf{2. 7}$$

where v_j and y_{A_j} are the charge and site fraction of the anion species and v_i and y_{C_i} are the charge and site fraction of the cation *C*, respectively; y_{Va} is the site fraction for a vacancy of charge *Q*-.

The molar Gibbs energy expression using the TSLM is:

$$G^{liq} = \sum_C \sum_A y_C y_A {}^\circ G_{C:A} + Q y_{Va} \sum_C y_C {}^\circ G_C + Q \sum_B y_B {}^\circ G_B - TS^{liq} + {}^{xs}G \qquad \textbf{2. 8}$$

where G^{liq} is the molar Gibbs energy of the liquid solution, ${}^\circ G_{C:A}$ is the Gibbs energy of the liquid constituent corresponding to the formula $C_{\nu_A} A_{\nu_C}$ and ${}^\circ G_C$ is the Gibbs energy of element C. The symbols y_B and ${}^\circ G_B$ correspond to the site fraction and the Gibbs energies of neutral B associates. The ${}^{xs}G$ term takes on the same form as that given in Eqns. 2. 4 and 2. 5 .

The configurational entropy S^{liq} is given by:

$$S^{liq} = -R\left[P\sum_{C} y_C \ln y_C + Q\left(\sum_{A} y_A \ln y_A + y_{Va} \ln y_{Va} + \sum_{B} y_B \ln y_B \right) \right] \qquad \textbf{2. 9}$$

2.4 Excess functions

An important part of modeling efforts is an expedient choice of an excess function that facilitates extrapolation from binary and ternary subsystems to multicomponent mixtures. For this reason, ${}^{xs}G$ is generally chosen as a function of binary interactions only. There are more sophisticated representations for ${}^{xs}G$, such as the three-suffix Margules and Whol's equations [27]which likely result in better modeling fidelity compared to experimental behavior, but these expression suffer from the fact that interaction parameters between all components in each subsystem starting from binary up to the formal order of the system are included making for unwieldy complexity. If possible and for practical purposes, the ${}^{xs}G$ equation should be chosen such that it is defined in terms of binary components or at most ternary interactions. This allows higher order systems to be extrapolated from binary and/or ternaries and therefore minimizes the experimental effort required to fit the adjustable parameters and describe the system.

2.5 Summary

The CEF and TSLM are being used within the thermodynamic modeling community for describing crystalline solids and ionic liquids. The complete Gibbs energy representation of a system, known as an assessment, is necessary for the calculation of phase equilibria. This requires gathering experimental measurements in

order to optimize the adjustable parameters of the models to produce the best fit to the data as possible. This laborious procedure, combined with complexity of many of the equations from this chapter, is best accomplished with the aid of state of the art CT software.

Continual advancements in computer speed and performance have facilitated the development and improvement of sophisticated CT codes and software packages that are central to the field of CT and allow descriptions of systems with an increasingly higher number of components and complex phases. One widely used approach to thermodynamic modeling is the CALPHAD method that aims to develop models that describe the phase equilibria and thermodynamic properties, can be extended to include higher order multicomponent systems, and can be confidently extrapolated into regions for which data do not exist. Finally, CT and the CALPHAD method essentially developed side by side and are therefore inextricably linked due to the widespread use of the CALPHAD approach within the CT community.

CHAPTER 3

CRYSTAL CHEMISTRY OF URANIA AND URANIA SOLID SOLUTIONS

"(Thermodynamics) is the only physical theory of universal content, which I am convinced, that within the framework of applicability of its basic concepts will never be overthrown."—Albert Einstein

Despite fission product accumulation and the resulting complex equilibria in a typical operational reactor fuel element, the major phase is the urania solid solution. It is therefore important to understand the chemistry of this compound since it drives many performance phenomena. A sound representation of the defect behavior is of paramount importance since it influences the thermal conductivity, oxygen potential and mobility, and mass transport of impurities in $UO_{2\pm x}$. A combination of experimental, semi-empirical static potential, and first principals approaches have been used to determine the types of defects in $UO_{2\pm x}$; the results are reviewed in this chapter. A critical assessment of the reported data is used to inform the CEF model for $U_{1-y}M_yO_{2\pm x}$ in order to develop the most accurate sublattice description of these phases as possible within the given framework.

3.1 The UO_2 crystal

Urania belongs to the CaF_2 (calcium fluorite) type of ionic crystals that consists of uranium cations occupying FCC sites. The UO_2 fluorite unit cell is shown in Fig. 3.1. In an ideal UO_2 crystal, oxygen anions are located at the tetrahedrally coordinated ¼ ¼ ¼, ¾ ¾ ¾ positions. Fundamental to the structure are octahedrally coordinated interstitial sites at the ½ ½ ½ [28] positions that accommodate oxygen atoms when the structure deviates from stoichiometry as UO_{2+x} or when Frenkel defects are present. Figure 3.2 shows the polyhedron formed at the two anion locations by nearest neighbor cations in the fluorite crystal.

In unirradiated UO_2, the defect structure is dominated by so called majority defects [29], tetrahedrally coordinated vacancies and octahedrally coordinated interstitials that give rise to the $UO_{2\pm x}$ notation for non-stoichiometric urania. Uranium vacancies or anti-sites exist in negligible concentrations [28, 30] due to a much higher formation energy and are therefore not considered in any of the defect models reviewed for $UO_{2\pm x}$ [31-34]; however, a change in the nominal valence from U^{4+} is sometimes referred to as an electronic defect [32, 35-37]. The evidence suggests that U^{5+} is the dominant oxidized state in pure $UO_{2\pm x}$ but U^{6+} plays an important role in the chemistry of ternary $U_{1-y}Ln_yO_{2\pm x}$ phases.

3.2 Oxygen defect clustering in UO_2

The true nature of defects in the UO_2 crystal is still the subject of debate with contradictory results from experiment and first principles calculations but there is a general consensus that some type of oxygen clustering occurs in UO_{2+x}. Willis [28] used a neutron diffraction technique to study the UO_2 structure and found that oxygen atoms do not sit in the octahedrally coordinated interstitial sites in hyperstoichiometric urania (UO_{2+x}) but instead form two sites, each displaced 1 Å along <110> and <111> directions. The author further posits that these defects agglomerate to form the so called

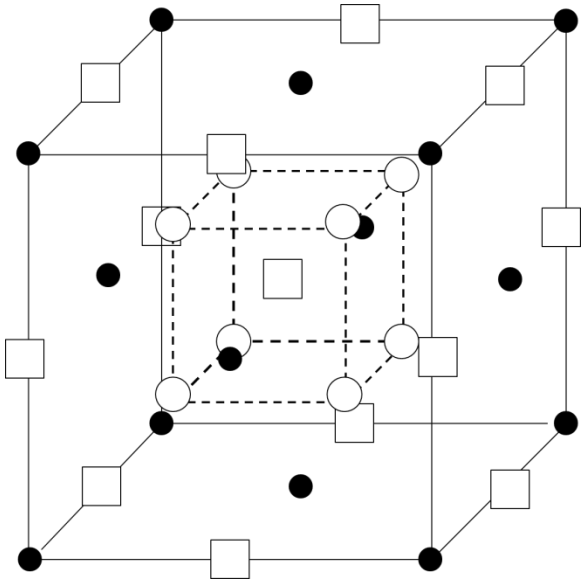

Fig. 3.1. The UO_2 fluorite unit cell after Willis [28]. The solid circles represent uranium cations while the unfilled circles are the oxygen anions. The squares show the octahedrally coordinated interstitial sites.

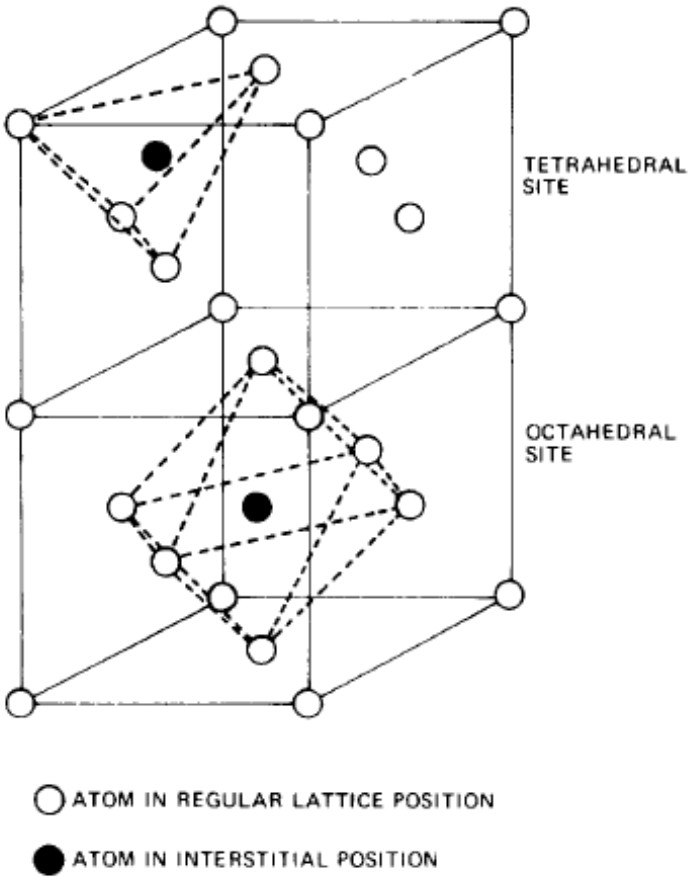

Fig. 3.2. Tetrahedral and octahedral interstices in an fcc crystal from [7].

2:2:2 or Willis cluster shown in Fig. 3.3(a). Park and Olander developed a thermochemical model of $UO_{2\pm x}$ that showed excellent agreement with μ_{O_2} measurements. The Gibbs energy of the phase is described using an extension of Kröger-Vink notation to include oxygen and vacancy (Va) clustering by introducing a Va dimer and a 2:2:2 with an assigned -1 effective charge to give a better fit to the μ_{O_2} data [33]. These defects are summarized in Table 3.1.

There seems to be some debate as to the extent and even the existence of the Willis defect (cluster). Park and Olander [33] claim that most oxygen interstitials form Willis clusters in hyperstoichiometric urania ($x > 0.01$) while others argue that the clustering phenomenon occurs only for large deviations from stoichiometry [38, 39]. A first principles investigations using density functional theory (DFT) found that the Willis cluster is not stable and the cuboctehedral cluster (COT) in combination with an octahedral interstitial are the predominate oxygen defects in UO_{2+x} [40, 41]. Andersson et al. [42] also found Willis defects to be unstable using DFT calculations and proposed a di-interstitial cluster where oxygen anions occupy the nearest neighbor octahedral sites shown in Fig. 3.3(b). At high O/M, domains of COTs, shown in Fig. 3.3(c), are believed to form. This type of oxygen ordering has been experimentally observed [43-46] and, as mentioned, confirmed to be a stable structure using DFT methods. The Willis defect appears to be a fragment of the COT as some of the O positions in the COT correspond to those proposed by Willis [45, 47]. It is therefore thought that UO_2 first oxidizes by incorporating 2:2:2 clusters and then COT domains as the phase progresses to U_4O_9 [48].

3.3 Dissolution of La and Gd in $UO_{2\pm x}$

A fundamental part of the CALPHAD methodology is the concept of *lattice stability* [49]. It comes from the idea that the Gibbs energy descriptions can be represented for all components in every phase of a system, that is, it can be extrapolated into regions of instability, expressed graphically in Fig. 3.4.

Table 3.1
Defects proposed by Park and Olander [33] for their $UO_{2\pm x}$ thermochemical model using Kröger-Vink for point defects and a new notation for clustering.

Notation	Definition	Effective Charge
$(2:2:2)'$	Willis defect	-1
$U_U^{\bullet}$	U^{5+} (hole)	+1
U_U'	U^{3+} (polaron)	-1
$(V:U:V)^{\bullet\bullet}$	Vacancy dimer	+2
O_i''	Octahedrally coordinated oxygen	-2
V_V^x	Octahedrally coordinated vacancy	0

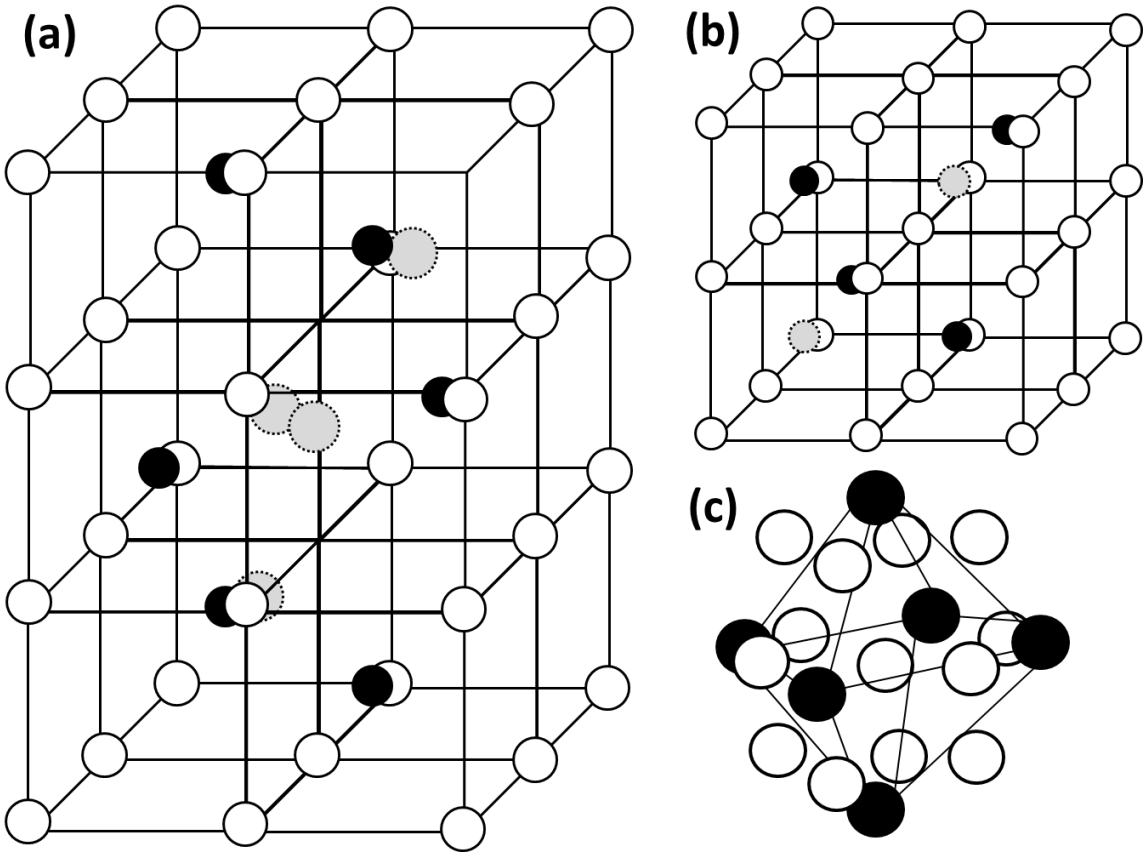

Fig. 3.3. Simple octahedrally coordinated interstitials (a), the di-interstitial (b), and the cuboctahedral cluster (c). In (a) and (b), the open circles are tetrahedrally coordinated 'normal' O sites, the dark filled circles represent U atoms and the light filled circles delineated by dashes are octahedrally coordinated O interstitials. The U atoms (dark circles) relative to the O cluster positions (open circles) are shown in (c).

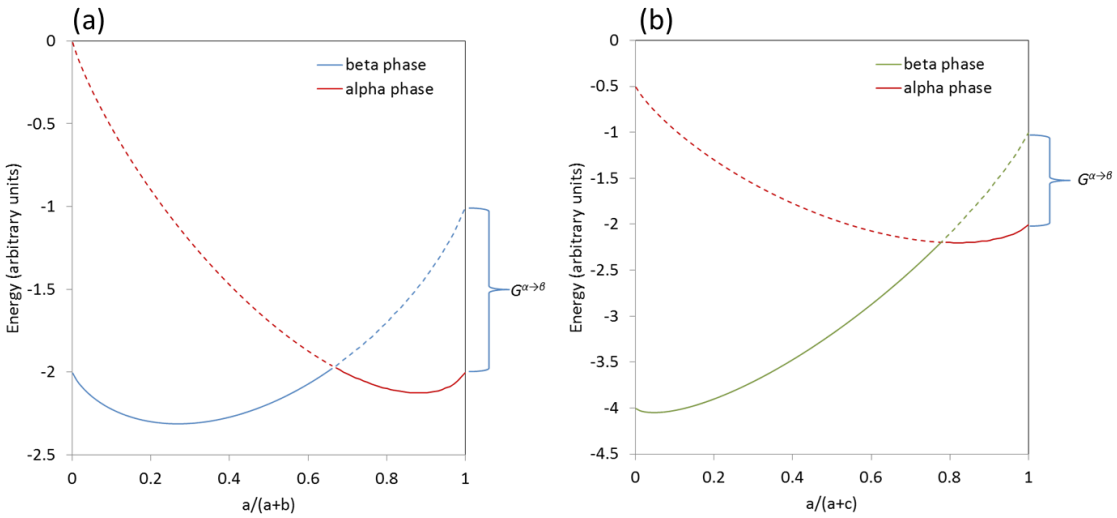

Fig. 3.4. Gibbs curves from the ideal solution model as a function of composition for the α and β phases in the hypothetical a-b and a-c systems. The dashed lines represent "extrapolations" into the unstable phase regions. The difference between the extrapolated end points and the pure stable phase is the lattice stability. Note that the lattice stability for pure *a* in both the *a*-*b* and *a*-*c* binaries are the same, i.e. the $G^{\alpha \rightarrow \beta}$ value is independent of the system.

Lanthanides (Ln) and Y, with a fixed 3+ valency, do not form a stable dioxide with a fluorite structure. However, these elements extensively dissolve in the cation sublattice of urania and exist in the fluorite phase as a constituent in the solid solution. To best model the $U_{1-y}Ln_yO_{2\pm x}$ solid solution using the CEF approach, the Gibbs energy of a fictive "LnO_2" with a fluorite structure is helpful and is approximated using *density functional theory* (DFT).

3.3.1 Lattice stabilities from DFT[1]

Ideally, DFT can provide the relative enthalpy for various crystal structures and thus the $H^{\alpha\to\beta}$ component of the lattice stability. This is accomplished by computing the total energy at absolute zero for an assemblage of particles by solving the time-independent Schrödinger equation using simplifying assumptions and approximations. A popular approach is the Kohn-Sham (K-S) method where the electrons are treated as non-interacting with the same density as that of the real system [50].

The total energies can then be used to compute differences between distinct crystallographic arrangements via:

$$\Delta E = E^{\alpha} - E^{\beta} \qquad \textbf{3. 1}$$

where

$$\Delta E \approx \Delta H \qquad \textbf{3. 2}$$

[1] The DFT computed lattice stabilities were provided by Dr. Dongwon Shin, Surface Processing and Mechanics Group, Materials Science and Technology Division, Oak Ridge National Laboratory, Oak Ridge TN in support of this work and therefore should not be construed to be an original contribution by the author.

Eqn. 3. 2 is assumed to be valid since at 1 bar pressure $P\Delta V \approx 0$. These results can then be compared to estimated $H^{\alpha\to\beta}$ based on extrapolations, used directly to determine the $S^{\alpha\to\beta}$ for stable phases, or serve as a first approximation to the lattice stability in an optimization procedure.

The lattice stability $\Delta G_{LnO_2}^{LnO_{1.5}\to LnO_2}$ for LaO_2 and GdO_2 in the fluorite phase were estimated as $\Delta E_{LnO_2}^{LnO_{1.5}\to LnO_2}$ from DFT calculations using the Vienna *Ab initio* package (VASP) [51, 52]. The total energies at $0\,K$ for the reference state Ln_2O_3 and fictive LnO_2 were computed for three different magnetic configurations and yielded results within ±0.26% of the average value; both Gd_2O_3 and La_2O_3 were treated as non-magnetic. The energy estimates for GdO_2 and LaO_2 were taken to be the lowest value of the three magnetic configurations.

The lattice stability for fluorite GdO_2 and LaO_2 were calculated to be +26.1 kJ/mol and +8.74 kJ/mol respectively using the relation:

$$\Delta E_{LnO_2}^{LnO_{1.5}\to LnO_2} = E_{LnO_2} - \left(E_{LnO_{1.5}} + \frac{1}{4} E_{O_2}^{gao} \right) \qquad \textbf{3. 3}$$

where E is the total energy of a given structure and ¼ of the E of O_2 gas was added to the sesquioxide $LnO_{1.5}$ compound to adjust for stoichiometry;

3.3.2 Lattice parameter

The lattice parameter of $U_{1-y}M_yO_2$ is observed to follow Vegard's law and can therefore be used to characterize the composition of the mixed oxide. There are two

correlations relating the ionic radii of the constituent elements to the lattice parameter; One is based on the hard sphere model and the other, developed by Kim [53], is empirical and given by Eqn. 3. 4:

$$d = a_0 + \sum_k [b(r_k - r_h) + c(z_k - z_h)]m_k \qquad \textbf{3. 4}$$

where r_h and z_h are the ionic radius and valence of the host metal; r_k and z_k are the ionic radius of the valence of the *k*th dopant metal. The constants a_0, b, and c for different host structures are given in Table 3.2.

The value for m_k is given by:

$$m_k = \frac{n_k M_k}{100 + \sum_k (n_k - 1)M_k} \times 100 \qquad \textbf{3. 5}$$

where n_k is the number of cations in the oxide formula of solute k and M_k is the mole percent of the *k*th dopant.

While Eqn. 3. 4 reproduces the lattice parameter change from dissolution of oxides in fluorite hosts with a fixed tetravalent metal, it does not correctly represent the unit cell contraction (or expansion in the case of La) observed for stoichiometric Ln^{3+} doped urania, i.e. $U_{1-y}Ln^{3+}{}_yO_{2.00}$. It is sometimes helpful to view the UO_2 lattice according to Fig. 3.5 where each uranium atom sits at the center of a simple cubic arrangement of oxygen anions [29]. Equation 3. 6 is derived from this geometry and the so called *hard sphere model* of ionic crystals where cations are assumed to contact their nearest neighbor anions.

Table 3.2
Host metal empirical constants after Kim [53].

Host	a	b	c
HfO_2	0.5098	0.0203	0.00022
ZrO_2	0.5120	0.0212	0.00023
CeO_2	0.5413	0.0220	0.00015
ThO_2	0.5596	0.0212	0.00011
UO_2	0.5468	0.0206	0.00013

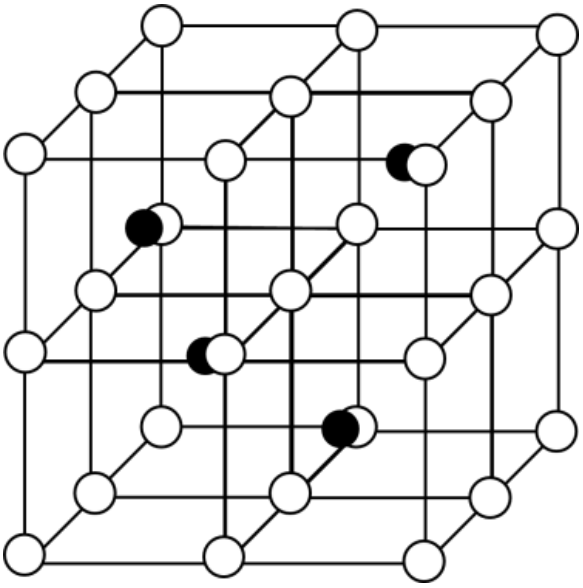

Fig. 3.5. Alternative UO_2 lattice structure. The unfilled circles represent oxygen anions while the solid circles are uranium cations occupying every other cube center.

$$d = \frac{4}{\sqrt{3}}\left[\sum_k x_k r_k + r_{O^{2-}}\right] \quad \textbf{3. 6}$$

Here, r_k is the ionic radii of species *k* is from Shannon [54] while x_k is the fraction of *k* on the cation sublattice. Ohmichi et al. [55] modified $r_{O^{2-}}$ to 1.368 Å to fit the observed unit cell dimension of UO_2. The authors then show the predominant oxidized state in $U_{1-y}Ln_yO_{2.00}$ is most likely U^{5+} using the following relation:

$$d = \frac{4}{\sqrt{3}}\left(y(r_{Ln}) + (y)r_{U^{5+}} + (1-2y)r_{U^{4+}} + r_{O^{2-}}\right) \quad \textbf{3. 7}$$

Experimentally determined lattice parameters agree exceptionally well with Eqn. 3. 7 as can be seen in Fig. 3.6.

3.3.2 Ionic radii

The U^{4+} cation is coordinated by 8 oxygen anions in an ideal stoichiometric UO_2 crystal and has an ionic radius of 1.00 Å [54]. According to Moss [56], a large difference in ionic radii correlates to limited solubility resulting from lattice strain in the host metal structure; this phenomenon has been observed for Ln dissolution in ThO_2 [57]. Beals and Handwerk [58] claim that rare earth elements with an ionic radius within a 20% difference to that of U^{4+} in the fluorite structure should form a solid solution. The 8-coordinated La^{3+}, Gd^{3+}, and Th^{4+} differ by 16%, 5.3%, and 5% respectively. Fig. 3.7 shows the lattice stability in the fluorite structure and ionic radius relationship for some Ln elements. Of the Ln's with a fixed 3+ valency, it is interesting that La appears to be the most stable in the fluorite structure but has the largest difference in ionic radius to U^{4+}. Yttrium cations, on the other hand, are closer in size to U^{4+}, but Y is predicted to

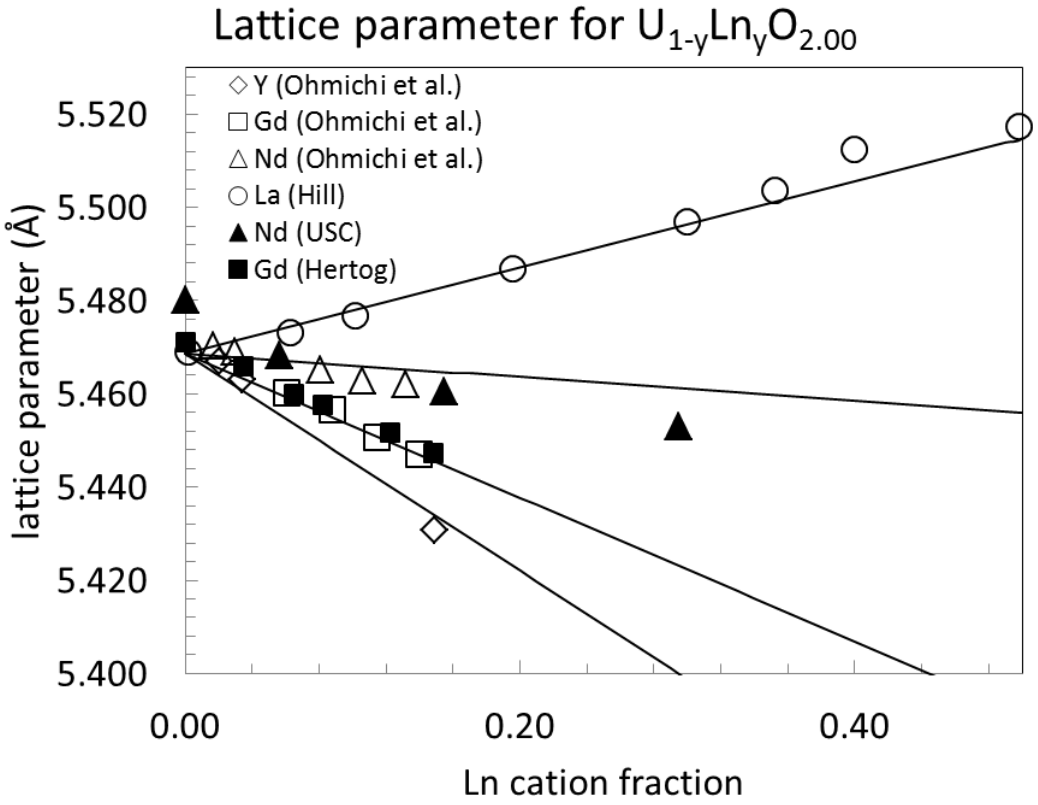

Fig. 3.6. Lattice parameter for stoichiometric $U_{1-y}La_yO_{2.00}$ versus Ln composition. Lines correspond to computed values from Eqn. 3. 7.

have the most positive lattice stability of those considered in Fig. 3.7. It seems the stability of the trivalent Ln's in the fluorite solution is influenced by both $\Delta G_{LnO_2}^{LnO_{1.5}\rightarrow LnO_2}$ and the degree of ionic radii mismatch, a relationship that is complicated by the multiple U oxidation states.

Vegard's law slope is observed to be smallest for Nd in $U_{1-y}Ln_yO_{2.00}$ followed by La, Gd, and Y as seen in Fig. 3.6. The ionic radius for 8-coordinated Nd^{3+} exhibits a positive difference of 0.109 Å from U^{4+}. When an Ln^{3+} is dissolved in a stoichiometric UO_2, quantities of U^{5+} equal to those of Ln^{3+} are formed from U^{4+} to compensate the charge imbalance caused by the aliovalent cation dopant assuming no other electronic defects. Since the positive difference between the ionic radii of Nd^{3+} and U^{4+} is closest to the negative change resulting from U^{5+} substituting U^{4+} (~0.12 Å), Nd doping in stoichiometric urania causes the smallest contraction in the lattice parameter of all the fixed 3+ valence lanthanides suggesting higher stability. The percent difference between the *effective* ionic radii given by Eqn. 3. 7 and that of U^{4+} for solid solutions at an O/M = 2 are given in Table 3.3. Thus, it is no surprise that both La and Nd are observed to exhibit the highest solubility in the fluorite solution since the trend is lower lattice strain and $\Delta G_{LnO_2}^{LnO_{1.5}\rightarrow LnO_2}$ with increasing 8-cordinated ionic radii suggesting higher stability in the phase.

$$r_{eff} = \frac{r_{Ln} + r_{U^{5+}}}{2} \qquad \textbf{3. 8}$$

3.3.4 Oxidation state of uranium in fluorite solid solutions

The fixed valence state of 3+ of an Ln dopant in urania not only has the effect of contracting or expanding the fluorite lattice, but also extends the stability of the

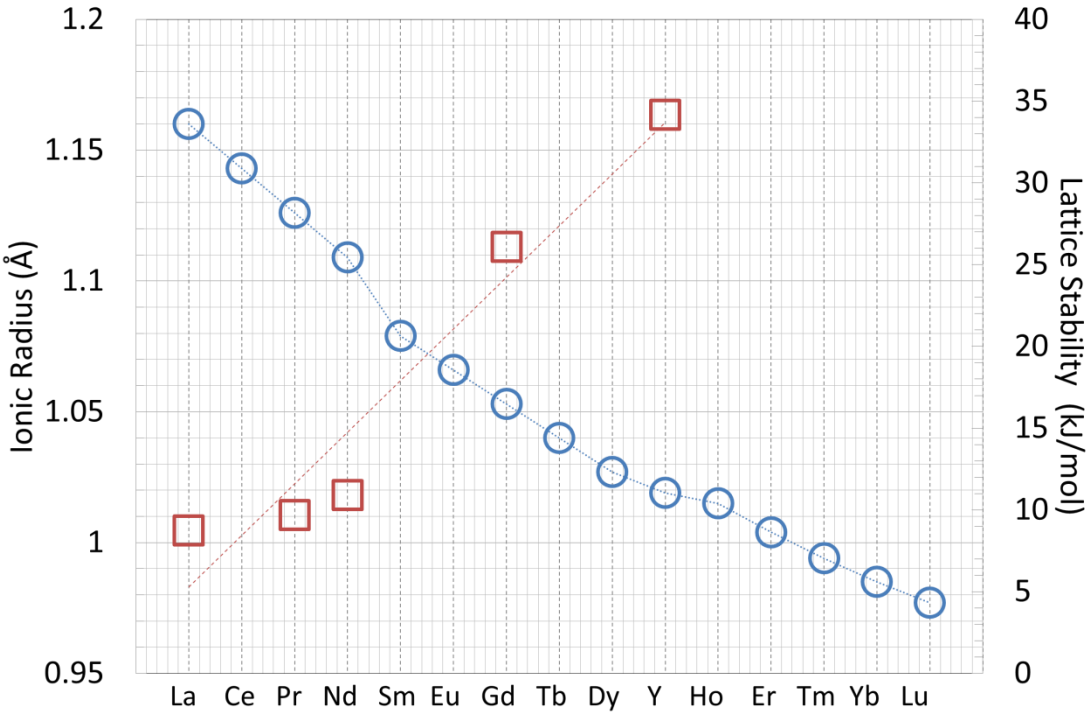

Fig. 3.7. Lattice stability (red squares) calculated from DFT versus ionic radii in 8-coordination (blue circles) of selected lanthanides from [54].

Table 3.3
Percent difference between U^{4+} radius and the effective ionic radius of an Ln^{3+}.

Element	$\frac{r_{eff} - r}{r} \times 100\%$
Y	-5.05%
Gd	-3.35%
Nd	-0.55%
La	+2.00%

hypostoichiometric phase, restricts the O/M values in the hyperstoichiometric region, and raises oxygen potentials relative to $UO_{2\pm x}$ for equivalent O/M values. Since the model for $UO_{2\pm x}$ after Guéneau et al. [31, 32] assumes only U^{3+}, U^{4+} and U^{5+} oxidation states for uranium atoms in the UO_2 structure, this imposes a hyperstoichiometric limit for $U_{1-y}Ln_yO_{2\pm x}$ as a function of Ln composition such that

$$O/M_{\max} = \frac{5-2y}{2} \qquad \textbf{3. 9}$$

Lindemer and Sutton [59] and Teske et al. [60] both report hyperstoichiometric $U_{1-y}Gd_yO_{2\pm x}$ data for $y \geq 0.50$ which are inconsistent with the model of Guéneau et al. [61] since electroneutrality precludes these compositions. Furthermore, experimentally determined phase relations show $U_{1-y}La_yO_{2\pm x}$ [62] and $U_{1-y}Nd_yO_{2\pm x}$ [63] exist at compositions that must include U^{6+} to achieve electro-neutrality. This is illustrated in Fig. 3.8.

Catlow [64] used static potential calculations to show the disproportionation reaction, $2U^{5+} \leftrightarrow U^{6+} + U^{4+}$, is energetically unfavorable in UO_2. Parks and Olander [33, 34] later developed defect models using only U^{3+},U^{4+} and U^{5+} for $UO_{2\pm x}$ and $U_{1-y}Gd_yO_{2\pm x}$ citing a subsequent review by Catlow [65] in which the author reaffirms that the majority charge transfer products are U^{3+} and U^{5+} but acknowledges that high temperatures may lead to generation of both U^{2+} and U^{6+} in urania.

Figure 3.9 shows the lattice parameter from XRD measurements made by Hill [66] for $U_{1-y}La_yO_{2\pm x}$. In this study, the author only observed the fluorite phase and attributed the change in slope in both (a) and (b) of Fig. 3.9 to be a consequence of U^{6+} formation. Indeed, in the region $0 \leq y \leq 0.5$, the lattice parameter can be modeled using Eqn. 3. 7 but for compositions corresponding to $y \geq 0.5$, a U^{6+} cation must be included to preserve charge neutrality; therefore the following equation is used:

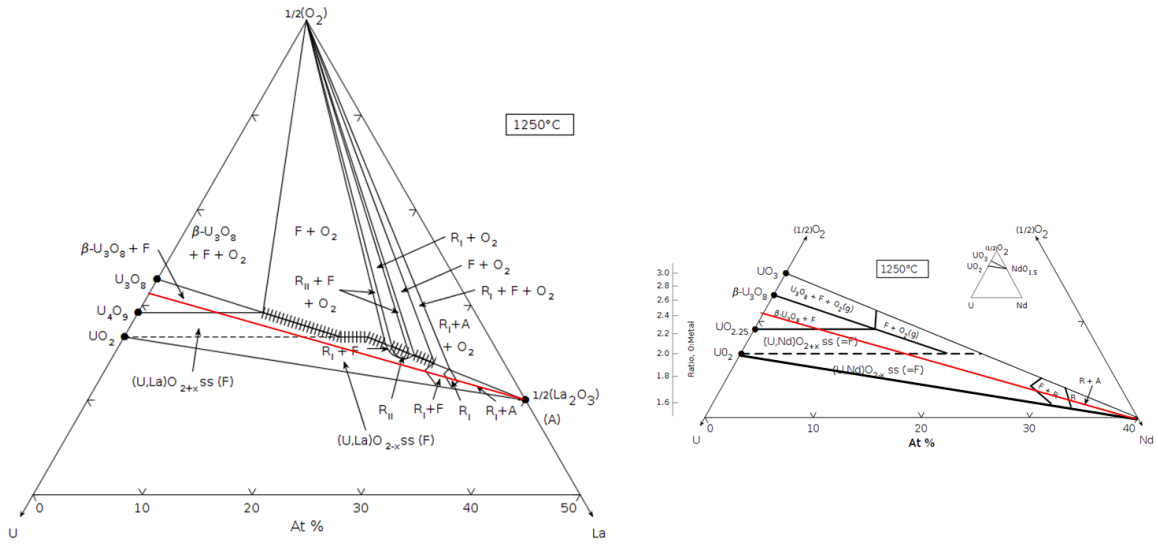

Fig. 3.8. Experimentally determined phase diagrams from [62] and [63]. The red line shows the oxygen rich extent of the fluorite phase considering U^{5+} as the maximum oxidation state. **(**Reprinted with permission of The American Ceramic Society, www.ceramics.org All rights reserved.)

$$d = \frac{4}{\sqrt{3}}\left(y(r_{La}) + (2y-1)r_{U^{5+}} + (2-3y)r_{U^{6+}} + r_{O^{2-}}\right) \quad \textbf{3. 10}$$

where y is the cation composition of La^{3+} and r_i are the ionic radii used by Ohmichi et al. [55] in Eqn. 3. 7. For $y \geq 0.667$ the phase must be hypostoichiometric assuming La^{4+} does not exist; therefore the O/M and cation concentrations were computed at 1.01325 bar O_2 pressure using the CEF model for $U_{1-y}La_yO_{2\pm x}$ developed in this work and then used in Eqn. 3. 10 to compute the lattice parameter for compositions in this region. Finally, while Eqn. 3. 10 captures the change in slope associated with increasing La concentrations for $y \geq 0.50$, the absolute values between the calculated and observed lattice parameters differ suggesting there is an issue with regard to the phases that are formed. A series of three rhombohedral fluorite derivative structures with ordering on both the cation and anion sublattices and a predominant 6+ oxidation state for U has been observed [62] to exist along the fully oxidized isopleth of the U-La-O ternary; these compositions would correspond to $y \geq 0.55$ in Fig. 3.9(b). Chen and Navrotsky [67] have pointed out that the lattice parameter is more sensitive to small amounts of C-type sesquioxide phases compared to the XRD pattern itself. Further, the metal cations lose oxygen coordination for $y \geq 0.667$. These phenomena could explain the discrepancy between the predicted and observed lattice parameter values; regardless, however, the slope given by Eqn. 3. 10 is the same as that from XRD measurements [66]suggesting U^{6+} plays an important role in the chemistry of U-La-O phases in high La compositional regions of the ternary.

While there is no reason to doubt that U^{6+} exists in the fluorite phase, the question is to what extent? From the evidence presented here it seems likely that this cation exists in negligible concentrations in pure UO_2 and only forms in consequential amounts when the phase is heavily doped with a trivalent Ln in oxygen rich regions of the phase space.

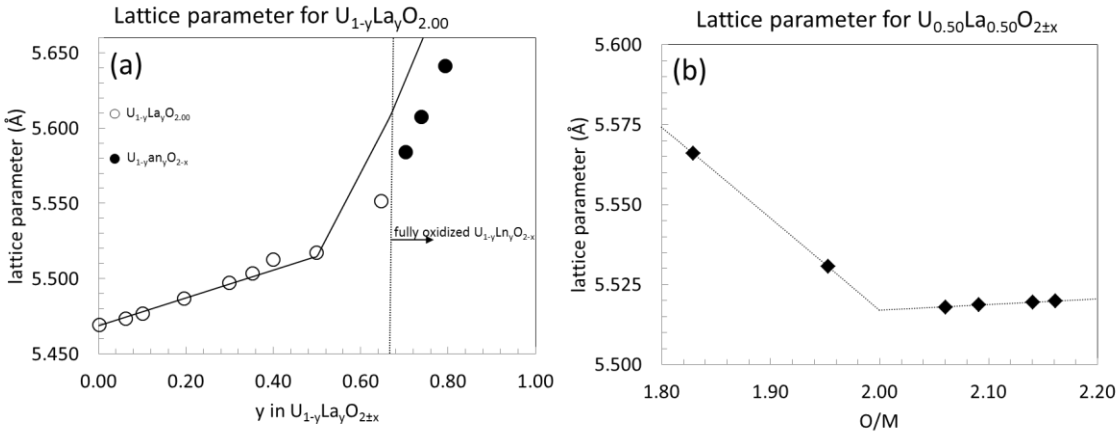

Fig. 3.9. (a) Lattice parameter for stoichiometric $U_{1-y}La_yO_{2\pm x}$ versus La composition. Lines correspond to computed values from Eqn. 3. 10 for $y \leq 0.5$ and Eqn. X for $y \geq 0.5$. (b) Oxygen to metal ratio effect on the lattice parameter of $U_{0.50}La_{0.50}O_{2\pm x}$. Lines are included for reference only to illustrate the abrupt change observed at O/M = 2.00.

3.4 Oxygen order-disorder transition

At sufficiently high temperatures the UO_2 fluorite structure becomes increasingly disordered whereby oxygen Frenkel pair formation distorts the anion occupants of nearest neighbor (NN) and next nearest neighbor (NNN) tetrahedral sites resulting in O defect concentrations that can reach as high as 20% [68, 69]. The total fraction of oxygen defects (n_d) determined by neutron diffraction [68] are shown in Fig. 3.10 for UO_2 and Fig. 3.11 for ThO_2. The phenomenon is known as an order-disorder (OD) or λ-transition, occurs at around 85% of the melting temperature (2670 K), and is characterized by a sharp increase and/or break in the heat capacity (c_p) versus temperature curve [70] as shown in Fig. 3.12. This behavior is common in fluorite type crystals and Fig. 3.13 shows analogous behavior for ThO_2.

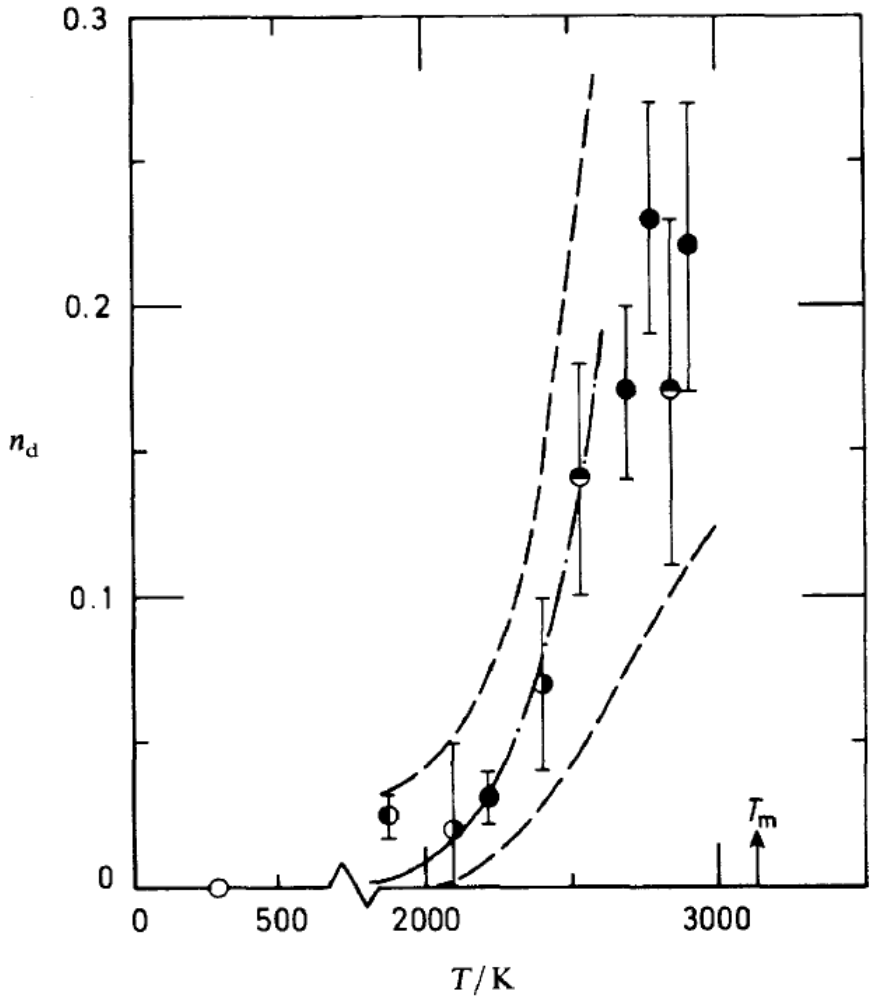

Fig. 3.10. Total fraction of oxygen defects (n_d) for stoichiometric UO_2 from neutron diffraction study performed by Hutchings [68].

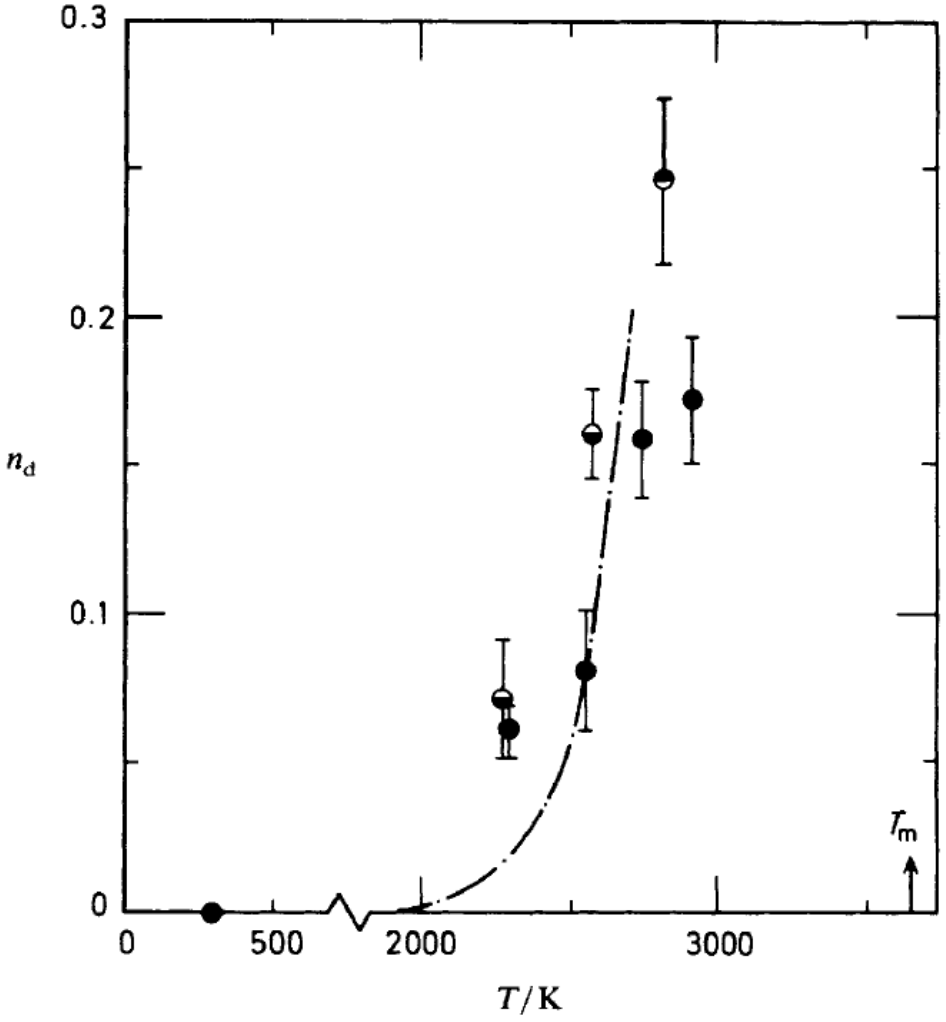

Fig. 3.11. Total fraction of oxygen defects (n_d) for stoichiometric ThO_2 from neutron diffraction study performed by Hutchings [68].

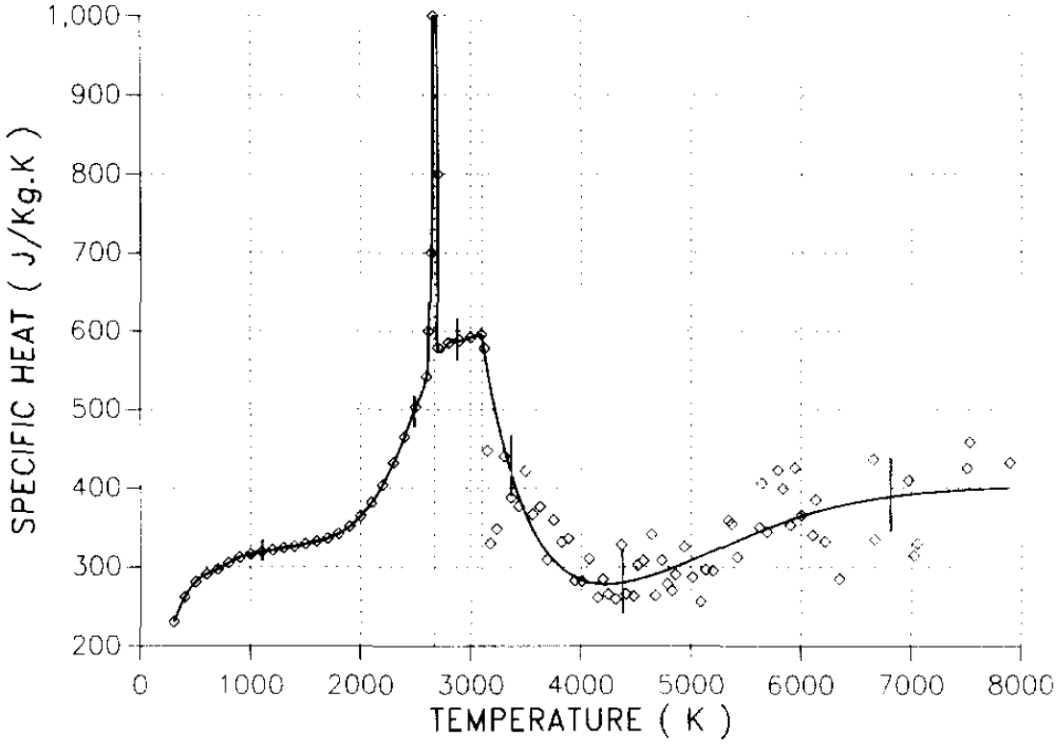

Fig. 3.12. Specific heat of UO_2 from [71]showing a discontinuity in c_p at ~2900 K believed to be due to oxygen Frenkel disorder. The second break in c_p at ~3100 K is from melting.

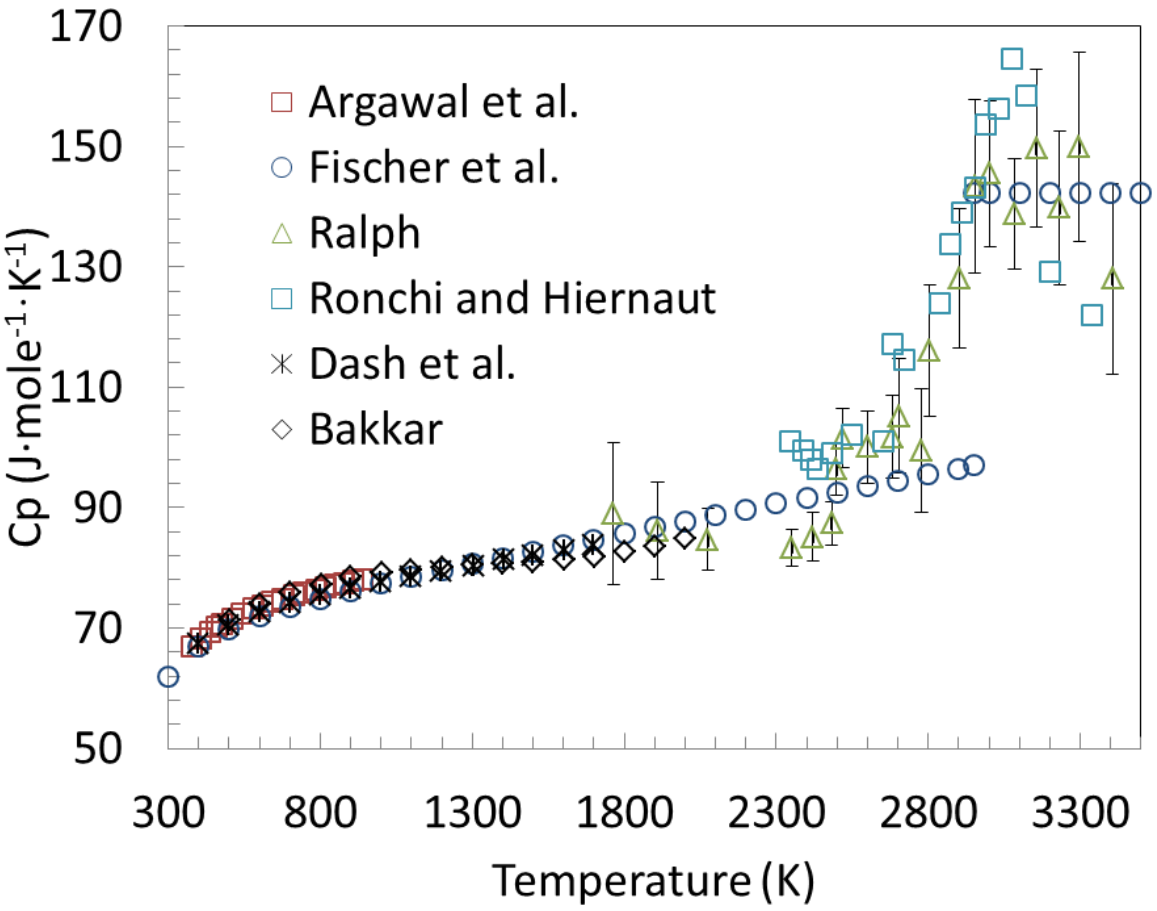

Fig. 3.13. Experimentally determined molar heat capacity from the studies for ThO_2 [69, 72-76] reviewed in this work.

CHAPTER 4

THERMODYNAMIC DATA FOR THE U-M-O TERNARY SYSTEMS

"Thermodynamics is a funny subject. The first time you go through it, you don't understand it at all. The second time you go through it, you think you understand it, except for one or two small points. The third time you go through it, you know you don't understand it, but by that time you are so used to it, it doesn't bother you anymore."

– Arnold Sommerfeld

Considered together, significant thermodynamic data is available in the open literature for the U-Ln-O systems. However, studies of individual systems are less complete. For example, there is very little ternary phase equilibria data for U-Gd-O but there exist melting measurements, heat capacity data, and an extensive body of work reporting equilibrium oxygen pressures over $U_{1-y}Gd_yO_{2\pm x}$ making the U-Gd-O system useful for benchmarking the solidus, liquidus, and oxygen pressure of $U_{1-y}Ln_yO_{2\pm x}$ phases [77]. On the other hand, the U-La-O, and U-Nd-O ternary diagrams in the vicinity of the fluorite solid solution at 1523 K have been well characterized but there is limited oxygen potential data for $U_{1-y}La_yO_{2\pm x}$, and $U_{1-y}Nd_yO_{2\pm x}$, as compared to $U_{1-y}Gd_yO_{2\pm x}$. Due to the chemical similarity of the fixed trivalent Ln elements, for this work they are considered as a group so as one system informs another where data is questionable, limited, or otherwise non-existent.

4.1 Thermodynamic data

Thermochemical studies for complex oxide phases generally present μ_{O_2} data as a function of composition and temperature. For simplicity, much of the data are reported as $RT \ln p_{O_2}$ or $\log p_{O_2}$.

Heat capacity is measured by calorimetric methods. Solid state phase relations are determined *in situ* using HTXRD (high temperature x-ray diffraction) or from quenched samples using standard room temperature XRD (x-ray diffraction) techniques. Thermal arrest, ceramogrpahic analysis, and simple visual observations were all reported for solidus/liquidus determinations in the U-Ln-O systems.

4.2 Gadolinium

Gadolinium is not a high yield fission or activation product; however, it is added as a burnable poison and can be present up to 10% by weight in fresh UO_2 fuel [78]. As previously mentioned, a substantial body of work reporting oxygen potential measurements as a function of temperature, Gd content, and oxygen-to-metal ratio (O/M) is available in the open literature. Teske et al. [60] and Nakamura [79] made solid state electromotive force (EMF) measurements while Lindemer and Sutton [59] and Yang et al. [80] used thermogravimetric analysis (TGA). Une and Oguma [81, 82] used both EMF and TGA methods to measure oxygen dissociation pressures over $U_{1-y}Gd_yO_{2\pm x}$. Lindemer and Sutton [59] reported data over the most extensive temperature and Gd compositional ranges. The data is summarized in Table 4.1.

Direct comparisons of the data collected by different authors could not be made since each study generally used different Gd compositions. When different studies did use the same *y* value in $U_{1-y}Gd_yO_{2\pm x}$, the temperatures did not correspond. An exception is the data reported by Lindemer and Sutton [59] and Yang et al. [80] for y = 0.169 and 1573 K and these measurements show good agreement. Each data set did show

Table 4.1
Compositional and temperature ranges of equilibrium oxygen pressure over $U_{1-y}Gd_yO_{2\pm x}$ by author.

Authors	Ref.	y	Temp. (K)	$-\log p_{O_2}$	O/M	Method
Lindemer and Sutton	25	0.00-0.800	1273-1773	21.13-0.99	1.617-2.168	TGA
Yang et al.	26	0.087-0.169	1473-1573	15.94-4.03	1.976-2.058	TGA
Nakamura	24	0.050-0.200	1273	9.82–4.65	2.003-2.179	EMF
Teske et al.	23	0.050-0.200	1223	16.03-5.99	1.998-2.055	EMF
Une and Oguma	27, 28	0.040-0.270	1273-1773	17.89-3.28	1.965-2.048	TGA/EMF

consistent trends in equilibrium oxygen pressure versus O/M with respect to changing Gd content and temperature except for the measurements made by Teske et al. [60] for y = 0.6 in the hyperstoichiometric range at 1223 K.

Krishnan et al. [83] performed heat capacity (c_p) and thermal expansion measurements on four different compositions of $U_{1-y}Gd_yO_{2\pm x}$ using differential scanning calorimetry (DSC) and high temperature X-ray diffraction (HTXRD) methods. The XRD results showed only FCC patterns except for the composition corresponding to y = 0.80 where the presence of a hexagonal phase was detected. Heat capacity data for the $U_{1-y}Gd_yO_{2\pm x}$ phase is summarized in Table 4.2. The measurements made by Krishnan et al. [83], Amaya et al. [84], and Takahashi and Asou [85] agreed reasonably well; however, Inaba et al. [86] reported heat capacities that were too high and deviated from the observed trend of decreasing c_p with increasing Gd content.

There are several reports of solidus and/or liquidus measurements along the pseudo-binary UO_2-$GdO_{1.5}$ isopleth and the methods are critically reviewed in [87]. The data from Yamanouchi et al.[88], Grossman et al. [89], Wada et al. [90], and selected data from Kang et al. [91] are judged to be most reliable. These authors used sealed capsules to avoid changes in oxygen stoichiometry of the sample. Studies using a reducing atmosphere [58, 92] were determined to be unreliable because significant oxygen evolution from non-stoichiometric oxides will occur at the high temperatures associated with melting onset. This is evidenced by the implausibly low solidus temperatures reported by Beals and Handwerk [58] In fact, Popov and Proselkov [87] point out the unlikelihood of such large differences in the slopes of the solidus and liquidus of $U_{1-y}Gd_yO_{2\pm x}$ reported in [58] near 100% UO_2 from thermodynamic relations for the binary systems [93]. Other reported measurements used a thermal arrest method [88, 89] and visual ceramographic analysis [90], all of which avoided compositional changes. Kang et al. [91] also performed thermal arrest measurements but only the liquidus data is reliable since the onset of melting was difficult to determine from the

Table 4.2
Method, composition and temperature range of authors reporting heat capacity data for $U_{1-y}Gd_yO_{2.}$

Author	Ref.	y	Temperature (K)	method
Krishnan et al.	33	0.100–0.800	298–800	DSC/HTXRD
Inaba et al.	36	0.044–0.142	310–1500	PC
Amaya et al.	34	0.000–0.270	325–1673	DSC
Takahashi and Asou	35	0.142	400–1000	DSC/PC

DSC – differential scanning calorimetry, PC – pulse calorimetry, HTXRD – high temperature X-ray diffraction

time-temperature plots, likely due to the extremely close solidus and liquidus temperatures in the system.

Very limited data exists for the Gd-O and U-Gd binary subsytems. Temperature-composition (T-x) diagrams are reported for Y-Y_2O_3 [94-102], Nd-Nd_2O_3 [103-106], and La-La_2O_3 [107, 108] but none were found for Gd-Gd_2O_3. One study reports solubility limits of the Ln elements in uranium liquid and vice-versa [109]. While the melting temperatures were not determined, the metals were observed to be effectively immiscible in both the solid and liquid states.

4.3 Lanthanum

The phase equilibria in the U-La-O and U-Nd-O systems are among the most extensively studied relative to other U-Ln-O ternaries. A section of U-La-O isotherm at 1523 K in and around the $U_{1-y}La_yO_{2\pm x}$ solid solution was well characterized by Diehl and Keller using HTXRD [62]; their results were used to determine the proposed phase diagram shown in Fig. 4.1.

Just as in all other U-Ln systems studied, the U and La condensed phases are practically immiscibility [109]. Oxygen potential-composition-temperature measurements were critically assessed in [110] and the reported self-consistent data [111-114] are summarized in Table 3. There are no solidus/liquidus measurements or pseudo-binary phase diagrams for UO_2-$LaO_{1.5}$ as there are for the UO_2-$GdO_{1.5}$ [58, 88-91], UO_2-$NdO_{1.5}$ [115], and UO_2-$YO_{1.5}$ [116], but the La-O system was assessed by Grundy et al. and the phase diagram using the models developed in that study is shown in Fig. 4.2.

Two of the rhombohedral phases, labeled RI and RII in Fig. 4.1, were first observed by Aitken et al. [117] and correspond to $U_1M_6O_{12}$ and $U_2M_6O_{15}$ respectively (M = La, Pr, Nd, Sm, Gd, Tb, Ho, Y, Tm, Yb, Lu). In the U-Y-O system, RI and RII exhibit some degree of metallic homogeneity and are written as $U_pY_{7-p}O_{12}$ ($1 \leq p \leq 3.4$) and

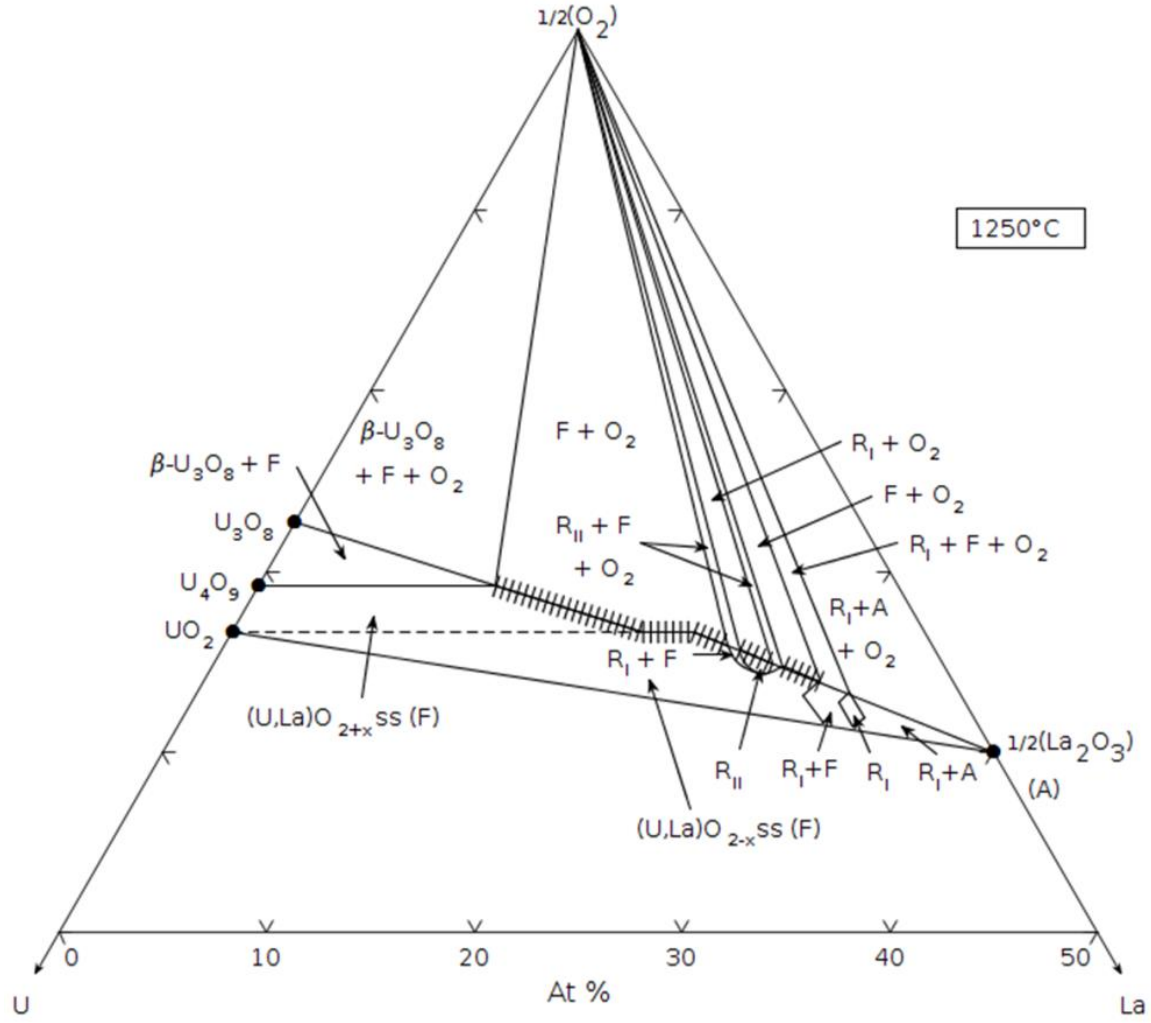

Fig. 4.1. Reported phase diagram for the U-La-O system adapted by [114] using the experimental work from [62]. **(**Reprinted with permission of The American Ceramic Society, www.ceramics.org All rights reserved.)

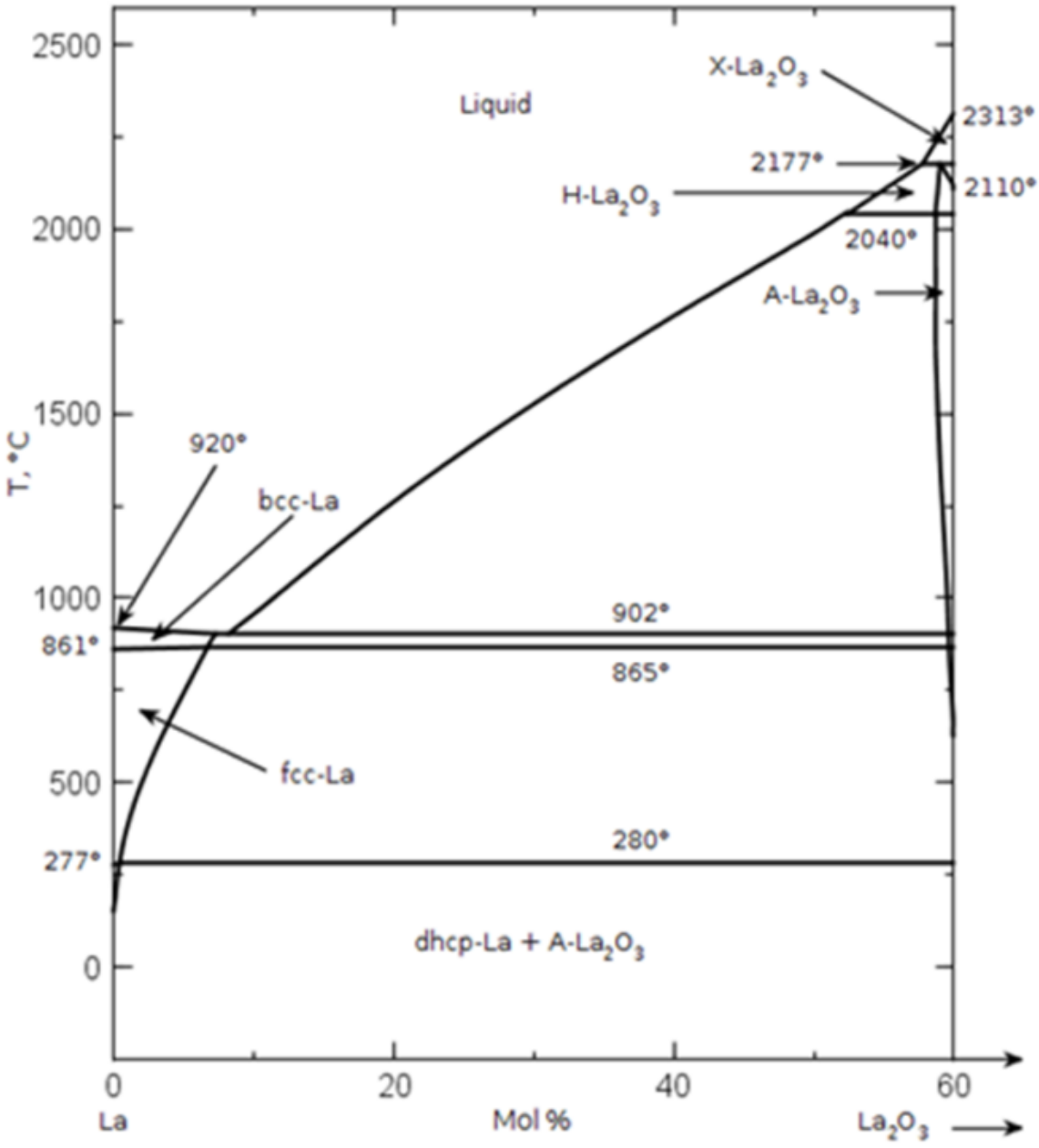

Fig. 4.2. Reported phase diagrams for the La-O system from [108] **(**Reprinted with permission of The American Ceramic Society, www.ceramics.org All rights reserved.)

$U_qY_{8-q}O_{15}$ ($2 \leq q \leq 3.9$) [117]. Both RI and RII are characterized as fluorite derivatives with ordering on the cation and anion sublattices. The RI structure is the most extensively studied and is synonymous with the so called delta (δ) phase. It belongs to the $R\bar{3}$ space group where U^{6+} and Ln^{3+} are in VI and VII fold coordination with oxygen anions respectively [118]. Diehl and Keller [87] identified a third rhombohedral fluorite derivative structure in the U-La-O system corresponding to $U_{1-y}La_yO_2$ ($0.55 \leq y \leq 0.667$) RIII. Further, these authors claim RII is stable, in contrast to the metastable nature of $U_qY_{8-q}O_{15}$ [117], and report some deviation from oxygen stoichiometry in the RI and RII [62] phases.This is expected behavior since U can exist in mixed valence combinations.

Stadlbauer et al. [114] also investigated phase relations in the U-La-O system and used an EMF method to measure equilibrium oxygen pressures versus temperature and composition in the vicinity of the $U_{1-y}La_yO_{2\pm x}$ phase. Finally, Rüdorff et al. [50] found the presence of rhombohedrally indexed lines from an XRD study of $U_{0.50}La_{0.50}O_{2.00}$ at 1403 ± 20 K which supports the evidence of an ordered RIII structure reported in [62].

Oxygen potential measurements versus temperature, composition, and O/M are rather limited for this system. A summary of the available data is presented in Table 4.3. The data from Hagemark and Broli [113], Stadlbauer et al. [114], and Yoshida [112] were judged to be consistent. Matsui and Naito [111] reported oxygen potentials that are too high compared to the balance of measurements according to the critical review in [110].

4.4 Thorium

From the 1950's to mid-1970's, there was considerable interest in thorium fuels that was not sustained due to new discoveries of uranium deposits [119]. India, however, has maintained a Th research program; therefore, there exists significant thermodynamic studies of Th containing systems. Thorium exists as a stable dioxide in the fluorite structure and is completely soluble in the UO_2 matrix; therefore it is of particular interest

Table 4.3
Compositional and temperature ranges of equilibrium oxygen pressure over $U_{1-y}La_yO_{2\pm x}$ by author.

Authors	Ref.	y	Temperature (K)	$-\log p_{O_2}$	O/M	Method
Hagemark and Broli	61	0.025-0.050	1373-1673	10.40-1.37	2.000-2.233	TGA
Stadlbauer et al.	60	0.087-0.169	873-1273	15.40-6.83	2.000-2.129	EMF
Matsui and Naito	63	0.010-0.050	1273	13.00-2.00	1.978-2.035	TGA
Yoshida	62	0.200	1173-1473	21.14-9.90	1.966-2.000	TGA

for benchmarking the behavior of $U_{1-y}M_yO_{2\pm x}$ where M is a fixed quatravalent cation. While Th can exhibit a 3+ valence state evidenced by the hypostoichiometric nature of ThO_{2-x} in reducing atmospheres at high temperatures, under the normal operating conditions of a nuclear reactor, Th^{4+} is the only cation expected.

The binary Th-ThO_2 phase diagram in Fig. 4.3 was determined experimentally by Benz [120] using a micrographic technique. It shows the fluorite thoria structure to be stoichiometric up to about 2027 K. Above this temperature, the phase exists as a hypostoichiometric solid solution. This behavior was confirmed by Ackermann and Tetenbaum [121] with thermogravimetry in the temperature range 2400 to 2655 K for $\log p_{O_2}$ values between -17 and -9. Benz [120] conducted a critical survey of the literature available at that time [122-126] and concluded the degree of hyperstoichiometry is too small to be detected. Indeed, equilibrium oxygen potential studies of $U_{1-y}Th_yO_{2+x}$ solid solutions with *y* values close to 1 [74, 127, 128] show a very limited range for *x* that can be completely attributed to oxidation of U; therefore the fluorite thoria phase is considered to be well represented by the formula ThO_{2-x}.

There are numerous studies reporting the enthalpy increment versus temperature for ThO_2 [75, 129-133] and there is good agreement between authors. The data presented in Fig. 4.4 [75] were taken over the most extensive temperature range and well represent the balance of measurements from the other investigations. Fig. 4.4 shows a change in slope at 2950 K that was characterized in a subsequent analysis of the data [134] as a discontinuity in the enthalpy increment, i.e. a first order phase transition of ThO_2. Ronchi and Hiernaut [69] performed laser pulse-heating experiments on ThO_2 and observed a lambda type transition analogous to that seen in UO_2. The behavior presents as a discontinuity in the heat capacity and is believed to be the result of significant oxygen disordering of the type discussed in Section 3.6. For ThO_2, Ronchi and Hiernaut [69] found this phenomenon to occur at 3090 K in the vicinity of, and likely the cause, of the change in slope observed by Fischer et al. [75].

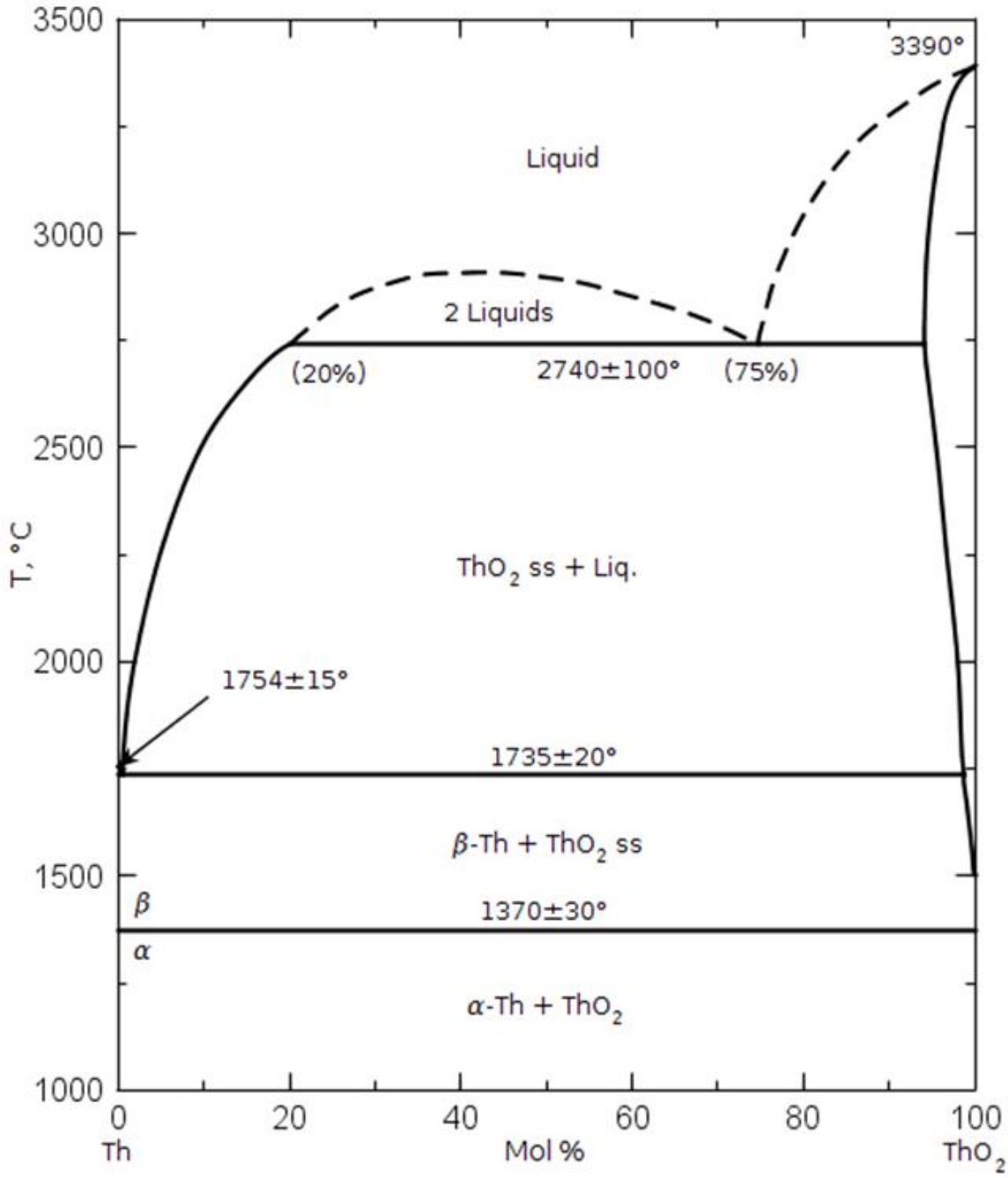

Fig. 4.3. Experimentally determined phase equilibria from [120] for the Th-O binary system. **(**Reprinted with permission of The American Ceramic Society, www.ceramics.org All rights reserved.)

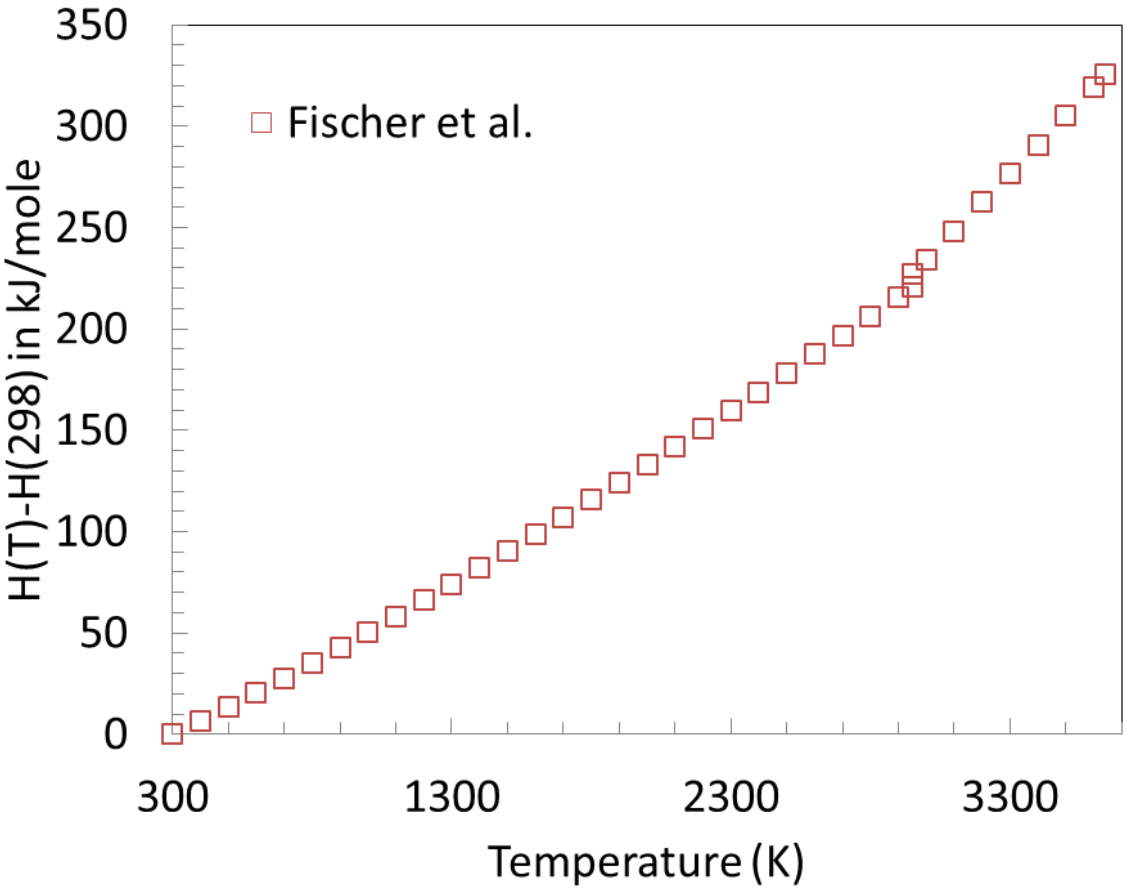

Fig. 4.4. Experimentally determined enthalpy increment from [75].

Fig. 3.14 shows good agreement between authors [69, 72-76] reporting molar heat capacity (c_p) up to ~2500 K. Fischer et al. [75, 134] observed an abrupt change to a constant c_p above 2950 K, but an analysis of the same enthalpy increment data from [75] by Ralph [76] yielded c_p values in better agreement with those from [69].

In the U-Th-O ternary, Dash et al. [74], Anderson et al.[122], Aronson and Clayton [135], Roberts et al. [136], Ugajin et al. [127, 128], Matsui and Naito [137], Anthonysamy et al. [138, 139], and Tanaka et al. [140] report equilibrium oxygen pressures over $U_{1-y}Th_yO_{2\pm x}$ versus composition and temperature. Additionally, Dash et al. [74], Anthonysamy et al. [138], Fischer et al. [134], Agarwal et al. [72], and Kandan et al. [141] measured c_p and enthalpy increments for $U_{1-y}Th_yO_2$. Aitken [142] and Alexander [143] used a transpiration technique to determine vapor pressures over $U_{1-y}Th_yO_{2\pm x.}$ while Ugajin et al. [127, 128] calculated them based on experimental p_{O_2} values. Yamawaki et al. [144] measured relative mass spectrometric intensities of gaseous species at various temperatures for $U_{1-y}Th_yO_{2+x}$ using a Knudsen cell but did not report quantitative partial pressure values. A summary of this data is given in Tables 4.4 and 4.5.

The oxygen potentials versus composition and temperature reported by Anderson et al. [122], Aronson and Clayton [135], and Ugajin et al. [127, 128] were judged to be most consistent. Roberts et al. [136] made measurements at compositions and temperatures close to those of Anderson et al. [122] but are too high in comparison. The μ_{O_2} values reported by Matsui and Naito [137] deviated substantially from the balance of comparable data close to an O/M = 2.000 while those from Anthonysamy et al. [139] were lower than for pure $UO_{2\pm x}$ at the same temperature in contradiction to the trend of increasing equilibrium oxygen pressure with increasing Th content. Ugajin et al. [127, 128, 139, 145], Matsui and Naito [137], and Anthonysamy et al. [139] all used a combination of H_2, CO, CO_2 gasses to fix μ_{O_2} over the mixed oxide sample; however, Ugajin et al. observed weight gain from solid carbon formation and corrected for it when calculating O/M. Both Matsui and Naito [137] and Anthonysamy et al. [139] used CO

and/or CO_2 in their studies but make no mention of C condensation; this is likely the cause of the discrepancies between these data and those from the other studies. Ugajin [127, 139] notes the log p_{O_2} values from Tanaka et al. [140] are too low likely resulting from sample oxidation prior to the O/M determination. Finally, the vapor pressures determined by Alexander et al. [146, 147] are inconsistent with the CEF model for pure $UO_{2\pm x}$.

Paul and Keller [148] investigated the U-Th-O phase equilibria at 1.01325 bar (1 atm) O_2 pressure from 1403 – 1823 K with HTXRD; the results of this study are shown in Fig. 4.5. The authors found that the U_3O_8 + $U_{1-y}Th_yO_{2\pm x}$ biphasic region decreases with increasing temperature and report the formation of $(U_{1-y}Th_y)_4O_9$ from dissolution of Th in U_4O_9 over the $0.0 \leq y \leq 0.5$ compositional range. Dash et al. confirmed the existence of a $UThO_5$ compound first observed by Boekschoten and Kema [149].

The solidus and liquidus along the UO2-ThO2 psuedobinary has been investigated by several authors and their results are compared in Fig. 4.6; the data show reasonable agreement. The solidus and liquidus appear to be very close and there is a minimum in both boundaries at ~ 5 mole % Th. Mumpton and Roy [150] proposed two "not-impossible" ternary phase diagrams shown in Fig. 4.7 from XRD analysis performed on $U_{1-y}Th_yO_{2+x}$ samples with y = 0.25, 0.50, 0.75, and 1.00 and corresponding to temperatures at 1573 K and below 1273 K.

Table 4.4
Compositional, temperature ranges, and methods of equilibrium vapor pressure measurements over $U_{1-y}Th_yO_{2+x}$ by author.

Author(s)	Ref.	y	Temperature (K)	Method
Dash et al.	[74]	0.8360–0.9804	1473	TGA
Anderson et al.	[122]	0.7560–0.9700	1003–1203	TGA
Roberts et al.	[136]	0.9403–0.9947	1123	Knudsen
Aronson and Clayton	[135]	0.0000–0.7100	1250	EMF
Tanaka et al.	[140]	0.7050–0.9520	1250	EMF
Ugajin et al.	[127, 128, 145]	0.0000–1.0000	1273–1473	TGA
Matsui and Naito	[137]	0.2000–1.0000	1282–1373	TGA
Anthonysamy et al.	[139]	0.5400–0.9000	1073–1173	EMF
Aitkin	[142]	0.5000–0.9370	1473–1873	Transpiration
Alexander et al.	[146, 147]	0.8000–0.9200	2373–2773	Transpiration
Yamawaki et al.	[144]	0.6000–0.9000	2025–2192	Knudsen

TGA – thermogravimetric analysis, EMF – electromotive force

Table 4.5
Method, composition and temperature range of authors reporting heat capacity data for $U_{1-y}Th_yO_{2.}$

Author	Ref.	y	Temperature (K)	Method
Dash et al.	[74]	0.100–0.800	298–800	DSC
Anthonysamy et al.	[138]	0.100–0.900	473–973	DC
Fischer et al.	[134]	0.700–0.920	2292–3437	IDC
Agarwal et al.	[72]	0.920–0.9804	376–991	CV
Kandan et al.	[141]	0.100–0.900	298–1805	DSC/DC

DSC – differential scanning calorimetry, DC – drop calorimetry, IDC – Inverse drop calorimetry, CV – Calvert calorimetry

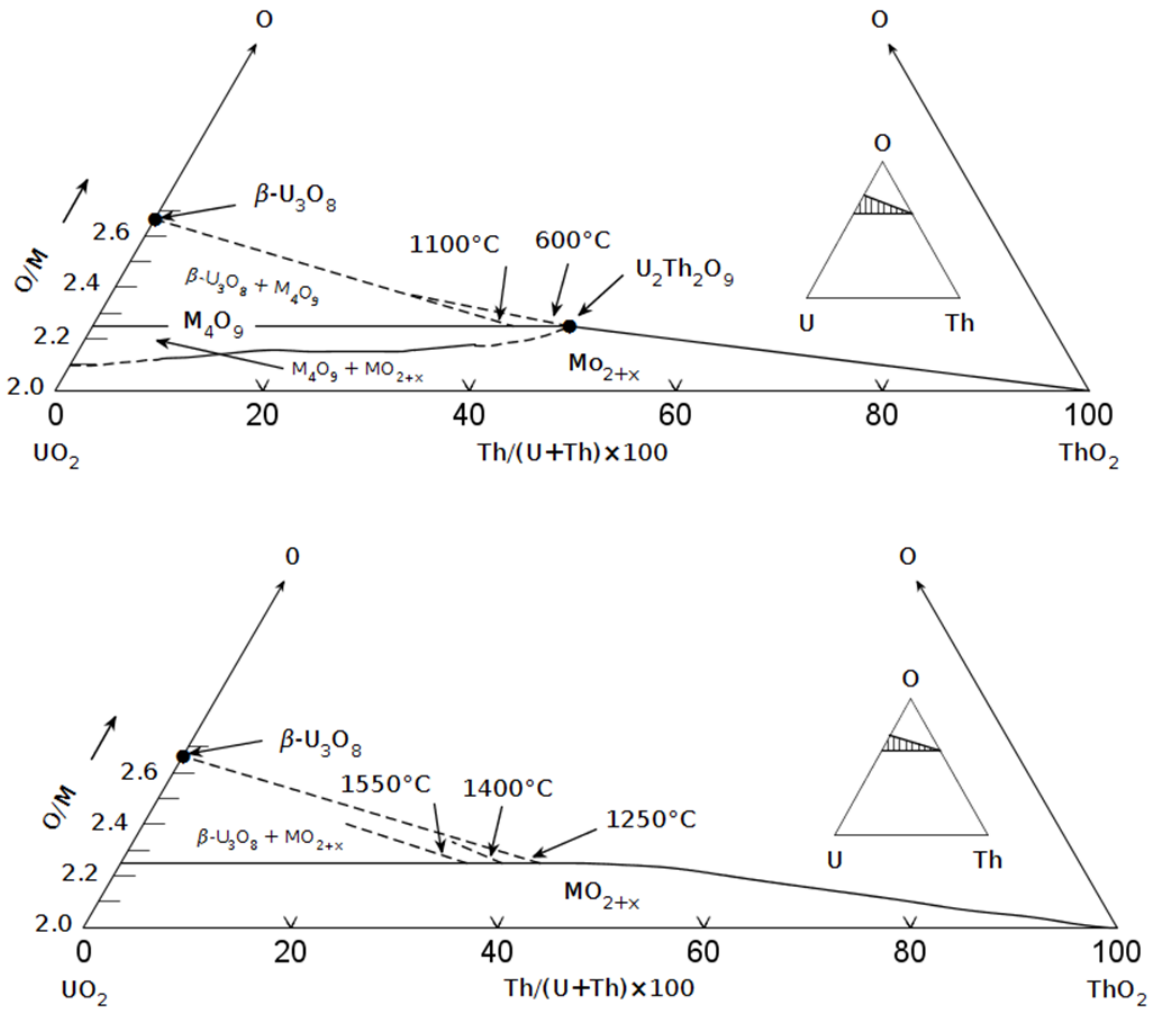

Fig. 4.5. Ternary U-Th-O phase diagrams proposed by Paul and Keller [148]and based on a HTXRD study of that system at 1.01325 bar O_2 pressure. **(**Reprinted with permission of The American Ceramic Society, www.ceramics.org All rights reserved.)

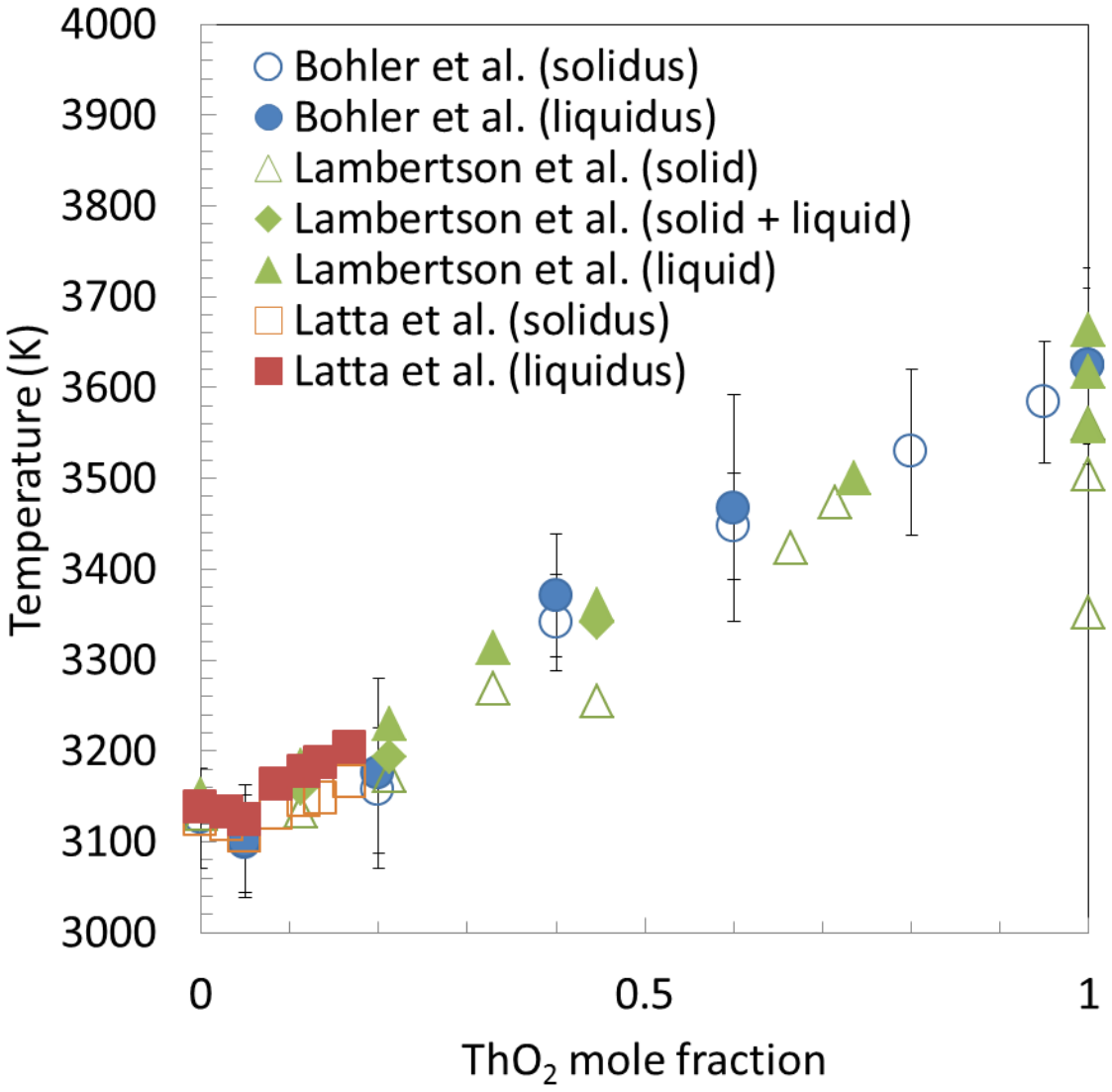

Fig. 4.6. Solidus (open symbols) and liquidus (closed symbols) data from [151-153]along the UO_2–ThO_2 psuedobinary isopleth.

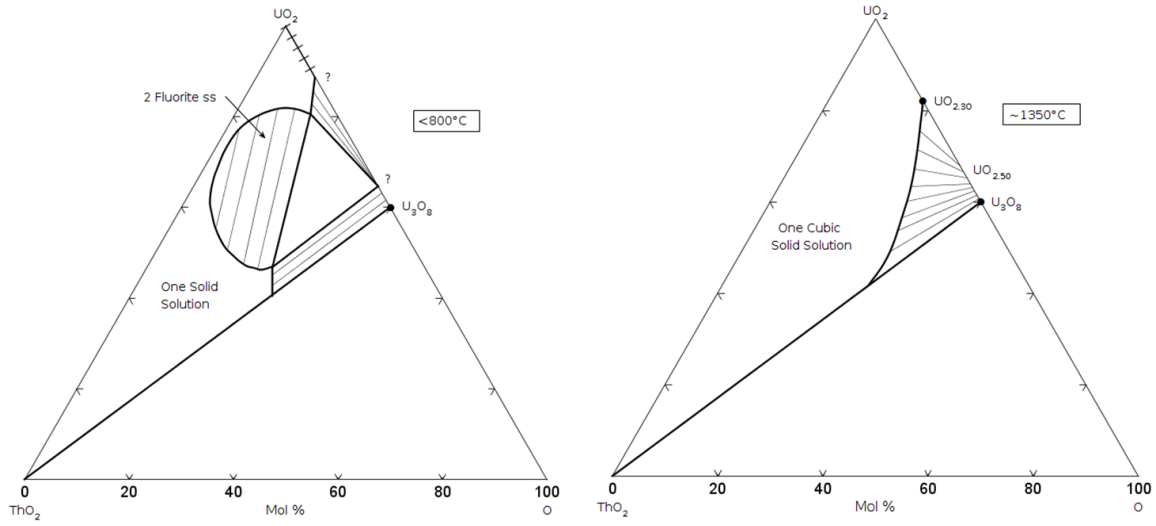

Fig. 4.7. *Not-impossible* pseudoternary phase diagram for the UO_2-ThO_2-O proposed by Mumpton and Roy [150]. **(**Reprinted with permission of The American Ceramic Society, www.ceramics.org All rights reserved.)

CHAPTER 5

EXPERIMENTAL

"For the second law, I will burn at the stake." – Heinz London

Thermogravimetric analysis (TGA) is used to characterize the oxygen pressure in equilibrium with $UO_{2\pm x}$ as a function of temperature and composition; there are many examples of U-O studies using this technique in the literature, see for example [7, 59, 145, 154]. The μ_{O_2} of the system is fixed and a microbalance measures the change in mass of $UO_{2\pm x}$ which is correlated to a change in O/M. The aim of the experimental effort reported here is to determine the μ_{O_2} effect on the O/M of the $U_{1-y}Th_yO_{2\pm x}$ solid solution to supplement existing data for the U-Th-O system.

5.1 Sample preparation[1]

Solid state thermodynamic studies can be limited by kinetically driven diffusion processes; therefore care must be taken to ensure that equilibrium is truly attained. Fortunately, the mobility of oxygen in urania phases is high in the temperature ranges (1273 K – 2023 K) of the studies undertaken in this work. Further, mixed oxides fabricated using the Modified Direct Denitration (MDD) process are characterized as

[1] The sample was prepared by Stewart L. Voit, Nuclear Fuel Materials Group, Fusion and Materials for Nuclear Systems Division, Oak Ridge National Laboratory, Oak Ridge, TN. The XRD analysis was performed by Dr. Chinthaka Silva, Radiation Effects and Microstructure Analysis, Materials Science and Technology Division, Oak Ridge National Laboratory, Oak Ridge, TN. These efforts support this work and do not represent an original contribution made by the author.

fully homogenized $U_{1-y}Th_yO_{2\pm x}$ solid solutions [155] compared to the traditional method of mechanical mixing of separate oxides, in this case UO_2 and ThO_2, requiring repeated crushing and sintering. This is time consuming and oftentimes produces an inadequately mixed product. On the other hand, the MDD process yields very fine grained microstructure oxides meaning diffusion paths are small and complete mixing is assumed to be attained.

The MDD procedure is as follows. Known ratios of UO_2 and ThO_2 starting materials are dissolved in nitric acid (HNO_3) and heated to ~353 K to form the metal nitrate $U_{1-y}Th_yO_{2\pm x}(NO_3)_2$. Ammonium nitrate is then added to produce a double salt given by $(NH_4)_2\ U_{1-y}Th_yO_{2\pm x}(NO_3)_4$ which is subsequently denitrated in a rotary kiln operating between 553 and 623 K to yield a free flowing intimately mixed powder of fully oxidized metals, i.e. UO_3 and ThO_2. The crystallite size for the individual oxides is on the order of 10 – 100 nanometers; hence the two phases are intimately mixed. After high temperature thermal treatment in an appropriate oxygen atmosphere to adjust the oxygen stoichiometry (conditioning), the powder forms a single phase 500-1500 mg $U_{1-y}Th_yO_{2\pm x}$ solid solution verified by XRD. Sample purity has been benchmarked form experience using ICP analysis that shows negligibly small quantities of foreign matter are introduced in the MDD process. It is determined that the effect of impurities are negligible for this work [156].

For this work, 372 mg and 1054 mg samples corresponding to $U_{0.95}Th_{0.05}O_{2\pm x}$ and $U_{0.80}Th_{0.20}O_{2\pm x}$ were prepared by the MDD method discussed above. Upon conditioning to an O/M = 2.000, XRD analysis was performed to confirm both the composition and the existence of a single phase FCC solid solution; an example of those results for the $U_{0.80}Th_{0.20}O_{2\pm x}$ sample are shown in Figure 5.1.

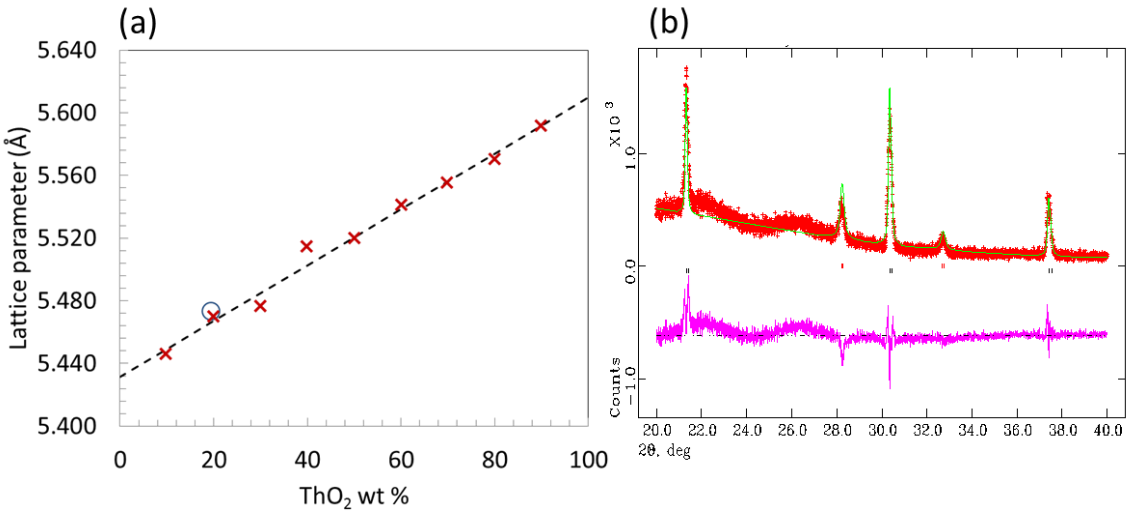

Fig. 5.1. (a) Vegard's law slope versus composition (dashed line) for the stoichiometric urania-thoria flourite solid solution determined from XRD measurments (red x symbols) in [157]. The lattice parameter for $U_{0.80}Th_{0.20}O_{2\pm x}$ mixed oxide (blue circle) used in this work corresponds to a sample of ~23 mole % thoria. (b) Reflections showing a single FCC phase for the $U_{0.80}Th_{0.20}O_{2\pm x}$ sample from XRD analysis performed by Dr. Chinthaka Silva at Oak Ridge National Laboratory.

5.2 Measurements

Thermogravimetric analysis using a NETZSCH STA 449 F1 Jupiter® scanning thermal analyzer, shown in Fig. 5.2, was performed to measure the relationship between the equilibrium oxygen pressure, temperature, and O/M for the $U_{1-y}Th_yO_{2\pm x}$ solid solutions. For a sample of known or U/Th ratio the temperature and total pressure (1 atm) is controlled by the STA 449 F1 while the p_{O_2} is fixed by an Environics® Series 2000 Computerized Multi-Component Gas Mixer by combining H_2, O_2 and/or H_2O gases in appropriate ratios. The equilibrium reaction is given by Eqn. 5. 1.

$$H_2 + \frac{1}{2}O_2 \leftrightarrow H_2O \qquad \textbf{5. 1}$$

At equilibrium, Eqn. 5. 2 holds.

$$\mu_{H_2O} - \mu_{H_2} - \frac{1}{2}\mu_{O_2} = 0 \qquad \textbf{5. 2}$$

For an ideal gas of species *i*, μ_i is calculated according to Eqn. 5. 3.

$$\mu_i = {}^{\circ}G_i + RT \ln p_i \qquad \textbf{5. 3}$$

Combining Eqns. 5. 2 and 5. 3 gives the following relationship.

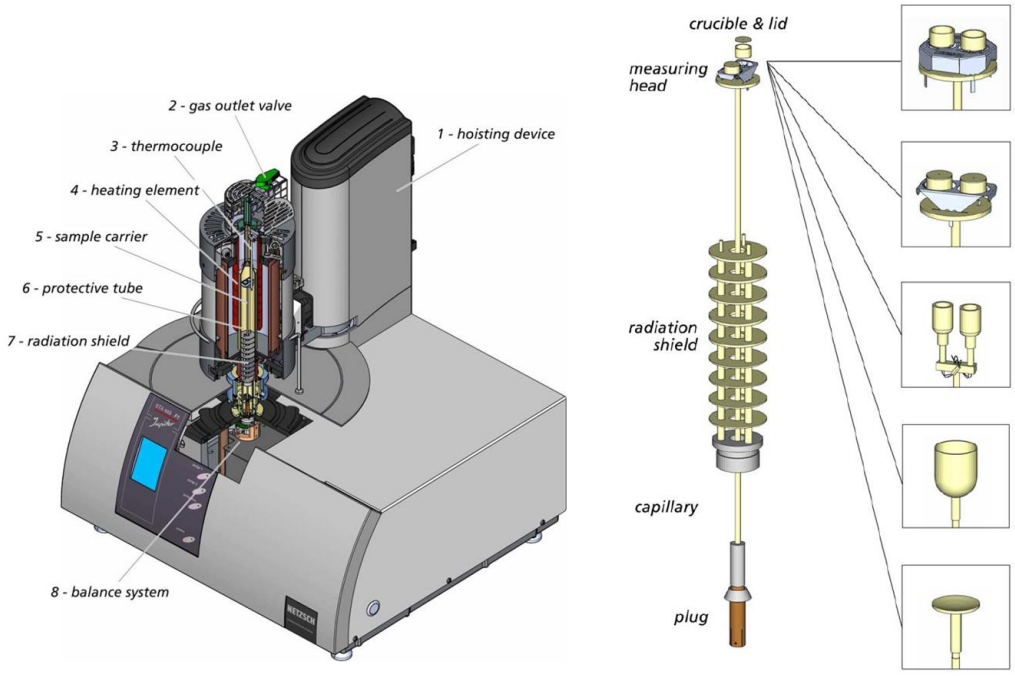

Fig. 5.2. Illustration of the NETZSCH STA 449 F1 Jupiter® scanning thermal analyzer and its basic components [158].

$$p_{O_2} = \frac{p_{H_2O}^2}{p_{H_2}^2} e^{\frac{2\Delta G_{rxn}}{RT}} \qquad \textbf{5 4}$$

The oxygen partial pressure was measured with a Centorr® Oxygen Monitor Model 2D at the outlet of the STA 449 F1. The sensor is a voltaic cell composed of a yttria stabilized zirconia (YSZ) electrolyte that operates at 1073 K to facilitate oxygen ion migration between the reference (ambient air | Pt) and the working (sample gas | Pt) electrodes when there exists an μ_{O_2} imbalance between the two. A high impedance electronic circuit registers the oxygen potential (pressure) difference between the two electrodes as a cell voltage; the two are related via the Nernst equation:

$$\Delta V = \frac{RT}{F} \ln\left(\frac{0.206atm}{p_{O_2}}\right) \qquad \textbf{5. 5}$$

where F is Faraday's constant. The range of the instrument is between 2E+05 to 1E-16 ppm oxygen content. Table 5.1 compares p_{O_2} measured by the Centorr unit to those calculated from Eqn. 5 4 for various flow rates typical for a TGA experiment; the percent difference of the logarithmic values are all within 5%; the excellent agreement means no calibration of the oxygen sensor was needed. Fig. 5.3 shows the recorded p_{O_2} signal versus time corresponding to the flow combinations given in Table 5.1.

The sample was placed in an alumina crucible from Netzsch instruments in a furnace lined with an alumina protective tube and heated with a silicon carbide or high temperature graphite resistance element. The mass change was electronically measured by a microbalance with a sensitivity of ±0.025μg and equilibrium was judged to occur when the rate of mass change was within the reported drift tolerance of the instrument

Table 5.1
Comparison of the calculated and measured oxygen partial pressure associated with different flow settings through the EGMS unit.

Ar-2%O_2	Ar-4.07%H_2	p_{O_2} (calculated)	p_{O_2} (measured)	$\frac{\log(p_{O_2}^{measured}) - \log(p_{O_2}^{calculated})}{\log(p_{O_2}^{calculated})} \times 100\%$
0.633	99.367	1.77E-17	3.95E-17	2.08%
5.683	94.317	1.77E-15	1.81E-15	0.07%
40.506	59.494	1.77E-12	1.39E-12	0.89%
49.252	50.748	1.85E-10	1.65E-10	0.51%
52.771	47.229	1.00E+03	1.35E+03	4.33%
75.072	24.928	1.03E+04	1.14E+04	1.15%

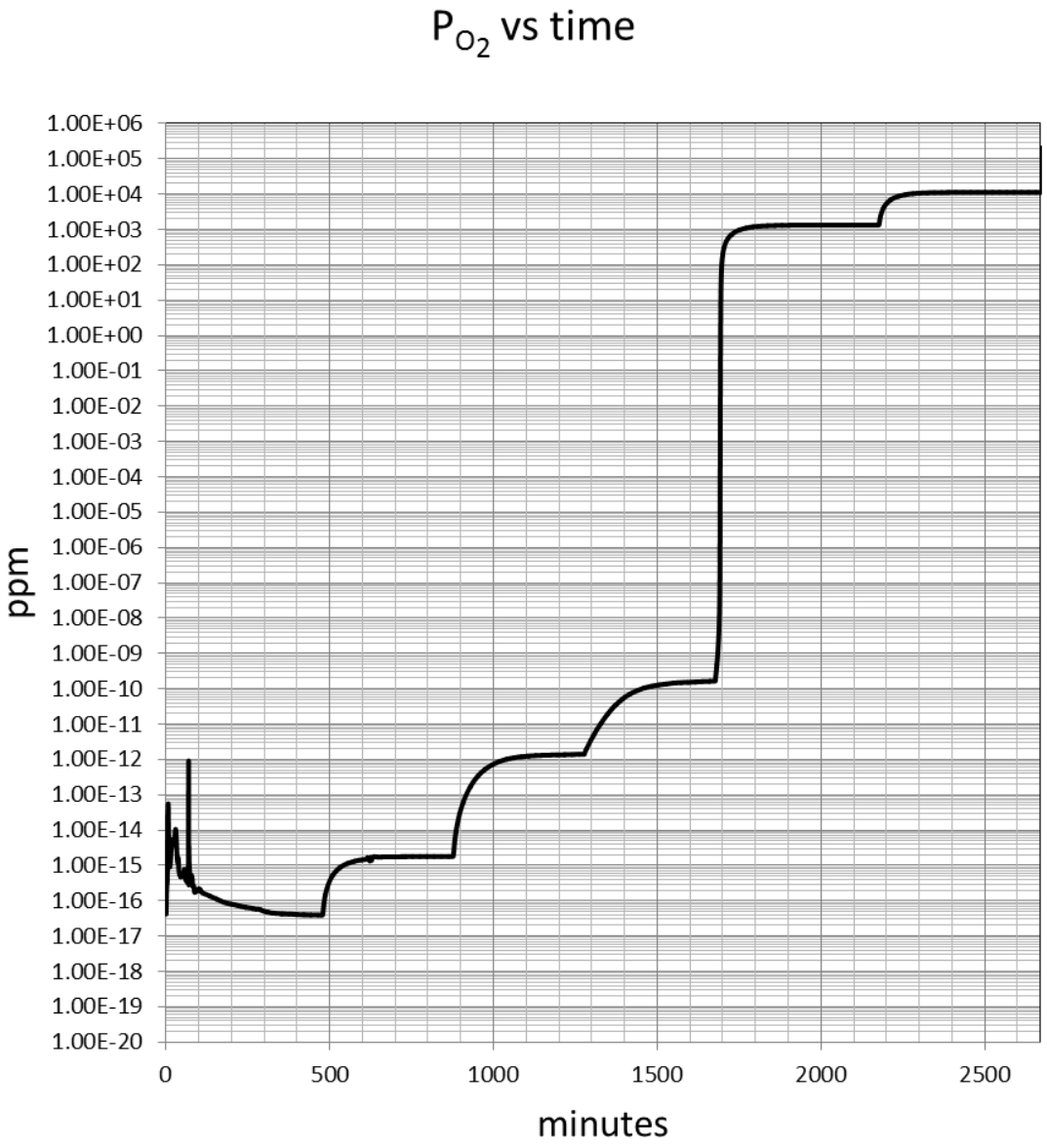

Fig. 5.3. The measured O_2 concentration from the Centorr unit using the test gas combinations given in Table 5.1 to verify instrument calibration.

(±10 μg/hr). The measurements were stored and displayed in real time using Proteus® Version 5.2.0, the STA 449 F1 data acquisition and analysis companion software.

The mixed oxide sample was first conditioned to a reference (O/M^{REF}), usually an O/M = 2.000. The mass change (Δm) from the reference to equilibrium with the designated oxygen pressure is used to calculate the resulting O/M from the relation given by Eqn. 5. 6 where mw_s and $mass_s$ are the molecular weight and mass of the mixed oxide respectively at the stoichiometry corresponding to O/M^{REF}. When the O/M changes imperceptibly with steep increases or decreases in p_{O_2}, the metal oxide is assumed to be at an O/M = 2.000. Fig. 5.4 shows that equilibrating a UO_{2+x} sample at oxygen pressures differing by 7 orders of magnitude resulted in a Δm outside the sensitivity of the instrument and hence the O/M change was indeterminably small. Thus, a reference can generally be found regardless of whether a standard for conditioning to O/M = 2.000 has been established at the temperature and compositions of interest.

$$O/M = O/M^{REF} + \frac{mw_s \times (\Delta m)}{16\frac{g}{mol} \times mass_s} \qquad \textbf{5. 6}$$

The experimental procedure was first validated using a ~500 mg sample of urania free of impurities and compared to measurements of Lindemer and Sutton [59] and Aronson and Belle [154]. Figure 5.5 shows that the agreement is very good and that the thermogravimetric method used in this work yields results consistent with accepted studies.

The result of a typical TGA run is shown in Fig. 5.6. In this particular case, the Δm of a $U_{0.95}Th_{0.05}O_{2+x}$ sample at 1573 K was measured at $\log p_{O_2}$ values corresponding to those from the flow combinations given in Table 5.2. The plateaus in Δm are labeled 1 – 5 and signify that equilibrium has been attained. The resulting O/M was calculated

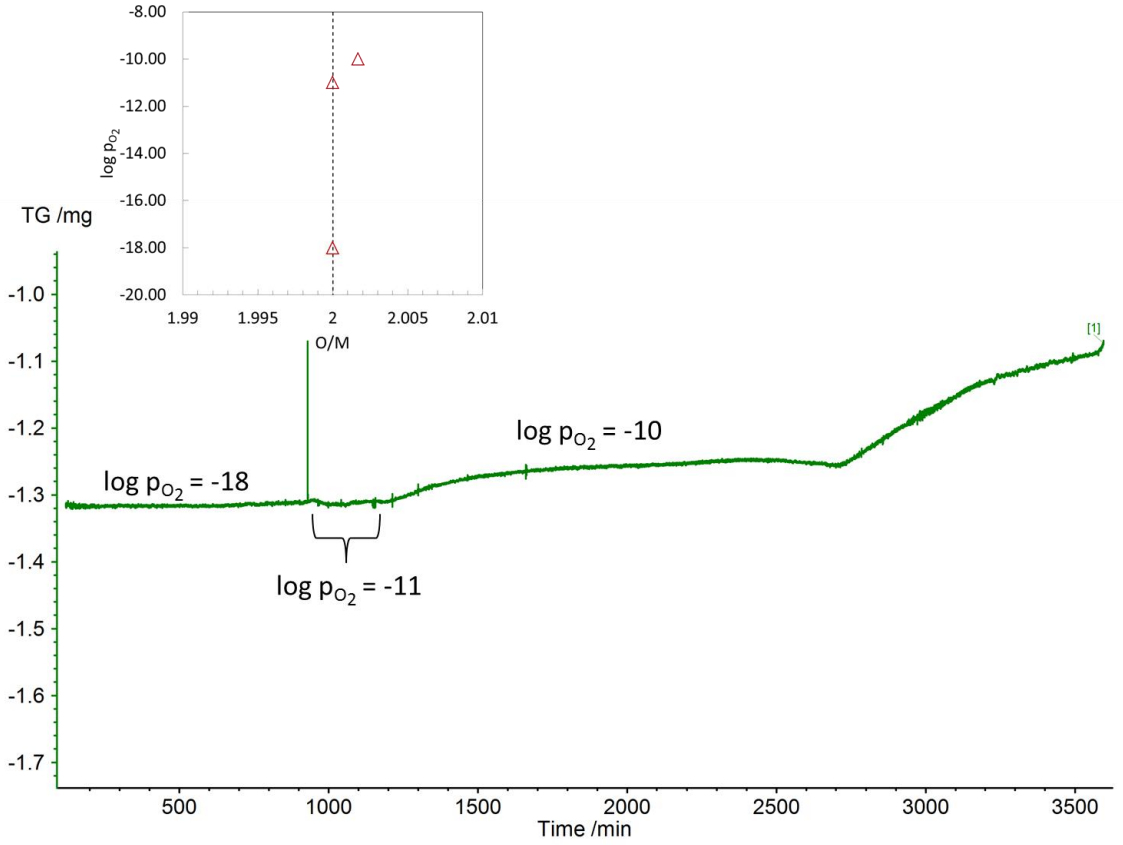

Fig. 5.4. Illustration of the mass change well within the limitations of the microbalance around O/M = 2.000 for $UO_{2\pm x}$ at 1350 K. The inset shows the corresponding log p_{O_2} and computed O/M relation from the measurement.

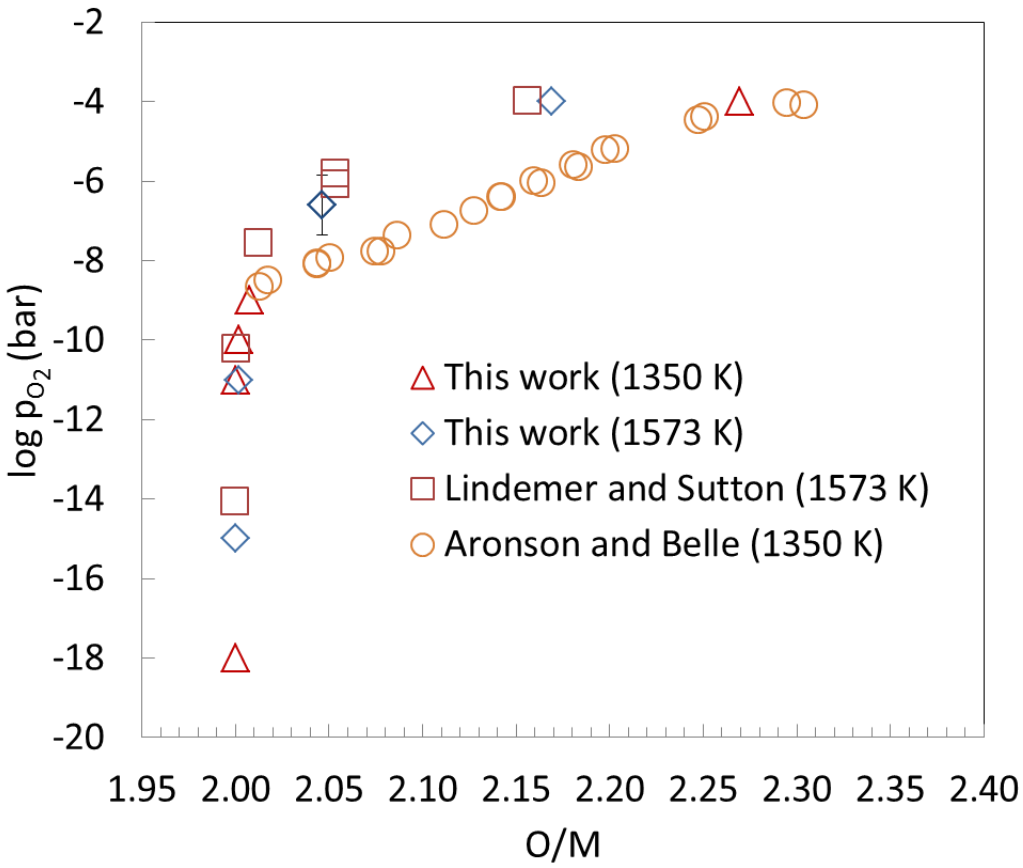

Fig. 5.5. Comparison of equilibrium oxygen pressures versus O/M for UO_{2+x} from this work using thermogravimetry to measurements of Aronson and Belle [154] and Lindemer and Sutton [59].

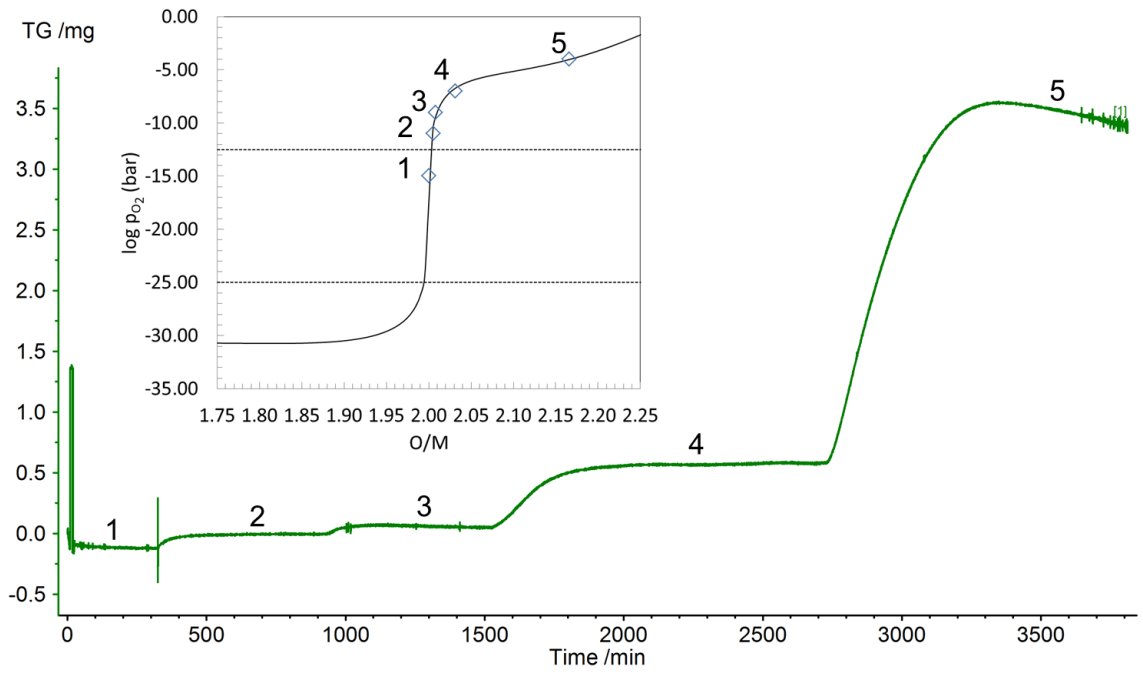

Fig. 5.6. Recorded mass change for the $U_{0.95}Th_{0.05}O_{2+x}$ sample at 1573 K. The inset shows the $\log p_{O_2}$ versus O/M relationship determined from the change in mass (symbols) and those computed (lines) using the CEF for $U_{0.95}Th_{0.05}O_{2+x}$.

Table 5.2
Flow combinations corresponding to the $\log p_{O_2}$ values used to measure the mass change of $U_{0.95}Th_{0.05}O_{2+x}$ at 1573 K in Fig. 5.6.

Flow	$\log p_{O_2}$	Ar-2%O_2 (cc/min)	Ar-4%H_2 (cc/min)
1	-15	0.668	99.332
2	-11	28.893	71.107
3	-9	46.935	53.065
4	-7	50.061	49.939
5	-4	50.667	49.333

using Eqn. 5. 6 and plotted against the log p_{O_2} in the inset of Fig. 5.6 where each number corresponds to the log p_{O_2} and O/M associated with each plateau in O/M.

At high temperatures, i.e. T ≥ 1573 K, and high O/M, the $U_{1-y}Th_yO_{2+x}$ sample lost weight from vaporization of metal containing species for all *y* values considered. This phenomenon has been observed for both pure urania and urania solid solutions [59, 159] . Because of the very high oxygen pressures, the following reaction is favored:

$$UO_2(g) + \frac{1}{2}O_2(g) \rightarrow UO_3(g) \qquad \textbf{5. 7}$$

so much so, the vapor pressure of UO_3 can reach values of 10^{-6} bar and greater above O/M = 2.15 at 1573 K as shown in Fig. 5.7; this is enough to cause mass loss equivalent to 0.063 mg/hr or more given a 110 cc/min process gas flow rate. This is why plateau 5 in Fig. 5.6 exhibits a downward slope after saturation with oxygen. Here, the sample is in a *psuedo*equilibrated state since it continues to vaporize UO_3 in order to establish a partial pressure associated with equilibrium losing both U and O. The O is quickly replaced by the process gas since the μ_{O_2} is fixed by the continuous flow; however the sample is becoming depleted in U. This is not a significant problem for measurements of UO_{2+x}; however for $U_{1-y}Th_yO_{2+x}$, the U/Th ratio is changing. Therefore, the mass of the $U_{1-y}Th_yO_{2+x}$ sample was chosen to be large enough such that sufficient U would be present to mitigate the vaporization effects corresponding to p_{UO_3} on the order of 10^{-4} bar.

The procedure for making measurements in regions where UO_3 vaporization is problematic involved first conditioning the sample to an O/M =2.000, oxidation to the desired p_{O_2} , then a rapid reduction back to O/M = 2.000. The difference in mass between the first and final O/M = 2.000 allowed a new U/Th ratio to be determined and the O/M to be calculated from the Δm from the last O/M = 2.000 plateaut. In order to collect data

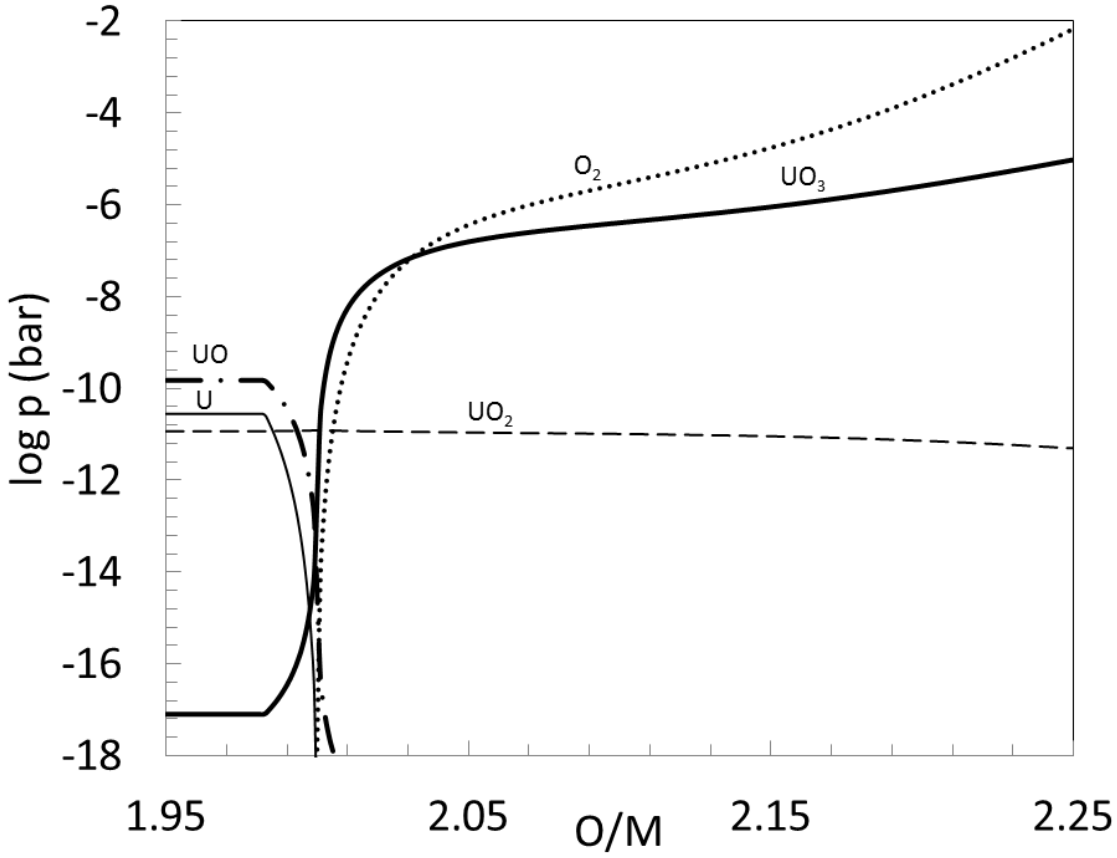

Fig. 5.7. Computed equilibrium vapor pressures of the major gaseous species over $UO_{2\pm x}$ at 1573 K.

in these regions, equilibrium was judged to be attained when the slope of the mass loss reached a constant rate subsequent to a maximum.

5.3 Approach to error analysis

The repeatability of the microbalance was observed to be ±40 μg making the total estimated error in O/M about ±0.001 and ±0.002 for the 1054 mg and 372 mg samples, respectively. The uncertainties were calculated by using Eqn. 5. 8 where q is a function of variables x_i, δq is one standard deviation (STD) in q, and δx_i is the STD associated with x_i [160].

$$\delta q = \sqrt{\left(\sum_i \frac{\partial q}{\partial x_i} \delta x_i \right)^2} \qquad \textbf{5. 8}$$

The Environics® Series 2000 sets initial amounts of O_2/H_2 or H_2O/H_2 mixes from gas bottles of known compositions supplied by AIR LIQUID™ that react to give oxygen pressures calculated by Eqn. 5 4. The estimated error in the calculated oxygen pressure is considered to propagate from three sources: composition of the gas bottles, flow rate in the Environics® Series 2000, and temperature of the system. The uncertainties associated with the determined values are summarized in Table 5.3.

The uncertainty in the temperature of the furnace is found from calibration of the thermocouple to the melting point standards for tin, zinc, aluminum, gold, silver, and nickel.

Assuming the ideal gas law applies, Eqn. 5. 9 holds

Table 5.3
Error sources and estimates for oxygen potential determination.

Source	Manufacturer	Uncertainty
Gas bottle composition	Air Liquide	±1 – 5% of reported composition
Mixed gas flow rate	Environics	±0.5% of the flow
Thermocouple	Netzsch	±0.12 – 0.44 K

$$n_i \propto x_i V = v_i \qquad \textbf{5. 9}$$

where n_i and x_i are the number of moles and composition of species *i* respectively and *V* is the total volume. Since Eqn. 5 4 depends only on relative amounts, it can be rewritten as

$$p_{O_2} = \frac{v_{H_2O}^2}{v_{H_2}^2} k \quad \text{where } k = e^{\frac{2\Delta G_{rxn}}{RT}} \qquad \textbf{5. 10}$$

The change in initial composition can be calculated by introducing the reaction extent variable (ξ) after Smith et al. [161] thus giving

$$p_{O_2} = \frac{v_{O_2}^i - \frac{1}{2}\xi}{V^i - \frac{1}{2}\xi} = \frac{\left(v_{H_2O}^i + \xi\right)^2}{\left(v_{H_2}^i - \xi\right)^2} k \qquad \textbf{5. 11}$$

where the superscript *i* represents the initial relative flow rate of the species corresponding to the subscript before reacting. Since ΔG_{rxn} is large and negative for H_2/O_2 flow combinations with oxygen as a limiting reagent, Eqn. 5. 11 is approximated by

$$p_{O_2} = \frac{\left(2x_{O_2}V_{O_2}\right)^2}{\left(x_{H_2}V_{H_2} - 2x_{O_2}V_{O_2}\right)^2} k \qquad \textbf{5. 12}$$

where V_i represents the flow of species *i* in an Ar carrier in cm^3/min.

If hydrogen limits the reaction, p_{O_2} can be estimated using Dalton's law of partial pressures such that

$$p_{O_2} = \frac{x_{O_2}V_{O_2} - \frac{1}{2}x_{H_2}V_{H_2}}{V_{O_2} + V_{H_2} - \frac{1}{2}x_{H_2}V_{H_2}} \qquad \textbf{5. 13}$$

The oxygen pressure for H_2O/H_2 flow combinations is conveniently estimated as

$$p_{O_2} = \frac{\left(x_{H_2O}V_{H_2O}\right)^2}{\left(x_{H_2}V_{H_2}\right)^2}k \qquad \textbf{5. 14}$$

The error is calculated by combining either Eqn. 5. 12, 5. 13, or 5. 14 with Eqn. 5. 8 to give the expression

$$\delta p_{O_2} = \sqrt{\left(\frac{\partial p_{O_2}}{\partial x_{O_2}}\delta x_{O_2}\right)^2 + \left(\frac{\partial p_{O_2}}{\partial x_{H_2}}\delta x_{H_2}\right)^2 + \left(\frac{\partial p_{O_2}}{\partial x_{H_2O}}\delta x_{H_2O}\right)^2 + \left(\frac{\partial p_{O_2}}{\partial V_{O_2}}\delta x_{O_2}\right)^2 + \left(\frac{\partial p_{O_2}}{\partial V_{H_2}}\delta x_{H_2}\right)^2 + \left(\frac{\partial p_{O_2}}{\partial V_{H_2O}}\delta x_{H_2O}\right)^2 + \left(\frac{\partial p_{O_2}}{\partial T}\delta T\right)^2} \qquad \textbf{5. 15}$$

The error associated with ξ can in principal be calculated; the value must be found either from predetermined values of p_{O_2} or by solving a third order polynomial based on

Eqn. 5. 11. Using the first approach, the two variables are not independent and therefore $\delta\xi$ cannot be found without first knowing δp_{O_2}. Solving for the roots of a third order polynomial was deemed too onerous and cumbersome to integrate into a master Microsoft© EXCEL spreadsheet for determining flow combinations corresponding to equilibrium oxygen pressures. Since the uncertainties given in Table 5.3 are only estimates, the assumptions and simplifications used to derive Eqn. 5. 12 – 5. 14 are deemed to give a good approximation of the uncertainty. Furthermore, the values from Table 5.3 are assumed to be upper bounds and are therefore divided by 4 for an estimate of one standard deviation (σ) according to the range rule.

5.4 Experimental Results

The results of the TGA measurements characterizing the equilibrium oxygen pressure versus O/M for UO_{2+x}, $U_{0.95}Th_{0.05}O_{2+x}$ and $U_{0.80}Th_{0.20}O_{2+x}$ are presented here in Fig. 5.8 (tabulated results are given in Appendix A). Fig. 5.9 shows that the $\log p_{O_2}$ for $U_{0.95}Th_{0.05}O_{2+x}$ and $U_{0.80}Th_{0.20}O_{2+x}$ as a function of O/M changes very little from that of pure UO_{2+x} and can be modeled with the CEF for pure urania. This is in agreement with the measurements made by Aronson and Clayton [135] for $U_{0.90}Th_{0.10}O_{2+x}$ and $U_{0.71}Th_{0.29}O_{2+x}$ at 1250 K. Further, that study [135] suggests that the μ_{O_2} behavior of $U_{1-y}Th_yO_{2+x}$ only begins to deviate significantly from that of UO_{2+x} at y values ~0.50. It is interesting to note that Anthonysamy et al. [139] showed the oxygen pressures over $U_{0.90}Th_{0.10}O_{2+x}$ and $U_{0.77}Th_{0.39}O_{2+x}$ at 1073 K and 1173 K to be lower than those predicted for UO_{2+x} using the CEF for that phase; however, the results from this work along with the critical analysis of the data in Section 4.4 suggests these measurements are most likely in error.

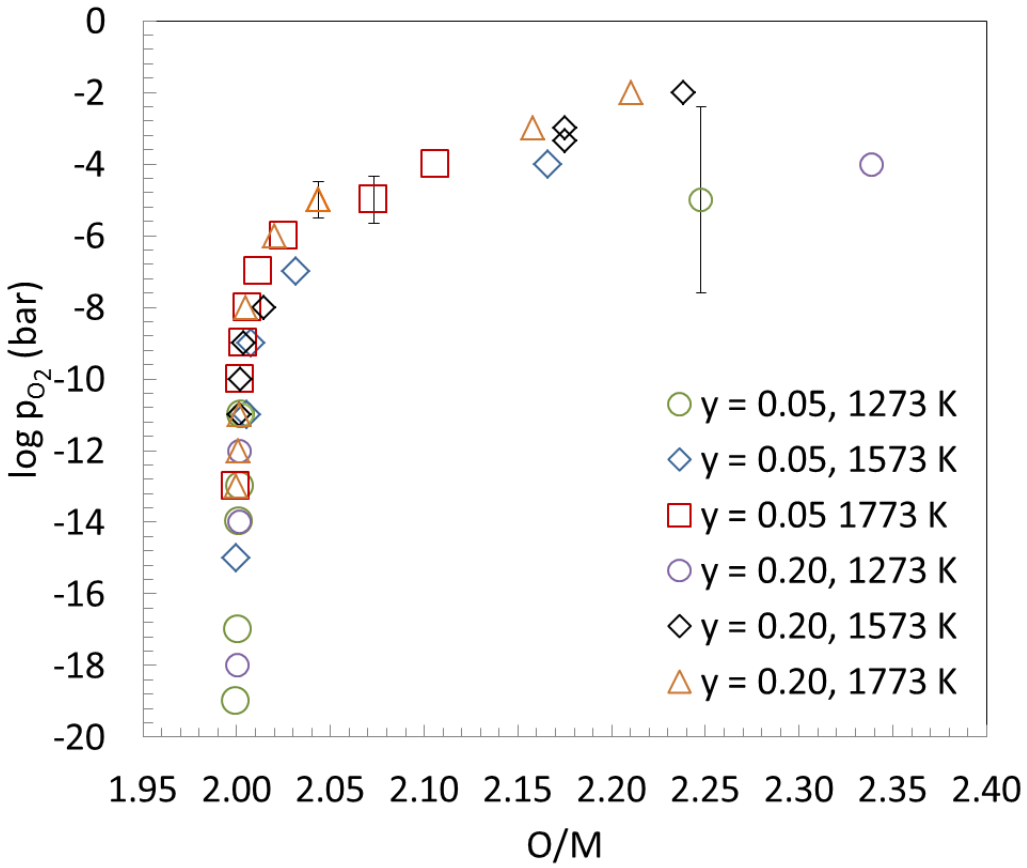

Fig. 5.8. Equilibrium oxygen pressures versus O/M relationship as a function of temperature and *y* for $U_{1-y}Th_yO_{2+x}$. The estimated uncertainty is shown as error bars when computed to be significant. A measurement of high error was taken to investigate the limitations of the instruments.

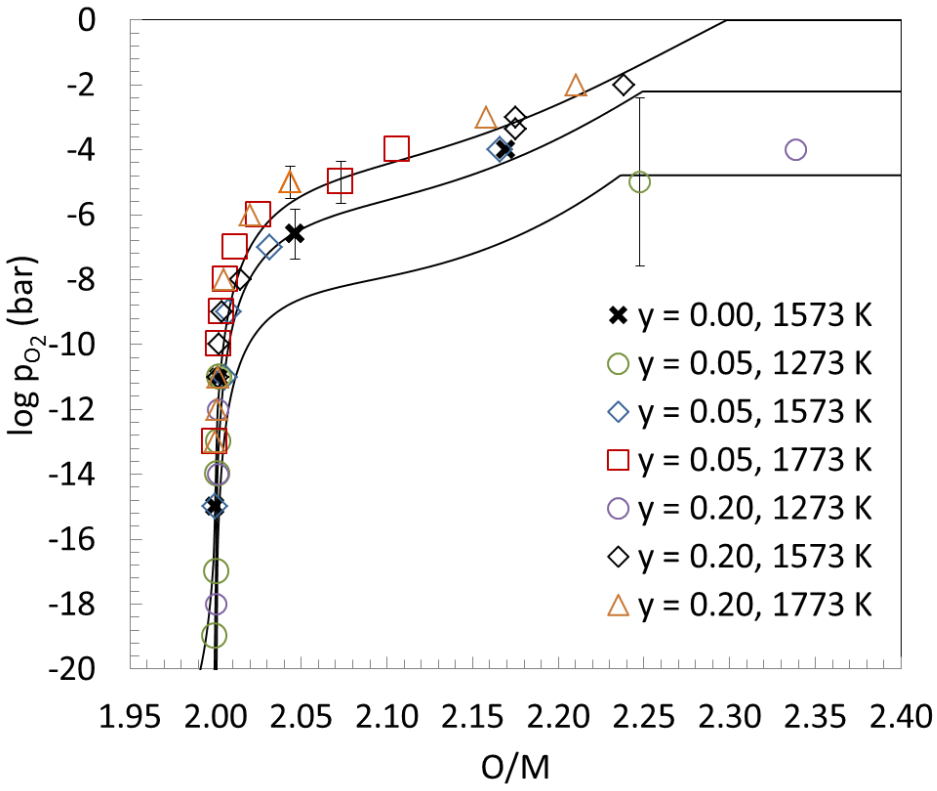

Fig. 5.9. Fit to experimentally determined equilibrium oxygen pressures for $U_{1-y}Th_yO_{2+x}$ using the CEF model for pure $UO_{2\pm x}$.

CHAPTER 6

MODELLING AND ASSESSMENTS

"With thermodynamics, one can calculate almost everything crudely; with kinetic theory, one can calculate fewer things, but more accurately; and with statistical mechanics, one can calculate almost nothing exactly." – Eugene Wigner

Generally, the thermodynamic description of multicomponent systems is developed by extension from those of lower order, i.e. unary, binaries, and ternaries. Fortunately, there exists a very large body of critically reviewed experimental studies for U-O and a well assessed database [31, 32] is available in the open literature. Therefore, this work uses the U-O assessment after Guéneau et al. [31, 32] as the fundamental subsystem for the U-M-O ternary. Since the fluorite $UO_{2\pm x}$ is the dominant phase in commercial nuclear fuel elements and because it readily dissolves many of the fission products, the most attention is given to faithfully reproducing the thermodynamic behavior in the vicinity of the urania solid solution region of the ternary phase space.

The U-O thermodynamic assessment of Guéneau et al. [31, 32] was performed using the CALPHAD method assuming all condensed phases behave independent of pressure. Apart from a significant quantity of phase equilibria measurements for the integral system, there are extensive studies reporting oxygen potential, heat capacity and melting temperatures for $UO_{2\pm x}$ due to the technological importance as it relates to nuclear fuel. The models developed in [32] well represented the reported thermodynamic behavior; a comparison of the U-O assessment to experimental data is shown in Fig. 6.1.

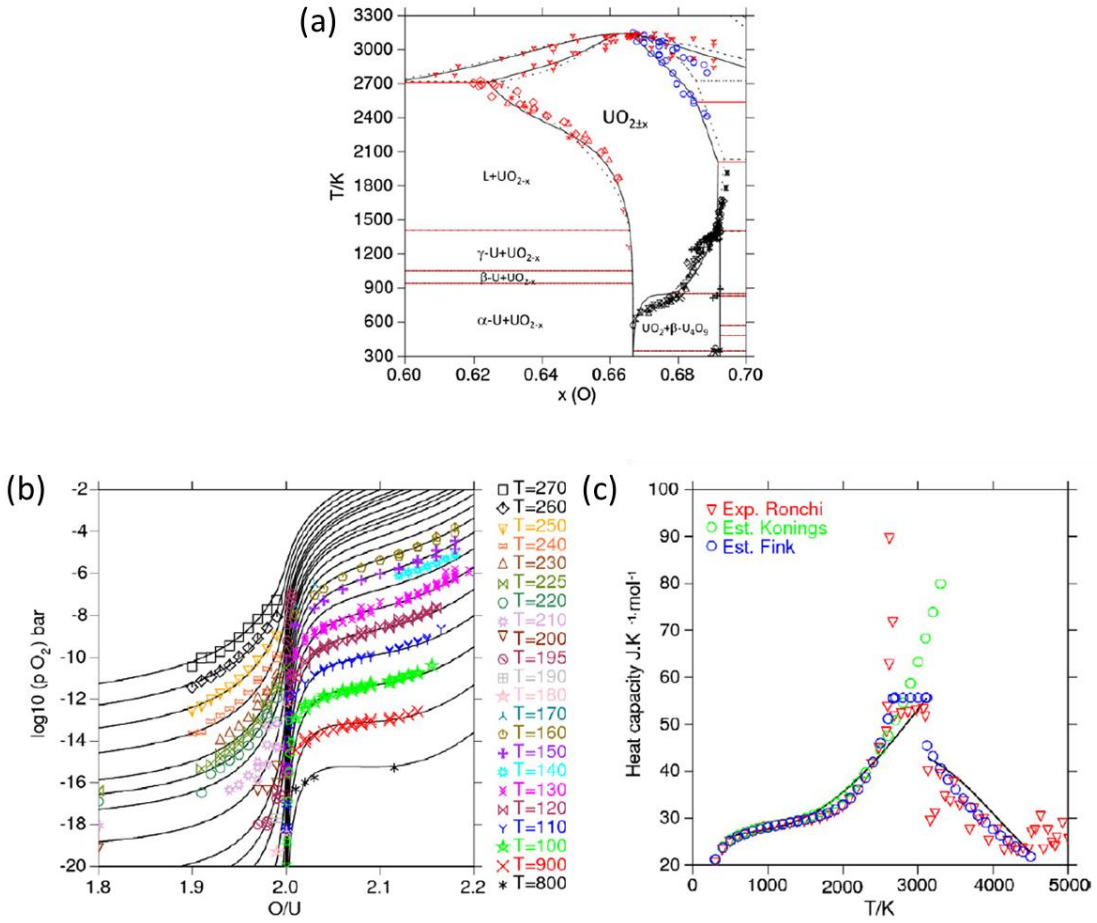

Fig. 6.1. Comparison of experimental and computed phase relations (a) oxygen pressure versus O/M (b), and heat capacity (c) in the U-O binary system from [32].

Using the CALPHAD approach, all the available data discussed in Chapters 4 and 5 were critically assessed and utilized to build the most accurate and comprehensive representation of the U-Gd-O, U-La-O, and U-Th-O systems as possible. In the current effort, the pressure dependence of the condensed phases is assumed to be negligible and all species are referred to the enthalpy of formation from their stable elements at standard state conditions of 298.15 K and 1 bar.

6.1 The gas phase

The gas phase is assumed to exhibit ideal behavior, therefore the Gibbs energy is defined as:

$$G^{gas} = \sum_i \left({}^{\circ}G_i + RT \ln x_i \right) + RT \ln \frac{p}{1bar} \qquad \textbf{6. 1}$$

where ${}^{\circ}G_i$ is the Gibbs energy function of component *i*. The major vapor species in the U-Gd-O, U-La-O, and U-Th-O systems are considered to be U, Gd, La_2, UO, GdO, LaO, La_2O_2, La_2O, ThO, UO_2, UO_3, and O_2 [7, 61, 162, 163] and their Gibbs functions come from the thermodynamic databases given in Appendix B–D.

6.2 Pure elements and stoichiometric phases

The compounds U_4O_9, U_3O_8, and UO_3 are treated as stoichiometric phases after Guéneau et al. [31, 32] as are the Gd_2O_3 and La_2O_3 sesquioxides. Gadolinium and La are treated as pure elemental metals with no U or O solubility. The Gibb functions are expressed as a power series with temperature as follows:

$$G = a + bT + cT\ln T + dT^2 + eT^3 + fT^{-1}... \quad \textbf{6. 2}$$

The coefficients for Eqn. 6. 2 are given in Appendix B–D.

6.3 The $UO_{2\pm x}$ phase

The compound energy formalism (CEF) is used to describe the Gibbs energy of the $UO_{2\pm x}$ phase. In the CEF model for $UO_{2\pm x}$ the first sublattice (i) contains cations in a cubic structure, the second sublattice (ii) is occupied by oxygen anions and vacancies in tetrahedrally coordinated with respect to the cations, and the third sublattice (iii) represents octahedrally coordinated sites for interstitial anions. Guéneau et al. [31, 32] therefore represent the ordering in the UO_2 crystal using the following sublattice model:

$$(U^{3+}, U^{4+}, U^{5+})_1 (O^{2-})_2 (Va^0)_1 \quad \textbf{6. 3}$$

The general form of the CEF as discussed in Chapter 2 is given here again as Eqn.6. 4.

$$G^{CEF} = \sum_k {}^{o}G_k \prod_s y_J^s + RT\left(\sum_s \sum_J n^s y_J^s \ln y_J^s\right) + {}^{xs}G \quad \textbf{6. 4}$$

The $G^{s.r.}$ term given for $UO_{2\pm x}$, given by Eqn. 2. 2, is a mechanical mixture of the following end-member compounds:

$U^{3+}:O^{2-}:O^{2-}$	$U^{4+}:O^{2-}:O^{2-}$	$U^{5+}:O^{2-}:O^{2-}$
$U^{3+}:O^{2-}:Va^{0}$	$U^{4+}:O^{2-}:Va^{0}$	$U^{5+}:O^{2-}:Va^{0}$
$U^{3+}: Va^{0}:O^{2-}$	$U^{4+}: Va^{0}:O^{2-}$	$U^{5+}: Va^{0}:O^{2-}$
$U^{3+}: Va^{0}:Va^{0}$	$U^{4+}: Va^{0}:Va^{0}$	$U^{5+}: Va^{0}:Va^{0}$

The entropy is estimated by assuming random mixing within each sublattice. The molar Gibbs energy is then:

$$\begin{aligned} G = {} & y^{i}_{U^{3+}} y^{ii}_{O} y^{iii}_{O} {}^{\circ}G_{U^{3+}:O:O} + y^{i}_{U^{3+}} y^{ii}_{O} y^{iii}_{Va} {}^{\circ}G_{U^{3+}:O:Va} + y^{i}_{U^{3+}} y^{ii}_{Va} y^{iii}_{O} {}^{\circ}G_{U^{3+}:Va:O} + y^{i}_{U^{3+}} y^{ii}_{Va} y^{iii}_{Va} {}^{\circ}G_{U^{3+}:Va:Va} + \\ & y^{i}_{U^{4+}} y^{ii}_{O} y^{iii}_{O} {}^{\circ}G_{U^{4+}:O:O} + y^{i}_{U^{4+}} y^{ii}_{O} y^{iii}_{Va} {}^{\circ}G_{U^{4+}:O:Va} + y^{i}_{U^{4+}} y^{ii}_{Va} y^{iii}_{O} {}^{\circ}G_{U^{4+}:Va:O} + y^{i}_{U^{4+}} y^{ii}_{Va} y^{iii}_{Va} {}^{\circ}G_{U^{4+}:Va:Va} + \\ & y^{i}_{U^{5+}} y^{ii}_{O} y^{iii}_{O} {}^{\circ}G_{U^{5+}:O:O} + y^{i}_{U^{5+}} y^{ii}_{O} y^{iii}_{Va} {}^{\circ}G_{U^{5+}:O:Va} + y^{i}_{U^{5+}} y^{ii}_{Va} y^{iii}_{O} {}^{\circ}G_{U^{5+}:Va:O} + y^{i}_{U^{5+}} y^{ii}_{Va} y^{iii}_{Va} {}^{\circ}G_{U^{5+}:Va:Va} + \\ & RT\left[\begin{matrix}\left(y^{i}_{U^{3+}} \ln y^{i}_{U^{3+}} + y^{i}_{U^{4+}} \ln y^{i}_{U^{4+}} + y^{i}_{U^{5+}} \ln y^{i}_{U^{5+}}\right) + \\ 2\left(y^{ii}_{O} \ln y^{ii}_{O} + y^{ii}_{Va} \ln y^{ii}_{Va}\right) + \left(y^{iii}_{O} \ln y^{iii}_{O} + y^{iii}_{Va} \ln y^{iii}_{Va}\right)\end{matrix}\right] + \\ & {}^{xs}G \end{aligned} \qquad \textbf{6. 5}$$

Of the possible end-members shown above, only U^{4+}:O:Va is neutral corresponding to the stoichiometric UO_2 compound. The others may only exist in electronically neutral combinations. In the CEF for $UO_{2\pm x}$ after Guéneau et al. [31, 32], the Gibbs energy of the end-members U^{3+}:Va:O, U^{4+}:Va:O, and U^{5+}:Va:O are considered unstable and given a constant value +100000 kJ/mol. The model from [32] defines a $UO_{2.5}$ compound as a neutral combination of U^{5+}:O:Va and U^{5+}:O:O according to Eqn. 6. 6 to represent a fully oxidized U, i.e. U^{5+} in the phase.

$${}^{\circ}G_{UO_{2.5}} = 0.5\,{}^{\circ}G_{U^{5+}:O:Va} + 0.5\,{}^{\circ}G_{U^{5+}:O:O} + RT\ln 0.5 \qquad \textbf{6. 6}$$

where the entropy of mixing term, $RT\ln 0.5$, originates from the octahedrally coordinated oxygen sublattice being ½ filled.

Guéneau et al. defined another compound $UO_{1.5}$ representing fully reduced U, i.e. U^{3+}, in the fluorite structure. It is expressed as a mixture of U^{3+}:O:Va and U^{3+}:Va:Va and given by Eqn. 6. 7 as follows:

$$^{\circ}G_{UO_{1.5}} = 0.75\,^{\circ}G_{U^{3+}:O:Va} + 0.25\,^{\circ}G_{U^{3+}:Va:Va} + 2RT\left(0.75\ln 0.75 + 0.25\ln 0.25\right) \quad \textbf{6. 7}$$

Here, $2RT\left(0.75\ln 0.75 + 0.25\ln 0.25\right)$ represents the entropic effect from mixing of O^{2-} and Va^{0} on the tetrahedrally coordinated sublattice.

By applying the convention after Grundy [164] of adding or subtracting the Gibbs energy of an appropriate amount of oxygen to adjust for stoichiometry, from Eqns. 6. 6 and 6. 7 the Gibbs energy of the remaining end-members are calculated using Eqns. 6. 8 – 6. 13

$$^{\circ}G_{U^{n+}:O:O} = {}^{\circ}G_{U^{n+}:O:Va} + 0.5\,^{\circ}G_{O_2(gas)} \quad \textbf{6. 8}$$

$$^{\circ}G_{U^{3+}:Va:Va} = {}^{\circ}G_{UO_{1.5}} - 0.75\,^{\circ}G_{O_2(gas)} - 2RT\left(0.75\ln 0.75 + 0.25\ln 0.25\right) \quad \textbf{6. 9}$$

$$^{\circ}G_{U^{4+}:Va:Va} = {}^{\circ}G_{UO_2} - {}^{\circ}G_{O_2(gas)} + \alpha^{4+} \quad \textbf{6. 10}$$

$$^{\circ}G_{U^{5+}:Va:Va} = {}^{\circ}G_{U^{5+}:O:Va} - {}^{\circ}G_{O_2(gas)} + \alpha^{5+} \quad \textbf{6. 11}$$

$$^{\circ}G_{U^{3+}:O:Va} = {}^{\circ}G_{U^{4+}:O:Va} - {}^{\circ}G_{U^{4+}:Va:Va} + {}^{\circ}G_{U^{3+}:Va:Va} \quad \textbf{6. 12}$$

$$^{\circ}G_{U^{5+}:O:Va} = {}^{\circ}G_{UO_{2.5}} - 0.25\,^{\circ}G_{O_2(gas)} - RT(\ln 0.5) \quad \textbf{6. 13}$$

where n = 3,4, and 5. The α^{n+} parameters are adjustments to the Gibbs energy of the end-members containing these terms in order to better fit the experimentally determined thermodynamic data.

It can be demonstrated that the CEF model for $UO_{2\pm x}$ can give a point defect description analogous to a classical Kröger-Vink treatment, see for example Sundman et al. [35]; however, as can be seen in Fig. 6.2, the model after Guéneau et al. [32] does not satisfactorily represent the OD transition giving oxygen Frenkel pair concentrations (n_f) at least an order of magnitude too low compared to those derived from experimental neutron diffraction studies [68, 69]. Figure 6.1(c) does show good agreement between computed and measured c_p data up to about 2500 K and the model correctly represents the increase in c_p beginning around 2000 K; however, this behavior is well reproduced by the reference Gibbs function used for the end-member compound $U^{4+}:O^{2-}:Va^0$ representing the stoichiometric UO_2 and the dominant constituent of the solution at O/M values near 2. Further, any excess c_p stems from substantial disproportionation of U^{4+} to U^{3+} and U^{5+}since these are the major defects at stoichiometry using this model.

6.4 The U-O liquid phase

The partially ionic two sublattice model [25] was used for the liquid phase with the following sublattice description:

$(U^{4+})_P(O^{2-},Va^{Q-},O)_Q$

where "O" is a neutral oxygen and $Va^{Q-}$is a charged vacancy.

To maintain charge neutrality, P and Q are defined as:

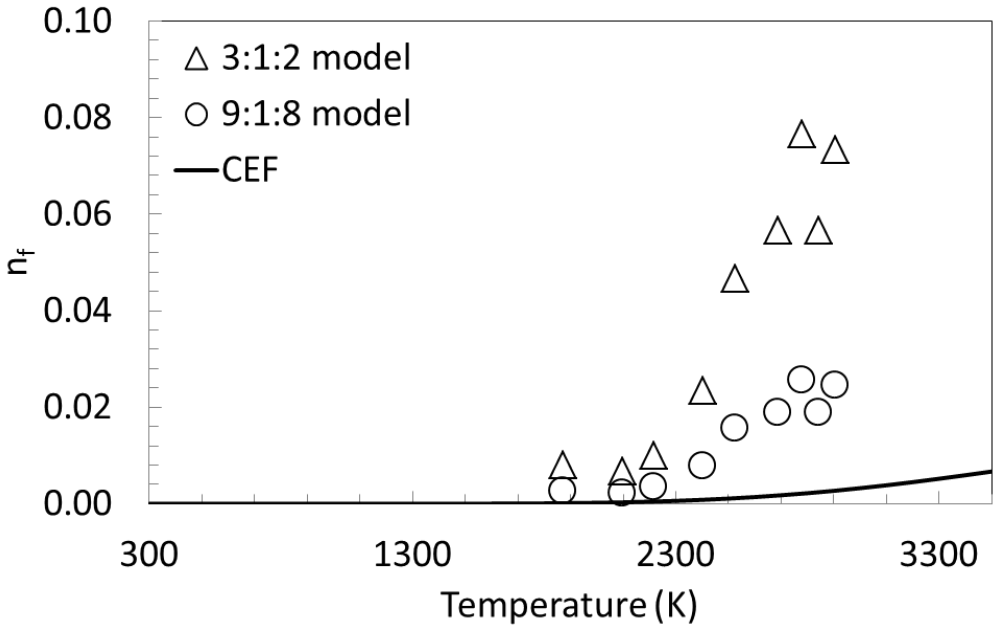

Fig. 6.2. Frenkel defect fraction determined by neutron diffraction (symbols) in [68]and computed from the CEF (line) developed by Guéneau et al. [32]for stoichiometric UO_2.

$$P = \sum_A \nu_A y_A + Q y_{Va} \qquad \textbf{6. 14}$$

$$Q = \sum_C \nu_C y_C \qquad \textbf{6. 15}$$

where ν_A and y_A are the charge and site fraction of the anion species and ν_C and y_C are the charge and site fraction of the cation *C*, respectively; y_{Va} is the site fraction for a vacancy of charge *Q*-. The Gibbs energy is defined by:

$$G^{liq} = y_{O^{2-}}{}^{\circ}G_{U^{4+}:O^{2-}} + y_{Va}{}^{\circ}G_{U^{4+}:Va} + Q y_O {}^{\circ}G_O - TS^{liq} + {}^{xs}G^{liq} \qquad \textbf{6. 16}$$

where ${}^{\circ}G_{U^{4+}:O^{2-}}$ and ${}^{\circ}G_{U^{4+}:Va}$ are the Gibbs energy of liquid UO_2 and U metal respectively. The symbols y_O and ${}^{\circ}G_O$ correspond to the site fraction and the Gibbs energy of neutral "O". The configurational entropy term S^{liq} is given by:

$$S^{liq} = -RQ\left(y_{O^{2-}} \ln y_{O^{2-}} + y_{Va} \ln y_{Va} + y_O \ln y_O\right) \qquad \textbf{6. 17}$$

and the excess Gibbs energy term, ${}^{xs}G^{liq}$, is described with the zeroth, first and second order interaction parameters from a Redlich-Kister [24] polynomial expansion:

$${}^{xs}G^{liq} = y_{U^{4+}} y_{O^{2-}} y_{Va}\left[{}^{liq}L^0_{U^{4+}:O^{2-}:Va} + \left(y_{O^{2-}} - y_{Va}\right){}^{liq}L^1_{U^{4+}:O^{2-}:Va} + \left(y_{O^{2-}} - y_{Va}\right)^2 {}^{liq}L^2_{U^{4+}:O^{2-}:Va}\right] \qquad \textbf{6. 18}$$

6.5 The rhombohedral UGd_6O_{12}

The rhombohedral δ phase ULn_6O_{12},, was first observed by Aitken et al.[117] in the U-Y-O system. It is a fluorite derivative structure belonging to the $R\bar{3}$ space group with ordering of both Ln and U on the cation sublattice and O and Va on the anion sublattice [118]. High temperature X-ray diffraction measurements in the U-La-O system suggest the δ phase is stable at least up to 1823 K exhibiting some degree of oxygen non-stoichiometry [62] but the limited extent and significant scatter in the reported data does not sufficiently describe a homogeneity range; therefore, it is assumed that UGd_6O_{12} is a stoichiometric compound. The heat capacity and standard state entropy values are taken from [165]; the standard state enthalpy of formation was determined assuming stability up to 1823 K above which UGd_6O_{12} undergoes a transition to fluorite $U_{1-y}Gd_yO_{2\pm x}$. The coefficients of the proposed Gibbs function are given in Table B.4. While two other rhombohedral phases are known to exist in other Ln-U-O systems [62, 117] they are yet to be observed in the system with Gd and are therefore not considered in this assessment.

6.6 The rhombohedral ULa_6O_{12-x} phase

The CEF [166] can describe long range ordering by proper selection of the sublattice representation. For example, Grundy et al. [164] modeled the perovskite $LaMnO_3$ phase by subdividing the cation sublattices since the La and Mn atoms occupy distinct crystallographic sites. This is indeed the case for the rhombohedral δ-phase (RI) represented by the general formula ULn_6O_{12}. It can be viewed as a fluorite derivative structure belonging to the $R\bar{3}$ space group with ordering of both Ln and U on the cation sublattice and O and Va on the anion sublattice [118]. Diehl and Keller [62] report the δ-phase in the U-La-O system exhibits hypostoichiometric behavior with a very narrow metallic homogeneity range. Due to the small compositional range with which the metal atoms deviate from stoichiometry, the RI phase can be adequately represented as ULa_6O_{12-x} and modeled using the CEF with the following sublattice description:

$(U^{4+},U^{5+},U^{6+})_1(La^{3+})_6(O^{2-},Va^0)_{12}$

where the Gibbs energy with no interaction parameters is defined as:

$$\begin{aligned} G^{\delta} = {} & y^{i}_{U^{4+}} y^{ii}_{La^{3+}} y^{iii}_{O} \circ G^{\delta}_{U^{4+}:La^{3+}:O} + y^{i}_{U^{4+}} y^{ii}_{La^{3+}} y^{iii}_{Va} \circ G^{\delta}_{U^{4+}:La^{3+}:Va} + \\ & y^{i}_{U^{5+}} y^{ii}_{La^{3+}} y^{iii}_{O} \circ G^{\delta}_{U^{5+}:La^{3+}:O} + y^{i}_{U^{5+}} y^{ii}_{La^{3+}} y^{iii}_{Va} \circ G^{\delta}_{U^{5+}:La^{3+}:Va} + \\ & y^{i}_{U^{6+}} y^{ii}_{La^{3+}} y^{iii}_{O} \circ G^{\delta}_{U^{6+}:La^{3+}:O} + y^{i}_{U^{6+}} y^{ii}_{La^{3+}} y^{iii}_{Va} \circ G^{\delta}_{U^{6+}:La^{3+}:Va} + \\ & RT\left[\left(y^{i}_{U^{4+}} \ln y^{i}_{U^{4+}} + y^{i}_{U^{5+}} \ln y^{i}_{U^{5+}} + y^{i}_{U^{6+}} \ln y^{i}_{U^{6+}}\right) + 12\left(y^{iii}_{O} \ln y^{iii}_{O} + y^{iii}_{Va} \ln y^{iii}_{Va}\right)\right] \end{aligned} \qquad \textbf{6. 19}$$

Here ${}^0G$ is the Gibbs energy for the subscripted end-member and y^s_J is the site fraction of constituent J on sublattice *s*.

The heat capacity function to describe the change in Gibbs energy with temperature was taken from [167] and assumed to be the same for each end member while the standard state enthalpy and entropy values were determined using phase relations from [62]

6.7 The rhombohedral $U_2La_6O_{15}$ phase

The rhombohedral $U_2La_6O_{15}$ (RII) phase was observed by Diehl and Kheller [62] to exhibit a narrow cation homogeneity range and to deviate very little in oxygen stoichiometry. The reflections for RII from HTXRD from [62] are reportedly the same as those for the RI phase in agreement with the study by Aitken et al. [117] of the analogous structures in the U-Y-O system. Due the similarities between the fluorite parent structure and the small observed departures from stoichiometry, it is quite likely that the observed compositional stability is within the limits of experimental error; therefore, this phase is treated as a stoichiometric compound. The heat capacity was calculated using the Neumann-Kopp rule while the standard state enthalpy and entropy were determined using

phase relations from [62]. The entropy at 298 K that best fit the phase equilibria data is 316 J·mole^{-1}·K^{-1} compared to the Neumann-Kopp value of 547 J·mole^{-1}·K^{-1}.

6.8 The rhombohedral $(U,La)_8O_{16}$ phase

Diehl and Keller [62] report a third rhombohedral (RIII) structure but failed to determine the space group. The RIII phase was observed to be stoichiometric with respect to oxygen with a substantial La homogeneity range between 55 and 67 %. The proposed formula from [62] is $(U,La)_8O_{16}$; therefore, the CEF sublattice model chosen to represent this phase is:

$(La^{3+},U^{5+},U^{6+})_4(La^{3+})_4(O^{2-})_{16}$

where the Gibbs energy, again with no interaction parameters, is defined as:

$$G^{RIII} = y^i_{La^{3+}} y^{ii}_{La^{3+}} y^{iii}_{O} {}^{\circ}G^{RIII}_{La^{3+}:La^{3+}:O} + y^i_{U^{5+}} y^{ii}_{La^{3+}} y^{iii}_{O} {}^{\circ}G^{RIII}_{U^{5+}:La^{3+}:O} + y^i_{U^{6+}} y^{ii}_{La^{3+}} y^{iii}_{O} {}^{\circ}G^{RIII}_{U^{6+}:La^{3+}:O} + RT\left[4\left(y^i_{La^{3+}} \ln y^i_{U^{4+}} + y^i_{U^{5+}} \ln y^i_{U^{5+}} + y^i_{U^{6+}} \ln y^i_{U^{6+}}\right)\right] \quad \textbf{6. 20}$$

6.9 Th-U solution phases

The models for the solid metallic α-U, β-U, γ-U, α-Th, β-Th and the liquid U-Th solution phases were taken from the CALPHAD assessment by Li et al. [168] and much of the details are left to that work. A comparison of the computed and experimentally determined phase equilibria for this system is presented in Section 6.3.2.

6.10 The $ThUO_5$ phase

This phase is treated as a stoichiometric compound. The c_p function was computed using the Neumann-Kopp rule and c_p values for UO_3 and ThO_2 from [169] while the H^{298} and S^{298} are taken from Dash et al.[74].

6.11 The $(U_{1-y}Th_y)_4O_9$ solution phase

A CEF model is used to describe the $(U_{1-y}Th_y)_4O_9$ phase with a two sublattice representation as follows:

$(Th^{4+},U^{4+},U^{5+})_4\ (O^{2-})_9$

This allows the phase to cover the $0 \leq y \leq 0.5$ compositional range as observed by Paul and Keller [148]. The 4+ and 5+ uranium cations have been observed to be the predominant oxidation states for U in this structure by Kvashnina et al. [170] using a spectroscopic technique; therefor, U^{6+} is assumed to exist in negligible concentrations. To be clear, this assumption may need to be modified and U^{6+} included to better represent the phase if experimental evidence arises to merit its addition; this is done for the $U_{1-y}Ln_yO_{2\pm x}$ and is described in more detail in Section 6.11. For simplicity, the phase is treated as stoichiometric with respect to oxygen.

The Gibbs energy is defined as:

$$G^{M_4O_9} = y^i_{Th^{4+}} y^{ii}_{O^{2-}} {}^{\circ}G^{M_4O_9}_{Th^{4+}:O^{2-}} + y^i_{U^{4+}} y^{ii}_{O^{2-}} {}^{\circ}G^{M_4O_9}_{U^{4+}:O^{2-}} + y^i_{U^{5+}} y^{ii}_{O^{2-}} {}^{\circ}G^{M_4O_9}_{U^{5+}:O^{2-}} + RT\left[4\left(y^i_{Th^{4+}} \ln y^i_{Th^{4+}} + y^i_{U^{4+}} \ln y^i_{U^{4+}} + y^i_{U^{5+}} \ln y^i_{U^{5+}}\right)\right] + {}^{xs}G^{M_4O_9} \quad \textbf{6. 21}$$

Zeroth order interaction parameters are used, therefore the ${}^{xs}G^{M_4O_9}$ is expressed as:

$$ {}^{xs}G^{M_4O_9} = y^i_{Th^{4+}} y^i_{U^{4+}} y^{ii}_{O^{2-}} {}^{M_4O_9}L^0_{Th^{4+}\cdot U^{4+}:O^{2-}} + y^i_{Th^{4+}} y^i_{U^{5+}} y^{ii}_{O^{2-}} {}^{M_4O_9}L^0_{Th^{4+}\cdot U^{5+}:O^{2-}} \quad \textbf{6. 22} $$

The Gibbs functions for the end members are those of γ-U_4O_9 from [32]; each was adjusted by adding $4RT\ln(0.5)$ that results from the entropy of mixing such that the Eqn. 6.7 is equivalent to that of pure γ-U_4O_9 when no Th is present. The H^{298} and S^{298} values for the fictive Th^{4+}:O^{2-} was selected as an adjustable parameter.

6.12 The U-M-O liquid phases

The TSLM [25] for U-O, discussed in Section 6.4, is extended to include either Ln^{3+} or Th^{4+}. Therefore, the sublattice model becomes:

$(Ln^{3+}, U^{4+})_P(O^{2-},Va^{Q-},O)_Q$

and

$(Th^{4+}, U^{4+})_P(O^{2-},Va^{Q-},O)_Q$

where "O" is a neutral oxygen species and $Va^{Q-}$is a charged vacancy.

To maintain charge neutrality, P and Q are defined as:

$$ P = \sum_A \nu_A y_A + Q y_{Va} \quad \textbf{6. 23} $$

$$ Q = \sum_C \nu_C y_C \quad \textbf{6. 24} $$

where ν_A and y_A are the charge and site fraction of the anion species and ν_C and y_C are the charge and site fraction of the cation *C*, respectively; y_{Va} is the site fraction for a vacancy of charge *Q*-.

The Gibbs energy is defined by:

$$G^{liq} = \sum_C \sum_A y_C y_A {}^{\circ}G_{C:A} + Q y_{Va} \sum_C y_C {}^{\circ}G_C + Q y_O {}^{\circ}G_O - TS^{liq} + {}^{xs}G^{liq} \qquad \textbf{6. 25}$$

where ${}^{\circ}G_{C:A}$ is the Gibbs energy of the liquid constituent corresponding to the formula $C_{\nu_A} A_{\nu_C}$ and ${}^{\circ}G_C$ is the Gibbs energy of element C. The symbols y_O and ${}^{\circ}G_O$ correspond to the site fraction and the Gibbs energy of neutral "O".

The configurational entropy term S^{liq} is given by:

$$S^{liq} = -R\left[P \sum_C y_C \ln y_C + Q\left(\sum_A y_A \ln y_A + y_{Va} \ln y_{Va} + y_O \ln y_O \right)\right] \qquad \textbf{6. 26}$$

and the excess Gibbs energy, ${}^{xs}G^{liq}$, term is described with the zeroth, first and second order interaction parameters from a Redlich-Kister [24] polynomial expansion for the U-Gd-O, U-La-O and U-Th-O melts according to Eqns. 6. 27 – 6. 29 respectively.

$$\begin{aligned} {}^{xs}G^{liq} = {} & y_{Gd^{3+}} y_{U^{4+}} y_{O^{2-}} \left[\begin{array}{l} {}^{liq}L^0_{Gd^{3+}\cdot U^{4+}:O^{2-}} + \left(y_{Gd^{3+}} - y_{U^{4+}}\right) {}^{liq}L^1_{Gd^{3+}\cdot U^{4+}:O^{2-}} + \\ \left(y_{Gd^{3+}} - y_{U^{4+}}\right)^2 {}^{liq}L^2_{Gd^{3+}\cdot U^{4+}:O^{2-}} \end{array} \right] + \\ & y_{Gd^{3+}} y_{U^{4+}} y_{Va} \, {}^{liq}L^0_{Gd^{3+}\cdot U^{4+}:Va} \\ & y_{U^{4+}} y_{O^{2-}} y_{Va} \left[{}^{liq}L^0_{U^{4+}:O^{2-}\cdot Va} + \left(y_{O^{2-}} - y_{Va}\right) {}^{liq}L^1_{U^{4+}:O^{2-}\cdot Va} + \left(y_{O^{2-}} - y_{Va}\right)^2 {}^{liq}L^2_{U^{4+}:O^{2-}\cdot Va} \right] \end{aligned} \qquad \textbf{6. 27}$$

$$
\begin{aligned}
{}^{xs}G^{liq} = {} & y_{La^{3+}} y_{U^{4+}} y_{O^{2-}} \left[\begin{array}{l} {}^{0}L^{liq}_{La^{3+}\cdot U^{4+}:O^{2-}} + \left(y_{La^{3+}} - y_{U^{4+}}\right)\left({}^{1}L^{liq}_{La^{3+}\cdot U^{4+}:O^{2-}}\right) + \\ \left(y_{La^{3+}} - y_{U^{4+}}\right)^{2}\left({}^{2}L^{liq}_{La^{3+}\cdot U^{4+}:O^{2-}}\right) \end{array} \right] + \\
& y_{La^{3+}} y_{U^{4+}} y_{Va}\, {}^{0}L^{liq}_{La^{3+}\cdot U^{4+}:Va} \\
& y_{U^{4+}} y_{O^{2-}} y_{Va} \left[{}^{0}L^{liq}_{U^{4+}:O^{2-}\cdot Va} + \left(y_{O^{2-}} - y_{Va}\right)\left({}^{1}L^{liq}_{U^{4+}:O^{2-}\cdot Va}\right) + \left(y_{O^{2-}} - y_{Va}\right)^{2}\left({}^{2}L^{liq}_{U^{4+}:O^{2-}\cdot Va}\right) \right]
\end{aligned}
\qquad \textbf{6. 28}
$$

$$
\begin{aligned}
{}^{xs}G^{liq} = {} & y_{Th^{4+}} y_{U^{4+}} y_{O^{2-}} \left[{}^{0}L^{liq}_{Th^{4+}\cdot U^{4+}:O^{2-}} + \left(y_{Th^{4+}} - y_{U^{4+}}\right)\left({}^{1}L^{liq}_{Th^{4+}\cdot U^{4+}:O^{2-}}\right) \right] + \\
& y_{Th^{4+}} y_{U^{4+}} y_{Va}\, {}^{0}L^{liq}_{Th^{4+}\cdot U^{4+}:Va} \\
& y_{U^{4+}} y_{O^{2-}} y_{Va} \left[{}^{0}L^{liq}_{U^{4+}:O^{2-}\cdot Va} + \left(y_{O^{2-}} - y_{Va}\right)\left({}^{1}L^{liq}_{U^{4+}:O^{2-}\cdot Va}\right) + \left(y_{O^{2-}} - y_{Va}\right)^{2}\left({}^{2}L^{liq}_{U^{4+}:O^{2-}\cdot Va}\right) \right] + \\
& y_{Th^{4+}} y_{O^{2-}} y_{Va} \left[{}^{0}L^{liq}_{Th^{4+}:O^{2-}\cdot Va} + \left(y_{O^{2-}} - y_{Va}\right)\left({}^{1}L^{liq}_{Th^{4+}:O^{2-}\cdot Va}\right) + \left(y_{O^{2-}} - y_{Va}\right)^{2}\left({}^{2}L^{liq}_{Th^{4+}:O^{2-}\cdot Va}\right) \right]
\end{aligned}
\qquad \textbf{6. 29}
$$

6.13 Fluorite-structure $U_{1-y}M_yO_{2\pm x}$ phases

A three sublattice CEF is used to describe the fluorite structure $U_{1-y}M_yO_{2\pm x}$ phase. The model presented in this work is an extension of that developed for $UO_{2\pm x}$ by Guéneau et al. [31, 32] discussed in Section 6.3. An important modification is the introduction of a U^{6+} species in the cation sublattice. As pointed out in Chapter 3, high temperature X-ray diffraction (HTXRD) studies in the U-La-O [62], U-Nd-O [63], and U-Pr-O [171] systems show single phase $U_{1-y}Ln_yO_{2\pm x}$ regions where electro-neutrality would preclude the existence of the phase without a U^{6+} cation assuming a fixed Ln^{3+} valence.

The sublattice model for the $U_{1-y}Ln_yO_{2\pm x}$ fluorite solution with a trivalent Ln is:

$(U^{3+},U^{4+},U^{5+},U^{6+},Ln^{3+})_1(O^{2-},Va^0)_2(O^{2-},Va^0)$

For the $U_{1-y}Th_yO_{2\pm x}$ phase it is:

$(U^{3+},U^{4+},U^{5+},U^{6+},Th^{3+},Th^{4+})_1(O^{2-},Va^0)_2(O^{2-},Va^0)$

The CEF model for $U_{1-y}Ln_yO_{2\pm x}$ is treated as a mixture of the end-members of the three sublattice description:

$U^{3+}:O^{2-}:O^{2-}$	$U^{4+}:O^{2-}:O^{2-}$	$U^{5+}:O^{2-}:O^{2-}$	$U^{6+}:O^{2-}:O^{2-}$	$Ln^{3+}:O^{2-}:O^{2-}$
$U^{3+}:O^{2-}:Va^0$	$U^{4+}:O^{2-}:Va^0$	$U^{5+}:O^{2-}:Va^0$	$U^{6+}:O^{2-}:Va^0$	$Ln^{3+}:O^{2-}:Va^0$
$U^{3+}: Va^0:O^{2-}$	$U^{4+}: Va^0:O^{2-}$	$U^{5+}: Va^0:O^{2-}$	$U^{6+}: Va^0:O^{2-}$	$Ln^{3+}: Va^0:O^{2-}$
$U^{3+}: Va^0:Va^0$	$U^{4+}: Va^0:Va^0$	$U^{5+}: Va^0:Va^0$	$U^{6+}: Va^0:Va^0$	$Ln^{3+}: Va^0:Va^0$

The Gibbs energy for the $U_{1-y}Ln_yO_{2\pm x}$ solid solution using Eqn. 2. 3 is thus:

$$
\begin{aligned}
G^{ss} = {} & y^{i}_{U^{3+}} y^{ii}_{O} y^{iii}_{O} \circ G^{F}_{U^{3+}:O:O} + y^{i}_{U^{3+}} y^{ii}_{O} y^{iii}_{Va} \circ G^{F}_{U^{3+}:O:Va} + y^{i}_{U^{3+}} y^{ii}_{Va} y^{iii}_{O} \circ G^{F}_{U^{3+}:Va:O} + y^{i}_{U^{3+}} y^{ii}_{Va} y^{iii}_{Va} \circ G^{F}_{U^{3+}:Va:Va} + \\
& y^{i}_{U^{4+}} y^{ii}_{O} y^{iii}_{O} \circ G^{F}_{U^{4+}:O:O} + y^{i}_{U^{4+}} y^{ii}_{O} y^{iii}_{Va} \circ G^{F}_{U^{4+}:O:Va} + y^{i}_{U^{4+}} y^{ii}_{Va} y^{iii}_{O} \circ G^{F}_{U^{4+}:Va:O} + y^{i}_{U^{4+}} y^{ii}_{Va} y^{iii}_{Va} \circ G^{F}_{U^{4+}:Va:Va} + \\
& y^{i}_{U^{5+}} y^{ii}_{O} y^{iii}_{O} \circ G^{F}_{U^{5+}:O:O} + y^{i}_{U^{5+}} y^{ii}_{O} y^{iii}_{Va} \circ G^{F}_{U^{5+}:O:Va} + y^{i}_{U^{5+}} y^{ii}_{Va} y^{iii}_{O} \circ G^{F}_{U^{5+}:Va:O} + y^{i}_{U^{5+}} y^{ii}_{Va} y^{iii}_{Va} \circ G^{F}_{U^{5+}:Va:Va} + \\
& y^{i}_{U^{6+}} y^{ii}_{O} y^{iii}_{O} \circ G^{F}_{U^{6+}:O:O} + y^{i}_{U^{6+}} y^{ii}_{O} y^{iii}_{Va} \circ G^{F}_{U^{6+}:O:Va} + y^{i}_{U^{6+}} y^{ii}_{Va} y^{iii}_{O} \circ G^{F}_{U^{6+}:Va:O} + y^{i}_{U^{6+}} y^{ii}_{Va} y^{iii}_{Va} \circ G^{F}_{U^{6+}:Va:Va} + \\
& y^{i}_{Ln^{3+}} y^{ii}_{O} y^{iii}_{O} \circ G_{Ln^{3+}:O:O} + y^{i}_{Ln^{3+}} y^{ii}_{O} y^{iii}_{Va} \circ G_{Ln^{3+}:O:Va} + y^{i}_{Ln^{3+}} y^{ii}_{Va} y^{iii}_{O} \circ G_{Ln^{3+}:Va:O} + y^{i}_{Ln^{3+}} y^{ii}_{Va} y^{iii}_{Va} \circ G_{Ln^{3+}:Va:Va} + \\
& RT \left[\begin{matrix} \left(y^{i}_{U^{3+}} \ln y^{i}_{U^{3+}} + y^{i}_{U^{4+}} \ln y^{i}_{U^{4+}} + y^{i}_{U^{5+}} \ln y^{i}_{U^{5+}} + y^{i}_{U^{6+}} \ln y^{i}_{U^{6+}} + y^{i}_{Ln^{3+}} \ln y^{i}_{Ln^{3+}} \right) + \\ 2\left(y^{ii}_{O} \ln y^{ii}_{O} + y^{ii}_{Va} \ln y^{ii}_{Va} \right) + \left(y^{iii}_{O} \ln y^{iii}_{O} + y^{iii}_{Va} \ln y^{iii}_{Va} \right) \end{matrix} \right] + \\
& {}^{xs}G
\end{aligned}
\qquad \textbf{6. 30}
$$

The CEF model for the $U_{1-y}Th_yO_{2\pm x}$ solid solution is treated as a mixture of the end-members of the three sublattice description:

$U^{3+}:O^{2-}:O^{2-}$	$U^{4+}:O^{2-}:O^{2-}$	$U^{5+}:O^{2-}:O^{2-}$	$U^{6+}:O^{2-}:O^{2-}$	$Th^{3+}:O^{2-}:O^{2-}$	$Th^{4+}:O^{2-}:O^{2-}$
$U^{3+}:O^{2-}:Va^0$	$U^{4+}:O^{2-}:Va^0$	$U^{5+}:O^{2-}:Va^0$	$U^{6+}:O^{2-}:Va^0$	$Th^{3+}:O^{2-}:Va^0$	$Th^{4+}:O^{2-}:Va^0$
$U^{3+}: Va^0:O^{2-}$	$U^{4+}: Va^0:O^{2-}$	$U^{5+}: Va^0:O^{2-}$	$U^{6+}: Va^0:O^{2-}$	$Th^{3+}: Va^0:O^{2-}$	$Th^{4+}: Va^0:O^{2-}$
$U^{3+}: Va^0:Va^0$	$U^{4+}: Va^0:Va^0$	$U^{5+}: Va^0:Va^0$	$U^{6+}: Va^0:Va^0$	$Th^{3+}: Va^0:Va^0$	$Th^{4+}: Va^0:Va^0$

Equation 6. 31 gives the Gibbs energy for the $U_{1-y}Th_yO_{2\pm x}$ as:

$$
\begin{aligned}
G^{ss} = {} & y^{i}_{U^{3+}} y^{ii}_{O} y^{iii}_{O} \circ G^{F}_{U^{3+}:O:O} + y^{i}_{U^{3+}} y^{ii}_{O} y^{iii}_{Va} \circ G^{F}_{U^{3+}:O:Va} + y^{i}_{U^{3+}} y^{ii}_{Va} y^{iii}_{O} \circ G^{F}_{U^{3+}:Va:O} + y^{i}_{U^{3+}} y^{ii}_{Va} y^{iii}_{Va} \circ G^{F}_{U^{3+}:Va:Va} + \\
& y^{i}_{U^{4+}} y^{ii}_{O} y^{iii}_{O} \circ G^{F}_{U^{4+}:O:O} + y^{i}_{U^{4+}} y^{ii}_{O} y^{iii}_{Va} \circ G^{F}_{U^{4+}:O:Va} + y^{i}_{U^{4+}} y^{ii}_{Va} y^{iii}_{O} \circ G^{F}_{U^{4+}:Va:O} + y^{i}_{U^{4+}} y^{ii}_{Va} y^{iii}_{Va} \circ G^{F}_{U^{4+}:Va:Va} + \\
& y^{i}_{U^{5+}} y^{ii}_{O} y^{iii}_{O} \circ G^{F}_{U^{5+}:O:O} + y^{i}_{U^{5+}} y^{ii}_{O} y^{iii}_{Va} \circ G^{F}_{U^{5+}:O:Va} + y^{i}_{U^{5+}} y^{ii}_{Va} y^{iii}_{O} \circ G^{F}_{U^{5+}:Va:O} + y^{i}_{U^{5+}} y^{ii}_{Va} y^{iii}_{Va} \circ G^{F}_{U^{5+}:Va:Va} + \\
& y^{i}_{U^{6+}} y^{ii}_{O} y^{iii}_{O} \circ G^{F}_{U^{6+}:O:O} + y^{i}_{U^{6+}} y^{ii}_{O} y^{iii}_{Va} \circ G^{F}_{U^{6+}:O:Va} + y^{i}_{U^{6+}} y^{ii}_{Va} y^{iii}_{O} \circ G^{F}_{U^{6+}:Va:O} + y^{i}_{U^{6+}} y^{ii}_{Va} y^{iii}_{Va} \circ G^{F}_{U^{6+}:Va:Va} + \\
& y^{i}_{Th^{3+}} y^{ii}_{O} y^{iii}_{O} \circ G^{F}_{Th^{3+}:O:O} + y^{i}_{Th^{3+}} y^{ii}_{O} y^{iii}_{Va} \circ G^{F}_{U^{3+}:O:Va} + y^{i}_{Th^{3+}} y^{ii}_{Va} y^{iii}_{O} \circ G^{F}_{U^{3+}:Va:O} + y^{i}_{Th^{3+}} y^{ii}_{Va} y^{iii}_{Va} \circ G^{F}_{U^{3+}:Va:Va} + \\
& y^{i}_{Th^{4+}} y^{ii}_{O} y^{iii}_{O} \circ G^{F}_{Th^{4+}:O:O} + y^{i}_{Th^{4+}} y^{ii}_{O} y^{iii}_{Va} \circ G^{F}_{U^{4+}:O:Va} + y^{i}_{Th^{4+}} y^{ii}_{Va} y^{iii}_{O} \circ G^{F}_{U^{4+}:Va:O} + y^{i}_{Th^{4+}} y^{ii}_{Va} y^{iii}_{Va} \circ G^{F}_{U^{4+}:Va:Va} + \\
& RT \left[\begin{matrix} \left(y^{i}_{U^{3+}} \ln y^{i}_{U^{3+}} + y^{i}_{U^{4+}} \ln y^{i}_{U^{4+}} + y^{i}_{U^{5+}} \ln y^{i}_{U^{5+}} + y^{i}_{U^{6+}} \ln y^{i}_{U^{6+}} + y^{i}_{Th^{3+}} \ln y^{i}_{Th^{3+}} + y^{i}_{Th^{4+}} \ln y^{i}_{Th^{4+}} \right) + \\ 2\left(y^{ii}_{O} \ln y^{ii}_{O} + y^{ii}_{Va} \ln y^{ii}_{Va} \right) + \left(y^{iii}_{O} \ln y^{iii}_{O} + y^{iii}_{Va} \ln y^{iii}_{Va} \right) \end{matrix} \right] + \\
& {}^{xs}G
\end{aligned}
\qquad \textbf{6. 31}
$$

The models for the $U_{1-y}M_yO_{2\pm x}$ phases from this work use the thermodynamic functions and interaction parameters from the $UO_{2\pm x}$ CEF representation developed by Guéneau et al. [32]; therefore, using only zeroth and first order terms with linear temperature dependence for the expansion, the excess Gibbs energies for $U_{1-y}Gd_yO_{2\pm x}$, $U_{1-y}La_yO_{2\pm x}$, and $U_{1-y}Th_yO_{2\pm x}$ are given by Eqn. 6. 32 – 6. 34 respectively:

$$
\begin{aligned}
{}^{xs}G = {} & y^{ii}_{Va} y^{iii}_{Va} \left(y^{i}_{U^{4+}} y^{i}_{Gd^{3+}} {}^{0}L^{F}_{U^{4+}\cdot Gd^{3+}:Va:Va} + y^{i}_{U^{5+}} y^{i}_{Gd^{3+}} {}^{0}L^{F}_{U^{5+}\cdot Gd^{3+}:Va:Va} \right) + \\
& y^{ii}_{O} y^{iii}_{Va} \left(\begin{matrix} y^{i}_{U^{3+}} y^{i}_{Gd^{3+}} {}^{0}L^{F}_{U^{3+}\cdot Gd^{3+}:O:Va} + y^{i}_{U^{3+}} y^{i}_{Gd^{3+}} \left(y^{i}_{U^{3+}} - y^{i}_{Gd^{3+}} \right) {}^{1}L^{F}_{U^{3+}\cdot Gd^{3+}:O:Va} + \\ y^{i}_{U^{4+}} y^{i}_{Gd^{3+}} {}^{0}L^{F}_{U^{4+}\cdot Gd^{3+}:O:Va} + y^{i}_{U^{4+}} y^{i}_{Gd^{3+}} \left(y^{i}_{U^{4+}} - y^{i}_{Gd^{3+}} \right) {}^{1}L^{F}_{U^{4+}\cdot Gd^{3+}:O:Va} + \\ y^{i}_{U^{5+}} y^{i}_{Gd^{3+}} {}^{0}L^{F}_{U^{5+}\cdot Gd^{3+}:O:Va} + y^{i}_{U^{5+}} y^{i}_{Gd^{3+}} \left(y^{i}_{U^{5+}} - y^{i}_{Gd^{3+}} \right) {}^{1}L^{F}_{U^{5+}\cdot Gd^{3+}:O:Va} \end{matrix} \right) + \\
& y^{ii}_{O} y^{iii}_{O} \left(y^{i}_{U^{4+}} y^{i}_{Gd^{3+}} {}^{0}L^{F}_{U^{4+}\cdot Gd^{3+}:O:O} + y^{i}_{U^{5+}} y^{i}_{Gd^{3+}} {}^{0}L^{F}_{U^{5+}\cdot Gd^{3+}:O:O} \right) + \\
& y^{ii}_{O} y^{iii}_{Va} \left(y^{i}_{U^{3+}} y^{i}_{U^{4+}} {}^{0}L^{F}_{U^{3+}\cdot U^{4+}:O:Va} + y^{i}_{U^{3+}} y^{i}_{U^{4+}} \left(y^{i}_{U^{3+}} - y^{i}_{U^{4+}} \right) {}^{1}L^{F}_{U^{3+}\cdot U^{4+}:O:Va} \right) + \\
& y^{i}_{U^{4+}} y^{i}_{U^{5+}} y^{ii}_{O} y^{iii}_{O} {}^{0}L^{F}_{U^{4+}\cdot U^{5+}:O:O}
\end{aligned}
\qquad \textbf{6. 32}
$$

$$
\begin{aligned}
{}^{xs}G^{F} = {} & y_{Va}^{ii} y_{Va}^{iii} \left(y_{U^{4+}}^{i} y_{La^{3+}}^{i} {}^{0}L^{F}_{U^{4+}\cdot La^{3+}:Va:Va} + y_{U^{5+}}^{i} y_{La^{3+}}^{i} {}^{0}L^{F}_{U^{5+}\cdot La^{3+}:Va:Va} \right) + \\
& y_{O}^{ii} y_{Va}^{iii} \left(\begin{array}{l}
y_{U^{3+}}^{i} y_{La^{3+}}^{i} {}^{0}L^{F}_{U^{3+}\cdot La^{3+}:O:Va} + y_{U^{3+}}^{i} y_{La^{3+}}^{i} \left(y_{U^{3+}}^{i} - y_{La^{3+}}^{i} \right) \times {}^{1}L^{F}_{U^{3+}\cdot La^{3+}:O:Va} + \\
y_{U^{4+}}^{i} y_{La^{3+}}^{i} {}^{0}L^{F}_{U^{4+}\cdot La^{3+}:O:Va} + y_{U^{4+}}^{i} y_{La^{3+}}^{i} \left(y_{U^{4+}}^{i} - y_{La^{3+}}^{i} \right) \times {}^{1}L^{F}_{U^{4+}\cdot La^{3+}:O:Va} + \\
y_{U^{5+}}^{i} y_{La^{3+}}^{i} {}^{0}L^{F}_{U^{5+}\cdot La^{3+}:O:Va} + y_{U^{5+}}^{i} y_{La^{3+}}^{i} \left(y_{U^{5+}}^{i} - y_{La^{3+}}^{i} \right) \times {}^{1}L^{F}_{U^{5+}\cdot La^{3+}:O:Va} + \\
y_{U^{6+}}^{i} y_{La^{3+}}^{i} {}^{0}L^{F}_{U^{6+}\cdot La^{3+}:O:Va}
\end{array} \right) + \\
& y_{O}^{ii} y_{O}^{iii} \left(y_{U^{4+}}^{i} y_{La^{3+}}^{i} {}^{0}L^{F}_{U^{4+}\cdot La^{3+}:O:O} + y_{U^{5+}}^{i} y_{La^{3+}}^{i} {}^{0}L^{F}_{U^{5+}\cdot La^{3+}:O:O} \right) + \\
& y_{O}^{ii} y_{Va}^{iii} \left(y_{U^{3+}}^{i} y_{U^{4+}}^{i} {}^{0}L^{F}_{U^{3+}\cdot U^{4+}:O:Va} + y_{U^{3+}}^{i} y_{U^{4+}}^{i} \left(y_{U^{3+}}^{i} - y_{U^{4+}}^{i} \right) \times {}^{1}L^{F}_{U^{3+}\cdot Y^{4+}:O:Va} \right) + \\
& y_{U^{4+}}^{i} y_{U^{5+}}^{i} y_{O}^{ii} y_{O}^{iii} {}^{0}L^{F}_{U^{4+}\cdot U^{5+}:O:O}
\end{aligned}
\qquad \textbf{6. 33}
$$

$$
\begin{aligned}
{}^{xs}G^{F} = {} & y_{O}^{ii} y_{O}^{iii} \left(y_{U^{4+}}^{i} y_{Th^{4+}}^{i} {}^{0}L^{F}_{U^{4+}\cdot Th^{4+}:O:O} + y_{U^{4+}}^{i} y_{Th^{4+}}^{i} \left(y_{U^{3+}}^{i} - y_{La^{3+}}^{i} \right) \times {}^{1}L^{F}_{U^{4+}\cdot Th^{4+}:O:O} \right) + \\
& y_{O}^{ii} y_{Va}^{iii} \left(y_{U^{4+}}^{i} y_{Th^{4+}}^{i} {}^{0}L^{F}_{U^{4+}\cdot Th^{4+}:O:Va} + y_{U^{5+}}^{i} y_{Th^{4+}}^{i} {}^{0}L^{F}_{U^{5+}\cdot Th^{4+}:O:Va} \right) + \\
& y_{O}^{ii} y_{O}^{iii} \left(y_{U^{5+}}^{i} y_{Th^{4+}}^{i} {}^{0}L^{F}_{U^{5+}\cdot Th^{4+}:O:O} \right) + \\
& y_{O}^{ii} y_{Va}^{iii} \left(y_{U^{3+}}^{i} y_{U^{4+}}^{i} {}^{0}L^{F}_{U^{3+}\cdot U^{4+}:O:Va} + y_{U^{3+}}^{i} y_{U^{4+}}^{i} \left(y_{U^{3+}}^{i} - y_{U^{4+}}^{i} \right) \times {}^{1}L^{F}_{U^{3+}\cdot U^{4+}:O:Va} \right) + \\
& y_{U^{4+}}^{i} y_{U^{5+}}^{i} y_{O}^{ii} y_{O}^{iii} {}^{0}L^{F}_{U^{4+}\cdot U^{5+}:O:O}
\end{aligned}
\qquad \textbf{6. 34}
$$

The Gibbs energies for the end-members created by the inclusion of the U^{6+} cation were first approximated as equal to their U^{5+} homologue and subsequently adjusted to reproduce the phase relations from 300 K to melting.

The convention for determining the Gibbs energies for the Gd and La containing end-members after Shin and Besmann [110] is

$$
{}^{\circ}G_{Gd^{3+}:O:O} = \frac{1}{2} {}^{\circ}G^{C}_{Gd_2O_3} + \frac{3}{4} {}^{\circ}G_{O_2} + \Delta E^{GdO_{1.5}\rightarrow GdO_2}_{GdO_{1.5}} + a_{Gd^{3+}:O:O} + b_{Gd^{3+}:O:O} \times T \qquad \textbf{6. 35}
$$

$$
{}^{\circ}G_{Gd^{3+}:O:Va} = \frac{1}{2} {}^{\circ}G^{C}_{Gd_2O_3} + \frac{1}{4} {}^{\circ}G_{O_2} + \Delta E^{GdO_{1.5}\rightarrow GdO_2}_{GdO_{1.5}} + a_{Gd^{3+}:O:Va} + b_{Gd^{3+}:O:Va} \times T \qquad \textbf{6. 36}
$$

$$
{}^{\circ}G_{Gd^{3+}:Va:Va} = \frac{1}{2} {}^{\circ}G^{C}_{Gd_2O_3} - \frac{3}{4} {}^{\circ}G_{O_2} + \Delta E^{GdO_{1.5}\rightarrow GdO_2}_{GdO_{1.5}} + a_{Gd^{3+}:Va:Va} + b_{Gd^{3+}:Va:Va} \times T \qquad \textbf{6. 37}
$$

$$
{}^{\circ}G_{La^{3+}:O:O} = \frac{1}{2} {}^{\circ}G^{A}_{La_2O_3} + \frac{3}{4} {}^{\circ}G_{O_2} + \Delta E^{LaO_{1.5}\rightarrow LaO_2}_{LaO_{1.5}} + a_{La^{3+}:O:O} + b_{La^{3+}:O:O} \times T \qquad \textbf{6. 38}
$$

$$
{}^{\circ}G_{La^{3+}:O:Va} = \frac{1}{2} {}^{\circ}G^{A}_{La_2O_3} + \frac{1}{4} {}^{\circ}G_{O_2} + \Delta E^{LaO_{1.5}\rightarrow LaO_2}_{LaO_{1.5}} + a_{La^{3+}:O:Va} + b_{La^{3+}:O:Va} \times T \qquad \textbf{6. 39}
$$

$$^{\circ}G_{La^{3+}:Va:Va} = \frac{1}{2}{}^{\circ}G^{A}_{La_2O_3} - \frac{3}{4}{}^{\circ}G_{O_2} + \Delta E^{LaO_{1.5}\rightarrow LaO_2}_{LaO_{1.5}} + a_{La^{3+}:Va:Va} + b_{La^{3+}:Va:Va} \times T \quad \textbf{6. 40}$$

where $^{\circ}G^{C}_{Gd_2O_3}$ and $^{\circ}G^{A}_{La_2O_3}$ are the Gibbs energy of bixbyite type (*Ia3* space group) C-form Gd_2O_3 and hexagonal A-form La_2O_3 (*P32/m* space group) [162]. The Gibbs energies of the Ln^{3+} end-members are obtained from the lattice stability, $\Delta E^{LnO_{1.5}\rightarrow LnO_2}_{GdO_{1.5}}$, calculated from DFT (Chapter 3), addition and subtraction of oxygen as noted above, and by introducing the a_i and b_i terms that serve to adjust the standard state enthalpy and entropy values.

The Th-containing end-members were calculated using analogous relations to those given by Eqns. 6. 35 – 6. 40 minus the lattice stability term and are therefore:

$$^{\circ}G_{Th^{3+}:O:Va} = {}^{\circ}G_{ThO_2} + a_{Th^{3+}:O:Va} + b_{Th^{3+}:O:Va} \times T \quad \textbf{6. 41}$$

$$^{\circ}G_{Th^{3+}:O:O} = {}^{\circ}G_{ThO_2} + 0.5{}^{\circ}G_{O_2} + a_{Th^{3+}:O:O} + b_{Th^{3+}:O:O} \times T \quad \textbf{6. 42}$$

$$^{\circ}G_{Th^{3+}:Va:Va} = {}^{\circ}G_{ThO_2} - {}^{\circ}G_{O_2} + a_{Th^{3+}:Va:Va} + b_{Th^{3+}:Va:Va} \times T \quad \textbf{6. 43}$$

$$^{\circ}G_{Th^{4+}:O:Va} = {}^{\circ}G_{ThO_2} \quad \textbf{6. 44}$$

$$^{\circ}G_{Th^{4+}:O:O} = {}^{\circ}G_{ThO_2} + 0.5{}^{\circ}G_{O_2} + a_{Th^{4+}:O:O} + b_{Th^{4+}:O:O} \times T \quad \textbf{6. 45}$$

$$^{\circ}G_{Th^{4+}:Va:Va} = {}^{\circ}G_{ThO_2} - {}^{\circ}G_{O_2} + a_{Th^{4+}:Va:Va} + b_{Th^{4+}:Va:Va} \times T \quad \textbf{6. 46}$$

The values for $^{\circ}G_{Gd^{3+}:Va:O}$, $^{\circ}G_{La^{3+}:Va:O}$, and $^{\circ}G_{U^{6+}:Va:O}$ were arbitrarily set to a constant +100,000 J/mol after Guéneau et al. [32] due to the unlikelihood of their formation. Those of $^{\circ}G_{Th^{4+}:Va:O}$ were given a constant value of 0 J/mol to allow the OD transformation (Sections 6.14.3 and 6.18) to be more easily represented.

6.14 Parameter optimization

The Optisage module of FactSage [61] was used to optimize the adjustable parameters of the models discussed in this chapter to find the best fit to the experimentally determined data. The thermodynamic functions for the U-O system come from Guéneau et al. [32] and [172]. Given the chemical similarity of the trivalent Ln elements, the available relevant studies of the U-Ln-O ternaries were treated collectively such that one system informs another where data maybe questionable or lacking. An iterative procedure was employed to simultaneously optimize all adjustable parameters for all the models in order to achieve a self-consistent set of values that sufficiently describes the thermodynamic behavior of each of the U-M-O systems. The thermodynamic functions and parameters resulting results from the optimization are given in Appendix B – D.

6.14.1 The U-Gd-O system

Since ternary phase equilibria for the U-Gd-O system are undetermined, Lindemer and Sutton [59] assumed the maximum extent of the $U_{1-y}Gd_yO_{2\pm x}$ to be the same as for $U_{1-y}Nd_yO_{2\pm x}$ in the U-Nd-O system. As a conservative approximation, for this work the phase boundary between the fluorite and the fluorite/Gd_2O_3 phase field is assumed to be a linear bound in the isothermal ternary plane between $U_{1-y}Gd_yO_{2\pm x}$ with the highest Gd composition at the lowest O/M reported in [59] and the fully reduced form of pure UO_{2-x}. The presence of a miscibility gap in the phase is expected since $U_{1-y}Ce_yO_{2\pm x}$, $U_{1-y}Nd_yO_{2\pm x}$, and $U_{1-y}La_yO_{2\pm x}$ [173] show a region of immiscibility and HTXRD [174] suggest evidence of this phenomenon at lower temperatures. These considerations together with solidus and liquidus data along the UO_2 – $GdO_{1.5}$ isopleth, the quite extensive μ_{O_2} versus O/M, heat capacity, and enthalpy increment data for the $U_{1-y}Gd_yO_{2\pm x}$ were used to optimize the adjustable parameters of the models comprising the U-Gd-O thermodynamic assessment.

6.14.2 The U-La-O system

The phase relations near melting along the UO_2-$LnO_{1.5}$ isopleths in the U-Gd-O, U-Nd-O, and U-Y-O systems were used as guides to inform approximate solidus/liquidus temperatures for the UO_2-$LaO_{1.5}$ psuedo-binary and therefore develop a model for the liquid phase in the U-La-O ternary. The pseudo-binary UO_2-$GdO_{1.5}$, UO_2-$NdO_{1.5}$, and UO_2-$YO_{1.5}$ systems were used to infer solidus and liquidus temperatures along the UO_2-$LaO_{1.5}$. This, along with the μ_{O_2} versus O/M data and extensive experimentally determined phase relations in the vicinity of fluorite $U_{1-y}La_yO_{2\pm x}$ permitted the development of models that well describe the thermodynamics of U-La-O and compare well to the U-Gd-O system where data is lacking.

6.14.3 The U-Th-O system

As mentioned in Section 6.7, a CALPHAD assessment of the U-Th has already been developed; therefore the focus was on correctly describing the Th-O binary and the phases of the U-Th-O ternary. Phase equilibria data for the Th-O binary, the U-Th-O ternary along with the OD transition Frenkel defect fractions, heat capacity, enthalpy increment and μ_{O_2} versus O/M measurements were used to develop the models to describe the integral U-Th-O system.

As mentioned, both UO_2 and ThO_2 undergo an anion OD transition and the CEF is capable of describing this phenomenon [166]. Mathematically, complete disorder for a stoichiometric fluorite MO_2 phase occurs when both oxygen sublattices are 2/3 filled assuming no other anion defects, i.e. clustering, displacements, etc. According to high temperature neutron diffraction studies of the OD phenomenon for UO_2 and ThO_2, up to about 20% of the total oxygen ions are displaced from their normal tetrahedrally coordinated positions. Of these, only a fraction are true Frenkel pairs while the rest are distorted NN or NNN that cluster in an arrangement akin to the Willis defect. Hutchings

[68] proposed two possible models, the 3:1:2 and alternatively the 9:1:8. Here, the first number is the total number of vacancies, the second references the interstitial O, and the third is the relaxed O's distorted from a normal site. The magnitude of Frenkel pair concentration (n_F) from [68] is on the order of 10^{-2} above 2000 K. However, the author points out that while the experimental technique used in [68] could well distinguish the total fraction of defective anions (n_d), quantifying n_F depends critically upon the model chosen. Therefore, n_F is not determined directly but computed from n_d.

While the CEF for $UO_{2\pm x}$ after Guéneau et al. [32] does not include a sublattice for the relaxed oxygen sites, the disordering phenomenon can be modeled considering only Frenkel defects and therefore the representation of many of the properties, like c_p and enthalpy increment can be improved. This would require a re-assessment of the U-O system, an effort beyond the scope of this work. However, as a proof concept, the CEF for ThO_{2-x} will include a description of the disordering behavior. This is done by imposing the following conditions:

$$\frac{dG_T^{ThO_2}}{dy} = 0 \qquad \textbf{6. 29}$$

and

$$\frac{d^2G_T^{ThO_2}}{dy^2} > 0 \qquad \textbf{6. 30}$$

where T is temperature and y generically represents any one of four anion sublattice site fractions since, at stoichiometry, these are not independent but are bound by the Eqns. 6. 31 – 6. 33. Equations 6. 29 and 6. 30 are sufficient conditions to ensure the Gibbs energy

of ThO_2 is at a minimum when *y* corresponds to that of an appropriate Frenkel defect concentration and temperature.

$$y_{O^{2-}}^{iii} = 2y_{Va}^{ii} \quad \textbf{6. 31}$$

$$y_{Va}^{iii} = 1 - 2y_{Va}^{ii} \quad \textbf{6. 32}$$

$$y_{O^{2-}}^{ii} = 1 - y_{Va}^{ii} \quad \textbf{6. 33}$$

6.15 Results for the U-Gd-O system

6.15.1 The Gd-O binary

Temperature-composition (T-x) diagrams are reported for Y-Y_2O_3 [94-102], Nd-Nd_2O_3 [103-106], and La-La_2O_3 [107, 108] but none were found for Gd-Gd_2O_3. The phase relations shown in Fig. 6.3(d) were computed using the models from this work. The TSLM contains no interaction parameters between Gd and O but follows from the optimization of the U-Gd-O ternary melting data whereby adjustments to the H^{298} and S^{298} of liquid Gd_2O_3 were made to best reproduce the reported solidus and liquidus data.

Figures 6.3(a)-(d) show that the phase relations for the Gd-O binary compared to other Ln-O systems. The agreement is best between Gd-O and the La-O diagrams particularly with regards to the slope of the oxygen rich liquidus and the eutectic composition occurring around 14 and 10 mole % Gd_2O_3 and La_2O_3 respectively. The Y-O system is exceptional in that the metallic phases are shown to have a remarkably high solubility for oxygen compared to those of Nd-O, La-O, and Gd-O. It is likely that the Gd_2O_3 polymorphs also exhibit some degree of oxygen homogeneity but due to the lack of data and the fact that the degree of non-stoichiometry is very small in the similar Ln_2O_3 phases, these compounds were treated as stoichiometric. The Gd metal allotropes

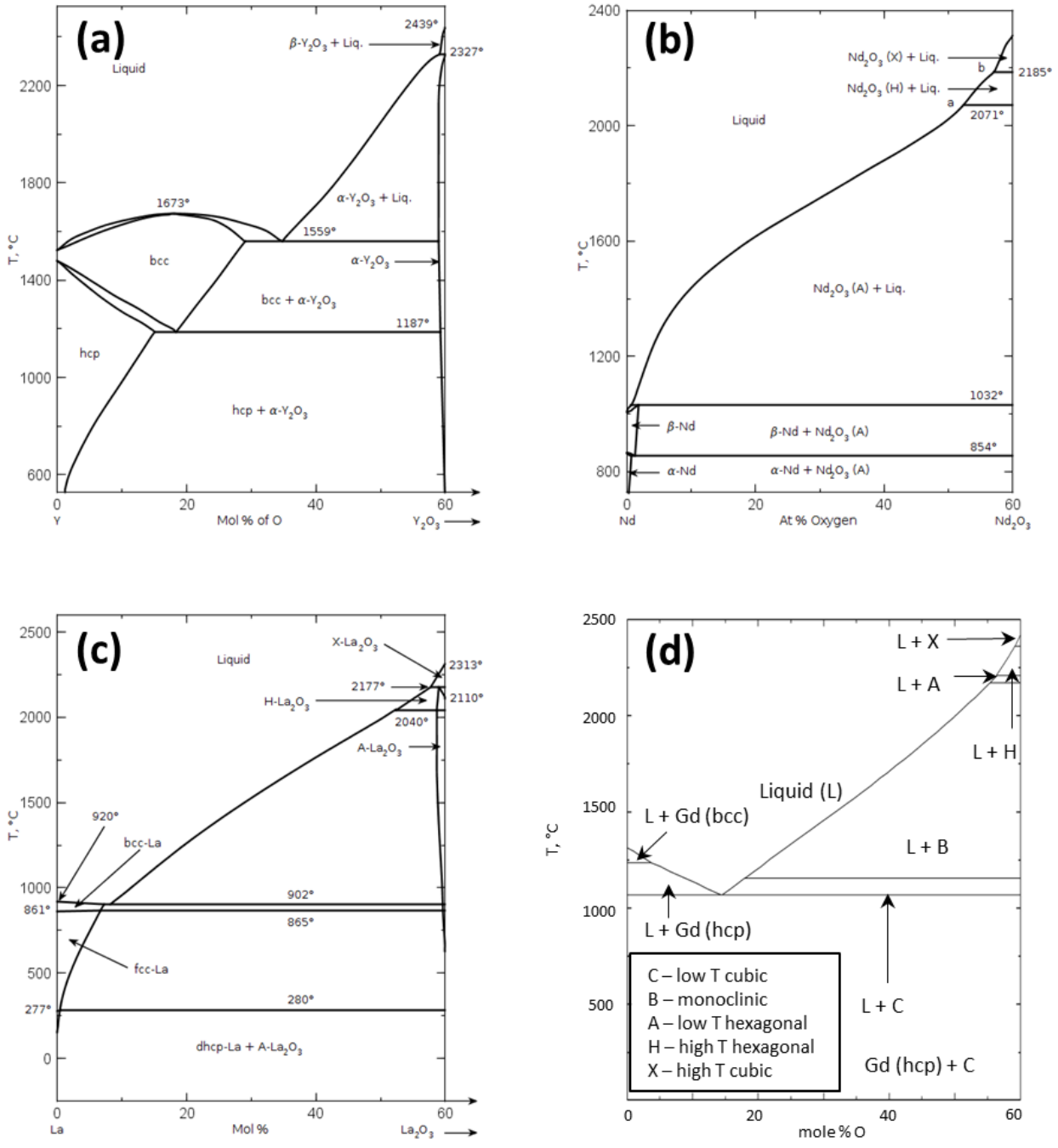

Fig. 6.3. Reported phase diagrams for the Y-O **(a)** Nd-O **(b)** and La-O **(c)** systems from [102, 105, 107]**.** **(**Reprinted with permission of The American Ceramic Society, www.ceramics.org All rights reserved.) The tentative T-x phase diagram for the Gd-O from this work is shown in **(d)**. (Gd_2O_3 polymorphs: C=low temperature cubic, B=monoclinic, A=low temperature hexagonal, H=high temperature hexagonal, X=high temperature cubic).

are also expected to accommodate very little oxygen; for simplicity they are treated as pure elements

6.15.2 The U-Gd binary

A tentative U-Gd binary diagram showing no U-Gd miscibility in the solid and liquid phases is presented in Fig. 6.4. While some degree of mutual solubility up to 0.1 wt % Gd in liquid uranium has been observed, the data is limited to one composition from one study [109]. No reported data for metallic U-Gd solid solutions exist and there is very limited data for similar Ln-U systems; therefore, all condensed phases were assumed to be immiscible for this assessment. The Gibbs functions for the U and Gd metallic polymorphs are given in Table B.1; a large positive interaction energy between U and Gd was added to the TSLM in order to reproduce the observed extensive immiscibility in the liquid.

6.15.3 The U-Gd-O ternary

The computed T-x diagram for the pseudo-binary UO_2-$GdO_{1.5}$ isoplethal section is shown in Fig. 6.5 and agrees well with the selected melting data. The extent of the single phase fluorite $U_{1-y}Gd_yO_{2\pm x}$ region is assumed to be comparable to those found in other trivalent U-RE-O systems due to the chemical similarity of the RE elements. Since only limited equilibrium studies for U-Gd-O are reported in the literature, the phase relations for U-Nd-O and U-La-O systems were used as guides. For parameter optimization, the phase boundary between the fluorite and the fluorite-Gd_2O_3 phase field was assumed to be a linear bound in the ternary plane between $U_{1-y}Gd_yO_{2\pm x}$ with the highest Gd composition at the lowest O/M reported by Lindemer and Sutton [59] and the fully reduced form of UO_{2-x}. Only very high Gd compositions (y>0.70) fall outside the single phase fluorite region as shown in Fig. 6.6. X-ray diffraction studies [58, 83, 175] suggest the maximum solubility of Gd in the fluorite UO_2 structure is between 52 and 62

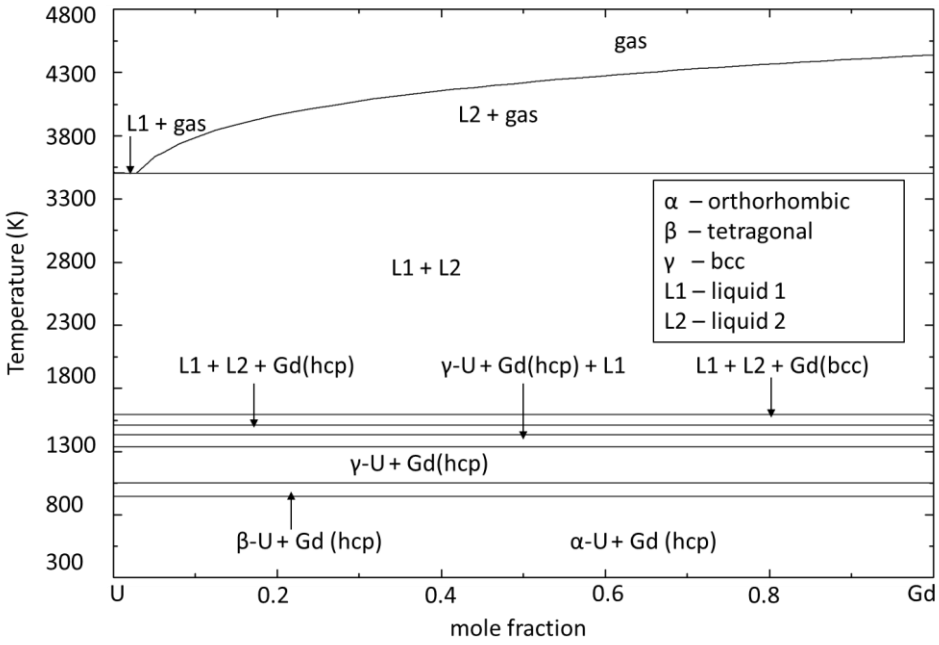

Fig. 6.4. Tentative U-Gd binary phase diagram computed using the partially ionic two-sublattice liquid model parameters derived from optimization of the pseudo-binary UO_2-$GdO_{1.5}$ system and assuming no intersolubility for both U and Gd metal phases.

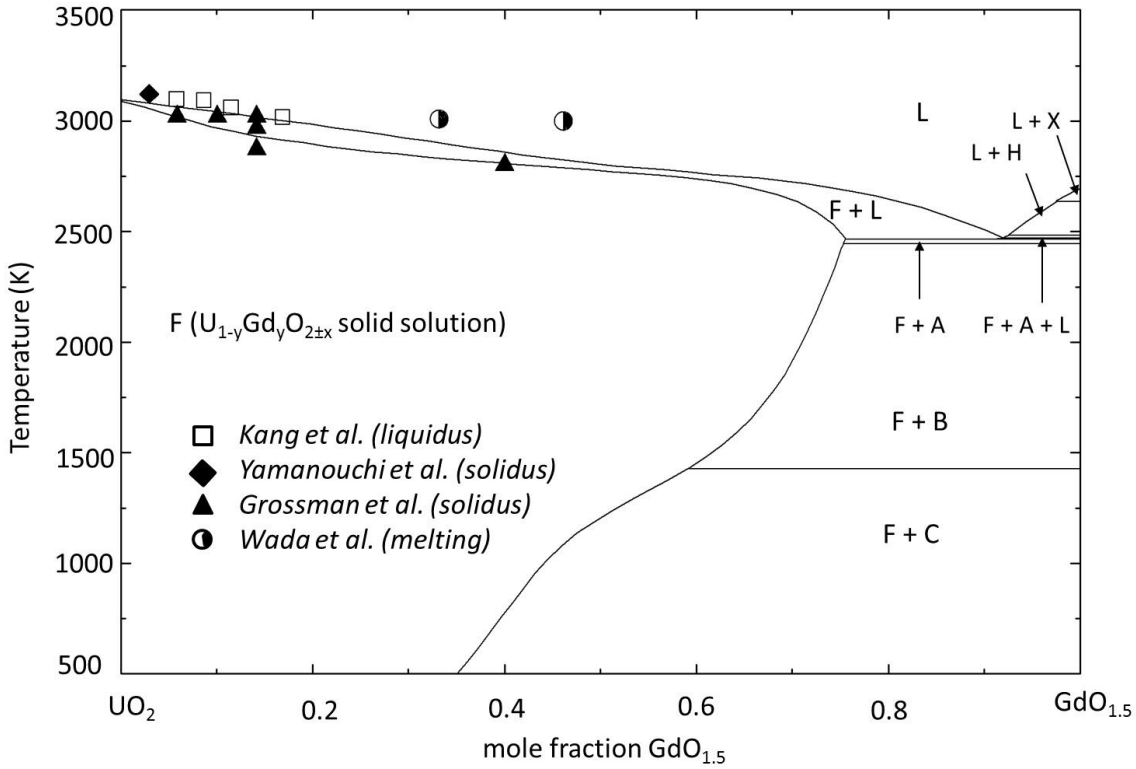

Fig. 6.5. Tentative phase diagram along the UO_2-$GdO_{1.5}$ isopleth. The data from Wada et al.[90] represents observed melting and does not distinguish between liquidus or solidus. (Gd_2O_3 polymorphs: C=low temperature cubic, B=monoclinic, A=low temperature hexagonal, H=high temperature hexagonal , X=high temperature cubic)

mole %; the computed phase diagrams shown in Figs. 6.6 and 6.7 are consistent with these results. A miscibility gap appears below 1273 K, as shown in Fig. 6.7(b), analogous to other Ln systems. The computed phase equilibria using the models presented in this work for the U-Gd-O system agree with those from experiments in similar U-Ln-O ternaries; however, in the absence of substantial phase stability data the diagrams in Figs.6.6-6.7 must be considered tentative.

Figure 6.8 compares $\log p_{O_2}$ versus O/M measurements from the literature [51, 53, 59, 79, 176, 177] with those computed from the models developed in this work; the agreement is good with a few exceptions. Figure 6.8(f) shows poor agreement between the CEF model and the values determined by Teske et al. [53], but these data were inconsistent with those reported by Yang et al. [80] and Lindemer and Sutton [59] at the same compositions and similar temperatures (±50 K). The measurements of Yang et al. [176] are very well represented by the model with the exception of hypostoichiometric values at y = 0.087 and 1573 K. These data are most likely in error since the observed trend does not match that of the balance of the measurements made by Yang et al. [176] as well as those of Lindemer and Sutton [59], Une and Oguma [51, 177], and Nakamura [79].

The CEF for $U_{1-y}Gd_yO_{2\pm x}$ agrees reasonably well with selected heat capacity measurements viewed to be the most reliable; a comparison to all the available experimental data is shown in Fig. 6.9. The CEF computed lattice stability for GdO_2 (76.75 kJ) however, is around three times the value determined from DFT (26 kJ).

6.16. Results for the U-La-O system

6.16.1 The La-O binary

A computed phase diagram for the La-O system is shown in Fig. 6.10. The liquid phase represented by Eqns. 6. 25, 6. 26 and 6. 28 for this binary contains no interaction parameters between La and O but follows from the optimization of the models for the

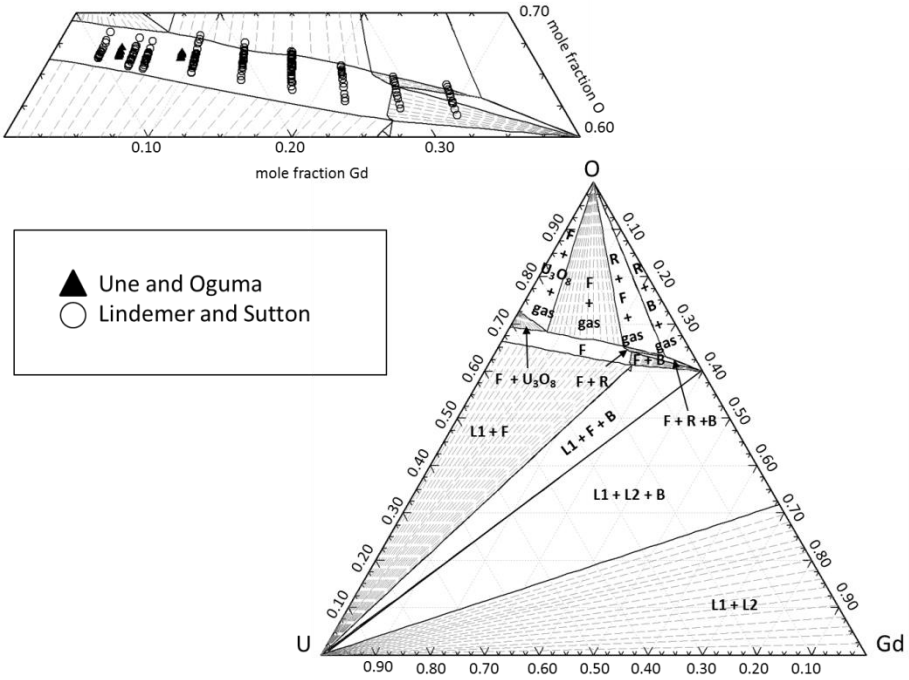

Fig. 6.6. Computed phase equilibria at 1773 K for U-Gd-O. The expanded section shows the single phase fluorite region overlaid with the compositions used in the oxygen potential measurements of Une and Oguma [81, 82] and Lindemer and Sutton [59]. (F=fluorite solid solution, R=rhombohedral UGd_6O_{12}, B=monoclindic Gd_2O_3, L1=liquid phase, L2=second liquid phase)

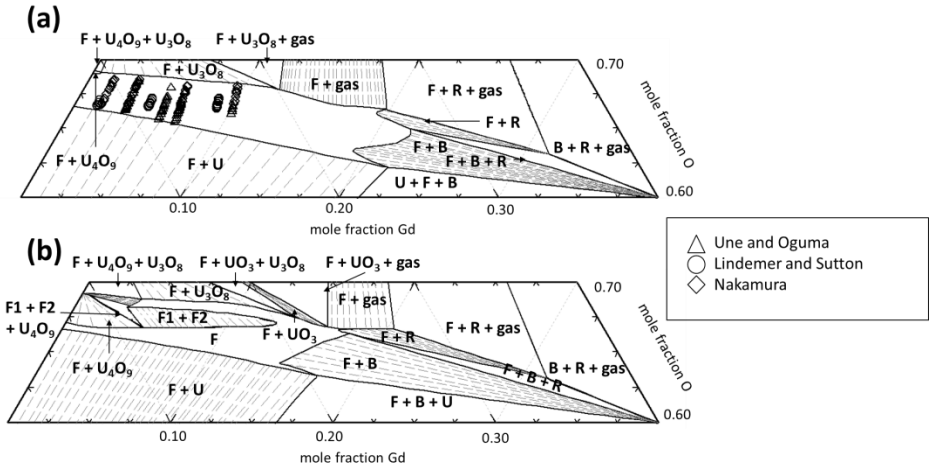

Fig. 6.7. Sections of computed phase diagrams at 1273 K (a) and 823 K (b) for U-Gd-O. In (a), the single phase fluorite region is overlaid with data from oxygen potential measurements of Une and Oguma [81, 82], Lindemer and Sutton [59], and Nakamura [79]. In (b), the CEF model for $U_{1-y}Gd_yO_{2\pm x}$ predicts a miscibility gap given by the F1 + F2 region. (F=single fluorite solution, F1+F2=two fluorite solutions, R=rhombohedral UGd_6O_{12}, B=monoclindic Gd_2O_3, L1=liquid phase, L2=second liquid phase)

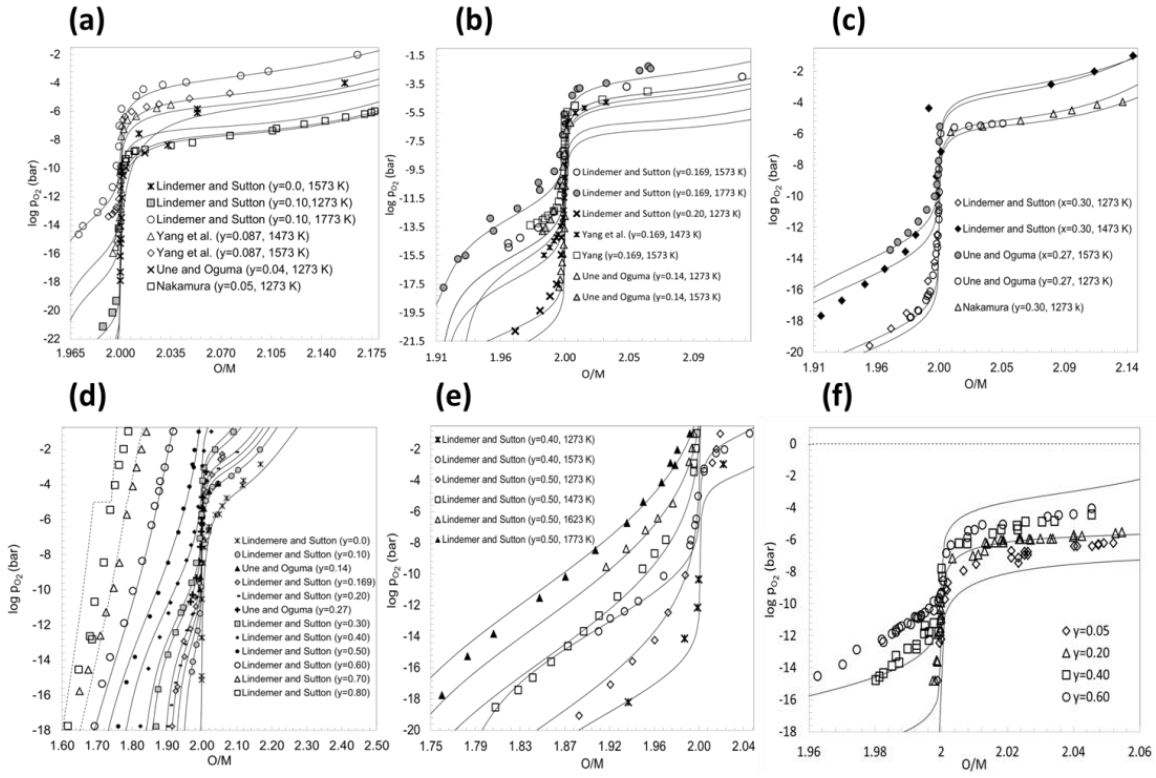

Fig. 6.8. Equilibrium oxygen pressures over $U_{1-y}Gd_yO_{2\pm x}$ vs. O/M. The computed results are the solid lines and experimental values are represented by symbols. The dashed lines in **(d)** represent compositions that fall outside of the single phase fluorite region.

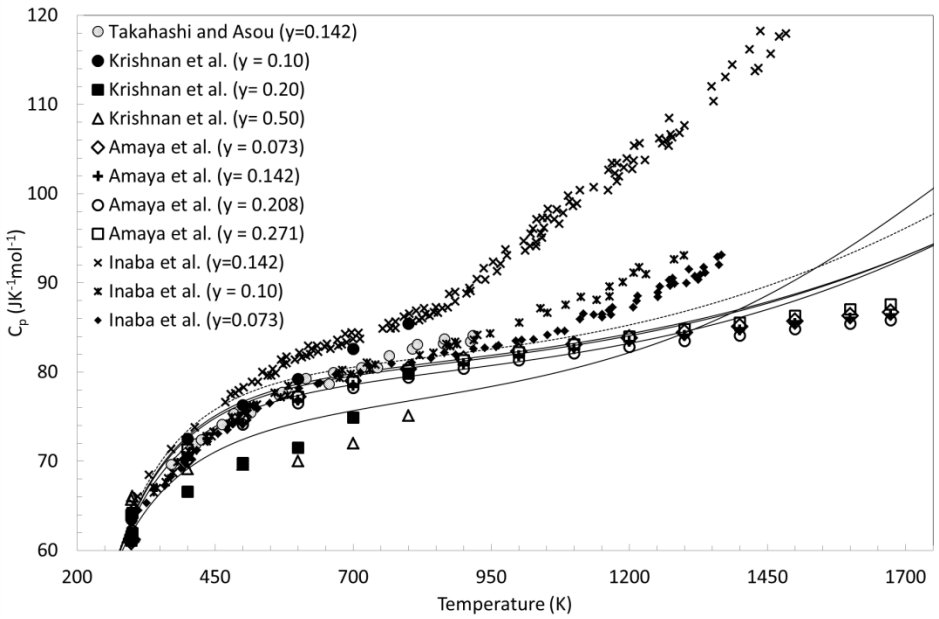

Fig. 6.9. Computed (lines) and experimental molar heat capacity (c_p) data (points) versus temperature for $U_{1-y}Gd_yO_2$. The dashed line represents the c_p for UO_2 computed from the CEF model.

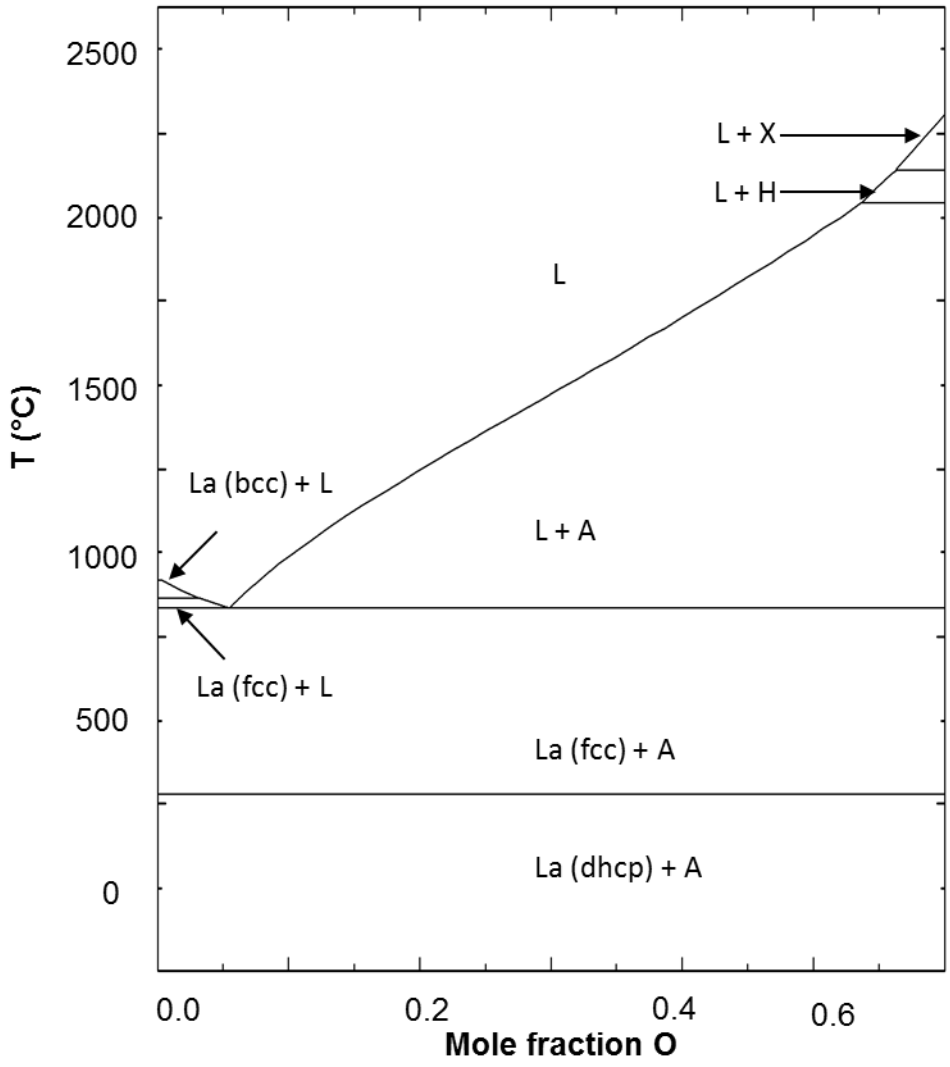

Fig. 6.10. The La-O binary phase diagram computed using the *ideal* partially ionic two-sublattice liquid model parameters derived from optimization of the inferred pseudo-binary UO_2-$LaO_{1.5}$ system.

integral ternary system. The phase relations determined from a study assessing the La-La_2O_3 binary[108] is given in Fig. 6.4(b) for comparison; both diagrams are tentative due to a lack of experimental data but both agree at least qualitatively. The major difference lies in the fact that [108] used a sublattice model to describe the solubility of oxygen in the metallic and sesquioxide phases. Although, combining the La-La_2O_3 assessment from [108] with this work was considered, it was ultimately decided to use the Gibbs functions for La allotropes from [169], and sesquioxides from [77], for three reasons. First, it was consistent with the previous published work assessing the U-Gd-O system [172]. Second, the La cation is only considered to exhibit a 3+ oxidation state in this work; the assessment from [108] allows for both La^{3+} and La^{2+} in the sublattice models for the La_2O_3 phases. Third, there is a lack of sufficient experimental data to confidently validate the models from [108]. Thus the La allotropes and the La_2O_3 polymorphs are represented as pure elements and stoichiometric compounds, respectively.

6.16.2 The U-La binary

As with the U-Gd binary, all condensed phases in this subsystem were assumed to be immiscible based on the extremely limited inter-solubilities of La and U in the metallic and liquid phases from [109]. A tentative diagram of the U-La binary is shown in Fig. 6.11. The modeling approach is the same as that described for the U-Gd system discussed in Section 6.13.2.

6.16.3 The U-La-O ternary

The CEF representation of $U_{1-y}La_yO_{2\pm x}$ fairly well reproduce critically assessed oxygen pressure measurements from [110] as seen in Fig 6.12. Most of the data are reported over single phase $U_{1-y}La_yO_{2\pm x}$. However, in Fig. 6.12(c), there is invariant oxygen potential for $O/M \geq 2.25$, a consequence of a three phase region. Indeed, at $T \leq$ 1073 K and $O/M \geq 2.25$, U_3O_8-U_4O_9- $U_{1-y}La_yO_{2\pm x}$ coexist and thus the oxygen pressure

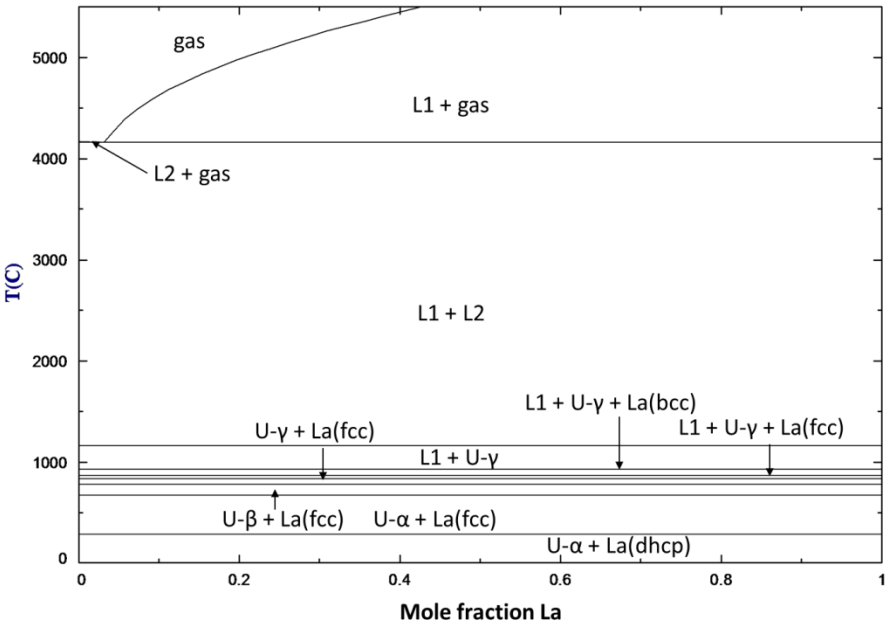

Fig. 6.11. U-La binary phase diagram computed using the partially ionic two-sublattice liquid model parameters derived from optimization of the inferred pseudo-binary UO_2-$LaO_{1.5}$ system assuming no inter-solubility between U and La.

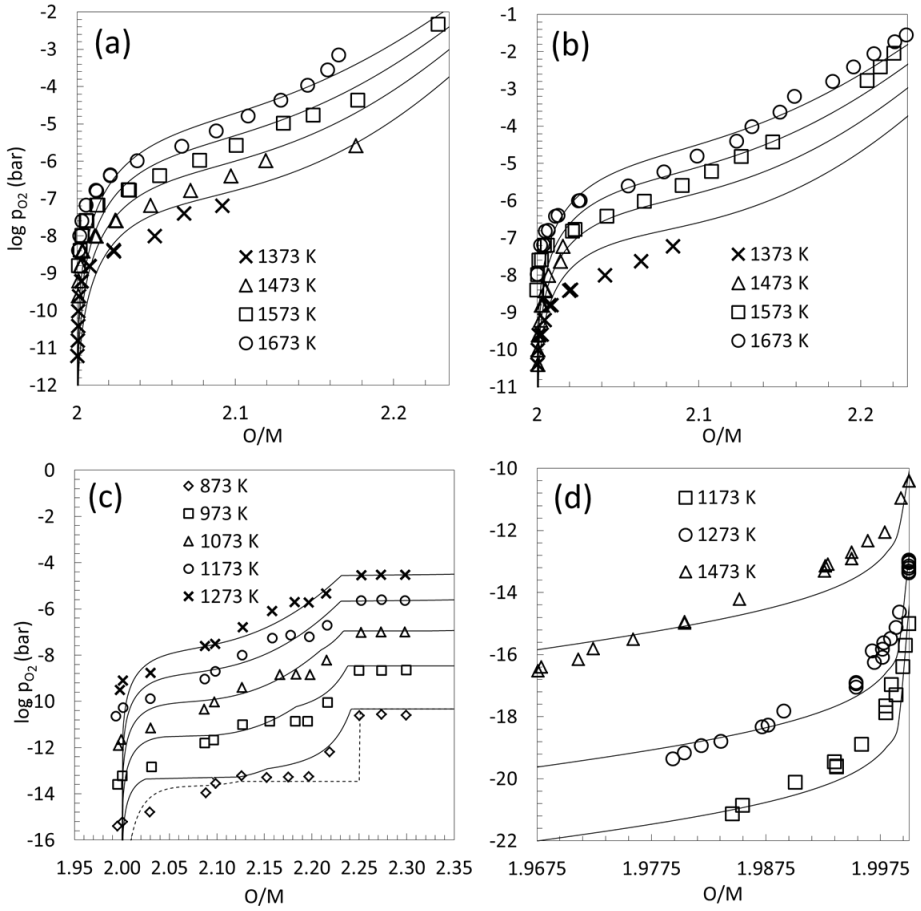

Fig. 6.12. Equilibrium oxygen pressures over $U_{1-y}La_yO_{2\pm x}$ vs. O/M. Individual measurements are the points shown for (a) y = 0.025 from [113], **(b)** y = 0.05 from [113], **(c)** y = 0.05 from [114], **(d)** and y = 0.20 from [112]. The computed results are the solid lines with the dashed lines in **(c)** representing $UO_{2\pm x}$ for reference.

does not vary with composition. However, at T > 1173 K, the p_{O_2} only appears to be constant; in reality, a very small increase in p_{O_2} with O/M change can be discerned and the models predict that this region corresponds to a $U_{1-y}La_yO_{2\pm x}$- U_3O_8 two-phase field which is not invariant.

The computed diagram for the isothermal section of U-La-O at 1523 K shown in Fig. 6.13 agrees remarkably well with the reported phase relations from [62] with a few exceptions. The authors claim to observe a U-La homogeneity range in both the RI and RII phases; however, as mentioned above this range is very small and it is likely to lie within the experimental error since some of the data appear contradictory for the $U_{1-y}La_yO_{2\pm x}$ –RI and $U_{1-y}La_yO_{2\pm x}$ –RII phase fields. Fig. 6.14 shows the computed fully oxidized U-La-O phase equilibria as a function of temperature and composition. The agreement between the computed phase diagram and the experimental data is good, but again, there are a few exceptions. First, Diehl and Keller [62] report single phase $U_{1-y}La_yO_{2\pm x}$ at 1473 K and 1373 K at ~50 mole % $LaO_{1.5}$, whereas the models show two-phase $U_{1-y}La_yO_{2\pm x}$ - RIII. One explanation is that the RIII phase was not observed by Diehl and Keller [62] since the structures are very similar and only around 0.3 and 0.17 mole fraction of RIII is predicted to be present at 1473 K and 1373 K, respectively. The computed equilibrium concentrations of $U_{1-y}La_yO_{2\pm x}$ and RIII approach parity at 50 mole % $LaO_{1.5}$ and 1273 K, but sluggish equilibration may account for incomplete transformation of $U_{1-y}La_yO_{2\pm x}$ →RIII. The situation may be similar with respect to the discrepancy between reported observations and the predicted coexistence of $U_{1-y}La_yO_{2\pm x}$-RI. In this case, however, the evidence is stronger that the RI phase was missed due to contradictory data at 1523 K showing both single $U_{1-y}La_yO_{2\pm x}$ and biphasic $U_{1-y}La_yO_{2\pm x}$ – RI at the same composition. Finally, Diehl and Keller [62] observed that long annealing times (~240 hours) were needed to obtain the $U_{1-y}La_yO_{2\pm x}$ →RII transition; therefore sluggish equilibration could explain the discrepancy between the computed RII-RIII equilibrium and the observed $U_{1-y}La_yO_{2\pm x}$ – RII coexistence below 1523 K.

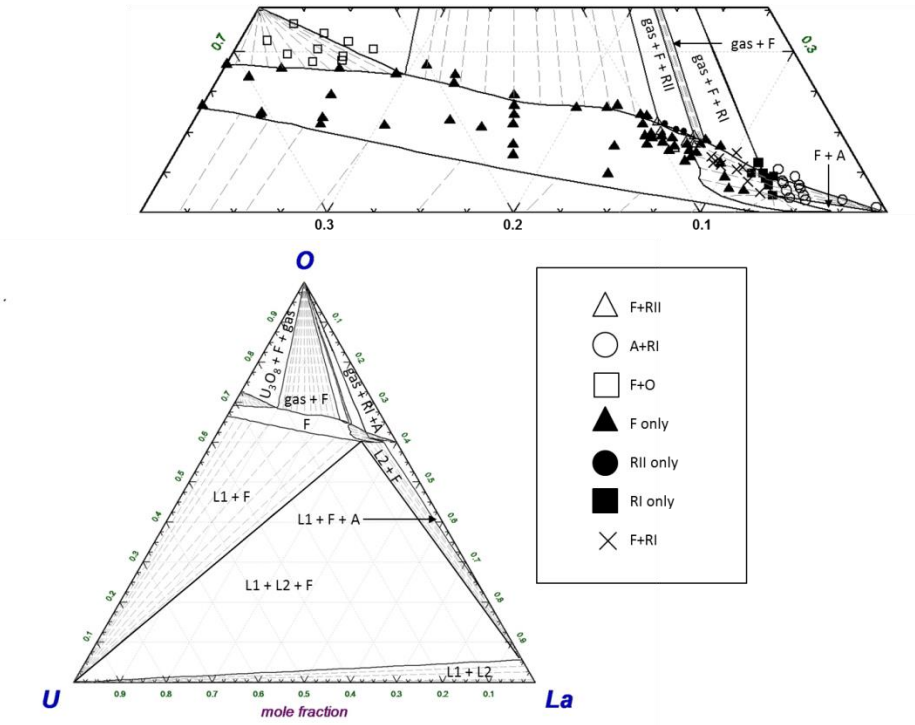

Fig. 6.13. Computed phase equilibria at 1523 K. The expanded section shows the phases in the vicinity of the single phase fluorite region together with points from experimentally observed phase equilibria [62]. (F=fluorite solid solution, RI=rhombohedral ULa_6O_{12-x}, RII= rhombohedral $U_2La_6O_{15}$, A=hexagonal La_2O_3, O=orthorhombic U_3O_8, L1=liquid phase, L2=second liquid phase)

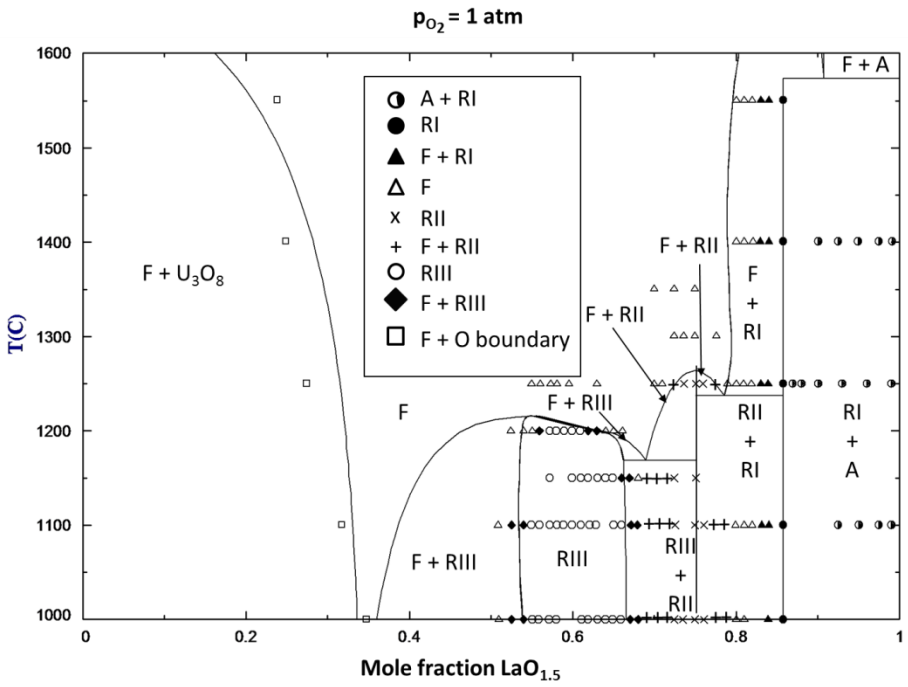

Fig. 6.14. Computed pseudo-binary diagram (lines) of fully oxidized U-La with the experimentally determined phase relations from [62] (points) shown as well. (F=fluorite solid solution, RI=rhombohedral ULa_6O_{12-x}, RII= rhombohedral $U_2La_6O_{15}$, A=hexagonal La_2O_3, O=orthorhombic U_3O_8)

As noted above, the phase relations along the UO_2-$GdO_{1.5}$ isopleth from [172] were used as a guide for UO_2-$LaO_{1.5}$; therefore the pseudo-binary UO_2-$LaO_{1.5}$ diagram shown in Fig. 6.15 is only tentative. The CEF lattice stability for $U_{1-y}La_yO_{2\pm x}$ is 0.77 kJ, an order of magnitude different from 8.74 kJ from DFT calculations.

6.17 Results for the U-Th-O system

6.17.1 The Th-O binary

Fig. 6.16 compares the experimentally determined enthalpy increment and the molar heat capacity (c_p) for ThO_2 to those computed with the CEF. The agreement is good up to ~3000 K where the wide scatter and large reported error associated with these measurements make them difficult to reproduce with the model. The CEF and TSLM representations for ThO_{2-x} and the Th-O melt developed in this work, , well reproduce both the equilibrium oxygen pressures from [121] and the phase equilibria from [120] as can be seen in Figs. 6.17 and 6.18.

6.17.2 The U-Th binary

The thermodynamic assessment of Li et al. [168] for the U-Th binary were used in this work to describe this system. The α, β, and liquid phases are represented with the regular solution model. The reference Gibbs energies for the pure elements and compounds come from [169, 178]. A comparison of the computed phase diagram and that proposed by Peterson [179] in a critical review of the experimental data is shown in Fig. 6.19.

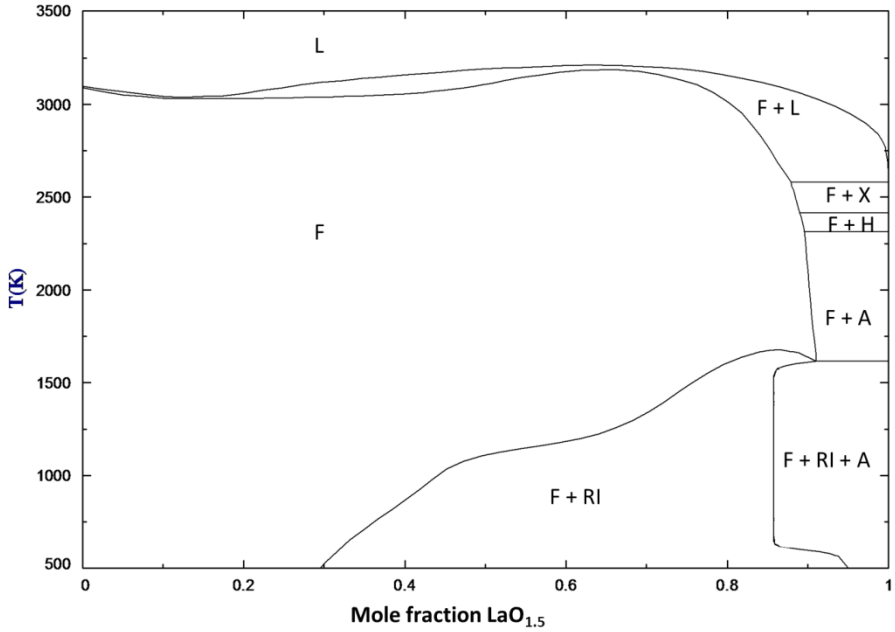

Fig. 6.15. Computed phase diagram along the UO_2-$LaO_{1.5}$ isopleth. (A=low temperature hexagonal, H=high temperature hexagonal, X=high temperature cubic, L=liquid, F=fluorite solid solution)

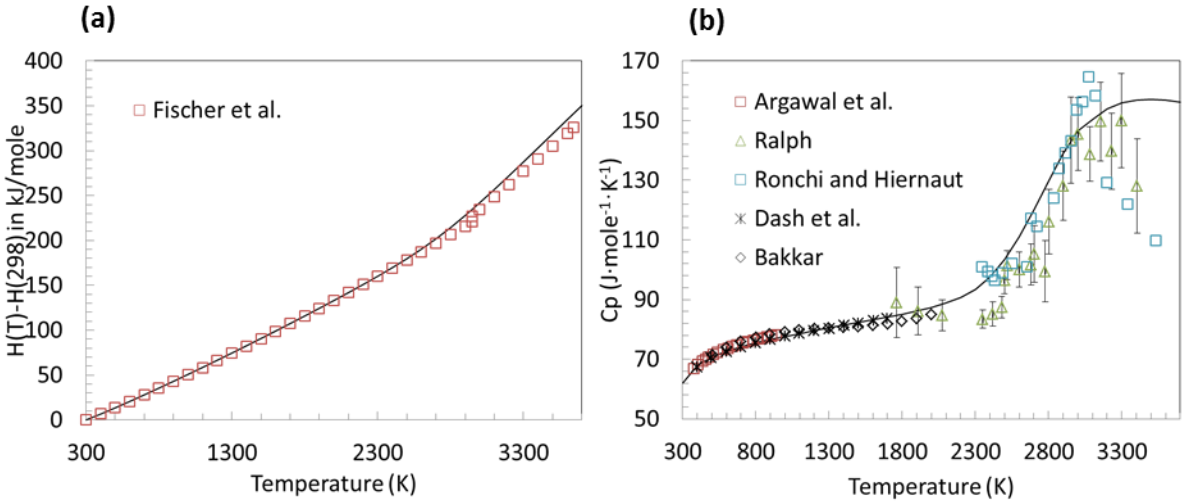

Fig. 6.16. (a) Enthalpy increment for ThO_2 determined by Fischer et al. [75]. (b) Experimentally determined molar heat capacity for ThO_2 from the studies [69, 72-76] reviewed in this work. Measured values are represented by symbols while those computed by the CEF are shown as solid lines.

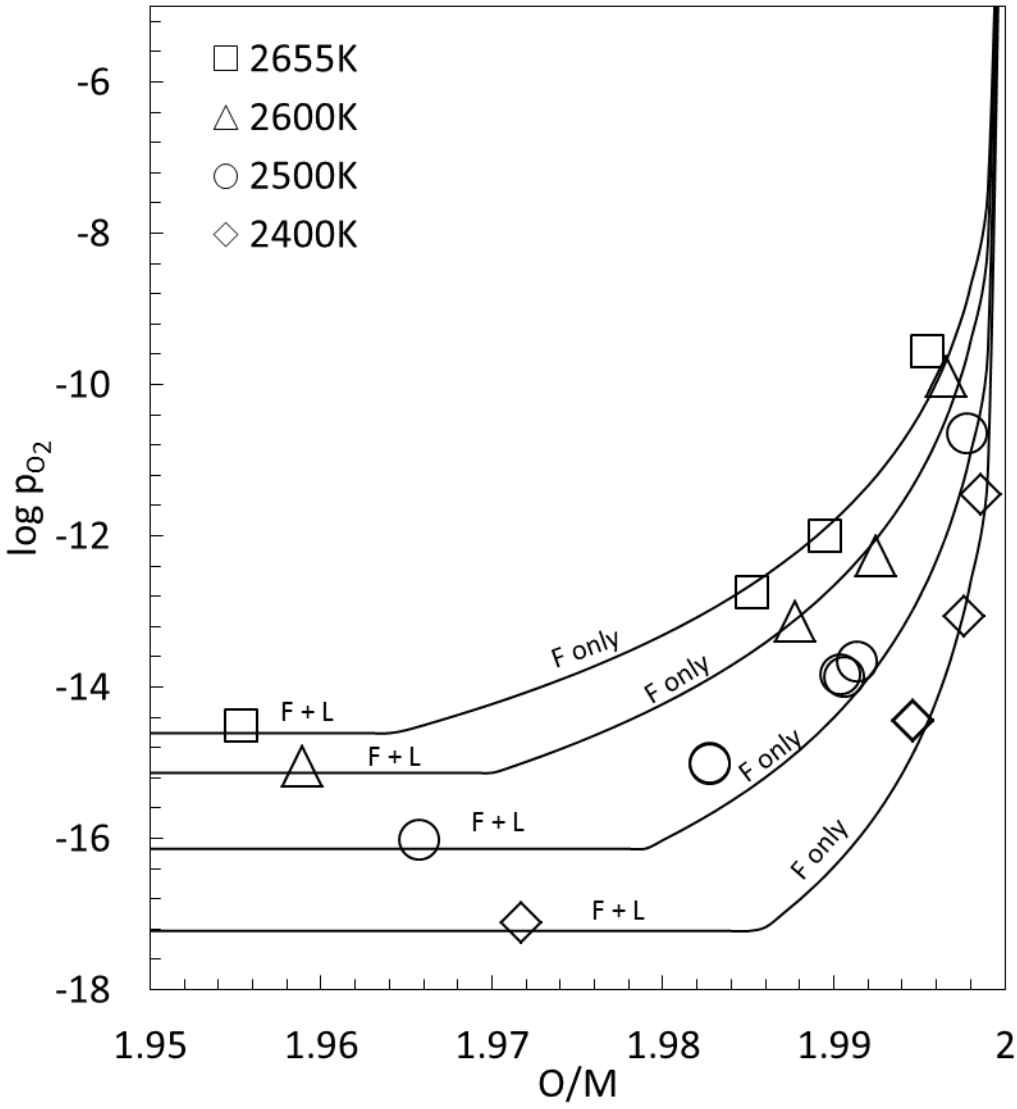

Fig. 6.17. Comparison of the computed (lines) versus experimental (points) equilibrium oxygen pressures from [121] over ThO2-x and the liquid. The CEF and TSLM accurately predict *log* p_{O_2} values corresponding to the ThO_{2-x} – liquid bi-phasic equilibria observed by Ackermann and Tetenbaum [121].

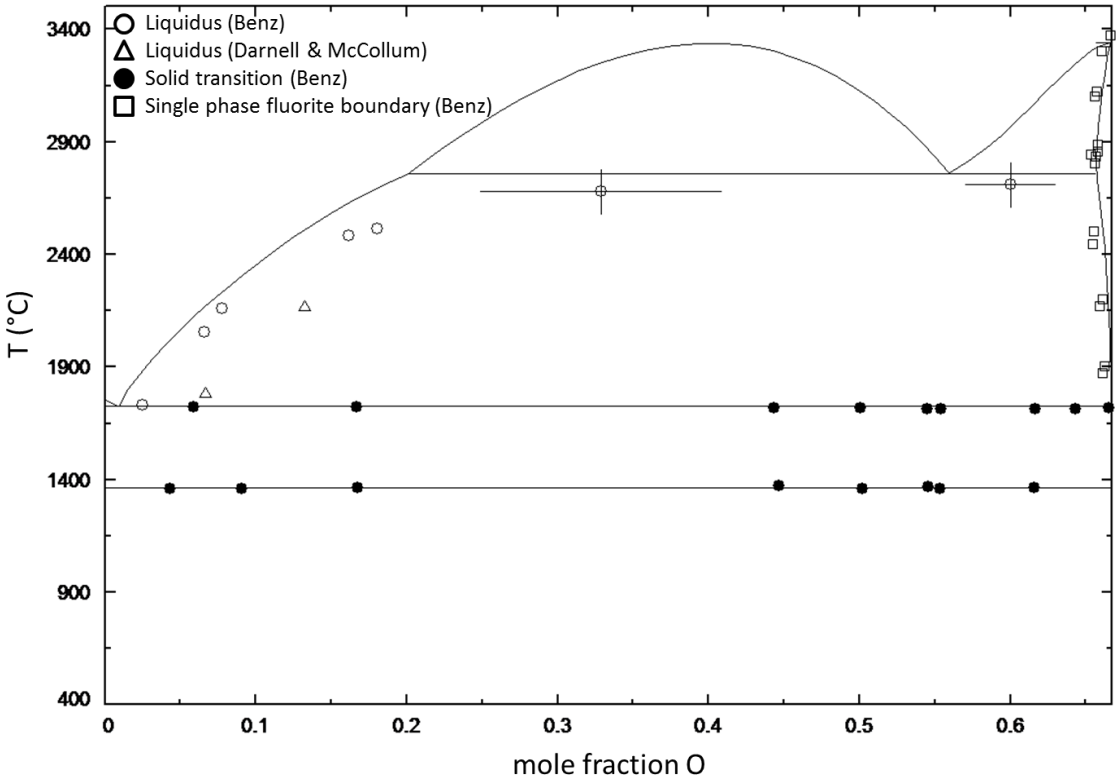

Fig. 6.18. Computed phase diagram for the Th-O binary from this work overlaid with experimental phase boundary data from [120, 181].

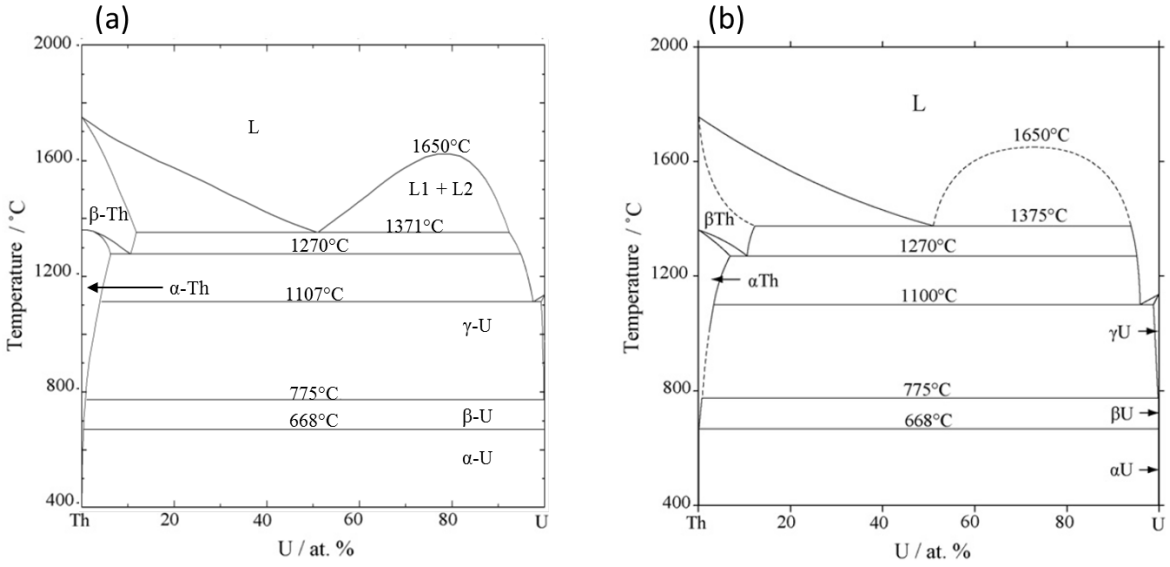

Fig. 6.19. A comparison of the computed (a) binary U-Th diagram using the thermodynamic parameters from [168] to that proposed by Peterson [179] based on experimental phase boundary determinations.

6.17.3 The U-Th-O ternary

Plots of $\log p_{O_2}$ versus O/M obtained from TGA experiments from this work for y = 0.05 and 0.20 versus computed values from the CEF for $U_{1-y}Th_yO_{2\pm x}$ are shown in Fig. 6.20(a) and (b). Figures 6.20(c), (d) and Fig. 6.21 compare the model predictions to equilibrium oxygen pressure measurements reported in the literature; the agreement is good. In general, the CEF well reproduces the experimentally determined c_p versus T plot [72, 76, 138, 141, 180] from 298 K to 3000 K for $U_{1-y}Th_yO_{2\pm x}$ shown in Fig. 6.22. The DSC measurements from Dash et al. [74] disagree with those from Argawal et al. [72] at similar compositions. Furthermore, they fall below that for pure thoria which is inconsistent with the trend of increasing c_p with increasing urania content. From 3000 K to melting there is wide scatter in the data but the model fit is reasonable.

The TSLM analogue of the regular solution representation for the U-Th melt was developed in order to integrate the model from [168] into the U-Th-O assessment. Figure 6.23 compares the predicted solidus and liquidus phase boundaries to the experimental data set judged to be most reliable [151, 153]. The measurements form [152] were criticized by Latta et al. [153]suggesting those samples were open to an unconditioned atmosphere that induced oxygen stoichiometric changes that considerably affect results. Indeed, Latta et al. [153] observed significantly different solidus and liquidus temperatures due to small changes in O/M; therefore the data from [152] were excluded in the optimization. Overall, the fit is good especially considering that the authors from [151] recommend moving the solidus towards higher Th compositions as shown in Fig. 6.24; unfortunately the magnitude of the shift was not quantified in that study.

Psuedoternary UO_2-ThO_2-O isotherms are presented in Fig. 6.25 and 6.26 and they compare well with the phase diagrams proposed by Mumpton and Roy [150] and Paul and Keller [148] discussed in Chapter 5. Fig. 6.25 shows low temperature equilibrium with the $UThO_5$ phase as suggested by Dash et al. [74]and Boekschoten and Kema [149]. The models from this work show $UThO_5$ to exist in the U-Th-O ternary up

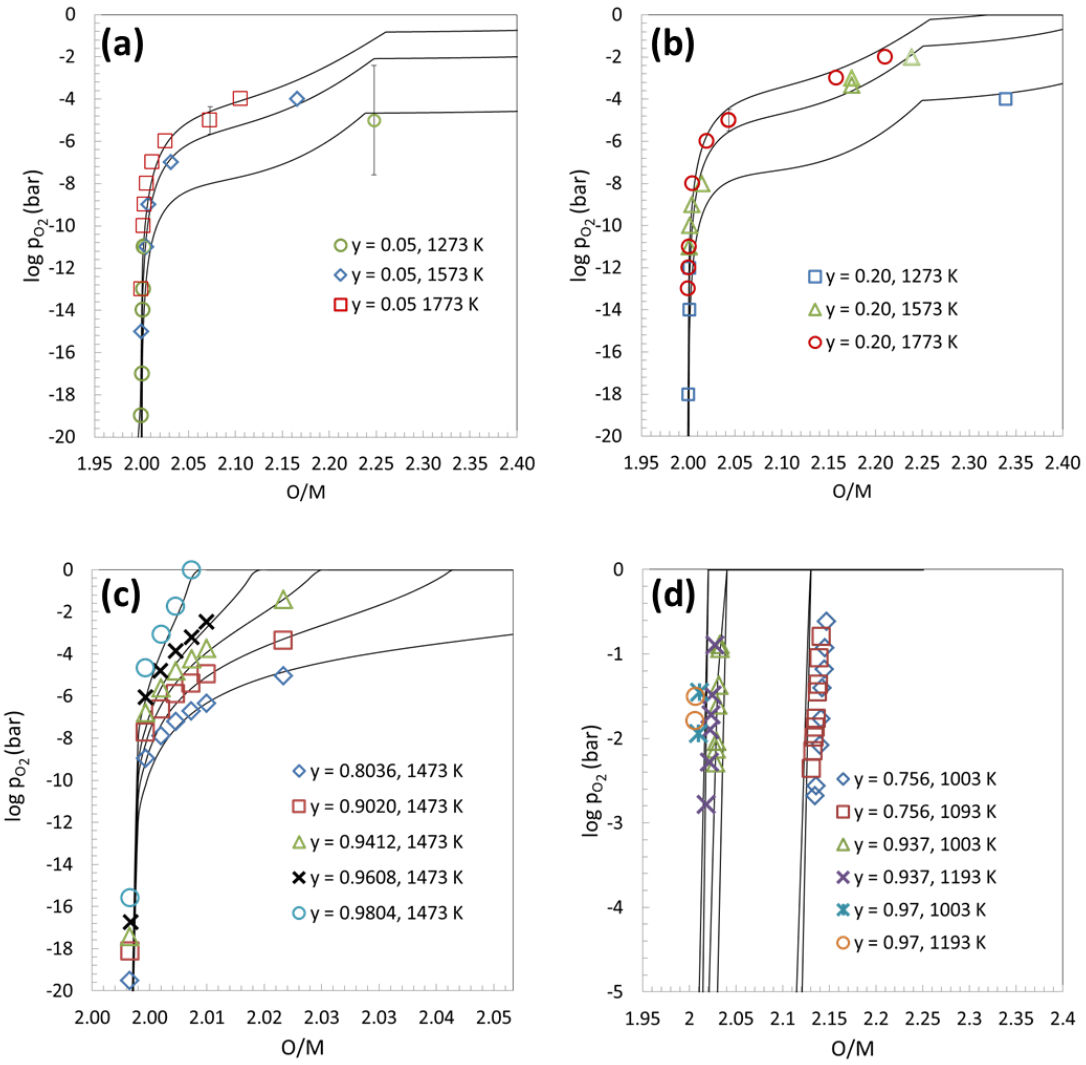

Fig. 6.20. Computed (lines) oxygen pressures compared to those (symbols) for $U_{1-y}Th_yO_{2+x}$ (a,b) obtained by TGA in this work, (c) a least squares curve fit from [74] of the data from a study by Ugajin et al. [72, 127, 128] and (d) those measured by Anderson et al. [122].

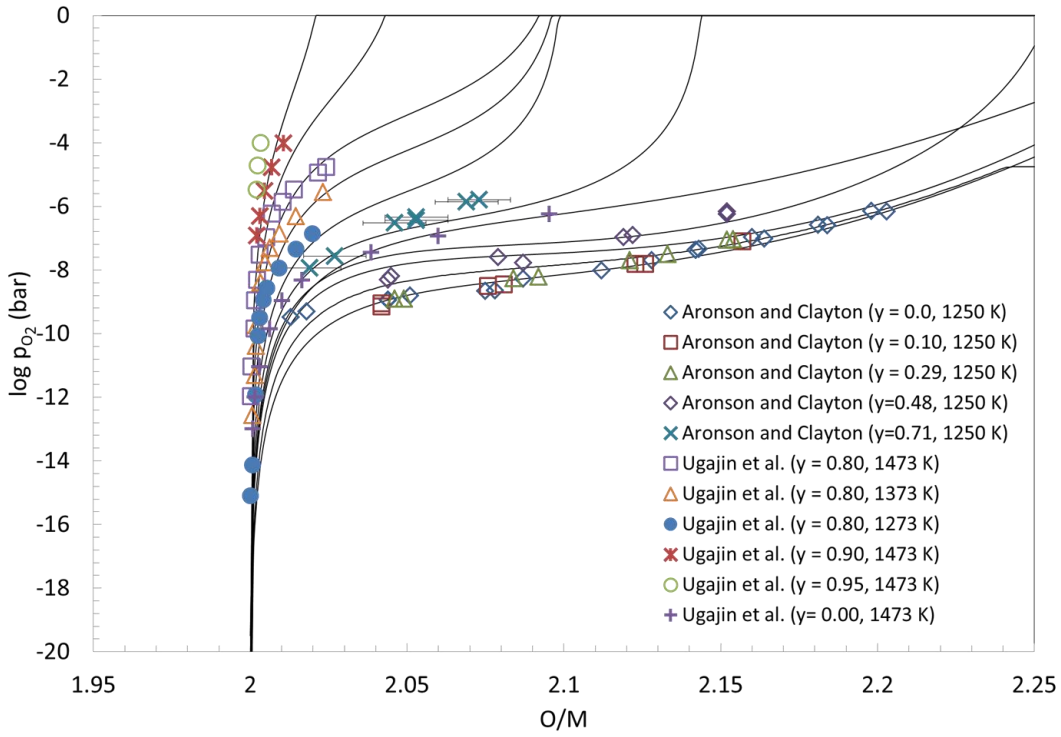

Fig. 6.21. Comparsion of the computed oxygen pressures over $U_{1-y}Th_yO_{2+x}$ using the CEF developed in this work (lines) and those determined experimentally (symbols) from [127, 128, 135].

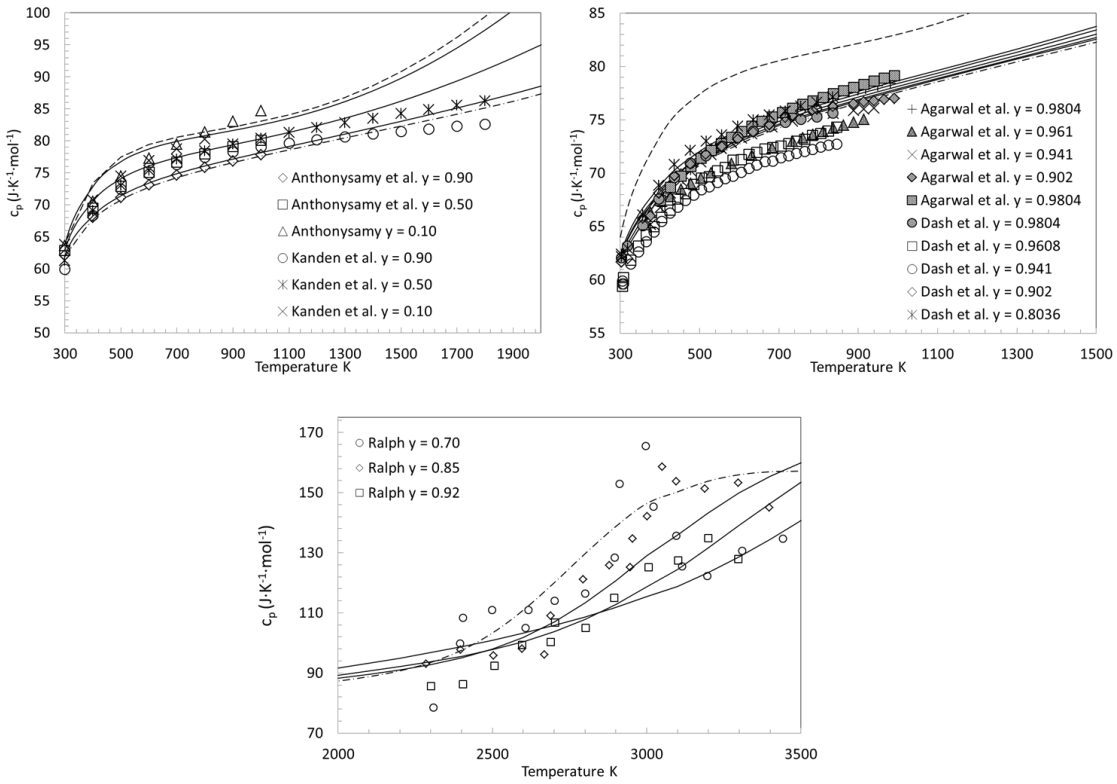

Fig. 6.22. Comparison of measured (symbols) and computed (lines) c_p values for $U_{1-y}Th_yO_2$. Heat capacity of pure urania is shown as dashed lines while that of pure thoria is represented by the dash dot.

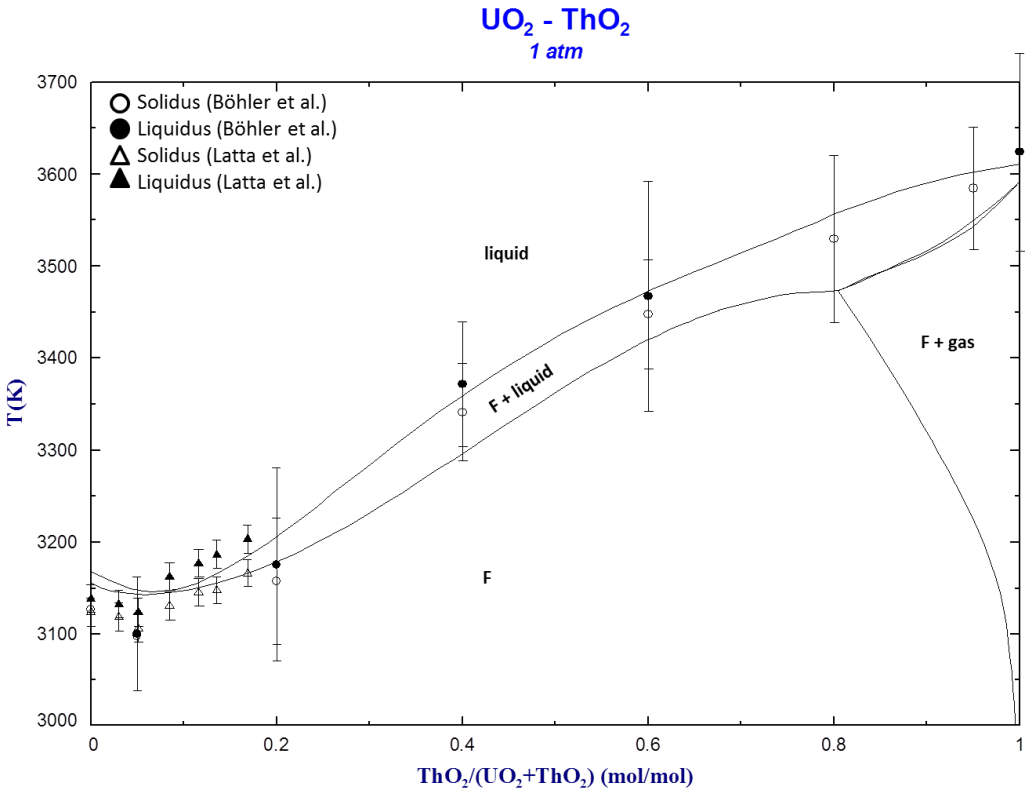

Fig. 6.23. Computed solidus and liquidus overlaid with melting data from [152].

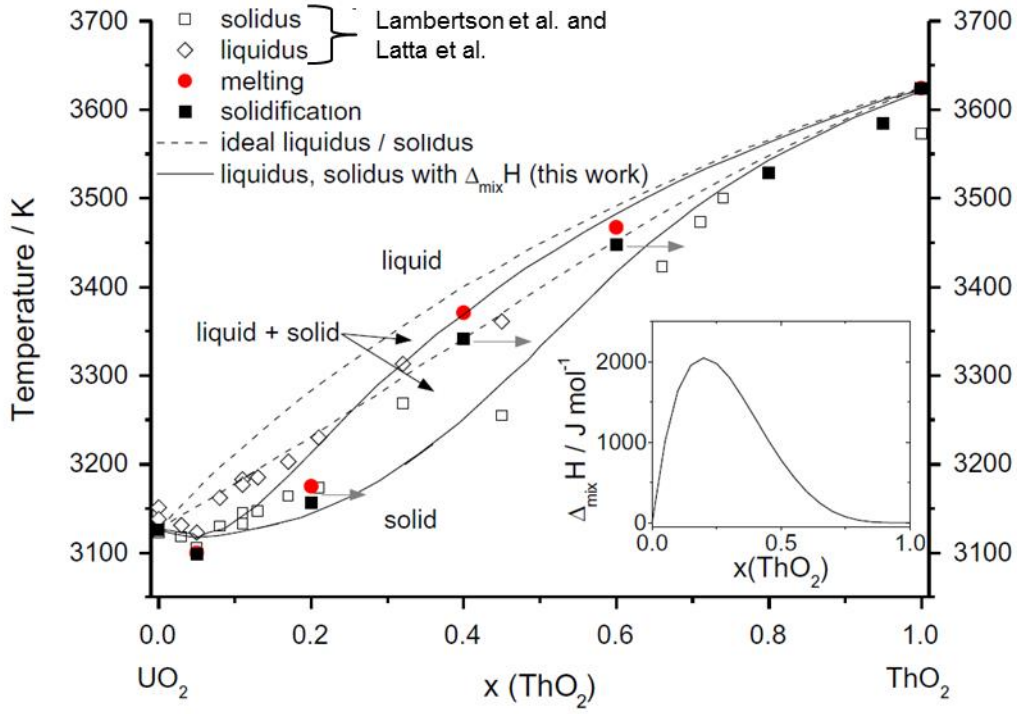

Fig. 6.24. Melting data (symbols) and proposed boundaries for UO_2–ThO_2 psuedobinary from Böhler et al. [151] (red circles and black squares). The authors recommend moving the solidus towards higher ThO_2 compositions due to segregation of the mixed oxide specimens during laser pulse experiments; this is represented by the arrows emanating from the closed squares.

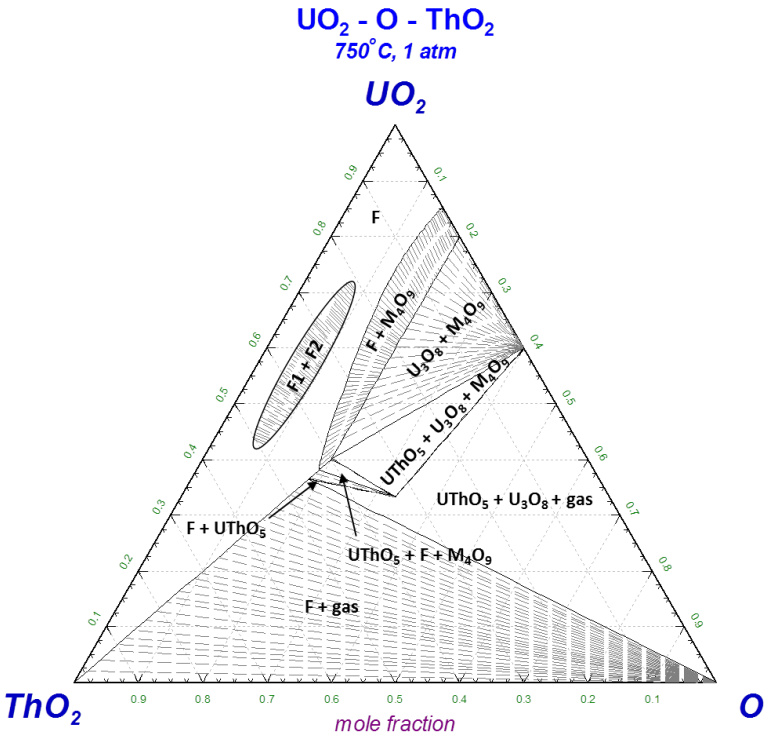

Fig. 6.25. Computed phase relations using the models developed in this work for the UO2-ThO2-O psuedoternary system at 1023 K.

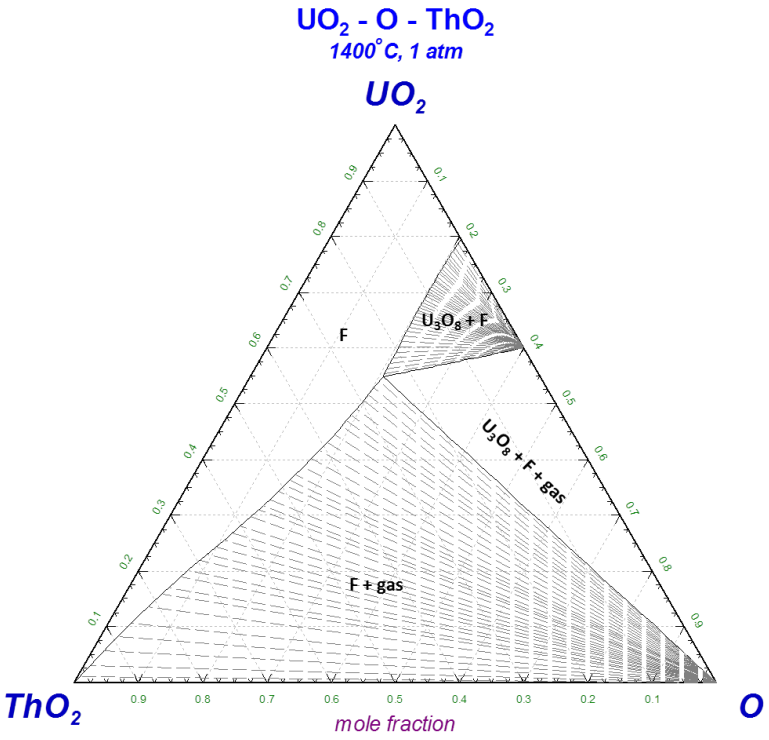

Fig. 6.26. Computed phase relations using the models developed in this work for the UO2-ThO2-O psuedoternary system at 1673 K.

to 1023 K consistent with a predicted stability of this compound below 1070 K as reported by Dash et al. [74].

6.18 Defect chemistry

For comparison, the defect and cation concentrations as a function of $\log p_{O_2}$ and O/M at 1773 K computed from the models developed in this work are shown for $U_{0.831}Gd_{0.169}O_{2\pm x}$, $U_{0.831}La_{0.169}O_{2\pm x}$, and $U_{0.831}Th_{0.169}O_{2\pm x}$ in Fig. 6.27. The U^{6+} concentration is minimal and only becomes significant for very high O/M values, consistent with U^{5+} as the predominant higher oxidation state [64, 65] in urania. Unlike the U-Gd-O and U-Th-O systems however, phase relations for U-La-O require U^{6+} to be included in the cation sublattice of the CEF in order to achieve electroneutrality at high La contents. The requirement also exists in the U-Nd-O system. The defect behavior for $U_{0.831}La_{0.169}O_{2\pm x}$ and $U_{0.831}Gd_{0.169}O_{2\pm x}$ are very similar with$U_{0.831}La_{0.169}O_{2\pm x}$ showing a slightly higher U^{6+} concentration at high O/M values.

For $U_{0.831}Th_{0.169}O_{2\pm x}$, the Th^{3+} concentration is negligible and U^{3+} charge compensates in the hypostoichiometric region over the O/M and $\log p_{O_2}$ intervals given in Fig. 6.27. This is consistent with a profoundly stable 4+ oxidation state for Th [182]. Consequently, much lower oxygen pressures are needed to reduce $U_{0.831}Th_{0.169}O_{2\pm x}$ compared to $U_{0.831}Gd_{0.169}O_{2\pm x}$ and $U_{0.831}La_{0.169}O_{2\pm x}$ since $U^{4+} \rightarrow U^{3+}$ formation is energetically unfavorable. Indeed, , there exists no oxygen potential measurements in the literature for the hypostoichiometric $U_{1-y}Th_yO_{2-x}$ region and only very limited $\log p_{O_2}$ vs O/M data for UO_{2-x} and ThO_{2-x} at very high temperatures. For Gd and La, the 3+ valence is the stable oxidation state thus permitting $U_{0.831}Gd_{0.169}O_{2\pm x}$ and $U_{0.831}La_{0.169}O_{2\pm x}$ to be more easily reduced.

Fig. 6.28 compares the CEF predicted n_f to those measured by Hutchings [68] and computed from a mean field model (MFM) by Ronchi and Hiernaut [69]. Assuming the 9:1:8 cluster represents the total anion defect arrangement, the agreement with [68] is

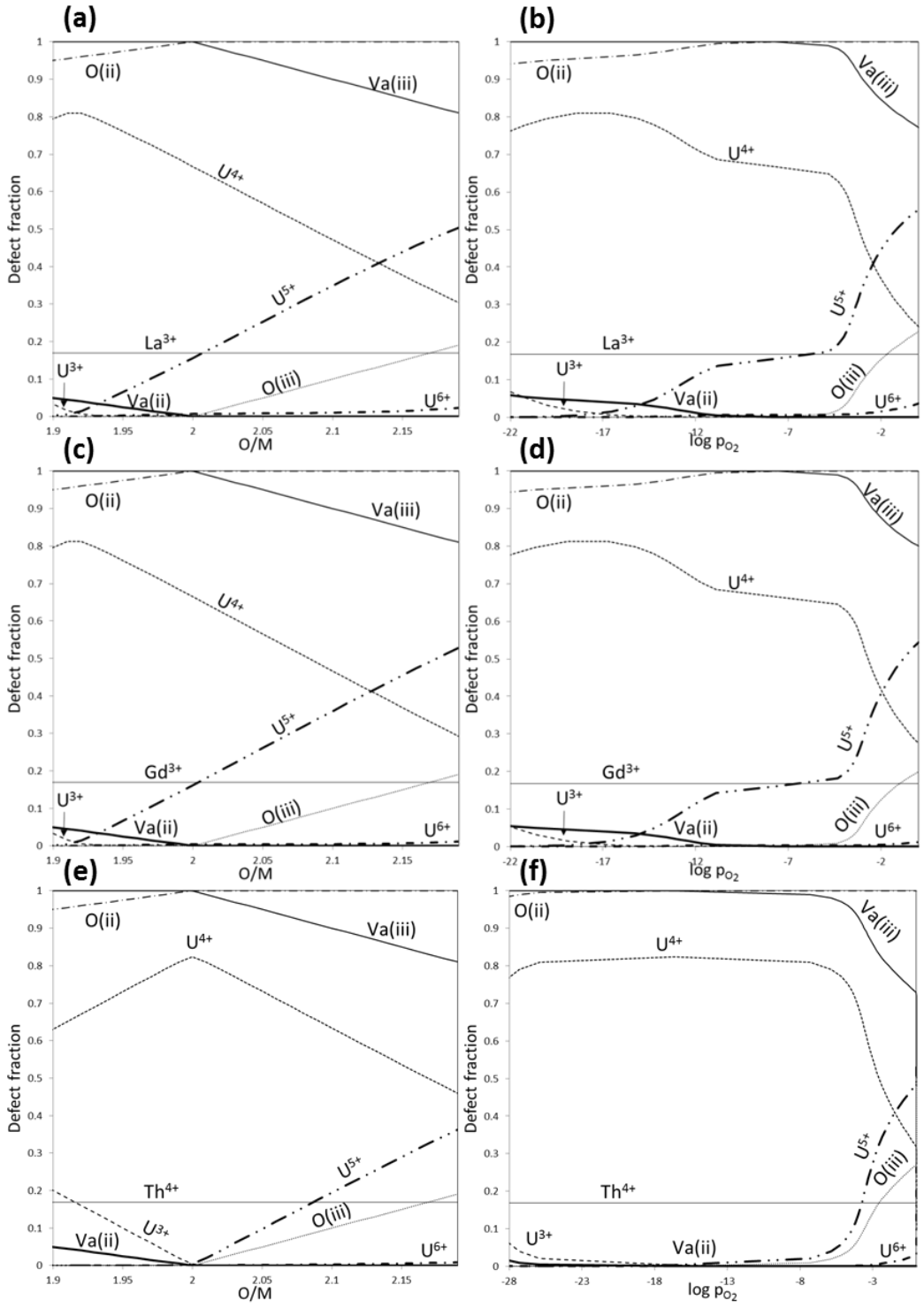

Fig. 6.27. Computed defect and cation concentrations as a function of $\log p_{O_2}$ and O/M at 1773 K for $U_{0.831}Gd_{0.169}O_{2\pm x}$ (a,b), $U_{0.831}La_{0.169}O_{2\pm x}$ (c,d), and $U_{0.831}Th_{0.169}O_{2\pm x}$(e,f).

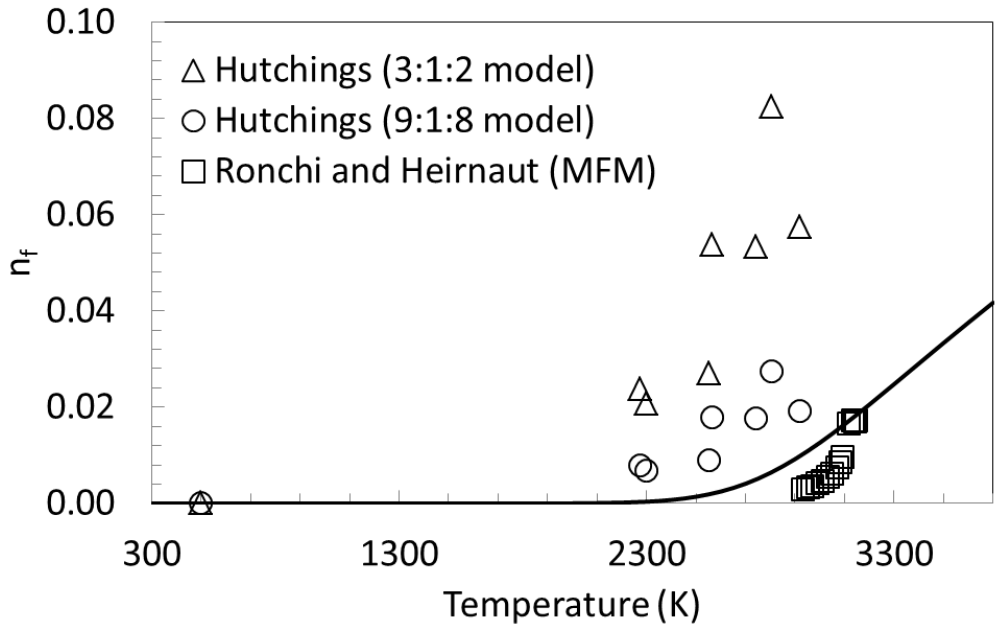

Fig. 6.28. Computed (lines) oxygen Frenkel defects using the CEF for ThO2 from this work and those determined from neutron diffraction [68]and a mean field model [69](symbols).

good especially considering n_f could not be determined directly and is calculated after assuming a relationship between n_d and n_f; the results compare better with those computed in [69].

The formation energy of a Frenkel defect (ΔG_{FPO}), shown in Figs. 6.29 as a function of temperature, was computed using the following relations after Sundman et al. [183] given in Eqns. 6. 30 and 6. 31:

$$\frac{y_{O^{2-}}^{iii} y_{Va}^{ii}}{y_{O^{2-}}^{ii} y_{Va}^{iii}} = e^{\left(\frac{-\Delta G_{FPO}}{RT}\right)} \qquad \textbf{6. 30}$$

$$\Delta G_{FPO} = \left(2y_{Va}^{ii} - 1.5\right)^{\circ}G_{Th^{4+}:O^{2-}:Va} + \left(1 - 2y_{Va}^{ii}\right)^{\circ}G_{Th^{4+}:O^{2-}:O^{2-}} + \left(0.5 - 2y_{Va}^{ii}\right)^{\circ}G_{Th^{4+}:Va:Va} - \left(2y_{Va}^{ii}\right)^{\circ}G_{Th^{4+}:Va:O^{2-}} \qquad \textbf{6. 31}$$

and is consistent with values determined by other methods (2.7 – 7.7 eV) for urania reviewed by Crocombette [41]. Figure 6.30 plots the temperature dependence of the enthalpy (ΔH_{FPO}) and entropy (ΔS_{FPO}) components of ΔG_{FPO} determined from Eqns. 6. 32 – 6. 33 derived using the Maxwell relation $S = -dG/dT$ and the fundamental definition $G = H - ST$.

$$\Delta S_{FPO} = -\frac{d\Delta G_{FPO}}{dT} \qquad \textbf{6. 32}$$

$$\Delta H_{FPO} = \Delta G_{GPO} - T\frac{d\Delta G_{FPO}}{dT} \qquad \textbf{6. 33}$$

Ronchi and Hyland [71] recommended representing c_p as a constant above the critical OD temperature for urania. To do this for ThO_2, adjustments were made to the c_p functions of the Th^{4+} containing end-members so that the molar heat capacity attains a

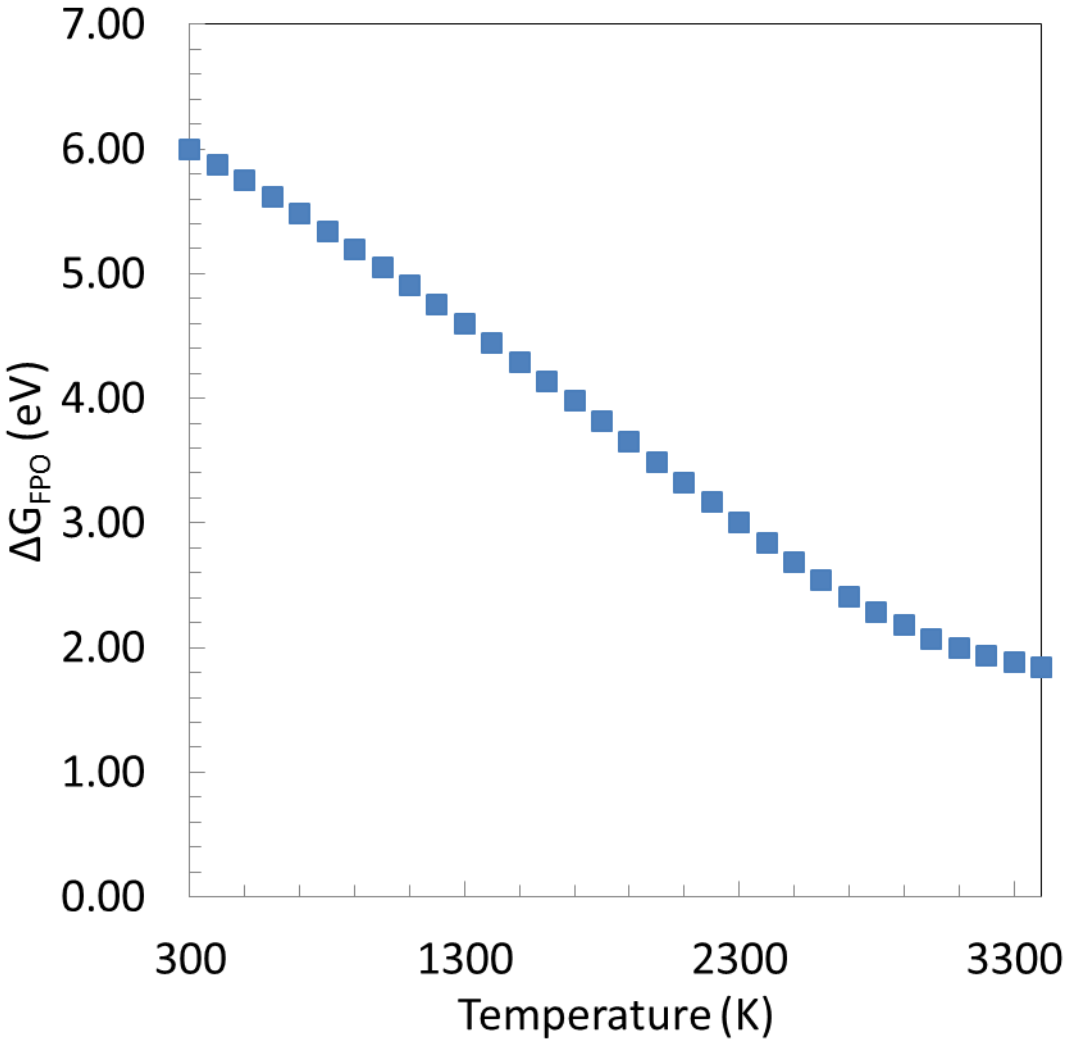

Fig. 6.29. Gibbs energy of reaction for a Frenkel defect in ThO_2 versus temperature from the CEF model developed in this work.

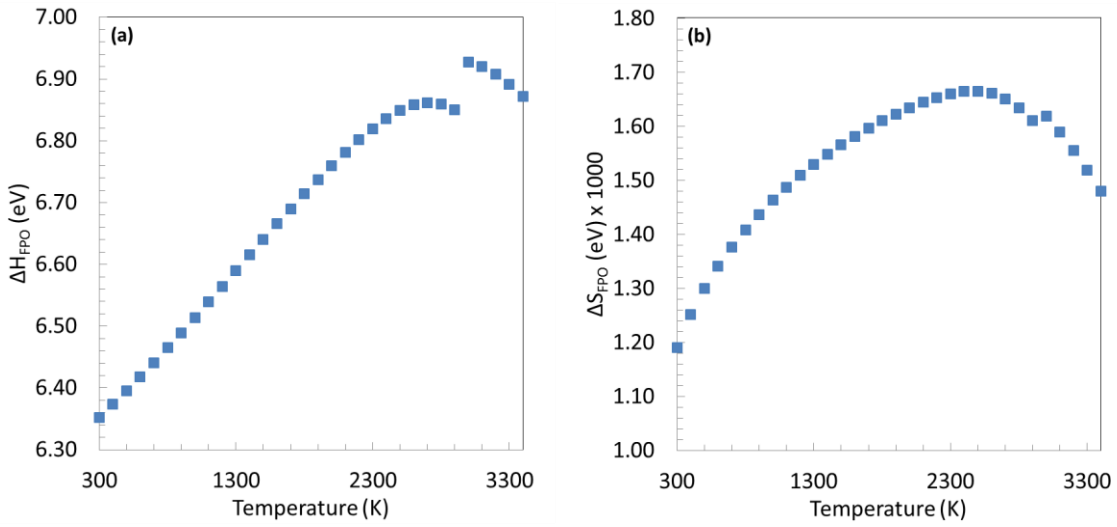

Fig. 6.30. Enthalpy (a) and entropy (b) of reaction for a Frenkel defect in ThO_2 versus temperature from the CEF model developed in this work.

near constant value above 3000 K; therefore, ΔH_{FPO} and ΔS_{FPO} correspondingly show a discontinuity at that temperature.

Considering the reasonable agreement with experimental, theoretical, and semi-empirical treatments of n_f and ΔG_{FPO} combined with a good fit to c_p resulting from significant n_f, the CEF for ThO_{2-x} may indeed well represent the oxygen Frenkel defect behavior of thoria and the approach should be applicable to phases that exhibit similar phenomenon.

CHAPTER 7

SUMMARY AND CONCLUSIONS

"In this house we obey the laws of thermodynamics!" – Homer Simpson

The models that comprise the assessments presented in this work are a significant step forward towards better understanding the chemical behavior of additions to U-O systems. The urania phase is the focus of intense research due to its complexity and technological importance as a commercial LWR fuel. Modeling the thermodynamics of $UO_{2\pm x}$ with the soluble fission products that are created during irradiation is fundamental for high fidelity physics based fuel performance simulations; there are three major contributions resulting from this work that aid in accomplishing this.

First, the phase relations for U-La-O determined by Diehl and Keller [62] at high La compositions show $U_{1-y}La_yO_{2\pm x}$ exists at O/M values whereby the average U oxidations state must be greater than +5 to achieve electro-neutrality; therefore, U6+was added as a constituent of the FCC cation sublattice. The inclusion of U^{6+} has practically no effect on the previously published U-O assessment from [32] as can be seen if Fig. 7.1 while permitting a more faithful representation of the observed phase relations in U-Ln-O systems at high Ln compositions.

Second, the CEF for fluorite ThO_{2-x} was developed and includes a simplified treatment of the phenomenon resulting from oxygen Frenkel disordering. The ThO_{2-x} model was then combined with that for $UO_{2\pm x}$ for a CEF representation of the $U_{1-y}Th_yO_{2\pm x}$ solution and shows good agreement with experimentally determined phase equilibria, μ_{O_2} and c_p data. This shows that the CEF can be used to describe not only the

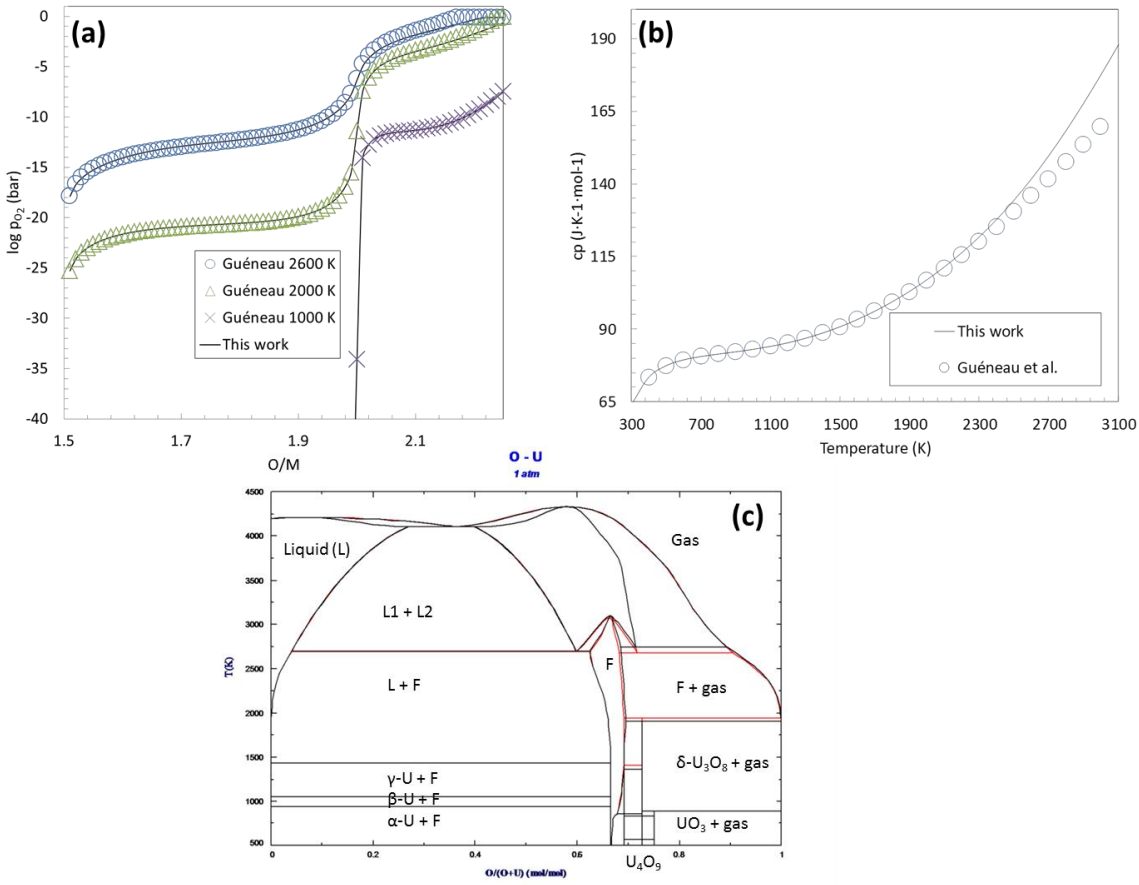

Fig. 7.1. A comparison of the computed oxygen pressures (a) and c_p (b) using the CEF for $UO_{2\pm x}$ modified to include U^{6+} from this work (solid lines) and the original from [32] (symbols). (c) Phase relations in the U-O system using the CEF from [32] (black lines) and the modified CEF from this work (red lines).

phase equilibria and thermodynamic properties but also the defect chemistry adding to its value as a tool for multi-scale fuel performance simulations.

Third, thermodynamic assessments of the U-Gd-O, U-La-O, and U-Th-O integral systems were developed using the CALPHAD approach and by extending the CEF and TSLM for the fluorite and liquid solutions respectively in the U-O binary. Gibbs energy functions for the RII $U_2La_6O_{15}$ and RI UGd_6O_{12} and $UThO_5$ compounds were derived while the CEF was also used to describe the RI ULa_6O_{12-x}, RIII $(U_{1-y}La_y)_8O_{16}$, and $(U_{1-y}Th_y)_4O_9$ solutions that exhibit a homogeneity range in the ternary U-M-O phase space.

The behavior of oxygen in the fluorite urania phases is complex. A major aim of this work is a better description of μ_{O_2} for $U_{1-y}M_yO_{2\pm x}$ since the chemical state of a nuclear fuel element is determined largely by μ_{O_2} and oxygen redistribution is driven by gradients in this crucial thermochemical property. The importance of faithful modeling this behavior is underscored in a study of coupled heat transport, oxygen diffusion, and thermal expansion in $UO_{2\pm x}$. Figure 7.2 shows that ignoring oxygen transport leads to dramatically different simulation results for the radial temperature and displacement distributions. Further, many properties of $UO_{2\pm x}$ and therefore $U_{1-y}M_yO_{2\pm x}$ vary significantly with *x* making a high fidelity representation of μ_{O_2} for $U_{1-y}M_yO_{2\pm x}$ a critical component to multi-physics fuel performance simulation efforts.

Solution models for multi-component urania phases that are as physical as possible facilitate broad use, such as integration in multi-physics and multi-scale fuel simulation programs. Since the system comprising a nuclear fuel element evolves with burnup, it is essential that models successfully representing important subsystems be versatile enough to permit extensions to include more fission and activation products for higher order thermodynamic descriptions; the CEF has proven to be a useful tool towards accomplishing this.

The models from this work were developed within the CALPHAD framework to permit confident extrapolations and give detailed descriptions of phase relations, material

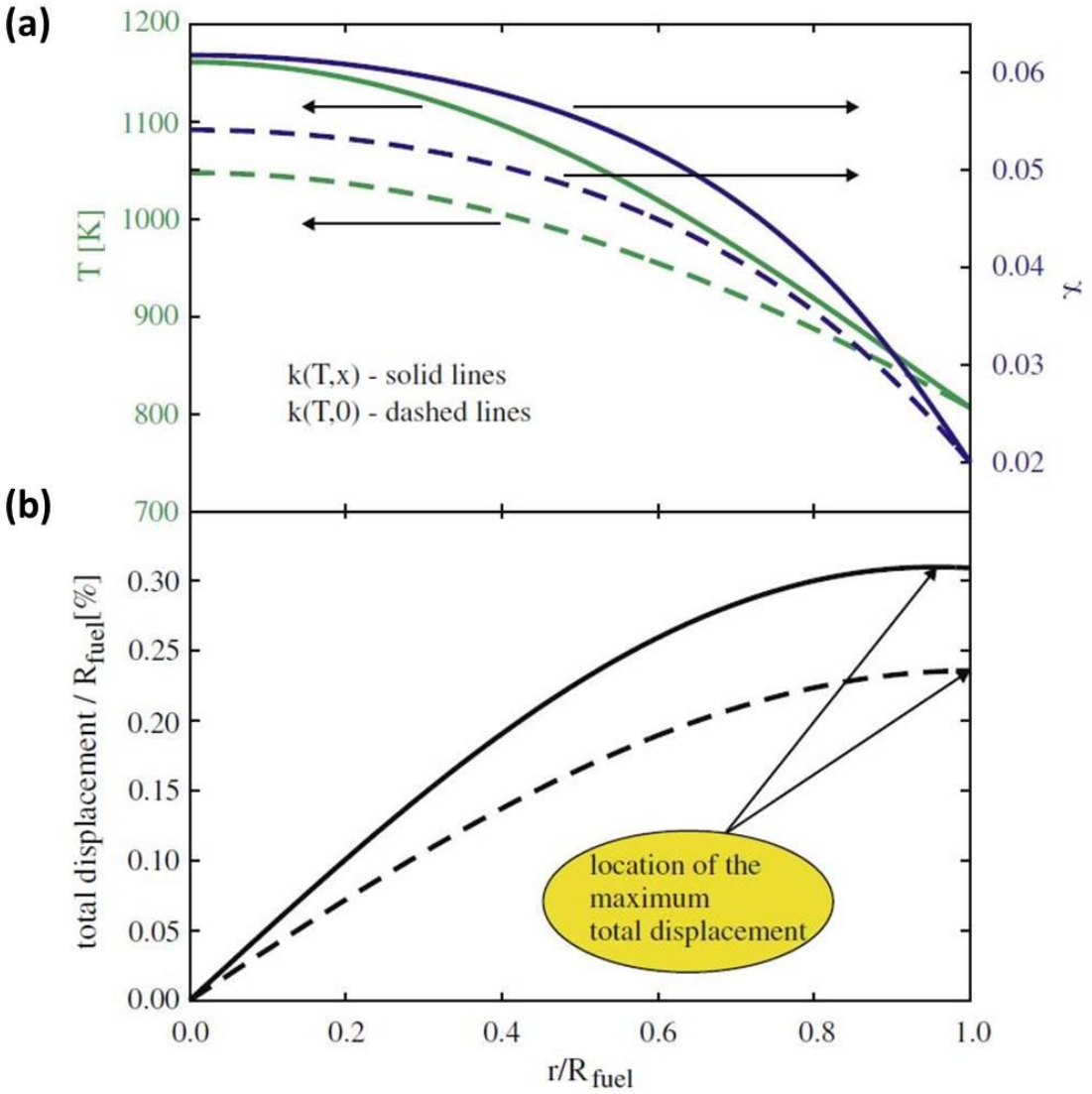

Fig. 7.2. **(a)** The radial steady-state temperature (green lines) and oxygen distribution (blue lines) with a thermal conductivity expression, κ, with (solid) and without (dashed) an oxygen compositional dependency and **(b)** total displacement as a function of fuel radius again with (solid) and without (dashed) a κ dependency on oxygen composition from [184].

properties, and defect equilibria fundamental to understanding the chemistry and predicting the behavior of fuel during operation.

CHAPTER 8

RECOMMENDATIONS

"Where there is no vision the people perish…" – Proverbs 29:18

In order to bridge the gap between macro- and microscopic modeling approaches, augmentations that may better represent the behavior of UO_2 can be introduced into the CEF for the phase. The model for $U_{1-y}M_yO_{2\pm x}$ is already rather physically descriptive since the sublattice representation is based on the long-range ordering (LRO) and defect chemistry of the UO_2 crystal; however, introducing short-range ordering (SRO) is the logical next step towards better agreement between first principles and CEF results for $U_{1-y}M_yO_{2\pm x}$. In Chapter 7, it was shown that he CEF is capable of describing the OD Frenkel disorder of fluorite oxides; therefore this treatment should be included when modeling the $UO_{2\pm x}$ phase since it forms the basis for the multicomponent descriptions. Additional sublattices could be included in the CEF for urania solid solutions to reproduce observed and/or proposed oxygen clustering phenomena. Finally, models and assessments should be continuously validated and updated as new information is attained; many measurements are needed to fill crucial gaps in the data to more accurately determine the behavior in the integral ternaries and binary subsystems.

8.1 Short range ordering

Recent density functional theory calculations [185] suggest the smaller cations prefer vacancies as next nearest neighbors in $U_{1-y}M_yO_{2\pm x}$. Further, Aizenshtein et al.

[186] and Chen and Navrotsky [67] posit SRO to explain the compositional variation in maxima of the enthalpy of formation as a function of cation radius in trivalent doped ceria and thoria solutions. To bring the present CEF for $U_{1-y}M_yO_{2\pm x}$ into better agreement with these studies, the approach suggested by Hillert [166] for introducing SRO is recommended. To do this, Eqn. 2. 3 is modified such that the surface of reference becomes a mechanical mixture corresponding to a probabilistic distribution (p_{end}) of end-members given by:

$$G^{CEF} = \sum_{end} p_{end} {}^{\circ}G_{end} \qquad \textbf{8. 1}$$

The entropy of mixing becomes:

$$s = -R\sum_{end} p_{end} \ln\left(\frac{p_{end}}{\prod_s y_J^s}\right) + R\left(\sum_s \sum_J n^s y_J^s \ln y_J^s\right) \qquad \textbf{8. 2}$$

such that the random mixing can be recovered when there is no tendency for SRO. The site fractions can be expressed in terms of p_{end} by summing over all p_{end} containing a particular species in the sublattice of interest. As an example, for $y_{U^{5+}}^i$ from Eqn. 6. 4

:

$$y_{U^{5+}}^i = p_{U^{5+}:O^{2-}:O^{2-}} + p_{U^{5+}:O^{2-}:Va} + p_{U^{5+}:Va:O^{2-}} + p_{U^{5+}:Va:Va} \qquad \textbf{8. 3}$$

The Gibbs energy from the CEF is then minimized with respect to p_{end} to represent both long- and short-range ordering.

8.2 Order – disorder transition

The $UO_{2\pm x}$ phase undergoes an oxygen order disorder (OD) transition as discussed in Section 3.6. The current CEF for $UO_{2\pm x}$ does not correctly describe this phenomenon; consequently, the c_p for UO_2 is poorly represented from 2500 K to melting [31] and extrapolations using the model in this range are likely in error for other thermodynamic properties as well. For transient departures from normal operating conditions in a reactor, accurately predicting fuel behavior depends on correctly describing the phase at temperatures where the OD transition occurs.

It was shown in Chapter 6 that the CEF can successfully represent both the c_p vs temperature relationship and the Frenkel defects associated with disordering for ThO_2. It is therefore recommended that the CEF for the UO_2 model be re-examined such that the OD transition, believed to be analogous to that in ThO_2 [68, 69], be better represented.

8.3 Oxygen clustering

At intermediate to high O/M values, neutron diffraction studies have shown oxygen to form Willis 2:2:2 and cuboctehedral type clusters as discussed in Chapter 3. These can be treated by adding an additional sublattice identified with one or both of these defects to the current representation.

The importance of representing the clustering phenomenon is underscored by the following example. Andersson et al. [42] used a kMC method to determine oxygen diffusivities in hyperstoichiometric urania. Fig. 8.1 shows that using a di-interstitial cluster model, the simulation results are in much better agreement with experimental values compared to simply treating the interstitials as randomly oriented on the octahedrally coordinated sites. Including SRO, oxygen clustering, and the OD transition in the CEF for urania phases may better represent the oxygen defect chemistry; coupling

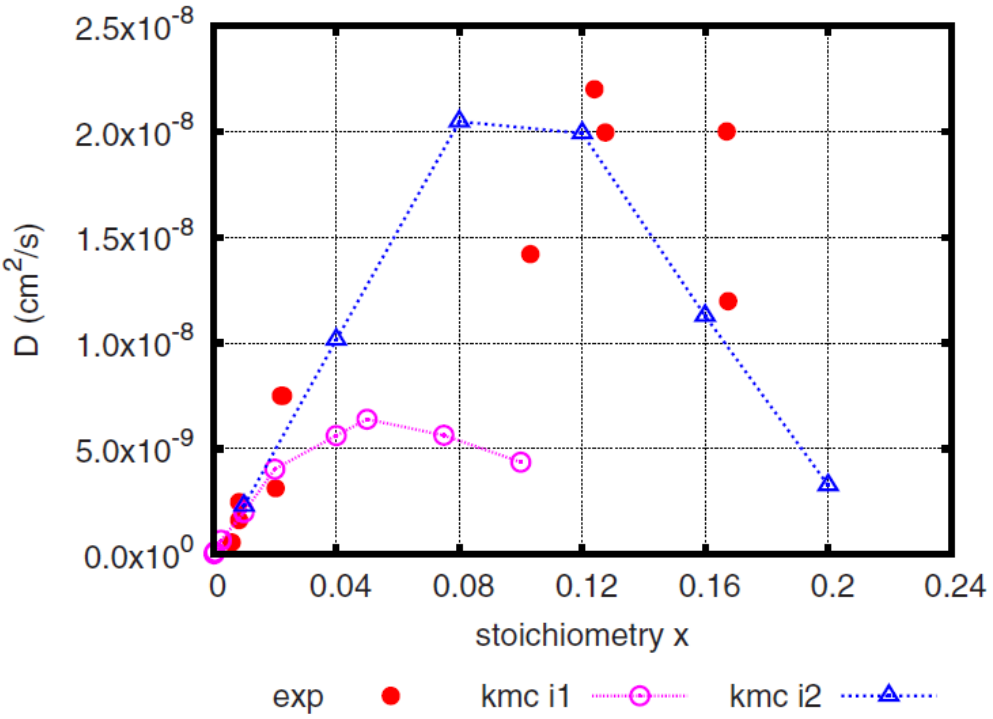

Fig. 8.1. Comparison of experimental (closed red circles) and calculated oxygen diffusivities for UO_{2+x} from kMC by Andersson et al. [42] using simple random (purple open circles) and di-interstitial (open blue triangles) models.

these models with diffusion simulations has the potential to yield higher fidelity oxygen transport results in fluorite structure based fuel.

8.4 Experimental studies

As discussed in Chapter 5, studies of U-Ln-O with a fixed trivalent Ln are analyzed as a group due to lack of data for many of the individual systems; therefore, this work calls for more comprehensive experimental investigations such as equilibrium HTXRD studies for further refinement of the U-Gd-O system. Melting measurements are needed for U-La-O and La-La_2O_3, since these are altogether lacking and should be expanded to include a broader compositional range for U-Gd-O and Gd-Gd_2O_3. There is only one study[109] characterizing the solubilities of RE and U in the metallic and liquid phases; therefore an experimental effort in this area is recommended as well. The data presented in Fig. 7.9(c) suggest the two phase $U_{1-y}La_yO_{2\pm x}$- U_4O_9 region may persist to higher temperatures in contrast to the computed equilibria from this work; therefore, further investigation is called for to determine whether this is the case, or simply an artifact of the measurements for $2.15 < x < 2.20$ and $T > 1073$ K. Lastly, there is a lack of sufficient experimental data to confidently validate the models from Grundy et al. [108]. An effort should be undertaken to determine O solubility in the metallic and sesquioxide polymorphs for La and the other Ln's.

8.5 Conclusions

Ultimately, the decision as to how descriptive the CEF for the UO_2 phase should be depends on a careful consideration of tractability and applicability. As the number of physical phenomena the model represents increases, so does the level of complexity. Sophisticated thermodynamic representations are of little use if the current or emerging state of the art computer programs are computationally unable to handle them. While the recommendations from Sections 8.2 and 8.3 can be immediately implemented, currently

there exists no software capable of utilizing the proposed modifications given by Eqns. 8. 1 – 8. 3 [166]. On the other hand, if application dictates it, as may be the case for multi-scale fuel performance simulation codes, a serious effort for more robust model and companion software development is warranted.

LIST OF REFERENCES

[1] P. Roberts, *Popular Science*, (2011)

[2] L. Riedinger, Fossil Fuel Resources, In, Knoxville, TN: University of Tennessee; 2011.

[3] T. L. Friedman, *Hot, flat, and crowded: Why we need a green revolution--and how it can renew America*, Macmillan, 2008.

[4] N. E. I. contributors, Nuclear Fuel Processes, In, online: Nuclear Energy Institute; 2014.

[5] F. M. Vanek, L. D. Albright, *Energy systems engineering: Evaluation & implementation*, 2008.

[6] H. Chichester, Introduction to Nuclear Reactors, Fuels, and Materials, In: Idaho National Laboratory; 2012.

[7] D. R. Olander, Fundamental aspects of nuclear reactor fuel elements, In: California Univ., Berkeley (USA). Dept. of Nuclear Engineering; 1976.

[8] U.S.NRC, Reactor Fuel Assembly, In, online; 2012.

[9] P.-Y. Chevalier, E. Fischer, B. Cheynet, *J. Nucl. Mater.*, 303 (1) (2002) 1-28.

[10] R. Devanathan, L. Van Brutzel, A. Chartier, C. Guéneau, A. E. Mattsson, V. Tikare, T. Bartel, T. Besmann, M. Stan, P. Van Uffelen, *Energy & Environmental Science*, 3 (10) (2010) 1406-26.

[11] M. Piro, In.

[12] M. Piro, Computation of Thermodynamic Equilibria Pertinent to Nuclear Materials in Multi-Physics Codes, In: Nuclear Engineering: Royal Military College of Canada; 2011.

[13] M. Piro, J. Banfield, K. T. Clarno, S. Simunovic, T. M. Besmann, B. Lewis, W. Thompson, *J. Nucl. Mater.*, 441 (1) (2013) 240-51.

[14] E. Moore, C. Guéneau, J.-P. Crocombette, B. Sundman, F. Hodaj, Assessment of a Diffusion Model in Non-Stoichiometric Uranium dioxide ($UO_{2\pm x}$), In: CALPHAD XLI, Berkeley, CA; 2012.

[15] P. Spencer, *CALPHAD*, 32 (1) (2008) 1-8.

[16] CALPHAD, In: http://www.thermocalc.com/academia/researchers/calphad/; 2014.

[17] M. ZINKEVICH, *Doing and Using, Max-Planck-Institut für Metallforschung, Germany*, (2003)

[18] W. B. White, S. M. Johnson, G. B. Dantzig, *The Journal of Chemical Physics*, 28 (5) (2004) 751-5.

[19] G. Eriksson, *Acta Chem. Scand.*, 25 (7) (1971) 2651-&.

[20] G. Eriksson, *Chemica Scripta*, 8 (3) (1975) 100-3.

[21] G. Eriksson, E. Rosen, *Chemica Scripta*, 4 (5) (1973) 193-4.

[22] J. Andersson, T. Helander, L. Höglund, P. Shi, B. Sundman, *CALPHAD*, 26 (2) (2002) 273-312.

[23] R. Konings, *Comprehensive Nuclear Materials: Online Version*, Newnes, 2011.

[24] O. Redlich, A. T. Kister, *Industrial and Engineering Chemistry*, 40 (2) (1948) 345-8.

[25] M. Hillert, B. Jansson, B. Sundman, *Metall. Trans. A*, 16 (1) (1985) 261-6.

[26] M. Temkin, *Acta. Phys. Chim. USSR*, 20 (1945) 411.

[27] J. M. Prausnitz, R. N. Lichtenthaler, E. G. de Azevedo, *Molecular thermodynamics of fluid-phase equilibria*, Pearson Education, 1998.

[28] B. T. Willis, *J. Chem. Soc., Faraday Trans. 2*, 83 (7) (1987) 1073-81.

[29] R. Grimes, C. Catlow, *Philosophical Transactions of the Royal Society of London. Series A: Physical and Engineering Sciences*, 335 (1639) (1991) 609-34.

[30] J. O. Andersson, A. F. Guillermet, M. Hillert, B. Jansson, B. Sundman, *Acta Metall.*, 34 (3) (1986) 437-45.

[31] C. Guéneau, D. Baichi, C. Labroche, B. Chatillon, B. Sundman, *J. Nucl. Mater.*, 304 (2002) 161.

[32] C. Guéneau, N. Dupin, B. Sundman, C. Martial, J. C. Dumas, S. Gosse, S. Chatain, F. De Bruycker, D. Manara, R. J. M. Konings, *J. Nucl. Mater.*, 419 (2011) 145-67.

[33] K. Park, D. R. Olander, *High Temperature Science*, 29 (1990) 203-22.

[34] K. Park, D. R. Olander, *J. Nucl. Mater.*, 187 (1) (1992) 89-96.

[35] B. Sundman, C. Guéneau, N. Dupin, *Acta Mater.*, 59 (15) (2011) 6039-47.

[36] M. Hillert, L. Staffansson, *Acta Chem. Scand.*, 24 (10) (1970) 3618-26.

[37] C. Guéneau, C. Chatillon, B. Sundman, *J. Nucl. Mater.*, 378 (2008) 257-72.

[38] C. Guéneau, E. Moore, N. Dupin, B. Sundman, Modeling the defect chemistry in non-stoichiometric UO2±x using the Compound Energy Formalism – A tentative link with other approaches, In: CALPHAD, Berkeley, CA; 2012.

[39] H. Matzke, *Journal of the Chemical Society, Faraday Transactions 2: Molecular and Chemical Physics*, 83 (7) (1987) 1121-42.

[40] H. Y. Geng, Y. Chen, Y. Kaneta, M. Kinoshita, *Appl. Phys. Lett.*, 93 (20) (2008) 201903--3.

[41] J.-P. Crocombette, *Phys. Rev. B J1 - PRB*, 85 (14) (2012) 144101.

[42] D. Andersson, T. Watanabe, C. Deo, B. Uberuaga, *Phys. Rev. B J1 - PRB*, 80 (6) (2009) 060101.

[43] F. Garrido, R. Ibberson, L. Nowicki, B. Willis, *J. Nucl. Mater.*, 322 (1) (2003) 87-9.

[44] A. Murray, B. Willis, *J. Solid State Chem.*, 84 (1) (1990) 52-7.

[45] B. Willis, *J. de Phys.*, 25 (5) (1964) 431-9.

[46] B. T. M. Willis, *Journal of the Chemical Society, Faraday Transactions 2: Molecular and Chemical Physics*, 83 (7) (1987) 1073-81.

[47] B. Willis, *Acta Crystallographica Section A: Crystal Physics, Diffraction, Theoretical and General Crystallography*, 34 (1) (1978) 88-90.

[48] S. D. Conradson, D. Manara, F. Wastin, D. L. Clark, G. H. Lander, L. A. Morales, J. Rebizant, V. V. Rondinella, *Inorg. Chem.*, 43 (22) (2004) 6922-35.

[49] N. Saunders, A. P. Miodownik, *CALPHAD (Calculation of Phase Diagrams): A Comprehensive Guide: A Comprehensive Guide*, Elsevier, 1998.

[50] H. L. Lukas, S. G. Fries, B. Sundman, *Computational thermodynamics: the Calphad method*, Cambridge university press Cambridge, 2007.

[51] G. Kresse, J. Furthmüller, *Comput. Mater. Sci.*, 6 (1) (1996) 15-50.

[52] G. Kresse, J. Furthmüller, *Phys. Rev. B J1 - PRB*, 54 (16) (1996) 11169-86.

[53] D.-J. Kim, *J. Am. Ceram. Soc.*, 72 (8) (1989) 1415-21.

[54] R. Shannon, *Acta Crystallographica Section A: Crystal Physics, Diffraction, Theoretical and General Crystallography*, 32 (5) (1976) 751-67.

[55] T. Ohmichi, S. Fukushima, A. Maeda, H. Watanabe, *J. Nucl. Mater.*, 102 (1) (1981) 40-6.

[56] S. C. Moss, *Diffuse Scattering and the Fundamental Properties of Materials*, (2009) 105.

[57] C. Keller, U. Berndt, H. Engerer, L. Leitner, *J. Solid State Chem.*, 4 (3) (1972) 453-65.

[58] R. J. Beals, J. H. Handwerk, *J. Am. Ceram. Soc.*, 110 (2-3) (1965) 311-3.

[59] T. B. Lindemer, A. L. S. Jr., *J. Am. Ceram. Soc.*, 71 (7) (1988) 553-61.

[60] K. Teske, C. Nebelung, H. Ullman, I. I. Kapshukov, L. V. Sudakov, A. S. Bevz, *J. Nucl. Mater.*, 188 (1992) 226-31.

[61] C. W. Bale, P. Chartrand, S. A. Degterov, S. Eriksson, K. Hack, R. B. Mahfoud, J. Melancon, A. D. Pelton, S. Petersen, *CALPHAD*, 26 (2002) 39.

[62] H. G. Diehl, C. Keller, *J. Solid State Chem.*, 3 (4) (1971) 621-36.

[63] C. Keller, A. Boroujerdi, *Journal of Inorganic and Nuclear Chemistry*, 34 (4) (1972) 1187-93.

[64] C. Catlow, *Proceedings of the Royal Society of London. A. Mathematical and Physical Sciences*, 353 (1675) (1977) 533-61.

[65] C. R. A. Catlow, *Journal of the Chemical Society, Faraday Transactions 2: Molecular and Chemical Physics*, 83 (7) (1987) 1065-72.

[66] D. C. HILL, *J. Am. Ceram. Soc.*, 45 (6) (1962) 258-63.

[67] W. Chen, A. Navrotsky, *J. Mater. Res.*, 21 (12) (2006) 3242-51.

[68] M. T. Hutchings, *Journal of the Chemical Society, Faraday Transactions 2: Molecular and Chemical Physics*, 83 (7) (1987) 1083-103.

[69] C. Ronchi, J. Hiernaut, *J. Alloys Compd.*, 240 (1) (1996) 179-85.

[70] E. Yakub, C. Ronchi, D. Staicu, *The Journal of Chemical Physics*, 127 (2007) 094508.

[71] J. Hiernaut, G. Hyland, C. Ronchi, *Int. J. Thermophys.*, 14 (2) (1993) 259-83.

[72] R. Agarwal, R. Prasad, V. Venugopal, *J. Nucl. Mater.*, 322 (2–3) (2003) 98-110.

[73] K. Bakker, E. Cordfunke, R. Konings, R. Schram, *J. Nucl. Mater.*, 250 (1) (1997) 1-12.

[74] S. Dash, S. C. Parida, Z. Singh, B. K. Sen, V. Venugopal, *J. Nucl. Mater.*, 393 (2) (2009) 267-81.

[75] D. Fischer, J. Fink, L. Leibowitz, *J. Nucl. Mater.*, 102 (1) (1981) 220-2.

[76] J. Ralph, *Journal of the Chemical Society, Faraday Transactions 2: Molecular and Chemical Physics*, 83 (7) (1987) 1253-62.

[77] M. Zinkevich, *Progress in Materials Science*, 52 (4) (2007) 597-647.

[78] J. D. Landry, F. C. Schoenig, L. N. Grossman, H. Bernatowicz, I. S. Jacobs, *J. Appl. Phys.*, 53 (11) (1982) 8260-2.

[79] A. Nakamura, *Zeitschrift für Physikalische Chemie, Bd*, 207 (1998) 223-43.

[80] J. H. Yang, K. S. Kim, K. W. Kang, K. W. Song, Y. H. Jung, *J. Nucl. Mater.*, 340 (2005) 171-8.

[81] K. Une, M. Oguma, *J. Nucl. Mater.*, 115 (1) (1983) 84-90.

[82] K. Une, M. Oguma, *J. Nucl. Mater.*, 110 (2–3) (1982) 215-22.

[83] R. V. Krishnan, G. Panneerselvam, P. Manikandan, M. Antony, K. Nagarajan, *Journal of Nuclear and Radiochemical Sciences*, 10 (1) (2009) 19-26.

[84] M. Amaya, K. Une, M. Hirai, *J. Nucl. Sci. Technol.*, 41 (2) (2004) 108-15.

[85] Y. Takahashi, M. Asou, *J. Nucl. Mater.*, 201 (0) (1993) 108-14.

[86] H. Inaba, K. Naito, M. Oguma, *J. Nucl. Mater.*, 149 (3) (1987) 341-8.

[87] S. G. Popov, V. N. Proselkov, Thermodynamic Assessment of Solidus and Liquidus of Urania-Gadolinia Fuels, In: Proceedings of Top Fuel 2009; 2009, pp. 378-84.

[88] S. Yamanouchi, T. Tachibana, K. Tsukui, M. Oguma, *J. Nucl. Sci. Technol.*, 25 (6) (1988) 528-33.

[89] L. N. Grossman, D. R. Packard, H. W. Hill, (U,Gd)$O_{2.00}$ Phase Equilibria at Hight Temperatures, In: Colloques Intern. CNRS No 205; 1972, p. 453.

[90] T. Wada, K. Noro, K. Tsukui, Behavior of UO_2-Gd_2O_3 fuel, In: Nuclear Fuel Performance, British Nuclear Energy Society Conference, London, England; 1973.

[91] K. W. Kang, J. H. Yang, J. H. Kim, Y. W. Rhee, D. J. Kim, K. S. Kim, K. W. Song, *Thermochim. Acta*, 455 (1–2) (2007) 134-7.

[92] T. Yamada, H. Matsuda, M. Yoshimura, *JOURNAL-HIGH TEMPERATURE SOCIETY*, 25 (1999) 71-9.

[93] C. H. Lupis, *Chemical thermodynamics of materials*, North-Holland New York et al., 1983.

[94] A. Boudene, K. Hack, A. Mohammad, D. Neuschütz, E. Zimmermann, G. Effenberg, S. Fries, H.-L. Lukas, R. Konetzki, R. Schmid-Fetzer, *High temperature and materials science*, 35 (2) (1996) 159-79.

[95] O. Carlson, *J. Phase Equlib.*, 11 (1) (1990) 61-6.

[96] J. Gröbner, U. Kolitsch, H. Seifert, S. Gomes Fries, H. Lukas, F. Aldinger, *Z. Metallk.*, 87 (2) (1996) 88-91.

[97] V. Lysenko, *Inorganic materials*, 32 (4) (1996) 392-6.

[98] H. Okamoto, *Journal of Phase Equilibria and Diffusion*, 32 (6) (2011) 574-.

[99] Q. Ran, H. Leo Lukas, G. Effenberg, G. Petzow, *Journal of the Less Common Metals*, 146 (1989) 213-22.

[100] V. Swamy, H. J. Seifert, F. Aldinger, *J. Alloys Compd.*, 269 (1–2) (1998) 201-7.

[101] W. E. Wang, *High temperature and materials science*, 37 (1) (1997) 13-22.

[102] M. Chen, B. Hallstedt, L. J. Gauckler, *Solid State Ionics*, 170 (3) (2004) 255-74.

[103] T. Fujisawa, S. Takai, C. Yamauchi, Solubility of Oxygen in Cerium and Neodymium, In: First International Conference on Processing Materials for Properties; 1993, pp. 917-20.

[104] D. Lemarchand, P. Vigier, B. Labulle, *Magnetics, IEEE Transactions on*, 26 (5) (1990) 2649-51.

[105] V. Lysenko, *Russian journal of physical chemistry*, 78 (2) (2004) 161-5.

[106] H. Sano, T. Yoshida, S. Takai, K. Kuroda, T. Fujisawa, C. Yamauchi, *JOURNAL-MINING AND MATERIALS PROCESSING INSTITUTE OF JAPAN*, 115 (1999) 49-53.

[107] M. Chen, B. Hallstedt, L. J. Gauckler, *CALPHAD*, 29 (2) (2005) 103-13.

[108] A. N. Grundy, B. Hallstedt, L. J. Gauckler, *J. Phase Equlib.*, 22 (2) (2001) 105-13.

[109] J. Haefling, A. Daane, *Trans. Met. Soc. AIME*, 215 (1959)

[110] D. Shin, T. M. Besmann, *J. Nucl. Mater.*, 433 (2013) 227-32.

[111] T. Matsui, K. Naito, *J. Nucl. Mater.*, 138 (1) (1986) 19-26.

[112] K. Yoshida, T. Arima, Y. Inagaki, K. Idemitsu, M. Osaka, S. Miwa, *J. Nucl. Mater.*, 418 (1–3) (2011) 22-6.

[113] K. Hagemark, M. Broli, *J. Am. Ceram. Soc.*, 50 (11) (1967) 563-7.

[114] E. Stadlbauer, U. Wichmann, U. Lott, C. Keller, *J. Solid State Chem.*, 10 (4) (1974) 341-50.

[115] W. Lambertson, M. Mueller, URANIUM OXIDE PHASE EQUILIBRIUM SYSTEMS: V, UO $ sub 2$-Nd $ sub 2$ O $ sub 3$ VI, U $ sub 3$ O $ sub 8$-MgO VII, U $ sub 3$ O $ sub 8$-TiO $ sub 2$. FINAL REPORT, In: Argonne National Lab.; 1954.

[116] ACerS-NIST PHASE EQUILIBRIA DIAGRAMS Version 4.0, In; 2013.

[117] E. A. Aitken, S. F. Bartram, E. F. Juenke, *Inorg. Chem.*, 3 (7) (1964) 949-54.

[118] M. Tang, K. S. Holliday, C. Jiang, J. A. Valdez, B. P. Uberuaga, P. O. Dickerson, R. M. Dickerson, Y. Wang, K. R. Czerwinski, K. E. Sickafus, *J. Solid State Chem.*, 183 (4) (2010) 844-8.

[119] T. F. Cycle, *International Atomic Energy Agency (IAEA) Technical Document*, 1450 (2005)

[120] R. Benz, *J. Nucl. Mater.*, 29 (1) (1969) 43-9.

[121] R. Ackermann, M. Tetenbaum, High-temperature thermodynamic properties of the thorium-oxygen system, In: Presented at the Intern. Colloq. on Mater. for High-

Temperature Energy, Toronto, 16 Jul. 1979 and Intern. Symp. on Thermodyn. of Nucl. Mater., Jeulich, West Germany, 29 Jan.-2 Feb. 1979; 1979.

[122] J. S. Anderson, D. N. Edgington, L. E. J. Roberts, E. Wait, *Journal of the Chemical Society (Resumed)*, 0 (0) (1954) 3324-31.

[123] I. Cohen, R. Berman, *J. Nucl. Mater.*, 18 (2) (1966) 77-107.

[124] M. Foex, *Comptes Rendus*, 215 (1942) 534-6.

[125] F. Hund, G. Niessen, *Z. Electrochem*, 56 (1952) 972-9.

[126] E. Lynch, J. Handwerk, C. Hoenig, *J. Am. Ceram. Soc.*, 43 (10) (1960) 520-4.

[127] M. Ugajin, *J. Nucl. Mater.*, 110 (2–3) (1982) 140-6.

[128] M. Ugajin, T. Shiratori, K. Shiba, *J. Nucl. Mater.*, 116 (2–3) (1983) 172-7.

[129] M. Hoch, H. L. Johnston, *The Journal of Physical Chemistry*, 65 (7) (1961) 1184-5.

[130] F. Jaeger, W. Veenstra, Exact Measurements of the Specific Heats of Solid Substances at High Temperatures, In: Proc. Acad. Sci. Amsterdam; 1934, pp. 61-6.

[131] J. Southard, *J. Am. Chem. Soc.*, 63 (11) (1941) 3142-6.

[132] J. R. Springer, E. A. Eldridge, N. U. Goodyear, T. R. Wright, J. F. Lagedrost, *BMI-X-10210*, (1967)

[133] A. C. Victor, T. B. Douglas, *J. Research Natl. Bur. Standards*, 65 (1961)

[134] D. F. Fischer, J. K. Fink, L. Leibowitz, J. Belle, *J. Nucl. Mater.*, 118 (2–3) (1983) 342-8.

[135] S. Aronson, J. C. Clayton, *The Journal of Chemical Physics*, 32 (3) (1960) 749-54.

[136] L. Roberts, L. Russel, A. Adwick, A. Walter, M. Rand, In: Proc. Intern. Conf. Peaceful Uses of Atomic Energy, second, Geneva; 1958, p. 215.

[137] T. Matsui, K. Naito, *J. Nucl. Mater.*, 132 (3) (1985) 212-21.

[138] S. Anthonysamy, J. Joseph, P. R. Vasudeva Rao, *J. Alloys Compd.*, 299 (1–2) (2000) 112-7.

[139] S. Anthonysamy, K. Nagarajan, P. R. V. Rao, *J. Nucl. Mater.*, 247 (0) (1997) 273-6.

[140] H. Tanaka, E. Kimura, A. Yamaguchi, J. Moriyama, THERMODYNAMIC PROPERTIES OF NON-STOICHIOMETRIC UO2--ThO2 SOLID SOLUTION BY ELECTRO-MOTIVE FORCE MEASUREMENTS, In: Kyoto Univ.; 1972.

[141] R. Kandan, R. Babu, P. Manikandan, R. Venkata Krishnan, K. Nagarajan, *J. Nucl. Mater.*, 384 (3) (2009) 231-5.

[142] E. A. Aitken, J. A. Edwards, R. A. Joseph, *The Journal of Physical Chemistry*, 70 (4) (1966) 1084-90.

[143] C. A. Alexander, *United States Patent*, (1986)

[144] M. Yamawaki, T. Nagasaki, M. Kanno, *J. Nucl. Mater.*, 130 (0) (1985) 207-16.

[145] M. UGAJIN, *J. Nucl. Sci. Technol.*, 20 (3) (1983) 228-36.

[146] C. A. Alexander, J. S. Ogden, G. W. Cunningham, Thermal stability of zirconia-s and thoria-base fuels (LWBR Development Program), In; 1967, p. Medium: X; Size: Pages: 27.

[147] C. A. Alexander, J. S. Ogden, W. M. Pardue, *Plutonium 1970 and other Actinides, ed. W.N. Miner*, New York, The Metallurgical Society of the American Institute of Mining, Metallurgical and Petroleum Engineers Inc.

[148] R. Paul, C. Keller, *J. Nucl. Mater.*, 41 (2) (1971) 133-42.

[149] H. Boekschoten, N. Kema, *Journal of Inorganic and Nuclear Chemistry*, 30 (1) (1968) 119-26.

[150] F. Mumpton, R. Roy, *J. Am. Ceram. Soc.*, 43 (5) (1960) 234-40.

[151] R. Böhler, A. Quaini, L. Capriotti, P. Çakır, O. Beneš, K. Boboridis, A. Guiot, L. Luzzi, R. Konings, D. Manara, *J. Alloys Compd.*, (2014)

[152] W. A. Lambertson, M. H. Mueller, F. H. Gunzel, *J. Am. Ceram. Soc.*, 36 (12) (1953) 397-9.

[153] R. Latta, E. Duderstadt, R. Fryxell, *J. Nucl. Mater.*, 35 (3) (1970) 347-9.

[154] S. Aronson, J. Belle, *The Journal of Chemical Physics*, 29 (1) (1958) 151-8.

[155] E. Walker, R. Vedder, G. Bell, *TRANSACTIONS-AMERICAN NUCLEAR SOCIETY*, 98 (2008) 116.

[156] S. L. Voit, Personal Communication, In.

[157] G. C. Silva, J. D. Hunn, C. Yeamans, G. S. Cerefice, K. R. Czerwinski, *Inorg. Chem.*, 50 (21) (2011) 11004-10.

[158] Netzsch, *TG-DTA/DSC Apparatus: STA 449 F1 Jupiter*, 2011.

[159] K. Hagemark, M. Broli, *Journal of Inorganic and Nuclear Chemistry*, 28 (12) (1966) 2837-50.

[160] J. R. Taylor, *An introduction to error analysis: the study of uncertainties in physical measurements*, University science books, 1997.

[161] J. M. Smith, H. C. Van Ness, M. M. Abbott, *An Introduction to Chemical Engineering Thermodynamics*, New York, McGraw-Hill, 1996.

[162] G.-y. Adachi, N. Imanaka, *Chemical reviews*, 98 (4) (1998) 1479-514.

[163] A. T. Dinsdale, *CALPHAD*, (1991) 317-425.

[164] N. A. Grundy, E. Povoden, T. Ivas, L. J. Gauckler, *CALPHAD*, 30 (1) (2006) 33-41.

[165] M. Sahu, K. Krishnan, M. K. Saxena, K. L. Ramakumar, *J. Alloys Compd.*, 482 (1–2) (2009) 141-6.

[166] M. Hillert, *J. Alloys Compd.*, (2001) 161-76.

[167] R. Venkata Krishnan, P. Manikandan, H. Jena, K. Nagarajan, *Thermochim. Acta*, 472 (1-2) (2008) 95-8.

[168] Z. Li, X. Liu, C. Wang, *J. Alloys Compd.*, 476 (1) (2009) 193-8.

[169] *Scientific Group Thermodata Europe (SGTE), Thermodynamic Properties of Inorganic Materials*, Heidelberg Berlin, Springer Verlag, 1999.

[170] K. Kvashnina, S. M. Butorin, P. Martin, P. Glatzel, *Phys. Rev. Lett.*, 111 (25) (2013) 253002.

[171] I. B. De Alleluia, M. Hoshi, W. G. Jocher, C. Keller, *Journal of Inorganic and Nuclear Chemistry*, 43 (8) (1981) 1831-4.

[172] J. W. McMurray, D. Shin, B. W. Slone, T. M. Besmann, *J. Nucl. Mater.*, (2014)

[173] H. Kleykamp, *J. Nucl. Mater.*, 206 (1) (1993) 82-6.

[174] L. Desgranges, Personal Communication, In.

[175] R. J. Beals, J. H. Handwerk, B. J. Wrona, *J. Am. Ceram. Soc.*, 52 (11) (1969) 578-81.

[176] S. G. Popov, V. N. Proselkov, V. A. Lysenko, *Atomic Energy*, 110 (4) (2011) 221.

[177] W. M. Olson, R. N. R. Mulford, *J. Phys. Chem.*, (1963) 952-4.

[178] A. Dinsdale, SGTE unary database, version. 4.4, In; 2011.

[179] D. Peterson, *J. Phase Equlib.*, 6 (5) (1985) 443-5.

[180] A. Yacout, *http://web.anl.gov/eesa/pdfs/nuclear_factsheets/nuclear_fuel_yacout.pdf*, (2011)

[181] A. J. Darnell, W. A. McCollum, In: North American Aviation (U.S.A) Report, NAA-SR 6498, Off. Tech. Sers., Dept. Comm., Wash. 25, DC; 1960.

[182] R. Ackermann, E. Rauh, R. Thorn, M. Cannon, *The Journal of Physical Chemistry*, 67 (4) (1963) 762-9.

[183] B. Sundman, C. Guéneau, N. Dupin, *Acta Mater.*, 59 (15) (2011) 6039-47.

[184] B. Mihaila, M. Stan, J. Ramirez, A. Zubelewicz, P. Cristea, *J. Nucl. Mater.*, 394 (2) (2009) 182-9.

[185] J. M. Solomon, V. Alexandrov, B. Sadigh, A. Navrotsky, M. Asta, *Acta Mater.*, 78 (0) (2014) 282-9.

[186] M. Aizenshtein, T. Y. Shvareva, A. Navrotsky, *J. Am. Ceram. Soc.*, 93 (12) (2010) 4142-7.

[187] R. J. Konings, O. Beneš, *J. Phys. Chem. Ref. Data*, 39 (2010) 043102.

APPENDIX

APPENDIX A

TABULATED EXPERIMENTAL RESULTS

Table A.1
Equilibrium oxygen pressures versus O/M relationship as a function of temperature and *y* for $U_{1-y}Th_yO_{2+x}$ in tabular form.

y	Temperature (K)	O/M	$\log p_{O_2}$	Error in $\log p_{O_2}$
0.0	1573	2.000	-15	0.056
0.0	1573	2.002	-11	0.288
0.0	1573	2.046	-6.6	0.747
0.0	1573	2.169	-4	0.262
0.0	1350	2.000	-18	0.079
0.0	1350	2.000	-11	0.116
0.0	1350	2.002	-10	0.269
0.0	1350	2.007	-9	0.806
0.0	1350	2.270	-4	0.270
0.05	1273	2.000	-19	0.079
0.05	1273	2.001	-17	0.079
0.05	1273	2.001	-14	0.080
0.05	1273	2.002	-13	0.086
0.05	1273	2.003	-11	0.321
0.05	1273	2.248	-5	2.595
0.05	1273	2.003	-11	0.321
0.05	1573	2.000	-15	0.055
0.05	1573	2.005	-11	0.056
0.05	1573	2.008	-9	0.067

Table A.1. Continued.

y	Temperature (K)	O/M	$\log p_{O_2}$	Error in $\log p_{O_2}$
0.05	1573	2.032	-7	0.349
0.05	1573	2.166	-4	0.265
0.05	1773	2.000	-13	0.041
0.05	1773	2.002	-10	0.041
0.05	1773	2.004	-9	0.041
0.05	1773	2.006	-8	0.042
0.05	1773	2.012	-7	0.044
0.05	1773	2.026	-6	0.06
0.05	1773	2.073	-5	0.653
0.05	1773	2.106	-4	0.041
0.20	1273	2.000	-18	0.079
0.20	1273	2.001	-14	0.08
0.20	1273	2.001	-12	0.128
0.20	1273	2.339	-4	0.268
0.20	1573	2.001	-11	0.056
0.20	1573	2.002	-10	0.057
0.20	1573	2.004	-9	0.067
0.20	1573	2.015	-8	0.124
0.20	1573	2.175	-3.35	0.041
0.20	1573	2.175	-3	0.262
0.20	1573	2.239	-2	0.055
0.20	1773	2.000	-13	0.041
0.20	1773	2.005	-8	0.044
0.20	1773	0.020	-6	0.135
0.20	1773	2.001	-12	0.041
0.20	1773	2.001	-11	0.041
0.20	1773	2.158	-3	0.48

Table A.1. Continued.

y	Temperature (K)	O/M	$\log p_{O_2}$	Error in $\log p_{O_2}$
0.20	1773	2.211	-2	0.041

APPENDIX B

U–Gd–O THERMODYNAMIC DATA

Table B.1
Gibbs functions for the models constituting the U-Gd-O assessment.

Thermodynamic parameters (J/mole)	Reference
Gas phase	[169]
${}^{\circ}G_{O_2}^{gas}$	[169]
${}^{\circ}G_{O_3}^{gas}$	[169]
${}^{\circ}G_{O}^{gas}$	[169]
${}^{\circ}G_{GdO}^{gas}$	[169]
${}^{\circ}G_{Gd}^{gas}$	[169]
${}^{\circ}G_{U}^{gas}$	[169, 187]
${}^{\circ}G_{UO_3}^{gas}$	[187]
${}^{\circ}G_{UO_2}^{gas}$	[187]
${}^{\circ}G_{UO}^{gas}$	[187]
Stoichiometric compounds	
${}^{\circ}G_{Gd}^{hcp}$	[169]
${}^{\circ}G_{Gd}^{bcc}$	[169]
${}^{\circ}G_{Gd_2O_3}^{C}$	[77]
${}^{\circ}G_{Gd_2O_3}^{B}$	[77]
${}^{\circ}G_{Gd_2O_3}^{A}$	[77]
${}^{\circ}G_{Gd_2O_3}^{H}$	[77]
${}^{\circ}G_{Gd_2O_3}^{X}$	[77]
${}^{\circ}G_{U}^{\alpha}$	[169]
${}^{\circ}G_{U}^{\beta}$	[169]
${}^{\circ}G_{U}^{\gamma}$	[169]
${}^{\circ}G_{UO_3}^{solid}$	[32]

Table B.1.Continued.

Thermodynamic parameters (J/mole)	Reference
${}^{\circ}G^{\alpha}_{U_3O_8}$	[32]
${}^{\circ}G^{\beta}_{U_3O_8}$	[32]
${}^{\circ}G^{\gamma}_{U_3O_8}$	[32]
${}^{\circ}G^{\delta}_{U_3O_8}$	[32]
${}^{\circ}G^{\alpha}_{U_4O_9}$	[32]
${}^{\circ}G^{\beta}_{U_4O_9}$	[32]
${}^{\circ}G^{\gamma}_{U_4O_9}$	[32]
${}^{\circ}G_{UGd_6O_{12}} = -6829939.38 + 976.47T - 222.418T\ln T - 3.2927E-01T^2 + 7.666667E-05T^3 - 363670T^{-1}$	This work
Fluorite SS: $(U^{3+},U^{4+},U^{5+},U^{6+},Gd^{3+})_1(O^{2-},Va^0)_2(O^{2-},Va^0)$	
$\Delta E^{GdO_{1.5}\rightarrow GdO_2}_{GdO_{1.5}} = 26092$	This work
${}^{\circ}G^{F}_{UO_2}$	[169]
${}^{\circ}G^{F}_{U^{3+}:O:O} = {}^{\circ}G^{F}_{U^{3+}:O:Va} + \frac{1}{2}{}^{\circ}G^{gas}_{O_2}$	[169]
${}^{\circ}G^{F}_{U^{3+}:O:Va} = {}^{\circ}G^{F}_{UO_2} - {}^{\circ}G^{F}_{U^{4+}:Va:Va} + {}^{\circ}G^{F}_{U^{3+}:Va:Va}$	[32]
${}^{\circ}G^{F}_{U^{3+}:Va:Va} = {}^{\circ}G^{F}_{UO_2} - {}^{\circ}G^{gas}_{O_2} + 747127 - 70.23T - 2RT\left[\frac{3}{4}\ln\left(\frac{3}{4}\right) + \frac{1}{4}\ln\left(\frac{1}{4}\right)\right]$	[32]
${}^{\circ}G^{F}_{U^{3+}:Va:O} = 100000$	[32]
${}^{\circ}G^{F}_{U^{4+}:O:O} = {}^{\circ}G^{F}_{UO_2} + \frac{1}{2}{}^{\circ}G^{gas}_{O_2}$	[32]
${}^{\circ}G^{F}_{U^{4+}:O:Va} = {}^{\circ}G^{F}_{UO_2}$	[32]
${}^{\circ}G^{F}_{U^{4+}:Va:Va} = {}^{\circ}G^{F}_{UO_2} - {}^{\circ}G^{gas}_{O_2} + 545210.5$	[32]
${}^{\circ}G^{F}_{U^{4+}:Va:O} = 100000$	[32]
${}^{\circ}G^{F}_{U^{5+}:O:O} = {}^{\circ}G^{F}_{U^{5+}:O:Va} + \frac{1}{2}{}^{\circ}G^{gas}_{O_2}$	[32]
${}^{\circ}G^{F}_{U^{5+}:O:Va} = {}^{\circ}G^{F}_{UO_2} - 58351.62 + 039.68T - RT\ln\left(\frac{1}{2}\right)$	[32]
${}^{\circ}G^{F}_{U^{5+}:Va:Va} = {}^{\circ}G^{F}_{U^{5+}:O:Va} - {}^{\circ}G^{gas}_{O_2} + 700000$	[32]

Table B.1.Continued.

Thermodynamic parameters (J/mole)	Reference
${}^{\circ}G^{F}_{U^{5+}:Va:O} = 100000$	[32]
${}^{\circ}G^{F}_{Gd^{3+}:O:O} = \frac{1}{2}{}^{\circ}G^{C}_{Gd_2O_3} + \frac{3}{4}{}^{\circ}G_{O_2} + \Delta E^{GdO_{1.5}\rightarrow GdO_2}_{GdO_{1.5}} + 72423.46 + 18.02T$	This work
${}^{\circ}G^{F}_{Gd^{3+}:O:O} = \frac{1}{2}{}^{\circ}G^{C}_{Gd_2O_3} + \frac{3}{4}{}^{\circ}G_{O_2} + \Delta E^{GdO_{1.5}\rightarrow GdO_2}_{GdO_{1.5}} + 72423.46 + 18.02T$	This work
${}^{\circ}G^{F}_{Gd^{3+}:Va:Va} = \frac{1}{2}{}^{\circ}G^{C}_{Gd_2O_3} - \frac{3}{4}{}^{\circ}G_{O_2} + \Delta E^{GdO_{1.5}\rightarrow GdO_2}_{GdO_{1.5}} + 542524.76 - 28.56T$	This work
${}^{\circ}G^{F}_{Gd^{3+}:Va:O} = 100000$	This work
${}^{\circ}G^{F}_{U^{6+}:O:O} = {}^{\circ}G^{F}_{U^{5+}:O:O} + 31961.2 + 0.498T$	This work
${}^{\circ}G^{F}_{U^{6+}:O:Va} = {}^{\circ}G^{F}_{U^{5+}:O:Va} + 31961.3 + 0.978T$	This work
${}^{\circ}G^{F}_{U^{6+}:Va:Va} = {}^{\circ}G^{F}_{U^{5+}:Va:Va} - 668038.4 - 2.062T$	This work
${}^{\circ}G^{F}_{U^{6+}:Va:O} = 100000$	This work
${}^{F}L^{0}_{U^{4+},U^{5+}:O:O} = -124936 - 21.68T$	This work
${}^{F}L^{0}_{U^{3+},U^{4+}:O:Va} = 40133.7$	[32]
${}^{F}L^{1}_{U^{3+},U^{4+}:O:Va} = 1076.4$	[32]
${}^{F}L^{0}_{U^{3+},Gd^{3+}:O:Va} = -50000$	This work
${}^{F}L^{1}_{U^{3+},Gd^{3+}:O:Va} = 500000$	This work
${}^{F}L^{0}_{U^{4+},Gd^{3+}:Va:Va} = -472654.32$	This work
${}^{F}L^{0}_{U^{4+},Gd^{3+}:O:Va} = -65000$	This work
${}^{F}L^{1}_{U^{4+},Gd^{3+}:O:Va} = 5000$	This work
${}^{F}L^{0}_{U^{4+},Gd^{3+}:O:O} = -100000$	This work
${}^{F}L^{0}_{U^{5+},Gd^{3+}:O:O} = -427050.06$	This work
${}^{F}L^{0}_{U^{5+},Gd^{3+}:Va:Va} = -875000 - 217.29T$	This work
${}^{F}L^{0}_{U^{5+},Gd^{3+}:O:Va} = -70000 - 10T$	This work
${}^{F}L^{1}_{U^{5+},Gd^{3+}:O:Va} = -54994.5$	This work
Liquid: $(Gd^{3+},U^{4+})_P(O^{2-},Va^{Q-},O)_Q$	
${}^{\circ}G^{liq}_{Gd^{3+}:O^{2-}} = -1733378 + 572.3402T - 114.534T\ln T - 0.007203T^2 + 540000T^{-1}$	[77]

Table B.1.Continued.

Thermodynamic parameters (J/mole)		Reference
${}^{\circ}G^{liq}_{Gd^{3+}:Va} = 6225.4407 + 88.80921T - 24.721413TlnT$ $- 0.2852405E-02T^{2} - .31467408E-06T^{3}$ $- 8665.7335T^{-1}$	298<T<1000	
${}^{\circ}G^{liq}_{Gd^{3+}:Va} = 146262.04 - 1208.7069T + 159.35208TlnT$ $- 0.10824714T^{2} + 0.10694551E-04T^{3}$ $- 19678357T^{-1}$	1000<T<1508	[169]
${}^{\circ}G^{liq}_{Gd^{3+}:Va} = -5397.314 + 192.33622T - 38.5075TlnT$	1508<T	
${}^{liq}L^{0}_{Gd^{3+},U^{4+}:O^{2-}} = 769964.6 - 320.82T$		This work
${}^{liq}L^{1}_{Gd^{3+},U^{4+}:O^{2-}} = 719997.34 - 276.70T$		This work
${}^{liq}L^{2}_{Gd^{3+},U^{4+}:O^{2-}} = 10006.25 - 28.97T$		This work
${}^{liq}L^{0}_{Gd^{3+},U^{4+}:Va} = 1.0E+06$		This work

APPENDIX C

U–La–O THERMODYNAMIC DATA

Table C.1
Gibbs functions for the models constituting the U-La-O assessment.

Thermodynamic parameters (J/mole)	Reference
Gas phase	
${}^{\circ}G_{O_2}^{gas}$	[169]
${}^{\circ}G_{O_3}^{gas}$	[169]
${}^{\circ}G_{O}^{gas}$	[169]
${}^{\circ}G_{LaO}^{gas}$	[169]
${}^{\circ}G_{La_2}^{gas}$	[169]
${}^{\circ}G_{La_2O}^{gas}$	[169]
${}^{\circ}G_{La_2O_2}^{gas}$	[169]
${}^{\circ}G_{U}^{gas}$	[169]
${}^{\circ}G_{UO_3}^{gas}$	[187]
${}^{\circ}G_{UO_2}^{gas}$	[187]
${}^{\circ}G_{UO}^{gas}$	[187]
Stoichiometric compounds	
${}^{\circ}G_{La}^{dhcp}$	[169]
${}^{\circ}G_{La}^{fcc}$	[169]
${}^{\circ}G_{La}^{bcc}$	[169]
${}^{\circ}G_{La_2O_3}^{A}$	[77]
${}^{\circ}G_{La_2O_3}^{H}$	[77]
${}^{\circ}G_{La_2O_3}^{X}$	[77]
${}^{\circ}G_{U}^{\alpha}$	[169]
${}^{\circ}G_{U}^{\beta}$	[169]
${}^{\circ}G_{U}^{\gamma}$	[169]

Table C.1.Continued.

Thermodynamic parameters (J/mole)	Reference
$^{\circ}G_{UO_3}^{solid}$	[32]
$^{\circ}G_{U_3O_8}^{\alpha}$	[32]
$^{\circ}G_{U_3O_8}^{\beta}$	[32]
$^{\circ}G_{U_3O_8}^{\gamma}$	[32]
$^{\circ}G_{U_3O_8}^{\delta}$	[32]
$^{\circ}G_{U_4O_9}^{\alpha}$	[32]
$^{\circ}G_{U_4O_9}^{\beta}$	[32]
$^{\circ}G_{U_4O_9}^{\gamma}$	[32]
$^{\circ}G_{U_2La_6O_{15}} = -8975017.608 + 3570.35355T - 573.361T\ln T + 2.928000E-04T^2 - 6.361983E-06T^3 + 4.161472E+06T^{-1} - 30000000T^{-2}$	This work
Fluorite SS: $(U^{3+},U^{4+},U^{5+},U^{6+},La^{3+})_1(O^{2-},Va^0)_2(O^{2-},Va^0)$	
$^{\circ}G_{La_2O_3} = -1834559.8 + 686.41611T - 119.72939\ T\ln T - 0.007115T^2 + 675024.4700T^{-1}$	[61]
$\Delta E_{LaO_{1.5}}^{LaO_{1.5}\rightarrow CaF_2} = 8739$	This work
$^{\circ}G_{UO_2}^{F}$	[169]
$^{\circ}G_{U^{3+}:O:O}^{F} = {}^{\circ}G_{U^{3+}:O:Va}^{F} + \frac{1}{2}{}^{\circ}G_{O_2}^{gas}$	[169]
$^{\circ}G_{U^{3+}:O:Va}^{F} = {}^{\circ}G_{UO_2}^{F} - {}^{\circ}G_{U^{4+}:Va:Va}^{F} + {}^{\circ}G_{U^{3+}:Va:Va}^{F}$	[32]
$^{\circ}G_{U^{3+}:Va:Va}^{F} = {}^{\circ}G_{UO_2}^{F} - {}^{\circ}G_{O_2}^{gas} + 747127 - 70.23T - 2RT\left[\frac{3}{4}\ln\left(\frac{3}{4}\right) + \frac{1}{4}\ln\left(\frac{1}{4}\right)\right]$	[32]
$^{\circ}G_{U^{3+}:Va:O}^{F} = 100000$	[32]
$^{\circ}G_{U^{4+}:O:O}^{F} = {}^{\circ}G_{UO_2}^{F} + \frac{1}{2}{}^{\circ}G_{O_2}^{gas}$	[32]
$^{\circ}G_{U^{4+}:O:Va}^{F} = {}^{\circ}G_{UO_2}^{F}$	[32]
$^{\circ}G_{U^{4+}:Va:Va}^{F} = {}^{\circ}G_{UO_2}^{F} - {}^{\circ}G_{O_2}^{gas} + 545210.5$	[32]
$^{\circ}G_{U^{4+}:Va:O}^{F} = 100000$	[32]

Table C.1.Continued.

Thermodynamic parameters (J/mole)	Reference
$^{\circ}G^{F}_{U^{4+}:Va:O} = 100000$	[32]
$^{\circ}G^{F}_{U^{5+}:O:O} = {}^{\circ}G^{F}_{U^{5+}:O:Va} + \frac{1}{2}{}^{\circ}G^{gas}_{O_2}$	[32]
$^{\circ}G^{F}_{U^{5+}:O:Va} = {}^{\circ}G^{F}_{UO_2} - 58351.62 + 039.68T - RT\ln\left(\frac{1}{2}\right)$	[32]
$^{\circ}G^{F}_{U^{5+}:Va:Va} = {}^{\circ}G^{F}_{U^{5+}:O:Va} - {}^{\circ}G^{gas}_{O_2} + 700000$	[32]
$^{\circ}G^{F}_{U^{5+}:Va:O} = 100000$	[32]
$^{\circ}G^{F}_{La^{3+}:O:O} = \frac{1}{2}{}^{\circ}G_{La_2O_3} + \frac{3}{4}{}^{\circ}G_{O_2} + \Delta E^{LaO_{1.5}\rightarrow CaF_2}_{LaO_{1.5}} - 173551.98 + 107.52T$	This work
$^{\circ}G^{F}_{La^{3+}:O:Va} = \frac{1}{2}{}^{\circ}G_{La_2O_3} + \frac{1}{4}{}^{\circ}G_{O_2} + \Delta E^{LaO_{1.5}\rightarrow CaF_2}_{LaO_{1.5}} - 140021.83 + 14.94T$	This work
$^{\circ}G^{F}_{La^{3+}:Va:Va} = \frac{1}{2}{}^{\circ}G_{La_2O_3} - \frac{3}{4}{}^{\circ}G_{O_2} + \Delta E^{LaO_{1.5}\rightarrow CaF_2}_{LaO_{1.5}} + 387211.19 + 9.80T$	This work
$^{\circ}G^{F}_{La^{3+}:Va:O} = 100000$	This work
${}^{F}L^{0}_{U^{4+},U^{5+}:O:O} = -124936 - 21.68T$	This work
${}^{F}L^{0}_{U^{3+},U^{4+}:O:Va} = 40133.7$	[32]
${}^{F}L^{1}_{U^{3+},U^{4+}:O:Va} = 1076.4$	[32]
${}^{F}L^{0}_{U^{3+},La^{3+}:O:Va} = -50000$	This work
${}^{F}L^{1}_{U^{3+},La^{3+}:O:Va} = 500000$	This work
${}^{F}L^{0}_{U^{4+},La^{3+}:Va:Va} = -472248.79$	This work
${}^{F}L^{0}_{U^{4+},La^{3+}:O:Va} = -48198.701$	This work
${}^{F}L^{0}_{U^{5+},La^{3+}:O:O} = -427681.07$	This work
${}^{F}L^{0}_{U^{5+},La^{3+}:O:Va} = -9350 - 50T$	This work
${}^{F}L^{0}_{U^{5+},La^{3+}:Va:Va} = -786023.31 - 217.00T$	This work
${}^{F}L^{0}_{U^{6+},La^{3+}:O:Va} = -75000$	This work

Liquid: $(La^{3+},U^{4+})_P(O^{2-},Va^{Q-},O)_Q$

Table C.1.Continued.

Thermodynamic parameters (J/mole)		Reference
${}^{\circ}G^{liq}_{La^{3+}:O^{2-}} = -1691745.0 + 636.34440T - 120.62900T\ln T - 0.68540000E\text{-}02T^2 + 808000.00T^{-1} - 10000000T^{-2}$		[77]
${}^{\circ}G^{liq}_{La^{3+}:Va} = 5332.6530 + 18.230120\ T - 11.018819T\ln T - 0.20171603E-01T^2 + 0.29377500E-05T^3 - 133541.00T^{-1}$	298<T<1134	[169]
${}^{\circ}G^{liq}_{La^{3+}:Va} = -3942.0031 + 171.01844T - 34.308800T\ln T$	1134<T<4000	[169]
${}^{liq}L^0_{La^{3+},U^{4+}:O^{2-}} = 770000.00 - 320.00T$		This work
${}^{liq}L^1_{La^{3+},U^{4+}:O^{2-}} = 720000.00 - 276.00T$		This work
${}^{liq}L^2_{La^{3+},U^{4+}:O^{2-}} = 10000.0 - 29.997T$		This work
${}^{liq}L_{La^{3+},U^{4+}:Va} = +1E6$		This work
RI: $(U^{4+},U^{5+},U^{6+})_1(La^{3+})_6(O^{2-},Va^0)_{12}$		
${}^{\circ}G^{RI}_{U^{4+}:La^{3+}:O} = -6594442.10 + 19.7705140T\text{-}119.7340T\ln T\text{-} 7.1130E\text{-}03T^2 + 675500T^{-1}$		This work
${}^{\circ}G_{U^{4+}:La^{3+}:Va} = -6624442.1 + 19.7705140T\text{-}119.7340T\ln T\text{-} 7.1130E\text{-}03T^2 + 675500T^{-1}$		This work
${}^{\circ}G^{RI}_{U^{5+}:La^{3+}:O} = -6390467.3 - 250.229T\text{-}119.7340T\ln T\text{-} 7.1130E\text{-}03T^2 + 675500T^{-1}$		This work
${}^{\circ}G^{RI}_{U^{5+}:La^{3+}:Va} = -6390467.3 - 250.2294T\text{-}119.7340T\ln T\text{-} 7.1130E\text{-}03T^2 + 675500T^{-1}$		This work
${}^{\circ}G^{RI}_{U^{6+}:La^{3+}:O} = -7283192.1 + 269.77051T\text{-}119.7340T\ln T\text{-} 7.1130E\text{-}03T^2 + 675500T^{-1}$		This work
${}^{\circ}G^{RI}_{U^{6+}:La^{3+}:Va} = -7339342.1 + 269.77051T\text{-}119.7340T\ln T\text{-} 7.1130E\text{-}03T^2 + 675500T^{-1}$		This work
RIII: $(La^{3+},U^{5+},U^{6+})_4(La^{3+})_4(O^{2-})_{16}$		This work
${}^{\circ}G^{RIII}_{La^{3+}:La^{3+}O^{2-}} = -9171306.753 + 3686.43212T - 603.642T\ln T + 9.529E\text{-}03T^2 - 8.483E\text{-}06T^3 + 4471296T^{-1} - 26666666.667T^{-2}$		This work
${}^{\circ}G^{RIII}_{U^{5+}:La^{3+}:O^{2-}} = -9139089.753 + 3556.43212T - 603.642T\ln T + 9.529E\text{-}03T^2 - 8.483E\text{-}06T^3 + 4471296T^{-1} - 26666666.667T^{-2}$		This work

Table C.1.Continued.

Thermodynamic parameters (J/mole)	Reference
$^{\circ}G^{RIII}_{U^{5+}:La^{3+}:O^{2-}} = -9139089.753 + 3556.43212T - 603.642T\ln T + 9.529E\text{-}03T^{2} - 8.483E\text{-}06T^{3} + 4471296T^{-1} - 26666666.667T^{-2}$	This work
$^{\circ}G^{RIII}_{U^{6+}:La^{3+}:O^{2-}} = -9109173.753 + 3686.43212T - 603.642T\ln T + 9.529E\text{-}03T^{2} - 8.483E\text{-}06T^{3} + 4471296T^{-1} - 26666666.667T^{-2}$	This work

APPENDIX D

U–Th–O THERMODYNAMIC DATA

Table D.1
Gibbs functions for the models constituting the U-Th-O assessment.

Thermodynamic parameters (J/mole)	Reference
Gas phase	
${}^{\circ}G_{O_2}^{gas}$	[169]
${}^{\circ}G_{O_3}^{gas}$	[169]
${}^{\circ}G_{O}^{gas}$	[169]
${}^{\circ}G_{ThO}^{gas}$	[169]
${}^{\circ}G_{ThO_2}^{gas}$	[169]
${}^{\circ}G_{U}^{gas}$	[169]
${}^{\circ}G_{UO_3}^{gas}$	[187]
${}^{\circ}G_{UO_2}^{gas}$	[187]
${}^{\circ}G_{UO}^{gas}$	[187]
Stoichiometric compounds	
${}^{\circ}G_{UO_3}^{solid}$	[32]
${}^{\circ}G_{U_3O_8}^{\alpha}$	[32]
${}^{\circ}G_{U_3O_8}^{\beta}$	[32]
${}^{\circ}G_{U_3O_8}^{\gamma}$	[32]
${}^{\circ}G_{U_3O_8}^{\delta}$	[32]
${}^{\circ}G_{U_4O_9}^{\alpha}$	[32]
${}^{\circ}G_{U_4O_9}^{\beta}$	[32]
${}^{\circ}G_{ThUO_5}^{solid} = -2612606.838 + 1112.42445T - 177.303T\ln T + 7.254711E-03T^2 - 3.304816E\text{-}06T^3 + 1.391627E+06T^{-1}$	This work
M_4O_9 SS: $(U^{4+},U^{5+},Th^{4+})_4(O^{2-},Va^0)_9$	

Table D.1.Continued.

Thermodynamic parameters (J/mole)	Reference
${}^{\circ}G^{\gamma}_{U_4O_9}$	[32]
${}^{\circ}G^{M_4O_9}_{U^{4+}:O^{2-}} = {}^{\circ}G^{\gamma}_{U_4O_9} - 4RT\left[\ln 0.5\right]$	This work
${}^{\circ}G^{M_4O_9}_{U^{5+}:O^{2-}} = {}^{\circ}G^{\gamma}_{U_4O_9} - 4RT\left[\ln 0.5\right]$	This work
${}^{\circ}G^{M_4O_9}_{Th^{4+}:O^{2-}} = {}^{\circ}G^{\gamma}_{U_4O_9} - 688000.0 + 63.08T$	This work
${}^{M_4O_9}L^0_{Th^{4+},U^{4+}:O^{2-}} = -130219.55$	This work
${}^{M_4O_9}L^0_{Th^{4+},U^{5+}:O^{2-}} = -1000.0 + 32.5T$	This work
Fluorite SS: $(U^{3+},U^{4+},U^{5+},U^{6+},Th^{3+},Th^{4+})_1(O^{2-},Va^0)_2(O^{2-},Va^0)$	
${}^{\circ}G^{F}_{UO_2}$	[169]
${}^{\circ}G^{F}_{ThO_2}$	[169]
${}^{\circ}G^{F}_{U^{3+}:O:O} = {}^{\circ}G^{F}_{U^{3+}:O:Va} + \frac{1}{2}{}^{\circ}G^{gas}_{O_2}$	[32]
${}^{\circ}G^{F}_{U^{3+}:O:Va} = {}^{\circ}G^{F}_{UO_2} - {}^{\circ}G^{F}_{U^{4+}:Va:Va} + {}^{\circ}G^{F}_{U^{3+}:Va:Va}$	[32]
${}^{\circ}G^{F}_{U^{3+}:Va:Va} = {}^{\circ}G^{F}_{UO_2} - {}^{\circ}G^{gas}_{O_2} + 747127 - 70.23T - 2RT\left[\frac{3}{4}\ln\left(\frac{3}{4}\right) + \frac{1}{4}\ln\left(\frac{1}{4}\right)\right]$	[32]
${}^{\circ}G^{F}_{U^{3+}:Va:O} = 100000$	[32]
${}^{\circ}G^{F}_{U^{4+}:O:O} = {}^{\circ}G^{F}_{UO_2} + \frac{1}{2}{}^{\circ}G^{gas}_{O_2}$	[32]
${}^{\circ}G^{F}_{U^{4+}:O:Va} = {}^{\circ}G^{F}_{UO_2}$	[32]
${}^{\circ}G^{F}_{U^{4+}:Va:Va} = {}^{\circ}G^{F}_{UO_2} - {}^{\circ}G^{gas}_{O_2} + 545210.5$	[32]
${}^{\circ}G^{F}_{U^{4+}:Va:O} = 100000$	[32]
${}^{\circ}G^{F}_{U^{5+}:O:O} = {}^{\circ}G^{F}_{U^{5+}:O:Va} + \frac{1}{2}{}^{\circ}G^{gas}_{O_2}$	[32]
${}^{\circ}G^{F}_{U^{5+}:O:Va} = {}^{\circ}G^{F}_{UO_2} - 58351.62 + 039.68T - RT\ln\left(\frac{1}{2}\right)$	[32]
${}^{\circ}G^{F}_{U^{5+}:Va:Va} = {}^{\circ}G^{F}_{U^{5+}:O:Va} - {}^{\circ}G^{gas}_{O_2} + 700000$	[32]
${}^{\circ}G^{F}_{U^{5+}:Va:O} = 100000$	[32]

Table D.1.Continued.

Thermodynamic parameters (J/mole)	Reference
$^{\circ}G^{F}_{U^{6+}:Va:Va} = {}^{\circ}G^{F}_{U^{5+}:Va:Va} - 668038.4 - 2.062T$	This work
$^{\circ}G^{F}_{U^{6+}:Va:O} = 100000$	This work
$^{\circ}G^{F}_{Th^{3+}:O:O} = {}^{\circ}G^{F}_{ThO_2} + \frac{1}{2}{}^{\circ}G_{O_2} + 453705.90 + 17.83T$	This work
$^{\circ}G^{F}_{Th^{3+}:O:Va} = {}^{\circ}G^{F}_{ThO_2} + 301206.99 - 21.77T$	This work
$^{\circ}G^{F}_{Th^{3+}:Va:Va} = {}^{\circ}G^{F}_{ThO_2} - {}^{\circ}G_{O_2} + 458916.73 - 86.91T$	This work
$^{\circ}G^{F}_{Th^{3+}:Va:O} = 0.00$	This work
$^{\circ}G^{F}_{Th^{4+}:O:O} = {}^{\circ}G^{F}_{ThO_2} + \frac{1}{2}{}^{\circ}G_{O_2} - 14012.33 + 17.14T$	This work
$^{\circ}G^{F}_{Th^{3+}:O:Va} = {}^{\circ}G^{F}_{ThO_2}$	This work
$^{\circ}G^{F}_{Th^{4+}:Va:Va} = {}^{\circ}G^{F}_{Th^{4+}:O:O} + 1269026.4 + 4.00T\ln T$	This work
$^{\circ}G^{F}_{Th^{4+}:Va:O} = 0.00$	This work
${}^{F}L^{0}_{U^{4+}\cdot U^{5+}:O:O} = -124936 - 21.68T$	This work
${}^{F}L^{0}_{U^{3+}\cdot U^{4+}:O:Va} = 40133.7$	[32]
${}^{F}L^{1}_{U^{3+}\cdot U^{4+}:O:Va} = 1076.4$	[32]
${}^{F}L^{0}_{Th^{3+}\cdot Th^{4+}:O:Va} = -51000$	This work
${}^{F}L^{0}_{U^{4+}\cdot Th^{4+}:Va:Va} = 750000 + 150T$	This work
${}^{F}L^{0}_{U^{4+}\cdot Th^{4+}:O:Va} = -9750 - 25T$	This work
${}^{F}L^{0}_{U^{4+}\cdot Th^{4+}:O:O} = 5000$	This work
${}^{F}L^{1}_{U^{4+}\cdot Th^{4+}:O:O} = 25000$	This work
${}^{F}L^{0}_{U^{5+}\cdot Th^{4+}:O:O} = -200500 - 20T$	This work
${}^{F}L^{0}_{U^{5+}\cdot Th^{4+}:O:Va} = -48621.53$	This work
Liquid: $(Th^{4+},U^{4+})_P(O^{2-},Va^{Q-},O)_Q$	
$^{\circ}G^{liq}_{U}$	[169]
$^{\circ}G^{liq}_{UO_2}$	[169]
$^{\circ}G^{liq}_{Th}$	[169]
$^{\circ}G^{liq}_{ThO_2}$	[169]

Table D.1.Continued.

Thermodynamic parameters (J/mole)	Reference
${}^{\circ}G_{Th^{4+}:Va} = {}^{\circ}G_{Th}^{liq}$	[169]
${}^{\circ}G_{Th^{4+}:O^{2-}} = {}^{\circ}G_{ThO_2}^{liq} - 165657.97 + 48.35T$	[168]
${}^{liq}L^{0}_{Th^{4+}\cdot U^{4+}:O^{2-}} = -182000$	This work
${}^{liq}L^{1}_{Th^{4+}\cdot U^{4+}:O^{2-}} = 45000$	This work
${}^{liq}L^{0}_{Th^{4+}\cdot U^{4+}:Va} = 31448 - 1.32T$	This work
${}^{liq}L^{1}_{Th^{4+}\cdot U^{4+}:Va} = -5858 + 0.311T$	This work
${}^{liq}L^{2}_{Th^{4+}\cdot U^{4+}:Va} = 67 + 4.852T$	This work
α-Th: $(Th,U)_1$	
${}^{\circ}G_{Th}^{\alpha}$	[169]
${}^{\circ}G_{U}^{\alpha-Th} = {}^{\circ}G_{U}^{\alpha-U} + 5000$	[168]
${}^{\alpha-Th}L^{0}_{Th\cdot U} = 40725 - 8.853T$	[168]
${}^{\alpha-Th}L^{1}_{Th\cdot U} = 10706 - 4.356T$	[168]
${}^{\alpha-Th}L^{2}_{Th\cdot U} = 193 + 0.154T$	[168]
β-Th,γ-U: $(Th,U)_1$	
${}^{\circ}G_{Th}^{\beta}$	[168]
${}^{\circ}G_{U}^{\gamma}$	[169]
${}^{\beta-Th}L^{0}_{Th\cdot U} = 34257 + 1.569T$	[168]
${}^{\beta-Th}L^{1}_{Th\cdot U} = -10061 + 0.324T$	[168]
${}^{\beta-Th}L^{2}_{Th\cdot U} = 10096 + 0.608T$	[168]
α-U: $(Th,U)_1$	
${}^{\circ}G_{Th}^{\alpha-U} = {}^{\circ}G_{Th}^{\alpha-Th} + 48000$	[168]
${}^{\circ}G_{U}^{\alpha}$	[169]
β-U: $(Th,U)_1$	
${}^{\circ}G_{Th}^{\beta-U} = {}^{\circ}G_{Th}^{\alpha-Th} + 52000$	[168]
${}^{\circ}G_{U}^{\beta}$	[169]

VITA

Jacob W. McMurray is the first of three children born in Kingsport, TN. He grew up in Scott County, VA, named after General Winfield Scott, in the small town of Weber City, nestled in the heart of the Clinch Mountains of the greater Appalachian Mountain range that stretches from Georgia to Maine. After attending Gate City High School, he went on to study Chemical Engineering at the University of Mississippi where he graduated Cum Laude with a B.S. in 2001. In 2000, Jacob completed two internships, one as an Energy Research Undergraduate Laboratory Fellow at Oak Ridge National Laboratory in Oak Ridge, TN and another at CTR Inc. of Charlotte, NC. After graduation, he went to work at AgWater Technologies in Harrisonburg, VA and later studied abroad in 2003 at the University of Guanajuato in Guanajuato Mexico where he met his wife Perla. Since that time, Jacob has served as an Americorp volunteer, taught English as a Second Language and Chemistry for Scott County Schools and worked as an engineering consultant for Blue Ocean Water Technology where he discovered his passion for sustainable and efficient energy storage and conversion. This experience led him to pursue a Ph.D. in Energy Science and Engineering to be better equipped to improve energy systems.